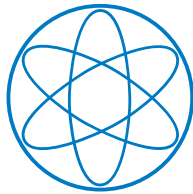# Few-Body Correlations in Many-Body Physics

Dissertation

von

Marcus Barth

Physik Department T34

Technische Universität München

# Technische Universität München

Physik Department
Lehrstuhl T34, Univ.-Prof. Dr. Wilhelm Zwerger

# Few-Body Correlations in
# Many-Body Physics

Marcus Barth

Vollständiger Abdruck der von der Fakultät für Physik
der Technischen Universität München zur Erlangung des akademischen Grades eines

Doktors der Naturwissenschaften (Dr.rer.nat)

genehmigten Dissertation.

| | |
|---|---|
| Vorsitzender: | Univ.-Prof. Christian Pfleiderer, Ph.D. |
| Prüfer der Dissertation: | 1. Univ.-Prof. Dr. Wilhelm Zwerger |
| | 2. Univ.-Prof. Dr. Hans-Werner Hammer<br>Technische Universität Darmstadt |
| | 3. Prof. Yusuke Nishida, Ph.D.<br>Institute of Technology Tokyo / Japan<br>(nur schriftliche Beurteilung) |

Die Dissertation wurde am 03.08.2015 bei der Technischen Universität München eingereicht und durch die Fakultät für Physik am 01.12.2015 angenommen.

## Zusammenfassung

In dieser Arbeit werden kalte Gase sowie das Elektronengas mittels zweier Methoden studiert, die im Prinzip dasselbe Ziel verfolgen: Die Beschreibung solcher Parameterregime, in denen die Wenigteilchenphysik über die kollektiven Vielteilcheneffekte dominiert. Die Operatorproduktentwicklung (OPE) aus der Quantenfeldtheorie wird verwendet, um das Hochfrequenzverhalten derjenigen Korrelationsfunktion zu extrahieren, welche die Antwort eines zweidimensionalen Fermi Gases mit Kontaktwechselwirkung auf eine externe Radiofrequenzstörung bestimmt. Aus diesem Hochfrequenzverhalten werden Summenregeln für das nullte und erste Moment des Radiofrequenzspektrums hergeleitet, welche diese Momente in Beziehung zur Teilchenzahl und dem Kontakt des Systems setzen. Die Eigenschaften der Spektralfunktion des zweidimensionalen Fermi Gases im nicht-entarteten Regime werden mittels einer Virialentwicklung bestimmt. Aus der Spektralfunktion werden Observablen wie die Zustandsdichte und die Impulsverteilung errechnet. Diese zeigen exzellente Übereinstimmung mit Tan's universellen Relationen. Im zweiten Teil dieser Arbeit wird die Virialentwicklung auf sowohl bosonische als auch fermionische dreidimensionale Quantengase angewendet. Virialkoeffizienten, Kontakte und Impulsverteilung werden bis zur dritten Ordnung in der Fugazität bestimmt, was Dreiteilchenkorrelationen in exakter Form einbezieht. Die Resultate stimmen exzellent mit (schon vorher) bekannten universellen Relationen überein. Im dritten Teil dieser Arbeit wird die OPE sowohl auf das zweidimensionale als auch das dreidimensionale wechselwirkende Elektronengas angewendet. In der Impulsverteilung und dem statischen Strukturfaktor ergibt sich ein algebraischer Abfall bei hohen Impulsen, in Übereinstimmung mit schon bekannten Resultaten von J. Kimball.

iv

**Abstract**

In this thesis, cold gases as well as the electron gas are analyzed with two expansion techniques that have, in essence, the same aim: To describe parameter regimes where the few-body aspect dominates over the collective many-body behavior. The Operator Product Expansion (OPE) of quantum field theory is used to extract high-frequency properties of the correlation function that determines the radio-frequency (RF) response of a two-dimensional Fermi gas with zero-range interactions. Exact sum rules that relate the zeroth and first moment of the radio-frequency spectrum to the particle number and the *contact* of the gas, are derived from these properties. A quantum cluster (virial-) expansion is employed to study the properties of the spectral function of the two-dimensional Fermi gas at small to moderate degeneracy. From the spectral function, observables like the density of states and the momentum distribution are calculated and are found to be in excellent agreement with Tan's universal relations. In the second part of the thesis, the cluster expansion is applied to both bosonic and fermionic three-dimensional quantum gases. Virial coefficients, contacts and momentum distribution are calculated up to third order in the fugacity. This includes three-particle correlations exactly. The results are are in excellent agreement with known universal relations. In the third part of this thesis, an OPE is applied to the problem of the interacting electron gas in both two and three dimensions. A power-law decay of the momentum distribution and the static structure factor at high momenta is found, compatible with earlier findings by J. Kimball.

# Contents

*Contents*

# List of Figures

# List of Tables

# Chapter 1

# Introduction

In this thesis, the many-body problem will be analyzed in the limits where the few-body aspects of the system dominate. In these cases, the complexity of the problem simplifies greatly and few-body results can be used to describe the many-body system. This makes it, for example, possible to extract exact relations for various correlation functions. Such exact relations are valuable, because they allow to obtain information about many-body correlations from experiment, which might not be accessible otherwise. From a theoretical standpoint, they are also of use because they allow to test numerical results for internal consistency. For the numerical results that will be shown in this thesis, such exact relations were indeed always used as a test.

Specifically, we use the operator product expansion (OPE) of quantum field theory, developed by Wilson and Kadanoff [1, 2], to extract exact relations from short-distance and short-time correlations of various correlation functions. The OPE is an expansion of local operators at different points in space-time, with respect to their separation. Recently, it was shown to converge both in relativistic [3, 4] and non-relativistic [5] conformal theories. Consider the product of two operators $A$ and $B$ at points $x$ and $y$ in space-time. The generic OPE of this operator product then reads

$$A(x)B(y) \;\; = \;\; \sum c_n(x - y)\mathcal{O}_n(y), \qquad (1.1)$$

where we chose to expand around the point $y$. The so called Wilson coefficients $c_n$ are complex valued functions of the separation $x - y$. The OPE orders operators

by their scaling dimensions, with operators of lowest scaling dimensions appearing earlier in the expansion. The lower the scaling dimension of an operator, the earlier it contributes in the expansion (ordered in "powers" of $x-y$). The scaling dimension of an operator can be obtained from the knowledge of the scaling of the operator product of $\mathcal{O}_n$ and its hermitian conjugate at small separations in times. For an operator composed of $N_F$ fermionic fields, for example, this correlation function scales like[1] $t^{-\Delta_n}\exp\left(-i\frac{N_F m r^2}{2t}\right)$, which defines the scaling dimension $\Delta_n$. This, for example, leads to the fact that the operator $\psi$ in $d$ spatial dimensions has scaling dimension $d/2$. Since the OPE in eq. 1.1 is an operator relation, it holds between any state (it is said to hold in the so called weak sense [6]). To determine the coefficients $c_n(x-y)$, we can hence use the simplest states that still allow for the extraction of a Wilson coefficient at a given order. In this thesis for example, we will only need to calculate *two-body* diagrams of both sides of the equation to extract the Wilson coefficients to the order we are interested in. Once the Wilson coefficient is fixed by this matching procedure, we can then infer the short-distance behavior of the correlator in any state. Of course, in the many-body system, we are unable to calculate the expectation values of the local operators on the right-hand side exactly. However, even without the explicit evaluation of these expectation values, the OPE gives rise to non-trivial exact relations between observables, which in turn can be also tested experimentally. For further introduction to the OPE, see the contributions of E. Braaten in [7], as well as the contribution of Y. Nishida and D. Son in the same reference. We will use the OPE in chapter 2.2 to extract the high-frequency behavior of the radio-frequency spectrum of a two-dimensional Fermi gas. In chapter 4, we will meet the OPE again while deriving high-momentum properties of the momentum distribution and static structure factor for the Coulomb gas.

The other method used in this thesis is the quantum cluster expansion, which we will also call virial expansion for simplicity[2]. It relies on the observation that in the limit of high temperatures, the fugacity $z = e^{\beta\mu}$, where $\mu$ is the chemical potential and $\beta = 1/k_B T$ denotes inverse temperature, is a small parameter. Hence, one can expand the grand-canonical partition function $\mathcal{Z}$ in terms of the fugacity, which results in an expansion of the form

$$\mathcal{Z} = \mathrm{Tr} e^{-\beta(H-\mu N)} = \sum_{N=0}^{\infty} z^N \mathrm{tr}_N e^{-\beta H}, \qquad (1.2)$$

---

[1] In most of this thesis, we will set $\hbar = 1$

[2] The difference between the two is very minor. The virial expansion expands in terms of small densities [8] $n\lambda_T^d$, the cluster expansion in terms of small fugacities $z$.

where $\text{tr}_N$ denotes the trace over a sector of the Hilbert space that contains $N$ particles. For small enough fugacities $z \ll 1$, truncating the expansion (1.2) becomes a good approximation, which greatly simplifies the problem, because in order to evaluate the traces, one now only needs to solve a *few-body* problem. The virial expansion can not only be defined for thermodynamic quantities, but also for correlation functions [9] in a diagrammatic formulation. In chapter 2.3, this allows us to calculate the single-particle spectral function of a two-dimensional Fermi gas. In chapter 3, we will use the virial expansion to extract three-body correlations in the momentum distribution of three-dimensional Bose/Fermi gases. In the bosonic case, these correlations are linked to the *Efimov effect* [10, 11].

# Chapter 2

# Two-dimensional Fermi gases

In both two and three dimensions, the ability to tune the interaction strength of a Fermi gas opens the possibility to probe different types of physics. In the three-dimensional system at low temperatures, for example, one finds a BCS-like superfluid at large and negative inverse scattering lengths, where the pairing of Fermions with opposite momentum close to the Fermi surface gives rise to superfluidity. At positive scattering lengths, there exists a true two-body bound state called the *dimer*. When the inverse scattering lengths become large on the positive $1/k_F a$-side, the energy of this bound state provides the dominant scale in the system. The system is now well approximated as a gas of structureless *bosonic* dimers. This is the so called BEC-side. Since there is no phase transition between these different values of the scattering length, the system exhibits the so called *BCS-BEC crossover* [7]. At zero density however, the two (BEC and BCS) limits are separated by a multicritical point [12, 13].

Fluctuations are generally more pronounced in two dimensions, which results, if the two-body potentials falls of sufficiently fast at large distances, in the absence of spontaneous symmetry breaking of a continuous symmetry at $T \neq 0$ [14, 15]. This is referred to as the Hohenberg-Mermin-Wagner theorem. The superfluid-normal transition in two dimensions is of the BKT-type [16, 17]. This that means correlation functions decay with a power-law at large distances, rather than approaching a constant, as is the case for true long range order. Mean field theory suggests that the transition temperature is around $T_c \approx 0.1 T_F$ for $E_D/E_F \approx 10$ [18], where $E_D$ denotes the energy of a two-body bound state (see sec. 2.1 below). The Fermi

energy in two dimensions and for a two-component balanced gas is given by $E_F = k_F^2/2m = \pi n/m$, where $n$ is the density and $m$ is the mass of the atoms. The critical temperature as a function of $E_D$ was calculated in [19], and they find $T_c/T_F \to 0$ as the two-body bound state energy $E_D$ is lowered from the BEC regime to the BCS regime. The realization of (quasi-) two-dimensional cold atom systems using deep one-dimensional optical lattices allows to study the peculiarities of the two-dimensional system also experimentally. Recently, the critical temperature was measured experimentally over a wide range of the crossover [20]. The enhanced fluctuations in two dimensions suggest that the effects of a pseudo-gap might be more pronounced. This will be one of our concerns in section 2.3.

In this chapter, we will extract some exact relations, as well as numerical predictions, for the two-dimensional Fermi gas. In sec. 2.1, a short introduction to our model and the relevant physical parameters will be given. In sec. 2.2, universal relations that hold for the radio-frequency transition rate of a two-dimensional Fermi gas will be derived. Sec. 2.3 will study the high-temperature limit of the spectral function of the system. Various other quantities, such as the density of states and the momentum distribution, will be extracted from the spectral function.

## 2.1 The model

This chapter will cover all the definitions and conventions we will need for our study of the high-frequency tail of the RF spectrum, as well as the high-temperature expansion of the spectral function. The low-energy scattering properties of a generic two-dimensional system can be characterized by the two-dimensional scattering length $a_2$ [21]. For low energies, where s-wave scattering dominates, the two-particle scattering amplitude between two fermions of different species can be approximated by [22]

$$f(k) \approx \frac{4}{-\cot \delta_0(k) + i} = \frac{4\pi}{\ln(1/k^2 a_2^2) + i\pi}. \tag{2.1}$$

Note that this scattering amplitude has a pole in the upper half of the complex $k$ plane for all real $a_2$. This means that in a system characterized by the two-dimensional scattering length in the above way, we always have a two-particle bound state – also called the *dimer* – with binding energy[1] $E_D = 1/ma_2^2$. In the case of cold atoms, two-dimensional systems are created by confining the motion of the particles

---

[1] A sign convention: Binding energies are positive, the energy of the bound state in question is the negative of the binding energy.

in one direction, which we chose to be the $z$-axis. Assuming an harmonic confinement with large oscillator frequency $\omega_z$, it can be shown [22] that the two-dimensional scattering length is determined by the three-dimensional scattering length of the atoms via

$$a_2(a) = l_z \sqrt{\frac{\pi}{B}} e^{-\sqrt{\frac{\pi}{2}} \frac{l_z}{a}} \tag{2.2}$$

The oscillator length of the confining potential $l_z = \sqrt{1/m\omega_z}$ is a measure for the strength of the confinement, and $B = 0.905..$ is a universal constant. The three-dimensional scattering length $a$ can be tuned by means of a Feshbach resonance. The above formula can be obtained as a limiting case of the relation

$$\frac{l_z}{a} = \int_0^\infty \frac{du}{\sqrt{4\pi u^3}} \left( 1 - \frac{e^{-\frac{\varepsilon_b}{\omega_z} u}}{\sqrt{\frac{1-\exp(-2u)}{2u}}} \right), \tag{2.3}$$

that relates the ratio $\varepsilon_b/\omega_z$ of the confinement induced bound state and oscillator frequency to the three-dimensional scattering length for *arbitrary* strength of the confinement. Assuming strong confinement $\varepsilon_b/\omega_z \ll 1$, we recover (2.2) when identifying $\frac{1}{ma_2^2} = E_D = \varepsilon_b$. The motion of the system becomes effectively two-dimensional, when $\omega_z \gg \mu, k_B T$, where $\mu$ is the chemical potential, and $T$ is temperature. In this case, the atoms can only occupy the ground state of the harmonic oscillator and the motion of the atoms in the $z$-direction is frozen out. The motion in the $x - y$ plane is then well described by the scattering amplitude (2.1). An effective theory that catches the scattering behavior (2.1) just contains local interactions between the different fermion species. The Hamiltonian density for this local theory reads

$$\mathcal{H} = \sum_\sigma \psi_\sigma^\dagger \left( -\frac{\nabla^2}{2m} \right) \psi_\sigma + \sum_{\sigma,\sigma'} \frac{g_{\sigma\sigma'}}{2} \psi_\sigma^\dagger \psi_{\sigma'}^\dagger \psi_{\sigma'} \psi_\sigma, \tag{2.4}$$

where all the fields are at the same position $\mathbf{x}$. $\sigma$ and $\sigma'$ run over the number of present fermion species (typically two, or three in the case of RF spectroscopy in section 2.2). The Hamiltonian operator $H = \int d^2 x \mathcal{H}(\mathbf{x})$ can be obtained from (2.4) by integration over all space. In order to model atoms in different internal spin states, the masses of the different species $\sigma$ were chosen to be equal. The results can be easily generalized to contain non-equal masses $m_\sigma$. The Lagrangian density, from which it is easier to read off the Feynman rules of the theory, is given by

$$\mathcal{L} = \sum_\sigma \psi_\sigma^\dagger \left( i\partial_t + \frac{\nabla^2}{2m} \right) \psi_\sigma - \sum_{\sigma,\sigma'} \frac{g_{\sigma\sigma'}}{2} \psi_\sigma^\dagger \psi_{\sigma'}^\dagger \psi_{\sigma'} \psi_\sigma. \tag{2.5}$$
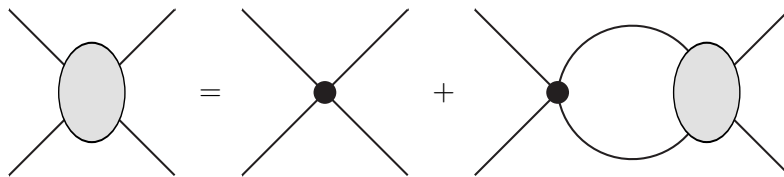
Figure 2.1: Integral equation for the scattering amplitude $\mathcal{A}$ of fermions of species 1 and 2. The integral equation corresponds to an infinite series of ladder diagrams.

It should be noted that this Lagrangian can be rewritten in terms of an auxiliary, non-dynamical, field $d$ [23, 24, 25]. This has the effect of reorganizing some diagrams of, for example, the operator product expansion in section 2.2. In this chapter, the auxiliary field trick is only employed for the calculation of the RF spectrum of a diatomic molecule. During the cluster expansion performed in chapter 3 however, the auxiliary field simplifies the calculation of symmetry factors for certain Feynman diagrams. In the remainder of this section, we will only deal with the case of two species $\sigma = 1, 2$ for the sake of notational simplicity. The case of three species is a straightforward generalization. The Feynman rules of the theory (2.5) for the case $\sigma = 1, 2$ are given in Appendix[2] A. Calculating the two-body scattering amplitude of different species via the Lippmann-Schwinger equation, diagrammatically depicted in fig. 2.1, reveals the need to regularize the theory. For more insight on the calculation of the scattering amplitude via the Lippmann-Schwinger equation, I refer to my diploma thesis on the one-dimensional Tan relations [27], where this issue was discussed in detail. Everything that changes in the case discussed here is the replacement of one-dimensional by two-dimensional momentum integrals. A cutoff-regulated coupling constant can be chosen to be

$$g \equiv g_{12}(\Lambda) \;\; = \;\; -\frac{2\pi}{m}\frac{1}{\log a_2 \Lambda}.\tag{2.6}$$

Another regularization scheme that works well in the present case is dimensional regularization [28]. In either renormalization scheme, the two-body scattering amplitude in the center of mass frame of two atoms of species 1 and 2 with momentum

---

[2]For the real time action defined by the Lagrangian (2.5), we will always use the conventions of the Appendix A. When continuing to imaginary time, however, it is more convenient to get rid of the various imaginary units $i$ attached to the propagators and vertices. In this case, we will use the conventions given in the book by Abrikosov *et al.* [26].

**k** and $-$**k** and (not necessarily on-shell) collision energy $E$ is given by

$$\mathcal{A}(E) \quad = \quad \frac{4\pi}{m} \frac{1}{\log(-ma_2^2 E)}.$$ (2.7)

In this thesis, the standard choice of the complex logarithm is implied, so that its branch cut in the complex plane lies on the negative real axis. Setting the energy on shell via $E \mapsto k^2/m + i\epsilon$, with an infinitesimal $\epsilon > 0$ to specify on which side of the branch cut the argument lies, one reproduces the standard form (2.1) of the two-dimensional scattering amplitude for a contact interaction in two dimensions. In the many-body system with a balanced population and total density $n$, the typical energy scale for colliding momenta is the Fermi energy $E_F = k_F^2/2m$, where the Fermi momentum is given by $k_F = \sqrt{2\pi n}$. This is why, for the many-body problem, one takes

$$g_{12}(k_F) \quad = \quad -\frac{2\pi}{m} \frac{1}{\log a_2 k_F}$$ (2.8)

to be the relevant measure of the coupling constant. In sec. 2.3, where the non-degenerate limit of the single particle spectral function is discussed, we will also use this definition to quantify the coupling constant.

It is interesting to note that the naive version of the theory (2.5) is indeed *scale invariant.* However, due to the need of a regularization scheme and the resulting flow (2.6) of the coupling constant, this scale invariance is broken. A naive but intuitive way of thinking about this is that once we introduce the cutoff scale $\Lambda$ in our integrals, we also introduce a scale into the Hamiltonian, and rescaling of the integrals via $t \mapsto t\lambda^2$, $\mathbf{x} \mapsto \mathbf{x}\lambda$ in the Lagrangian density does not leave it invariant (which it would if we were to integrate over $\mathbb{R}^2$). This behavior of having a symmetry at the ultra violet level, which is then broken due to renormalization of the quantum fluctuations, is called an *anomaly.* The most prominent example of such a behavior is perhaps the so called chiral anomaly of quantum chromodynamics [29]. An introductory discussion of the anomaly discussed here can be found in [30]. It turns out that due to this anomaly, the trace of the stress-energy tensor does not have the form a scale invariant theory and receives corrections from the *contact* (see below) [31].

Like in one and three dimensions [32, 33, 34], it can be shown from an Operator Product Expansion[3], that the momentum distribution of the two-component 2D

---

[3]The OPE for the momentum distribution in two dimensions is complicated by the phenomenon

Fermi gas has a high-momentum tail that decays like

$$n_\sigma(\mathbf{k}) \longrightarrow \frac{C}{k^4} + \dots \tag{2.9}$$

for large momenta $k$. The coefficient $C$ is the *same* for *both* species. Other approaches to prove the behavior (2.9) include the use of Tan's selector distributions [36, 37] or clever use of zero-distance boundary conditions [38] for the many-body wavefunction. The coefficient $C$, called the *contact*, contains information about the amplitude for two particles to be close together. It can be related to thermodynamic quantities of the system [36, 39, 40, 38]. Those thermodynamic universal relations include, for example, a generalization of the pressure relation of the ideal gas and a relation that expresses the energy of the system as a functional of the momentum distribution only. The static structure factor also contains the contact in its high-momentum tail. Using the Hellman-Feynman theorem

$$\frac{\partial E}{\partial \log a_2} = \left\langle \frac{\partial H}{\partial \log a_2} \right\rangle \tag{2.10}$$

together with the relation

$$\frac{dg}{d\log a_2} \underbrace{=}_{(2.6)} \frac{mg^2}{2\pi}, \tag{2.11}$$

one can, from the adiabatic theorem [36, 38]

$$C = 2\pi m \frac{\partial E}{\partial \log a_2}, \tag{2.12}$$

infer the definition of the contact in second quantized form:

$$C = m^2 \int d^2R \left\langle g^2 \psi_1^\dagger \psi_2^\dagger \psi_2 \psi_1(\mathbf{R}) \right\rangle \equiv \int d^2R \langle \mathcal{C}(\mathbf{R}) \rangle \tag{2.13}$$

Given the definition (2.13), it is easy to see that the contact is related to the $1-2$ pair correlation function at zero distances. More specifically, the contact defines

---

called *operator mixing* (see [35] for a short introduction). One finds that the leading order non-analytic term in the short-distance expansion of the one-particle density matrix is given by a term $\sim |\mathbf{r}|^2 \log |\mathbf{r}| \psi_1^\dagger \psi_2^\dagger \psi_2 \psi_1$, which gives a $\sim 1/k^4$ decay after Fourier transform. The OPE will not be performed here, since enough derivations for eq. (2.9) are available in the given references. We will also encounter operator mixing for the quartic derivative operators in the 2D electron gas in sec. 4.5.2.

the average number of ↑↓ pairs in a small sphere around the origin (homogeneous system) via [38]

$$N_{\mathrm{pair}} \xrightarrow{s \to 0} \frac{C}{4\pi} s^2 \log^2 s, \tag{2.14}$$

where $s$ denotes the radius of the sphere. Hence, it is indeed a measure for the probability of two particles being close together. In section 2.2, we will relate the contact to the high-frequency tail of the radio frequency response function, when one of the spin states is transferred to a third spin state via a radio frequency pulse. In addition, the universal relations provide a beautiful way to test self-consistency of our numerical results in section 2.3.

Having defined our model and the *contact*, we are now prepared to approach the problems in the following sections. In section 2.2, additional universal relations for RF spectroscopy, that involve the contact, will be derived. We will be able to make use of one of these very relations already in chapter 2.3, that deals with the high-temperature limit of the spectral function of the two-dimensional Fermi gas.

## 2.2 Radio-frequency spectroscopy

Essentially, the idea of radio-frequency (RF) spectroscopy in cold atoms is to transfer a spin state into another one via a (typically) radio-frequency pulse. The energy that is needed for the transition is recorded. This can give information about, for example, the underlying dispersion relations for the atom, and quite generally, how interaction effects change the energy landscape for the particles [41, 42]. It can also be used to control of the population (im)balance between different spin states [43]. Due to the Zeemann effect, different hyperfine states have different energies, where the energy difference depends on the strength of the magnetic field. At given magnetic field $B$ and for an isolated atom, let $\hbar\omega_0 = \hbar\omega_0(B)$ be the energy needed to transfer a hyperfine state into the final hyperfine state we aim for. For consistency with later terminology, let us call the initially populated state $|2\rangle$ and the final spin state $|3\rangle$. If the atom is not subject to interactions, $\omega_0$ defines the energy needed to transfer the atom from state $|2\rangle$ to $|3\rangle$. However, interactions may change this picture drastically. How this is coming about is illustrated in figure 2.2 for the case of *momentum resolved* RF spectroscopy. Imagine a particle with momentum $\mathbf{k}$. When the initial and final state are non-interacting, the particle dispersions are just the ones of free particles $\varepsilon_2(\mathbf{k}) = \varepsilon_3(\mathbf{k}) = \mathbf{k}^2/2m$. The typical momentum of a RF photon is very small compared to typical atomic momenta,
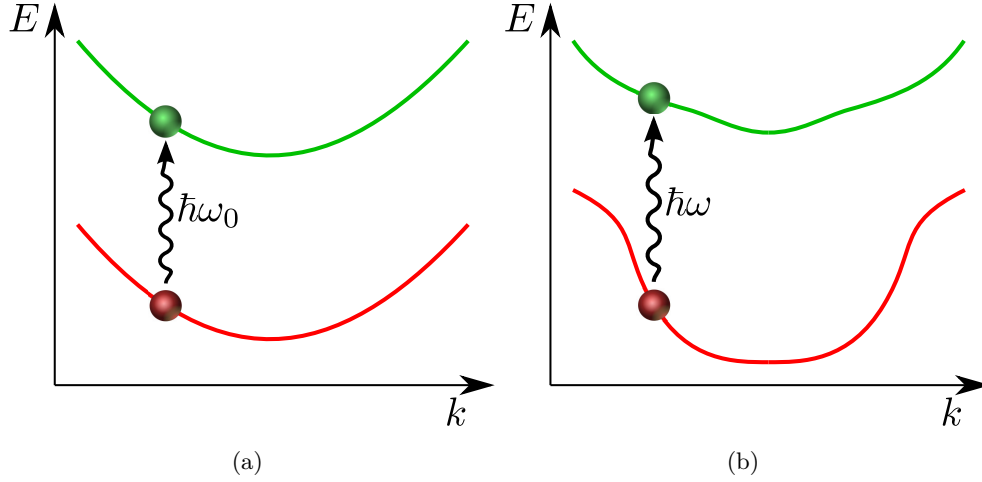
Figure 2.2: A sketch of the principles behind momentum resolved RF spectroscopy. An atom with momentum $\mathbf{k}$ is excited from its initial state $|2\rangle$ (red) to a final state $|3\rangle$ (green). In the case 2.2(a) of no interactions, the particle dispersions are just the ones of free particles. In the case 2.2(b) of strong initial and final state interactions, which are not necessarily of the same strength, the "dispersion relations" change. Note that in this naive picture, we ignore the fact that it is no longer sensible to talk about a dispersion relation in the case of strong interactions, since momentum is not a good quantum number.

so zero momentum transfer during the transition is a very good approximation: $\mathbf{k}_{\text{initial}} = \mathbf{k}_{\text{final}}$. Thus, the energy needed to transfer $|2\rangle$ into $|3\rangle$ is constant for non-interacting particles, as shown in figure 2.2(a). In the case where both the final and initial states are interacting with possibly different interaction strengths, the notion of a dispersion relation is not well defined anymore, because the momenta of the particles are not conserved during a scattering process. However, there still might be peaked structures in the spectral function of the system that resemble a dispersion relation. These are the curves that are illustrated in figure 2.2(b). The energy needed to transfer $|2\rangle$ into $|3\rangle$ will now be, in particular, a function of momentum. Momentum resolved RF spectroscopy can be used to measure the spectral function of an interacting state, if the respective final state is non-interacting. In order to achieve the momentum resolution in experiment, the momentum distribution of the

final state particles is determined via a time-of-flight measurement after the action of the RF pulse. This is the method used in the experiments by Fröhlich *et al.* to measure the spectral function of the two-dimensional Fermi gas [44]. In this section we will only deal with the non-momentum resolved case, where we implicitly average over *all* momenta.

In this part of the thesis, the contact parameter will be connected to high-frequency properties and sum rules of the RF spectrum. The problem, for example the relevant correlator that will be expanded later on, will be set up in a formal manner in 2.2.1. Linear response theory is a key ingredient that is needed for this formal setup. In section 2.2.2, the short time operator product expansion (OPE) for the RF correlator is performed. In section 2.2.3, the high-frequency behavior of the RF response function is extracted from the OPE and connected to the contact. In section 2.2.4, exact sum rules for the RF spectrum are derived. Finally, in section 2.2.5, the analytically solvable example of RF spectroscopy of a single dimer is treated. It is used as a check of the results of the preceding sections. As we will see, in the limit of big dimer binding energies, our predictions fit very well with the experiments by Sommer *et al.* [45]. All the results obtained in sec. 2.2 were published in an article [46] together with Eric Braaten, Christian Langmack and Wilhelm Zwerger.

## 2.2.1 Linear response

In this section, we will concentrate on a two-dimensional system composed of two interacting species $\sigma = 1, 2$. They interact with interaction strength $g = g_{12}$. Spin species $|2\rangle$ is converted, via a radio-frequency transition, to a third internal spin state $|3\rangle$ ($\sigma = 3$). As discussed in the previous section, this allows to extract information about various correlations of the interacting system. For a naive visualization of generic processes that might happen, see figure 2.3. The third spin may also be subject to so called final state interactions $g' = g_{13} \neq 0$, $g'' = g_{23} \neq 0$. A crucial assumption in the following will be that the final spin state $|3\rangle$ is –initially– *unpopulated*. This will allow, for the given problem, to set $g'' = 0$. In a formal way, this can be seen from the OPE that will follow. If we were to include the coupling $g_{23}$, the first operators that would have a Wilson coefficient that is connected to the interactions of 2 and 3 are the operators $\psi_1^\dagger \psi_2^\dagger \psi_3^\dagger \psi_3 \psi_2 \psi_1$ and Galilean invariant derivatives of $\psi_2^\dagger \psi_2^\dagger \psi_2 \psi_2$. Both operators only contribute at higher orders in our expansion. In consequence, we can omit the coupling $g_{23}$ altogether. Note that this
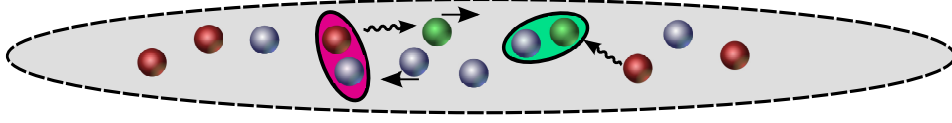
Figure 2.3: An illustration of the system we have in mind. Due to the confinement in $z$ direction, our gas forms a pancake structure, as indicated by the gray region. When the confinement becomes strong enough, the gas effectively becomes two-dimensional. During RF spectroscopy, RF photons hit atoms in state $|2\rangle$ (red) which are transferred into state $|3\rangle$ (green). The first spin state $|1\rangle$ (blue) can have interactions with atoms of species 2 and 3. In a naive two particle picture, processes could include the breaking of a $1-2$ bound state (purple) into $1-3$ scattering states, for which the RF photon is required to provide energy in addition to the one of the bare transition, or the conversion of a $1-2$ scattering state into a $1-3$ dimer (teal). Of course, both dimer - dimer and scattering - scattering state transitions are allowed as well.

were not true if we were to allow for initial population of species 3. An intuitive picture of why the coupling $g_{23}$ only comes in at higher orders is the following: Due to the Pauli exclusion principle and the *exchange correlation hole* connected to it [47], it is far less likely to find two particles of species 2 close together, than it is to find a particle of species 1 and species 2 in close proximity. Consequently, after the RF pulse transfers an atom from state $|2\rangle$ to $|3\rangle$, the first $1-3$ interaction occurs at a shorter timescale than the first $2-3$ interaction.

The – explicitly time dependent – Hamiltonian of the external radio-frequency field that drives the transitions from species 2 to 3 is given by

$$H_\Omega = \frac{\Omega}{\sqrt{2}} \int d^d x \left[ e^{i\mathbf{k}_L \cdot \mathbf{x} - i\omega t} \psi_3^\dagger(\mathbf{x}) \psi_2(\mathbf{x}) + e^{-i\mathbf{k}_L \cdot \mathbf{x} + i\omega t} \psi_2^\dagger(\mathbf{x}) \psi_3(\mathbf{x}) \right]. \quad (2.15)$$

The so called Rabi frequency $\Omega$ is connected to the dipole matrix element of states $|2\rangle$ and $|3\rangle$ (also see [48]), as well as the intensity of the RF field. It determines the frequency at which the population gets coherently transferred between the states. As mentioned earlier, we will omit the momentum $\mathbf{k}_L$ of the RF photon in the following, since it is close to zero compared to typical atomic momenta. The full Hamiltonian of the problem is given by sum of the Hamiltonians defined by equations (2.15) and

(2.4):

$$H \;\; = \;\; H_{(2.4)} + H_\Omega \equiv H_0 + H_\Omega \tag{2.16}$$

Note that since we did not include an energy offset in the kinetic term of the Hamiltonian (2.4), what we will be calculating in the following is a shifted RF spectrum, because $\omega = \omega_L - \omega_0$ is the frequency difference between the photon and the bare transition from $|2\rangle$ to $|3\rangle$. Typical RF experiments measure the change of the occupation in species $|3\rangle$ due to the presence of the RF field. The associated RF current, that describes the rate of change in the population of species 3, is given by

$$
\begin{aligned}
\hat\Gamma \;\; = \;\; \dot N_3 = i\,[H, N_3] &= i\left[H, \int d^d y\, \psi_3^\dagger(\mathbf{y})\psi_3(\mathbf{y})\right] \\
&= i \int d^d y \left( \left[H_0, \psi_3^\dagger(\mathbf{y})\psi_3(\mathbf{y})\right] + \left[H_\Omega, \psi_3^\dagger(\mathbf{y})\psi_3(\mathbf{y})\right]\right),
\end{aligned} \tag{2.17}
$$

where the Heisenberg equation of motion for the particle number operator $N_3$ was used. Using the equal time anti-commutation relations for the fields $\psi_\sigma$, a short calculation reveals

$$\int d^d y \left[H_0, \psi_3^\dagger \psi_3(\mathbf{y})\right] = 0 \tag{2.18a}$$

$$\int d^d y \left[H_\Omega, \psi_3^\dagger \psi_3(\mathbf{y})\right] = \frac{\Omega}{\sqrt{2}} \int d^d x \left[\psi_2^\dagger \psi_3(\mathbf{x})e^{i\omega t} - \psi_3^\dagger \psi_2(\mathbf{x})e^{-i\omega t}\right]. \tag{2.18b}$$

Equation (2.18a) reflects the fact that the unperturbed theory conserves particle number. This is also true for the other two species $\sigma = 1, 2$, and can be easily seen from the Hamiltonian density (2.4). It does not contain a term that can convert the different species into each other. Linear response theory, essentially an expansion in a time dependent perturbation (see [49] for a very nice introduction), in $H_\Omega(t)$ results in the following expression for the RF current:

$$\Gamma = \langle\hat\Gamma(t)\rangle \;\; = \;\; -i \int_{-\infty}^{\infty} dt'\, \Theta(t-t')\langle\left[\hat\Gamma(t), H_\Omega(t')\right]\rangle \tag{2.19}$$

The time evolution of the operators on the right hand side of the equation is generated only by $H_0$. The expectation value is here taken to be in the canonical ensemble of the unperturbed part [49] $\langle..\rangle = Z^{-1}\mathrm{tr}[e^{-\beta H_0}..]$, where $\beta = 1/k_B T$. Note that linear response theory will provide a good description of the system only as long as the effect of the perturbation does not dominate its dynamics. For our case, this means it will be valid for times where the population change in species 2 and 3 will

be small. Inserting eqs. (2.17), (2.18a) and (2.18b) into eq. (2.19) yields

$$\Gamma = -i\frac{\Omega^2}{2}\int_{-\infty}^{\infty}dt'\Theta(t-t')\int d^dx\,d^dx'\left\langle e^{i\omega(t-t')}[\psi_2^\dagger\psi_3(\mathbf{x},t),\psi_3^\dagger\psi_2(\mathbf{x}',t')]\right.$$
$$+e^{i\omega(t+t')}[\psi_2^\dagger\psi_3(\mathbf{x},t),\psi_2^\dagger\psi_3(\mathbf{x}',t')]+e^{-i\omega(t+t')}[\psi_3^\dagger\psi_2(\mathbf{x},t),\psi_3^\dagger\psi_2(\mathbf{x}',t')]$$
$$\left.+e^{-i\omega(t-t')}[\psi_3^\dagger\psi_2(\mathbf{x},t),\psi_2^\dagger\psi_3(\mathbf{x}',t')]\right\rangle. \tag{2.20}$$

Keeping in mind that both the canonical average and the time evolution are generated by $H_0$, and that the unperturbed Hamiltonian conserves particle number $[H_0, N_\sigma] = 0$, we see that the two terms in the middle vanish due to the unequal number of creation and annihilation operators of the same species. In addition, the retarded commutators are only functions of the time difference $t-t'$, which allows the substitution $(t - t') \to t$ to simplify notation. Thus, within linear response, the RF current is actually independent of time. We can further identify the fourth term to be the complex conjugate of the first one via the relation $[A^\dagger B, C^\dagger D]^\dagger = -[B^\dagger A, D^\dagger C]$. The result for the RF current reads

$$\Gamma(\omega) = \Omega^2\Re\left[\int_{-\infty}^{\infty}dt\Theta(t)e^{i\omega t}\int d^dx d^dx'\left\langle[\psi_2^\dagger\psi_3(\mathbf{x},t),\psi_3^\dagger\psi_2(\mathbf{x}',0)]\right\rangle\right]$$
$$= \Omega^2\Im\left[i\int_{-\infty}^{\infty}dt\Theta(t)e^{i\omega t}\int d^dx d^dx'\left\langle[\psi_2^\dagger\psi_3(\mathbf{x},t),\psi_3^\dagger\psi_2(\mathbf{x}',0)]\right\rangle\right]. \tag{2.21}$$

The RF spectrum is thus defined by the *spectral function* of the operator $A = \int \psi_2^\dagger\psi_3$. Note that $\Gamma(\omega)$ should not be confused with the Fourier transform of $\Gamma(t)$ in equation (2.17). The implicit $\omega$ dependence was always there, contained in the perturbation's Hamiltonian $H_\Omega$. In the following sections, we will usually prefer the second form of the RF spectrum above. We see that the RF response is determined by the Fourier transform of the *retarded* Green's function of the operator $\int \psi_2^\dagger\psi_3$.

Up to this point, we have only used the assumption that particles of species 3 are absent at time zero to simplify notation by setting the coupling constant $g_{23}$ to zero. However, in an, with respect to species 3, empty initial state, the second part of the retarded commutator does not actually contribute, since the annihilation operator $\psi_3$ is to the right of the creation operator $\psi_3^\dagger$. Thus, we can, under the assumption of no initial population of particles of species 3, connect the retarded correlator to the *time-ordered* one:

$$\Gamma(\omega) = \Omega^2\Im\left[i\int dt\,e^{i(\omega+i\epsilon)t}\int d^dx d^dx'\left\langle T_t\psi_2^\dagger\psi_3(\mathbf{x},t)\psi_3^\dagger\psi_2(\mathbf{x}',0)\right\rangle\right], \tag{2.22}$$

where a small $\epsilon > 0$ was introduced to enforce time integration only to run from 0 to $\infty$. Actually, had we been completely careful about the derivation, this small $\epsilon$ could be traced back to the *adiabatic switching on* procedure of the perturbation, that is implicit in the linear response formalism. See [49] for details. The symbol $T_t$ stands for the time ordered product of the operators, with the additional constraint that operators at equal times shall be ordered like in equation (2.22). Defining the RF operator

$$\mathcal{O}_{\text{rf}}(\omega, \mathbf{R}) \;\;=\;\; \int dt e^{i\omega t} \int d^d r \, T_t \psi_2^\dagger \psi_3\Big(\mathbf{R} + \frac{\mathbf{r}}{2}, t\Big)\psi_3^\dagger \psi_2\Big(\mathbf{R} - \frac{\mathbf{r}}{2}, 0\Big), \quad (2.23)$$

we can express the RF spectrum as the imaginary part of the equilibrium expectation value of $\mathcal{O}_{\text{rf}}$:

$$\Gamma(\omega) \;\;=\;\; \Omega^2 \int d^d R \, \Im\Big[\langle \mathcal{O}_{\text{rf}}(\omega + i\epsilon, \mathbf{R})\rangle\Big] \qquad (2.24)$$

We performed the substitution $\mathbf{r} = \mathbf{x} - \mathbf{x}'$ and $\mathbf{R} = (\mathbf{x} + \mathbf{x}')/2$, which has determinant one and therefore does not contribute any numerical factors. To extract the high-frequency behavior of the RF spectrum, the RF operator $\mathcal{O}_{\text{rf}}$ will be expanded in an operator product expansion. Our derivation until now did not actually depend on the dimensionality of the system. In fact, in the next subsection 2.2.2, I will present a way to obtain the OPE that only depends on the dimensionality of the system via the form of the *scattering amplitude*. The results will thus also hold for the three-dimensional case. The asymptotic behavior of $\Gamma(\omega)$ at large $\omega$ for the three-dimensional case, as well as the sum rules that can be derived from it, were already known before we started our project on the two-dimensional case. Those relations were derived by Punk *et al.* [50, 51] and Braaten *et al.* [52]. For Bosons, a similar approach also revealed sub-leading corrections that are related to the *Efimov effect* [53]. The relations for the three-dimensional case will be stated in sections 2.2.3 and 2.2.4 for comparison with the two-dimensional case, on which our main focus lies.

## 2.2.2 Operator Product Expansion for the response function

In this section, a short-time (high-frequency) OPE for the operator $\mathcal{O}_{\text{rf}}$, defined in equation (2.23), will be established. It will allow extraction of high-frequency behavior and sum rules for the RF transition rate $\Gamma(\omega)$. The short-time and -

distance OPE in the present case has the general form

$$\psi_2^\dagger \psi_3 \left(\mathbf{R} + \frac{\mathbf{r}}{2}, t\right) \psi_3^\dagger \psi_2 \left(\mathbf{R} - \frac{\mathbf{r}}{2}, 0\right) = \sum_n \tilde{c}_n(\mathbf{r}, t) \mathcal{O}_n(\mathbf{R}, 0), \qquad (2.25)$$

where the $\mathcal{O}_n$ are local operators and $\tilde{c}_n(\mathbf{r}, t)$ are the Wilson coefficients. The high-frequency OPE for $\mathcal{O}_{\mathrm{rf}}$ can thus, using equation (2.23), be written as

$$\mathcal{O}_{\mathrm{rf}}(\omega, \mathbf{R}) = \sum_n c_n(\omega) \mathcal{O}_n(\mathbf{R}), \qquad (2.26)$$

where the $\mathcal{O}_n(\mathbf{R})$ are the same local operators as in eq. (2.25) (acting at time $t = 0$) and the Wilson coefficients are

$$c_n(\omega) = \int dt e^{i\omega t} \int d^d r \, \tilde{c}(\mathbf{r}, t). \qquad (2.27)$$

It will be advantageous to directly perform the matching in frequency space. The integration $\int d^d r$ is also directly performed to simplify some diagrams. It makes $\mathcal{O}_{\mathrm{rf}}$ a "half momentum conserving" vertex in the sense that the sum of the momenta of the particles of species 2 has to equal the sum of momenta of species 3, also see appendix A.2 on the Feynman rules for operator vertices. In addition, due to the integration $\int dt \exp i\omega t$, the vertex that acts at time $t$ corresponds to an energy injection $-\omega$. The vertex at time zero is not integrated over, and thus has no energy conservation rules.

Since the OPE (2.26) is an operator equation, it has to hold between arbitrary states. The simplest possible state is the vacuum state. The matrix element of the RF operator in this state is zero, which sets the Wilson coefficient of (linearly independent) operators that do not vanish in the vacuum to zero. For states that only contain a particle of species 1, the argument is completely analogous. Keep in mind that we are only looking at a subspace-OPE, because, during the matching process, we will be ignoring any initial and final states that contain particles of species 3. The simplest non-vanishing matrix element of the left hand side of eq. (2.26) is given by states that only contain one particle of species 2. The matching in this so called *one-particle sector* will be performed in the next subsection.

**One-particle sector**

It is useful to invest some preliminary thought on which operators one expects on the right hand side of the OPE (2.26). Quite generally, we expect the operators that contribute to the OPE to be ordered by their scaling dimensions (also see below),

where operators with higher scaling dimension should have Wilson coefficients that decay faster as $\omega \to \infty$. This scheme might be complicated by an *anomalous dimension* for some operators [35, 33]. The symbol $L$ shall stand for dimensions of length (inverse momentum). Including all operators[4] of scaling dimensions $L^{-d-2}$ and $L^{-2d}$ that can still have a non-zero Wilson coefficient, we have the following ansatz for the OPE (2.26):

$$
\begin{aligned}
\mathcal{O}_{\mathrm{rf}}(\omega, \mathbf{R}) \;=\; & c_{2^\dagger 2}(\omega)\, \psi_2^\dagger \psi_2(\mathbf{R}) + c_{i,\partial n_2}(\omega)\, \partial_i \left( \psi_2^\dagger \psi_2 \right)(\mathbf{R}) + c_{i,J_2}(\omega)\, J_{2,i}(\mathbf{R}) \\
& + c_{2^\dagger \mathcal{D}2}(\omega)\, \psi_2^\dagger i \mathcal{D} \psi_2(\mathbf{R}) + c_{\mathcal{D}2^\dagger 2}(\omega)\, (i\mathcal{D}\psi_2)^\dagger \psi_2(\mathbf{R}) \\
& + c_{\partial^2 n_2, ij}(\omega)\, \partial_i \partial_j \left( \psi_2^\dagger \psi_2 \right)(\mathbf{R}) + c_{2^\dagger \partial^2 2, ij}(\omega) \left( \psi_2^\dagger \overleftrightarrow{\partial_i}\, \overleftrightarrow{\partial_j}\, \psi_2 \right)(\mathbf{R}) \\
& + c_{\partial J_2, ij}(\omega) \left( \partial_i J_{2,j}(\mathbf{R}) + \partial_j J_{2,i}(\mathbf{R}) \right) \\
& + c_{1^\dagger 2^\dagger 21}(\omega)\, \psi_1^\dagger \psi_2^\dagger \psi_2 \psi_1(\mathbf{R}) + \ldots
\end{aligned}
\tag{2.28}
$$

The shorthands

$$
\psi_2^\dagger i \mathcal{D} \psi_2(\mathbf{R}) \;=\; \psi_2^\dagger \left( i\partial_t + \frac{\nabla^2}{2m} \right) \psi_2(\mathbf{R})
\tag{2.29a}
$$

$$
(i\mathcal{D}\psi_2)^\dagger \psi_2(\mathbf{R}) \;=\; \psi_2^\dagger \left( -i\overleftarrow{\partial_t} + \frac{\overleftarrow{\nabla}^2}{2m} \right) \psi_2(\mathbf{R})
\tag{2.29b}
$$

$$
J_{2,i}(\mathbf{R}) = -\frac{i}{2m} \left( \psi_2^\dagger \overleftrightarrow{\partial_i} \psi_2 \right)(\mathbf{R}) \;=\; -\frac{i}{2m} \left( \psi_2^\dagger \partial_i \psi_2 - (\partial_i \psi_2^\dagger)\psi_2 \right)(\mathbf{R})
\tag{2.29c}
$$

were introduced to simplify notation. Einstein summation convention is implied here for the indices $i, j$:

$$
\sum_{i,j} A_{ij} B_{ij} \equiv A_{ij} B_{ij}
\tag{2.30}
$$

Note that it is not strictly necessary to group the derivatives on the operators like in (2.28). Any other linearly independent set is equally fine. The advantage of the choice above is that it makes the dependence on the *current* operators of species 2 explicit. The scaling dimensions of the operators can be calculated as follows: A space derivative $\partial_i$, by definition, contributes $L^{-1}$. In the non-relativistic case, a time derivative $\partial_t$ contributes $L^{-2}$. From the requirement that the action be dimensionless, we can infer the dimension of a field $\psi_\sigma$ to be $L^{-d/2}$. Since our theory

---

[4] As you might have noticed, this is strictly speaking not true. In the case $d = 3$, we are missing quite a lot of operators of dimension $L^{-6}$. Since focus lies on the two-dimensional case, let us omit these operators. Their Wilson coefficients can be shown to decay like $\omega^{-3}$, which makes our results for the three-dimensional case correct up to $\omega^{-3}$. This will suffice to give non-trivial results even in the 3D case.

(a) $\mathcal{O}_{\mathrm{rf}}$          (b) Local one-particle operators

Figure 2.4: Diagrams for the matching in the one-particle sector. 2.4(a) describes the matrix element of the RF operator $\mathcal{O}_{\mathrm{rf}}$ we want to expand. 2.4(b) is the diagram for all the one-particle operators $\sim \psi_2^\dagger \psi_2$ on the right hand side of the OPE (2.28). The full lines stand for an atom of species 2, the dashed line for the propagation of an atom of species 3. In both diagrams, the external legs have incoming energy and momentum $(E, \mathbf{p})$ and outgoing $(E', \mathbf{p}')$.

is Galilean invariant, only Galilean invariant combinations of $\partial_t$ and $\nabla$ were used in the OPE (2.28). When allowing for all combinations, we will only find Galilean invariant combinations during the matching process. The only two-particle operator up to dimension $L^{-2d}$, in the subspace of no population of species 3, is the operator $\psi_1^\dagger \psi_2^\dagger \psi_2 \psi_1$. It is also referred to as *contact density*, because it is closely related to the contact in equation (2.13).

To match the Wilson coefficients of the one-particle operators, the OPE (2.28) is now evaluated in scattering states $\langle E', \mathbf{p}'|, |E, \mathbf{p}\rangle$ that contain an incoming particle of species 2 with energy and momentum $(E, \mathbf{p})$ and and outgoing particle of species 2 with energy and momentum $(E', \mathbf{p}')$. The shorthand $\langle ...\rangle = \langle E', \mathbf{p}'|...|E, \mathbf{p}\rangle$ will be used to keep the formulas clean. An alternative way of thinking about the matrix elements is that we calculate the *amputated* Green's functions of all the operators on the left-hand and right-hand side with the afore mentioned incoming and outgoing energies and momenta.

**Matrix element of $\mathcal{O}_{\mathbf{rf}}$**    Using the Feynman rules for the operator $\mathcal{O}_{\mathrm{rf}}$ given in appendix A.2, we have for its matrix element, which is diagrammatically shown in figure 2.4(a):

$$
\begin{aligned}
\langle \mathcal{O}_{\mathrm{rf}}(\omega, \mathbf{R}) \rangle \;=\;& e^{i(\mathbf{p}-\mathbf{p}')\cdot\mathbf{R}} \frac{i}{E' + \omega - \frac{(\mathbf{p}+\mathbf{p}')^2}{8m} + i\epsilon} \\
\approx\;& e^{i(\mathbf{p}-\mathbf{p}')\cdot\mathbf{R}} \left\{ \frac{i}{\omega} - \frac{i}{\omega^2}\left[ E' - \frac{(\mathbf{p}+\mathbf{p}')^2}{8m} \right] + \mathcal{O}(\omega^{-3}) \right\} \\
=\;& e^{i(\mathbf{p}-\mathbf{p}')\cdot\mathbf{R}} \left\{ \frac{i}{\omega} - \frac{i}{\omega^2}\left[ E' - \frac{\mathbf{p}'^2}{2m} \right] - \frac{i}{8m\omega^2}\left[\mathbf{p} - \mathbf{p}'\right]^2 \right. \\
& \left. - \frac{i}{4m\omega^2}\left[ (\mathbf{p}'-\mathbf{p})\cdot(\mathbf{p}'+\mathbf{p}) \right] + \mathcal{O}(\omega^{-3}) \right\} \quad (2.31)
\end{aligned}
$$

For the last equality, the identity

$$
-\frac{(\mathbf{p}+\mathbf{p}')^2}{8} \;=\; -\frac{\mathbf{p}'^2}{2} + \frac{(\mathbf{p}-\mathbf{p}')^2}{8} + \frac{(\mathbf{p}'-\mathbf{p})\cdot(\mathbf{p}'+\mathbf{p})}{4} \qquad (2.32)
$$

was used. The important point is that equation (2.31) holds $\forall\, \mathbf{R}, \mathbf{p}, \mathbf{p}' \in \mathbb{R}^d$ and all energies $E, E'$ that are still small enough to justify the expansion with respect to large frequencies $\omega$. This allows us to compare this matrix element to matrix elements of the local one-particle operators as function of all of these variables.

**Matrix elements of the right-hand side operators**    The matrix elements of the one-particle operators, in the states with incoming momentum and energy $(E, \mathbf{p})$ and outgoing momentum and energy $(E', \mathbf{p}')$, can all be diagrammatically represented by diagram 2.4(b). In appendix A.2, it is demonstrated how to derive the Feynman rules for the operator vertices. The Feynman rules for the one-body operators are essentially given in the matrix elements below. They only depend on the incoming and outgoing energies and momenta of the lines that are connected to the vertex. The matrix element of the only dimension $L^{-d}$ operator is given by

$$
\left\langle \psi_2^\dagger \psi_2(\mathbf{R}) \right\rangle \;=\; e^{i(\mathbf{p}-\mathbf{p}')\cdot\mathbf{R}}. \qquad (2.33)
$$

The matrix elements of dimension $L^{-d-1}$ operators are

$$
\left\langle \partial_i \left( \psi_2^\dagger \psi_2 \right)(\mathbf{R}) \right\rangle \;=\; i(p_i - p_i')e^{i(\mathbf{p}-\mathbf{p}')\cdot\mathbf{R}} \qquad (2.34\mathrm{a})
$$

$$
\langle J_{2,i}(\mathbf{R}) \rangle \;=\; \frac{p_i + p_i'}{2m} e^{i(\mathbf{p}-\mathbf{p}')\cdot\mathbf{R}}. \qquad (2.34\mathrm{b})
$$

Last, but not least, the matrix elements of the one-particle operators of dimension $L^{-d-2}$ calculate to

$$
\left\langle \psi_2^\dagger i \mathcal{D} \psi_2(\mathbf{R}) \right\rangle = \left( E - \frac{\mathbf{p}^2}{2m} \right) e^{i(\mathbf{p}-\mathbf{p}')\cdot\mathbf{R}} \tag{2.35a}
$$

$$
\left\langle \left( i \mathcal{D} \psi_2 \right)^\dagger \psi_2(\mathbf{R}) \right\rangle = \left( E' - \frac{\mathbf{p}'^2}{2m} \right) e^{i(\mathbf{p}-\mathbf{p}')\cdot\mathbf{R}} \tag{2.35b}
$$

$$
\left\langle \partial_i \partial_j \left( \psi_2^\dagger \psi_2 \right) (\mathbf{R}) \right\rangle = -(p_i - p_i')(p_j - p_j') e^{i(\mathbf{p}-\mathbf{p}')\cdot\mathbf{R}} \tag{2.35c}
$$

$$
\left\langle \left( \psi_2^\dagger \overleftrightarrow{\partial_i} \overleftrightarrow{\partial_j} \psi_2 \right) (\mathbf{R}) \right\rangle = -(p_i + p_i')(p_j + p_j') e^{i(\mathbf{p}-\mathbf{p}')\cdot\mathbf{R}} \tag{2.35d}
$$

$$
\left\langle \left( \partial_i J_{2,j}(\mathbf{R}) + \partial_j J_{2,i}(\mathbf{R}) \right) \right\rangle = -\frac{i}{2m} \Bigg[ (p_i' - p_i)(p_j + p_j')
$$
$$
+ (p_j' - p_j)(p_i + p_i') \Bigg] e^{i(\mathbf{p}-\mathbf{p}')\cdot\mathbf{R}}. \tag{2.35e}
$$

To compare these matrix elements to the matrix element of $\mathcal{O}_{\text{rf}}$, the identities

$$
(\mathbf{p}' - \mathbf{p}) \cdot (\mathbf{p}' + \mathbf{p}) = \frac{1}{2}\delta_{ij} \Bigg[ (p_i' - p_i)(p_j + p_j') + (p_j' - p_j)(p_i + p_i') \Bigg] \tag{2.36a}
$$

$$
(\mathbf{p} - \mathbf{p}')^2 = \delta_{ij}(p_i - p_i')(p_j - p_j') \tag{2.36b}
$$

are useful. $\delta_{ij}$ is the Kronecker symbol. Using equations (2.36) and comparing the matrix element on the left-hand side, equation (2.31), with the matrix elements on the right-hand side, given by equations (2.33) - (2.35), we obtain the following result for the OPE of $\mathcal{O}_{\text{rf}}$ in the one-particle sector:

$$
\mathcal{O}_{\text{rf}}(\omega, \mathbf{R})|_{\text{1p.}} = \frac{i}{\omega} \psi_2^\dagger \psi_2(\mathbf{R}) - \frac{i}{\omega^2} \left( i \mathcal{D} \psi_2 \right)^\dagger \psi_2(\mathbf{R}) + \frac{i}{8m\omega^2} \delta_{ij} \, \partial_i \partial_j \left( \psi_2^\dagger \psi_2 \right) (\mathbf{R})
$$
$$
+ \frac{1}{4\omega^2} \delta_{ij} \left[ \partial_i J_{2,j}(\mathbf{R}) + \partial_j J_{2,i}(\mathbf{R}) \right] + \mathcal{O}(\omega^{-3}) \tag{2.37}
$$

The Wilson coefficients of all the other one-particle operators in (2.28) are zero. The only Wilson coefficient that is still undetermined is the one of the contact density $\psi_1^\dagger \psi_2^\dagger \psi_2 \psi_1$. Matrix elements containing two or more particles are required to fix this coefficient.

**Two-particle sector**

The simplest possible states that have a non-vanishing matrix element of $\psi_1^\dagger \psi_2^\dagger \psi_2 \psi_1$ are two-particle states that contain one particle of species 1 and one particle of species 2. Since this operator does not contain any time or space derivatives, it

suffices to use states that have vanishing incoming and leaving momenta $\pm \mathbf{0}$ and energies $0$. It is useful to define the following integrals:

$$\mathcal{I}(E) = \int_{\mathbf{q}} \frac{i}{E - \frac{\mathbf{q}^2}{m} + i\epsilon} \tag{2.38}$$

$$\mathcal{K}(E,\omega) = \int_{\mathbf{q}} \frac{i}{E + \omega - \frac{\mathbf{q}^2}{m} + i\epsilon} \frac{i}{E - \frac{\mathbf{q}^2}{m} + i\epsilon} \tag{2.39}$$

$$= \frac{i}{\omega} \left( \mathcal{I}(E) - \mathcal{I}(E+\omega) \right)$$

$$\mathcal{M}(E,\omega) = \int_{\mathbf{q}} \left( \frac{i}{E - \frac{\mathbf{q}^2}{m} + i\epsilon} \right)^2 \frac{i}{E + \omega - \frac{\mathbf{q}^2}{m} + i\epsilon} \tag{2.40}$$

$$= \left( \frac{i}{\omega} \right)^2 \left( \mathcal{I}(E+\omega) - \mathcal{I}(E) \right) + \frac{i}{\omega} \int_{\mathbf{q}} \left( \frac{i}{E - \frac{\mathbf{q}^2}{m} + i\epsilon} \right)^2$$

The symbol $\int_{\mathbf{q}}$ is a shorthand for integration over momenta: $\int_{\mathbf{q}} \equiv \int d^d q / (2\pi)^d$. Note that $\mathcal{I}(E)$ is convergent neither in two nor in three dimensions. However, within a consistent renormalization scheme, the differences of $\mathcal{I}$ are finite. The integral $\mathcal{I}$ is also the one that occurs in the Lippmann-Schwinger equation, diagrammatically shown for the $1-2$ scattering amplitude $\mathcal{A}$ in figure 2.1:

$$\frac{1}{\mathcal{A}(E)} = -\frac{1}{g} - i\mathcal{I}(E) \tag{2.41}$$

$$\frac{1}{D(\omega)} = -\frac{1}{g'} - i\mathcal{I}(\omega) \tag{2.42}$$

As mentioned earlier, in this thesis, cutoff regularization is used for the problem. The two-dimensional regularization scheme is given by (2.6). The three-dimensional cutoff regulated coupling constant is defined via

$$g(\Lambda) = \frac{4\pi a/m}{1 - \frac{2a\Lambda}{\pi}} \tag{2.43}$$

and completely analogous for $g'$. The amplitude $D(\omega)$ is the scattering amplitude for particles of species 1 and 3. In explicit form, it reads

$$D(\omega) = \frac{4\pi}{m} \frac{1}{\log(-ma_2'^2 \omega)} \qquad \text{(2D)} \tag{2.44}$$

$$D(\omega) = \frac{4\pi/m}{-\frac{1}{a'} + \sqrt{-m\omega}} \qquad \text{(3D)} \tag{2.45}$$

where the binding energy $E_D' = 1/ma'^2$ of the $1-3$ bound state is given by the two- (or three-)dimensional $1-3$ scattering length $a'$. Completely analogous formulas
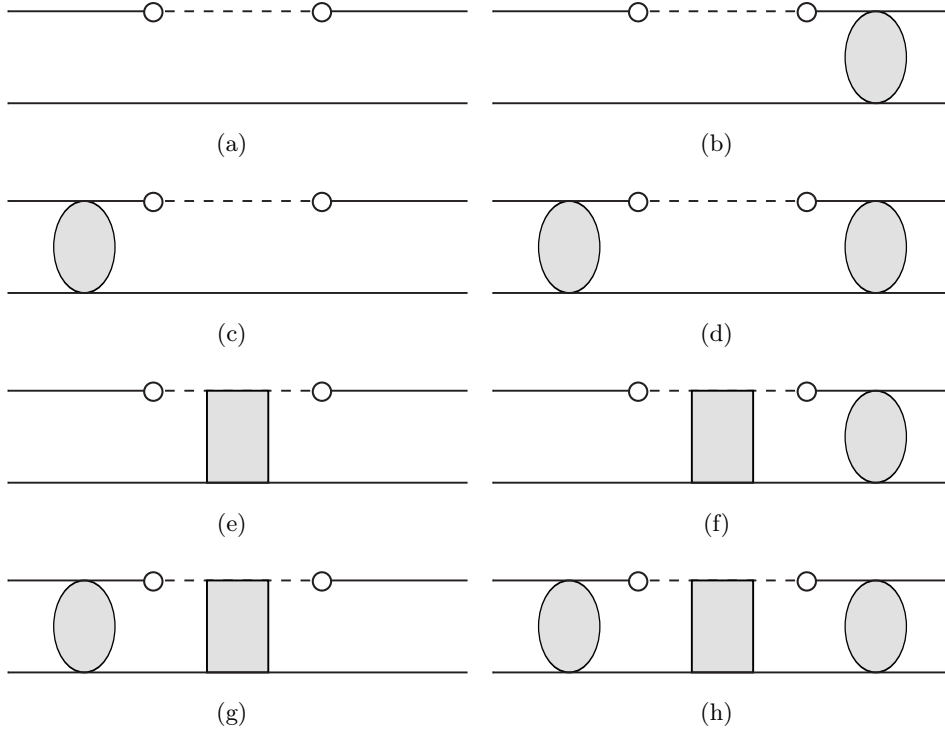
Figure 2.5: Diagrams contributing to the matrix element of $\mathcal{O}_{\mathrm{rf}}(\omega, \mathbf{R})$ in two-particle states. The big gray blob is the two-particle scattering amplitude for 1-2 scattering $i\mathcal{A}$, the big gray rectangle is the 1-3 scattering amplitude $iD$. The incoming and outgoing energies are $(0, \pm\mathbf{0})$.

hold for the $1-2$ scattering amplitude $\mathcal{A}$. The dependence on the scattering lengths will be mostly omitted from here on out, the amplitudes will be expressed in terms of the binding energies $E_D$ and $E'_D$. Diagrammatically, a gray blob indicates the amplitude $i\mathcal{A}$ for scattering of particles 1 and 2. A gray box will stand for $iD$, the scattering of particles 1 and 3.

**Matrix element of $\mathcal{O}_{\mathrm{rf}}$**  For the matrix element of the RF operator $\mathcal{O}_{\mathrm{rf}}$ in the states with $(0, \pm\mathbf{0})$, we have eight possible diagrams that contribute. They are shown figure 2.5. The full matrix element is given by the sum of these diagrams. There are exactly eight diagrams because of the $2\cdot2\cdot2$ possibilities to have scattering before, in between, and after the action of the vertices.

A word about the energy integration in all the diagrams that will follow: Consider,

for example, diagram 2.5(d). The lines in between the two amplitudes are not determined by energy and momentum conservation at the gray blobs. We thus have

$$
\begin{aligned}
2.5(d) \quad &= \quad (i\mathcal{A}(0))^2 \int \frac{dq_0}{2\pi} \int_{\mathbf{q}} \left( \frac{i}{q_0 - \frac{\mathbf{q}^2}{2m} + i\epsilon} \right)^2 \frac{i}{\omega + q_0 - \frac{\mathbf{q}^2}{2m} + i\epsilon} \frac{i}{-q_0 - \frac{\mathbf{q}^2}{2m} + i\epsilon} \\
&= \quad (i\mathcal{A}(0))^2 \int_{\mathbf{q}} \left( \frac{i}{-\frac{\mathbf{q}^2}{m} + i\epsilon} \right)^2 \frac{i}{\omega - \frac{\mathbf{q}^2}{m} + i\epsilon}. \tag{2.46}
\end{aligned}
$$

For the second equality, the fact that all but one pole lie in the *lower* half complex $q_0$-plane, is used. Since the integrand decays fast enough at infinity, it is possible to close the contour in the upper half $q_0$ plane. The arc does not contribute due to the fast decay. Evaluation of the integral via the residue theorem is now possible. The winding number of the contour around the pole is positive, and the Residue contributes a factor $-2\pi i$ times all the other propagators evaluated at $-\mathbf{q}^2/2m + i\epsilon$. All the undetermined energy integrations in other diagrams will be determined in the precisely same way. The same method was already implicitly used to eliminate the integration over the loop energy in the Lippmann-Schwinger equations (2.41) and (2.42).

If we were using states where the particles have incoming and outgoing four-momenta $(E/2, \pm\mathbf{p})$ and $(E'/2, \pm\mathbf{p}')$, diagram 2.5(a) would contain a delta function on the incoming and leaving four momenta of the particle of species 1. This can be understood from the fact that we contract those two external legs with each other. In our case of zero incoming and leaving four-momenta, we write $\delta_{(0,\mathbf{0})}$ as a shorthand for this delta function. In addition, the inner leg of the species 2 particle in diagrams 2.5(b) and 2.5(c) goes on shell, which is not a major complication, since this also happens for the diagrams of $\psi_2^\dagger \psi_2$, as we will see below. The contributions of diagrams 2.5(a) - 2.5(h) to the matrix element of $\mathcal{O}_{\mathrm{rf}}$, expressed via the integrals

(2.38)-(2.40), are given by

$$2.5(a) \quad = \quad \frac{i}{\omega}\delta_{(0,\mathbf{0})} \tag{2.47a}$$

$$2.5(b) \quad = \quad \frac{i}{i\epsilon}\frac{i}{\omega}i\mathcal{A}(0) \tag{2.47b}$$

$$2.5(c) \quad = \quad \frac{i}{i\epsilon}\frac{i}{\omega}i\mathcal{A}(0) \tag{2.47c}$$

$$2.5(d) \quad = \quad (i\mathcal{A}(0))^2\mathcal{M}(0,\omega) \tag{2.47d}$$

$$\stackrel{(2.40)}{=} \quad (i\mathcal{A}(0))^2\left[\left(\frac{i}{\omega}\right)^2(\mathcal{I}(\omega)-\mathcal{I}(0)) + \frac{i}{\omega}\int_{\mathbf{q}}\left(\frac{i}{-\frac{\mathbf{q}^2}{m}+i\epsilon}\right)^2\right]$$

$$2.5(e) \quad = \quad \left(\frac{i}{\omega}\right)^2 iD(\omega) \tag{2.47e}$$

$$2.5(f) \quad = \quad \frac{i}{\omega}iD(\omega)i\mathcal{A}(0)\mathcal{K}(0,\omega)$$

$$\stackrel{(2.39)}{=} \quad \left(\frac{i}{\omega}\right)^2(\mathcal{I}(0)-\mathcal{I}(\omega))iD(\omega)i\mathcal{A}(0) \tag{2.47f}$$

$$2.5(g) \quad = \quad \frac{i}{\omega}iD(\omega)i\mathcal{A}(0)\mathcal{K}(0,\omega)$$

$$\stackrel{(2.39)}{=} \quad \left(\frac{i}{\omega}\right)^2(\mathcal{I}(0)-\mathcal{I}(\omega))iD(\omega)i\mathcal{A}(0) \tag{2.47g}$$

$$2.5(h) \quad = \quad (i\mathcal{A}(0))^2iD(\omega)(\mathcal{K}(0,\omega))^2$$

$$\stackrel{(2.39)}{=} \quad \left(\frac{i}{\omega}\right)^2 iD(\omega)(\mathcal{I}(0)-\mathcal{I}(\omega))^2(i\mathcal{A}(0))^2. \tag{2.47h}$$

The diagrams were expressed in terms of the Lippmann-Schwinger integral $\mathcal{I}$ to simplify matching process with the one particle operators.

**Matrix elements of the right-hand side operators** The right-hand side of the OPE (2.28) is now evaluated in the same states containing one particle of species 1 and one particle of species 2. The incoming and outgoing momenta and energies are of course again $(0, \pm\mathbf{0})$. All the operators with Wilson coefficients that are already matched to zero will not be evaluated.

**One-particle operators** The four diagrams for the evaluation of the matrix elements of the local one-particle operators are presented in figure 2.6. The resulting expressions for these diagrams are given in table 2.1. The matrix element is again the sum of all the corresponding diagrams. The contributions of the two second derivative operators $\partial_i\partial_j\left(\psi_2^\dagger\psi_2\right)$ and $(\partial_i J_{2,j} + \partial_j J_{2,i})$ are zero, because energy and
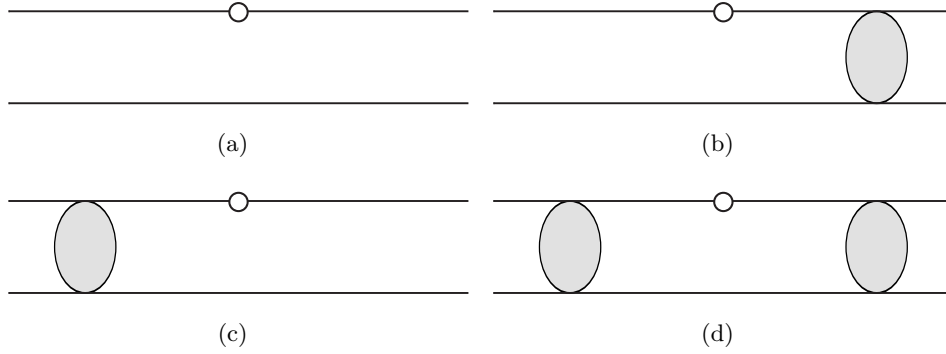
Figure 2.6: Diagrams for the matrix elements of local one-particle operators (already matched in section 2.2.2).

| | $2.6(a)$ | $2.6(b)$ | $2.6(c)$ | $2.6(d)$ |
|---|---|---|---|---|
| $\left\langle \psi_2^\dagger \psi_2(\mathbf{R}) \right\rangle$ | $\delta_{(0,0)}$ | $\frac{i}{i\epsilon} i\mathcal{A}(0)$ | $\frac{i}{i\epsilon} i\mathcal{A}(0)$ | $(i\mathcal{A}(0))^2 \int_{\mathbf{q}} \left( \frac{i}{-\frac{\mathbf{q}^2}{m}+i\epsilon} \right)^2$ |
| $\left\langle (i\mathcal{D}\psi_2)^\dagger \psi_2(\mathbf{R}) \right\rangle$ | $0$ | $0$ | $0$ | $(i\mathcal{A}(0))^2 i\mathcal{I}(0)$ |
| $\left\langle \partial_i \partial_j (\psi_2^\dagger \psi_2)(\mathbf{R}) \right\rangle$ | $0$ | $0$ | $0$ | $0$ |
| $\left\langle (\partial_i J_j + \partial_j J_i)(\mathbf{R}) \right\rangle$ | $0$ | $0$ | $0$ | $0$ |

Table 2.1: Matrix elements of local one-particle operators in two-particle states.

momentum conservation at the scattering vertices fix incoming and leaving momenta at the operator vertex to be equal, cf. eqs. (2.35c) and (2.35e). The kinetic one-particle operator $(i\mathcal{D}\psi_2)^\dagger \psi_2$ has only one non-zero matrix element, because, in diagrams 2.6(a)-2.6(c), the external legs are on-shell. Since its Feynman rule is basically the free equation of motion, this yields vanishing matrix elements.

Comparing the results of table 2.1 with equations (2.47a)-(2.47d), we see that diagrams 2.6(a)-2.6(c) entirely match diagrams 2.5(a) - 2.5(c) when using the already determined (see eq. (2.37)) Wilson coefficients

$$c_{2^\dagger 2}(\omega) = \frac{i}{\omega} \tag{2.48}$$

$$c_{\mathcal{D}2^\dagger 2} = -\frac{i}{\omega^2}. \tag{2.49}$$
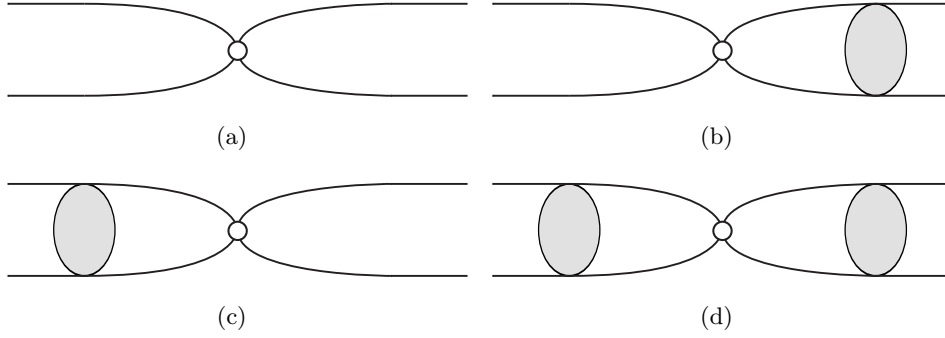
Figure 2.7: Diagrams for the matrix element of $\psi_1^\dagger \psi_2^\dagger \psi_2 \psi_1(\mathbf{R})$.

For diagram 2.5(d), given by equation (2.47d), the only part that is not matched by the one-particle operators is the one that contains the Lippmann-Schwinger integral $\mathcal{I}(\omega)$. This remaining part, as well as the other four diagrams 2.5(e)-2.5(h), will be matched by the lowest dimensional two-particle operator, as we will see below.

**Two-particle operators** The matrix element of the lowest dimensional two-particle operator $\psi_1^\dagger \psi_2^\dagger \psi_2 \psi_1$ is given by the sum of the diagrams shown in figure 2.7. The Feynman rule of the operator is connected to the total incoming and the total outgoing momentum of the attached lines: $e^{i(\mathbf{P}_{\text{in}} - \mathbf{P}_{\text{out}}) \cdot \mathbf{R}}$. In particular, it yields a factor of one for vanishing total momentum, as is the case for the external states we are using. Evaluation of the diagrams yields

$$\left\langle \psi_1^\dagger \psi_2^\dagger \psi_2 \psi_1(\mathbf{R}) \right\rangle = \left(1 + i\mathcal{A}(0)\mathcal{I}(0)\right)^2 \overset{(2.41)}{=} \frac{\mathcal{A}(0)^2}{g^2}, \tag{2.50}$$

where the Lippmann-Schwinger equation (2.41) was used to simplify the expression. The following remark about renormalization is important: the operator of the contact density $\mathcal{C} = m^2 g^2 \psi_1^\dagger \psi_2^\dagger \psi_2 \psi_1$ has finite matrix elements as $\Lambda \to \infty$, in contrast to the bare operator. Because of this, it will be more useful to absorb the $g^2$ from the Wilson coefficient directly into the definition of the operator later on.

The part of the matrix element of the RF operator $\mathcal{O}_{\text{rf}}$ that is not yet matched

by the matrix elements of the one particle operators is given by the sum

$$
\begin{aligned}
\langle \mathcal{O}_{\mathrm{rf}} \rangle |_{\mathrm{rest}} \quad &= \quad \underbrace{(i\mathcal{A}(0))^2 \left(\frac{i}{\omega}\right)^2 \mathcal{I}(\omega)}_{\text{still unmatched part of 2.5}(d)} \\
&\quad + \underbrace{iD(\omega)\left(\frac{i}{\omega}\right)^2 \left[1 + (\mathcal{I}(0) - \mathcal{I}(\omega))i\mathcal{A}(0)\right]^2}_{\text{sum of diagrams 2.5}(e)-2.5(h)} \\
\overset{(2.41),\,(2.42)}{=} \quad &\mathcal{A}^2(0)\frac{i}{\omega^2}\left[\frac{1}{g'} + \frac{1}{D(\omega)}\right] + iD(\omega)\left(\frac{i}{\omega}\right)^2 \Bigg[\frac{\mathcal{A}^2(0)}{g^2} \\
&\quad -2\mathcal{I}(\omega)i\mathcal{A}(0) - 2i\mathcal{I}(\omega)i\mathcal{I}(0)\mathcal{A}^2(0) + i^2\mathcal{I}^2(\omega)\mathcal{A}^2(0)\Bigg] \\
\overset{(2.41),\,(2.42)}{=} \quad &\mathcal{A}^2(0)\frac{i}{\omega^2}\left[\frac{1}{g'} + \frac{1}{D(\omega)}\right] + iD(\omega)\left(\frac{i}{\omega}\right)^2 \mathcal{A}^2(0) \\
&\quad \times \Bigg[\frac{1}{g^2} + 2\left(\frac{1}{g'} + \frac{1}{D(\omega)}\right)\frac{1}{\mathcal{A}(0)} \\
&\qquad -2\left(\frac{1}{g'} + \frac{1}{D(\omega)}\right)\left(\frac{1}{g} + \frac{1}{\mathcal{A}(0)}\right) + \left(\frac{1}{g'} + \frac{1}{D(\omega)}\right)^2 \Bigg] \\
= \quad &\mathcal{A}^2(0)\frac{i}{\omega^2}\left[\left(\frac{2}{g} - \frac{1}{g'}\right) - D(\omega)\left(\frac{1}{g} - \frac{1}{g'}\right)^2\right]. \tag{2.51}
\end{aligned}
$$

The Lippmann-Schwinger equations (2.42) and (2.41) were used to eliminate the integrals $\mathcal{I}$ in favor of the amplitudes $\mathcal{A}$ and $D$. This is also the reason why our matching process works for both the two- and three-dimensional problem. We just have to plug in the expressions for the amplitudes in the end to get the corresponding result. As you might have noticed, this part of the matrix element is not finite. However, the divergence cancels against the part that was matched by the kinetic operator $(i\mathcal{D}\psi_2)^\dagger \psi_2$, such that the total matrix element is indeed well defined. This point will be clarified further in the next subsection 2.2.3, when the high-frequency behavior of the RF spectrum is extracted from the OPE.

Comparison of the unmatched part (2.51) with the matrix element of the operator $\psi_1^\dagger \psi_2^\dagger \psi_2 \psi_1$, given in equation (2.50), yields

$$
c_{1\dagger 2\dagger 21}(\omega) = g^2 \frac{i}{\omega^2}\left[\left(\frac{2}{g} - \frac{1}{g'}\right) - D(\omega)\left(\frac{1}{g} - \frac{1}{g'}\right)^2\right] \tag{2.52}
$$

for its Wilson coefficient. The Wilson coefficient carries the right renormalization to make the matrix elements finite. Let us from now on absorb the coupling $g^2$ into the operator and talk about $\mathcal{C}(\mathbf{R}) = m^2 g^2 \psi_1^\dagger \psi_2^\dagger \psi_2 \psi_1$ instead. Note that in two

dimensions, apart from factors of mass, the coupling $g$ is dimensionless, while in three dimensions, it carries dimensions of length. Thus, in both cases, the *renormalized* operator $\mathcal{C}(\mathbf{R})$ carries dimensions of $L^{-4}$. This change in scaling dimensions under renormalization is often referred to as an *anomalous dimension.* Since the operator $\mathcal{C}(\mathbf{R})$ acquires such an anomalous dimension in the three-dimensional case, this is actually, in retro-respect, a justification for not including the higher order terms $\sim \omega^{-3}$ into the OPE.

In summary, we have determined the large-frequency OPE of the RF operator $\mathcal{O}_{\text{rf}}(\omega, \mathbf{R})$ – in the subspace of no population of species 3 – to be

$$
\begin{aligned}
\mathcal{O}_{\text{rf}}(\omega, \mathbf{R}) \;=\; & \frac{i}{\omega}\,\psi_2^\dagger \psi_2(\mathbf{R}) - \frac{i}{\omega^2}\,(i\mathcal{D}\psi_2)^\dagger\,\psi_2(\mathbf{R}) + \frac{i}{8m\omega^2}\delta_{ij}\,\partial_i\partial_j\left(\psi_2^\dagger\psi_2\right)(\mathbf{R}) \\
& + \frac{1}{4\omega^2}\delta_{ij}\left[\partial_i J_{2,j}(\mathbf{R}) + \partial_j J_{2,i}(\mathbf{R})\right] \\
& + \frac{i}{\omega^2}\frac{1}{m^2}\left[\left(\frac{2}{g} - \frac{1}{g'}\right) - D(\omega)\left(\frac{1}{g} - \frac{1}{g'}\right)^2\right]\mathcal{C}(\mathbf{R}) + \mathcal{O}(\omega^{-3}). \quad (2.53)
\end{aligned}
$$

The implications for the asymptotic high-frequency behavior of the RF current $\Gamma(\omega)$ will be discussed in the next subsection.

### 2.2.3 Large-frequency behavior

For the two-dimensional Fermi gas, Sommer *et al.* [54] proposed that the high-frequency tail of the RF spectrum decays quadratically $\sim \omega^{-2}$ for large frequencies. As we will see below, this is true only in the special case of *vanishing final state interactions* $g' = 0$. Our results can be understood as a natural generalization that takes into account the effect of interactions between particles 1 and 3 after the excitation of a type-2 atom.

In the case of the three-dimensional Fermi gas, a high-frequency tail of the RF response function was predicted [55, 50, 51] that decays like $\omega^{-3/2}$ (for vanishing final state interactions). This result was extended in [52] via the same methods presented here. In the case of finite final state interactions $g' \neq 0$, one has a high-frequency tail that decays like $\omega^{-5/2}$. As we will see below, we are able to extract all of these results from the OPE given in equation (2.53). In consequence, the three-dimensional case serves as a crosscheck for our results in two dimensions.

The RF response is defined as the imaginary part of the (equilibrium) expectation value of the RF operator $\mathcal{O}_{\text{rf}}$, cf. eq. (2.24). As a first step in extracting the high-frequency properties of the RF spectrum, the expectation value of the OPE (2.53)

is taken. For this, we will exploit the equation of motion[5] of the kinetic operator $(i\mathcal{D}\psi_2)^\dagger\psi_2$, which can be extracted from the action (2.5) by varying the fields $\psi_2$ or $\psi_2^\dagger$. Equivalently, one can take the commutator of the fields with the Hamiltonian. In our case of vanishing $g_{23}$, the equation of motion is given by

$$\left\langle (i\mathcal{D}\psi_2)^\dagger\psi_2(\mathbf{R}) \right\rangle = \frac{1}{g}\langle \mathcal{C}(\mathbf{R})\rangle. \tag{2.54}$$

Plugging the equation of motion (2.54) into the expectation value of the OPE (2.24) yields

$$
\begin{aligned}
\langle \mathcal{O}_{\mathrm{rf}}(\omega,\mathbf{R})\rangle &= \frac{i}{\omega}\left\langle \psi_2^\dagger\psi_2(\mathbf{R})\right\rangle + \frac{i}{8m\omega^2}\delta_{ij}\left\langle \partial_i\partial_j\left(\psi_2^\dagger\psi_2\right)(\mathbf{R})\right\rangle \\
&\quad + \frac{1}{4\omega^2}\delta_{ij}\left\langle \left[\partial_i J_{2,j}(\mathbf{R}) + \partial_j J_{2,i}(\mathbf{R})\right]\right\rangle \\
&\quad + \frac{i}{\omega^2}\frac{1}{m^2}\left[\left(\frac{1}{g}-\frac{1}{g'}\right) - D(\omega)\left(\frac{1}{g}-\frac{1}{g'}\right)^2\right]\langle \mathcal{C}(\mathbf{R})\rangle + \dots \\
&= \frac{i}{\omega}\,n_2(\mathbf{R}) + \frac{i}{8m\omega^2}\left[\nabla^2 n_2(\mathbf{R}) - 4im\nabla\cdot\mathbf{J}_2(\mathbf{R})\right] \\
&\quad + \frac{i}{\omega^2}\frac{1}{m^2}\left[\left(\frac{1}{g}-\frac{1}{g'}\right) - D(\omega)\left(\frac{1}{g}-\frac{1}{g'}\right)^2\right]\langle \mathcal{C}(\mathbf{R})\rangle + \dots \tag{2.55}
\end{aligned}
$$

where $n_2(\mathbf{R})$ is the local density of type-2 atoms. Likewise, $\mathbf{J}_2(\mathbf{R})$ is the corresponding local current density.

The next simplification arises from the integration of the OPE over all positions $\mathbf{R}$. The term containing the curvature of the density and the divergence of the current density can be shown[6] to vanish when requiring canonical boundary conditions for the quantum fields $\psi_\sigma$. From a physical point of view, we can also infer, from the fact that we use equilibrium expectation values together with current conservation

$$\underbrace{\frac{\partial N_2}{\partial t}}_{=0} + \int d^d R\,\nabla\cdot\mathbf{J}_2(\mathbf{R}) = 0, \tag{2.56}$$

that the term containing the current density has to vanish. Note that in the RF experiment, there *is* a change in the population of species 2, because it is excited

---

[5]Note that we have not used the equation of motion during the matching process, since the equation of motion is, by definition, not fulfilled for particles that are not on-shell. The one-particle matrix elements we used to match the one-particle operators indeed had general (off-shell) energies $E, E'$, and so do the loop integrations.

[6]Expand the terms with respect to their definitions in terms of the fields. Use Gauss' theorem to turn the volume integral into an integral over the surface of $\mathbb{R}^d$. The integral has to vanish, because, due to the canonical boundary conditions, the fields should vanish at infinity.

into state $|3\rangle$. However, this effect is of higher order and not covered in the linear response formalism we employ. In a similar fashion, we can also state that the divergence of the density gradient vanishes locally in a translationally invariant state. The system will be approximated to be translation invariant in section 2.3 on the spectral function of the two-dimensional Fermi gas. Taking into account the above arguments, the integrated version of the OPE can be simplified to

$$\int d^d R \langle \mathcal{O}_{\rm rf}(\omega, \mathbf{R}) \rangle = \frac{i}{\omega} N_2 + \frac{i}{\omega^2} \left[ \left( \frac{1}{g} - \frac{1}{g'} \right) - D(\omega) \left( \frac{1}{g} - \frac{1}{g'} \right)^2 \right] \frac{C}{m^2}$$
$$+ \mathcal{O}(\omega^{-3}). \quad (2.57)$$

$N_2$ is the total number of particles of species 2, $C$ is the extensive contact defined by equations (2.13) and (2.9).

The only still unperformed step in order to connect the OPE to the high-frequency behavior of the RF spectrum, is to set $\omega \to \omega + i\epsilon$ and take the imaginary part of the resulting expression in the limit of $\epsilon \to 0$. In order to do so, we need to plug in the explicit forms (2.44) and (2.45) of the $1 - 3$ two particle scattering amplitude in two or three dimensions, respectively. Both the contact $C$ and the particle number $N_2$ are real numbers $\geq 0$. Due to the identities [56]

$$\lim_{\epsilon \to 0} \frac{1}{\omega + i\epsilon} = \mathcal{P} \frac{1}{\omega} - i\pi \delta(\omega) \quad (2.58)$$

$$\Rightarrow \lim_{\epsilon \to 0} \frac{1}{(\omega + i\epsilon)^2} = \mathcal{P} \frac{1}{\omega^2} + i\pi \delta'(\omega), \quad (2.59)$$

where $\mathcal{P}$ denotes the principal part and $\delta'(\omega)$ the distributional derivative of the delta function, the imaginary parts of the terms with a pure $1/(\omega + i\epsilon)$ and $1/(\omega + i\epsilon)^2$ behavior vanish for large frequencies $\omega \to \infty$. The equalities above are also a way to understand how the sum rules, that are derived in the next subsection 2.2.4, come about.

**Three-dimensional case** In order to convince ourselves that our results are consistent with earlier findings [52, 50, 55], the three-dimensional case will be treated first. The amplitude $D$ takes the form (2.45), and, after a short calculation, one finds

$$\Gamma(\omega) = \Omega^2 \frac{C}{4\pi m} \left( \frac{1}{a} - \frac{1}{a'} \right)^2 \Im \left[ \frac{1}{(\omega + i\epsilon)^2} \frac{1}{-\frac{1}{a'} + \sqrt{-m\omega - i\epsilon}} \right] + \dots$$

$$= \Omega^2 \frac{C}{4\pi \sqrt{m}} \left( \frac{1}{a} - \frac{1}{a'} \right)^2 \frac{1}{\omega^{\frac{3}{2}}} \frac{1}{\frac{1}{a'^2} + m\omega} + \dots \quad (2.60)$$

for the high-frequency behavior of the RF spectrum $\Gamma(\omega)$. The fact that $\omega \to \infty > 0$ and $\epsilon > 0$ was used in the above equation to uniquely determine on which side of the branchcut the argument of the square root lies. The imaginary part of the $1/(\omega+i\epsilon)$ and $1/(\omega + i\epsilon)^2$ terms vanishes for $\omega > 0$ due to eqs. (2.58) and (2.59). Note that $a$ and $a'$ denote the three dimensional scattering lengths. Equation (2.60) is exactly the $\sim 1/\omega^{5/2}$ tail given in [52]. In the limit of vanishing final state interactions $1/a' \to \infty$, this simplifies to a $\sim 1/\omega^{3/2}$ tail as given in [51].

**Two-dimensional case**   As we have seen, our results are consistent with earlier findings for RF spectroscopy on a three dimensional Fermi gas. In the two-dimensional case, all that changes in the OPE (2.57) is the form of the amplitude $D$, which now has an inverse logarithmic form, given by eq. (2.44). Insertion of the amplitude into the OPE yields

$$
\begin{aligned}
\Gamma(\omega) &= \Omega^2 \frac{C}{m^2} \left( -\frac{m}{4\pi} \log(a_2^2/a_2'^2) \right)^2 \frac{4\pi}{m} \Im \left[ \frac{1}{(\omega+i\epsilon)^2} \underbrace{\frac{1}{\log(-m\omega a_2'^2 - i\epsilon)}}_{= \frac{1}{\log(-m\omega a_2'^2) - i\pi}} \right] + \dots \\
&= \Omega^2 \frac{C}{4m\omega^2} \frac{\log^2(a_2^2/a_2'^2)}{\log^2(m\omega a_2'^2) + \pi^2} + \dots,
\end{aligned}
\tag{2.61}
$$

where (2.6) was used to rewrite the coupling constants $g$ and $g'$ in terms of the two-dimensional scattering lengths. The imaginary part of $1/(\omega + i\epsilon)$ and $1/(\omega + i\epsilon)^2$ does again not contribute for $\omega > 0$. In summary, we have, for the two-dimensional contact-interacting Fermi gas, derived the

> **High-frequency asymptotics of the RF spectrum**
>
> The radio-frequency absorbtion spectrum $\Gamma(\omega)$ of the two-dimensional Fermi gas at high frequencies decays as
>
> $$
> \Gamma(\omega) \overset{\omega \to \infty}{\longrightarrow} \Omega^2 \frac{C}{4m\omega^2} \frac{\log^2(E_D/E_D')}{\log^2(\omega/E_D') + \pi^2},
> \tag{2.62}
> $$
>
> where $\Omega$ is the Rabi frequency of the transition from state $|2\rangle$ to state $|3\rangle$, and the constant $C$ is the contact of atom species 1 and 2, defined in equation (2.13). $E_D = 1/ma_2^2$ ($E_D' = 1/ma_2'^2$) denotes the energy of the two-particle bound state in the initial (final) state, where $a_2$ ($a_2'$) is the corresponding two-dimensional scattering length.

One key observation is that the asymptotic RF spectrum (2.62) vanishes when the interaction strengths of the initial and final states are equal: $E_D = E'_D$. This can be understood from the fact that the RF pulse merely rotates a spin in this case [57]. In other words the initial and final states have the same energy. This results in an RF spectrum that is proportional to a $\delta$ function peak, which can be understood even from the simple picture, involving the dispersion relations of the initial and final states, that is presented in figure 2.2. Another interesting limit, that will also be useful later on in our discussion of the high-temperature properties of the system in sec. 2.3, is the one of vanishing final state interactions $E'_D \to \infty, a'_2 \to 0$. In this case, we are just left with the simple scaling behavior

$$\Gamma(\omega) \stackrel{\omega \to \infty}{\Longrightarrow} \Omega^2 \frac{C}{4m\omega^2}, \tag{2.63}$$

which is indeed consistent with the form $\sim 1/\omega^2$, originally proposed in [54]. Experimentally, this means that in the case of vanishing final state interactions, one can fit a $1/\omega^2$ tail to the high frequency part of the measured spectrum to extract the contact, and hence various thermodynamic properties, of the system [58]. The contact measured in this way fits zero-temperature Quantum Monte carlo predictions [59] quite well [58]. As it turns out however, in the experiments conducted in [54, 44, 58], the anomalous logarithmic scaling (2.62) fits the high-frequency tails even better[7], indicating that final state interactions are *not* negligible.

The logarithmic scaling violations $\sim 1/\omega^2 \log^2 \omega$ in (2.62) can be traced back to the logarithmic form of the scattering amplitude. For the scattering amplitude to be finite (non-zero), we had to break the scale invariance of the theory with the running coupling constant (2.6). The logarithmic scaling violations – that differ from a simple power law – can be seen as an implicit consequence of the breaking of scale invariance during renormalization of the quantum fluctuations.

### 2.2.4 Sum rules

As we will see in this subsection, not only can the contact be extracted from the high-frequency tail (2.62), it can also be connected to a property of the RF spectrum that is called the *clock shift*. Historically, the clock shift got its name from its connection to a tiny change in the energy of hyperfine transitions due to interaction

---

[7]On a personal note: It is an extraordinary moment in a theorist's life, when the experimentalist tells him that his theoretical results solved (some of the) problems the experimentalist was experiencing.

effects between, for example, cesium atoms. These atoms are also used to keep the standard time. The clock shift quantifies a systematic error in these atomic clocks. However, because of the sum rules that will be derived below, and the possibility to extract the contact parameter from them, the clock shift for the two-dimensional Fermi gas turns out to provide useful information rather than being a nuisance. For the three-dimensional gas, analogous sum rules, that connect the clock shift to the contact, were derived in [50, 48] using a commutator approach. They were later re-derived in [52] using the techniques presented below.

The clock shift is defined as the ratio of the first and zeroth moment of the RF spectrum. The first moment $\int d\omega \, \omega \Gamma(\omega)$ will contain information about the contact of the system. The zeroth moment $\int d\omega \Gamma(\omega)$ will turn out to be connected to the number of species-2 atoms in the gas before the RF pulse excites some of the atoms into the state $|3\rangle$. In order to keep the derivation as general as possible, consider an integral over the RF spectrum with weighting function $f$:

$$I_f = \int_{-\infty}^{\infty} d\omega \, f(\omega) \Gamma(\omega) \tag{2.64}$$

The aim is to express this integral as a contour integral in the complex $\omega$-plane. The results that follow are valid when the weight function $f(\omega)$ is analytic and, in addition, real on the real axis $\Im[\omega] = 0$. Furthermore, the weight function has to fulfill $f(\omega^*) = f^*(\omega)$. The weighting functions of interest, 1 and $\omega$, have all of these properties. As a reminder: the RF spectrum $\Gamma(\omega)$ is connected to the imaginary part of the matrix element of the RF operator $\mathcal{O}_{\mathrm{rf}}(\omega + i\epsilon)$ via equation (2.24). In the complex $\omega$-plane, the correlator $\langle \mathcal{O}_{\mathrm{rf}}(\omega) \rangle$ will have singularities *on* the real axis, namely branch cuts and / or poles. Consider now the contour integral

$$I_C = \frac{\Omega^2}{2} \int_{\gamma_A + \gamma_B} d\omega \, f(\omega) \left\langle \int d^2R \, \mathcal{O}_{\mathrm{rf}}(\omega, \mathbf{R}) \right\rangle, \tag{2.65}$$

where the contour $\gamma_A$ runs slightly above, and the contour $\gamma_B$ slightly below the real axis. In addition, the contours run in opposite direction. An illustration of the contours and a typical branch cut structure is shown in figure 2.8(a). To show that the contour integral is equal to the one over all real frequencies, $I_C = I_f$, we require the property

$$\left( i \int d^2R \, \langle \mathcal{O}_{\mathrm{rf}}(\omega, \mathbf{R}) \rangle \right)^* = i \int d^dR \, \langle \mathcal{O}_{\mathrm{rf}}(\omega^*, \mathbf{R}) \rangle. \tag{2.66}$$

This property can be proven by use of a Lehmann representation. Define the

(a) Original contour  (b) Deformed to a large circle
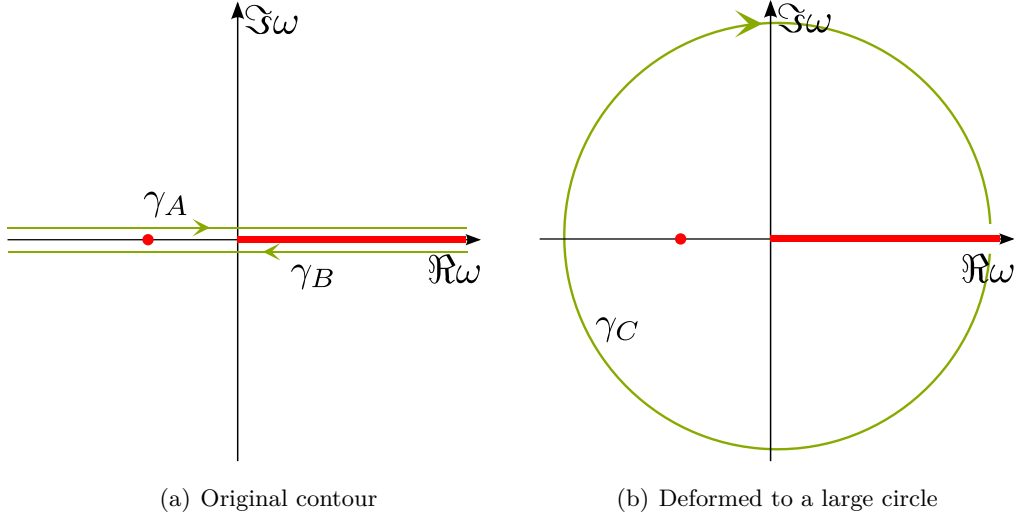
Figure 2.8: Contours of integration (green) in the complex $\omega$-plane. Poles and branch cuts on the real axis are colored red. 2.8(a) shows the two counter-running contours just below and above the real axis. They are equivalent to the integral (2.64). 2.8(b) shows the contours deformed into a large circle. As its radius approaches infinity ,the OPE (2.57) becomes exact on the circle.

operator $A = \int d^d x \psi_2^\dagger \psi_3(\mathbf{x})$ and choose a $\omega$ in the upper complex plane. We have, for the matrix element of $\mathcal{O}_{\rm rf}$:

$$
\begin{aligned}
i \int d^d R \left\langle \mathcal{O}_{\rm rf}(\omega, \mathbf{R}) \right\rangle &= i \int_0^\infty dt \, e^{i\omega t} \left\langle A(t) A^\dagger(0) \right\rangle \\
&= i \int_0^\infty dt \, e^{i\omega t} \sum_{n,m} \frac{e^{-\beta E_n}}{Z} e^{it(E_n - E_m)} |\langle n|A|m\rangle|^2 \\
&= -\sum_{n,m} \frac{e^{-\beta E_n}}{Z} \frac{|\langle n|A|m\rangle|^2}{\omega - (E_m - E_n)} \qquad (2.67)
\end{aligned}
$$

The indices $n$ stand for the sum connected to the trace of the expectation value, containing $N_2$ particles of species 2 and no particles of species 3. The index $m$ originates from the insertion of an identity operator in the subspace of $N_2 - 1$ species-2 particles and 1 atom of type 3. From the form (2.67), since all quantities except for the complex frequency are evidently real, we can immediately read off the property (2.66). In essence, it is connected to the fact that *retarded* and *advanced*

Green's functions are connected to each other via complex conjugation. We can parametrize $\gamma_A$ and $\gamma_B$ by $\bar{\omega} + i\epsilon$ and $\bar{\omega} - i\epsilon$, $\bar{\omega} \in \mathbb{R}$ respectively. To account for the difference in directions, we have to introduce an additional minus sign in the $\gamma_B$ integral. Starting from (2.65), we have

$$
\begin{aligned}
I_C &= \frac{\Omega^2}{2} \int d^2R \int_{-\infty}^{\infty} d\bar{\omega} f(\bar{\omega}) \left[ \mathcal{O}_{\mathrm{rf}}(\bar{\omega} + i\epsilon, \mathbf{R}) - \mathcal{O}_{\mathrm{rf}}(\bar{\omega} - i\epsilon, \mathbf{R}) \right] \\
&\stackrel{(2.66)}{=} \frac{\Omega^2}{2}(-i) \int d^2R \int_{-\infty}^{\infty} d\bar{\omega} f(\bar{\omega}) \left[ i\mathcal{O}_{\mathrm{rf}}(\bar{\omega} + i\epsilon, \mathbf{R}) - (i\mathcal{O}_{\mathrm{rf}}(\bar{\omega} + i\epsilon, \mathbf{R}))^* \right] \\
&= \Omega^2 \int d^2R \int_{-\infty}^{\infty} d\bar{\omega} f(\bar{\omega}) \Im \left[ i\mathcal{O}_{\mathrm{rf}}(\bar{\omega} + i\epsilon, \mathbf{R}) \right] \stackrel{(2.64)}{=} I_f.
\end{aligned}
$$

The fact that $f$ is analytic near the real axis, such that $f(\bar{\omega} + i\epsilon) = f(\bar{\omega} - i\epsilon)$ when $\epsilon \to 0$, was used.

When there are no poles in the upper or lower complex plane, the contour integral $I_C$ is equal to the integral over a large circle at infinity, depicted in figure 2.8(b). From the Lehmann representation (2.67), we see that there can only be poles or branch cuts in the upper or lower complex plane, if there exists an energy eigenvalue $E_n$ with non-vanishing imaginary part. Since our Hamiltonian $H_0$ is Hermitian, this will not be the case. Note, however, that the arguments above do *not* hold for so called optical models, where one tries to model a decay via the inclusion of complex coupling constants $g$, $g'$ (see, for example [60]). The property (2.66) will, in particular, not be valid, since that would amount to the introduction of an exponentially growing instability for every decay channel that is being modeled. On a large circle with radius $|\omega| \to \infty$, the operator product expansion (2.57) becomes *exact*. For the derivation of sum rules of the form (2.64), it is thus sufficient to look at the contour integral of (2.57) on an infinite circle.

As a final piece of preparatory work, consider the integral

$$
\begin{aligned}
\mathcal{B}(x) &= \int_{\bar{\epsilon}}^{2\pi - \bar{\epsilon}} dt \frac{4\pi/m}{\sqrt{(\pi - t)^2 + \log^2 x}} \\
&= \frac{4\pi}{m} \log \left( \frac{\pi - \bar{\epsilon} + \sqrt{(\pi - \bar{\epsilon})^2 + \log^2 x}}{-\pi + \bar{\epsilon} + \sqrt{(\pi - \bar{\epsilon})^2 + \log^2 x}} \right),
\end{aligned}
\tag{2.68}
$$

where, in particular, $x > 1$. This makes the integral always well defined, even in the limit $\bar{\epsilon} \to 0$. For $x \to \infty$, $\mathcal{B}(x)$ vanishes:

$$
\lim_{x \to \infty} \mathcal{B}(x) = 0
\tag{2.69}
$$

In the following, $\mathcal{B}(x)$ will be used as an upper bound for some of the contour integrals. Hence, in the $x \to \infty$ limit, these integrals have to be zero.

**Sum rule for $f(\omega) = 1$**   The aim is to derive the sum rule for the normalization $\int d\omega \Gamma(\omega)$ of the RF spectrum. From the derivation of the 3D sum rules that used a commutator approach, we can infer, since the commutators in question do not change, that the normalization of the spectrum has to be connected to the number of particles of species 2 [50, 48]. This is exactly what we will find. The circular contour is denoted by $\gamma_C$. It can be parametrized as

$$\begin{aligned} \gamma_C(t) &= \Lambda_\omega e^{-it}, \qquad t \in ]\bar{\epsilon}, 2\pi - \bar{\epsilon}[ \\ \dot{\gamma}_C(t) &= -i\Lambda_\omega e^{-it}. \end{aligned} \qquad (2.70)$$

$\Lambda_\omega$ is a high-frequency cutoff that will be sent to infinity in the end of the calculation. The small $\bar{\epsilon}$ is related to the $\epsilon$ in (2.64) by the trigonometric identity

$$\sin \bar{\epsilon} = \frac{\epsilon}{\Lambda_\omega}. \qquad (2.71)$$

The evaluation of the $1/\omega$ term in the OPE (2.57) is straightforward:

$$\frac{\Omega^2}{2} N_2 \int_{\gamma_C} d\omega \frac{i}{\omega} = \pi \Omega^2 N_2 \qquad (2.72)$$

In a similar fashion, the integral over the pure $1/\omega^2$ term is given by

$$\frac{\Omega^2}{2} \frac{C}{m^2} \left( \frac{1}{g} - \frac{1}{g'} \right) \int_{\gamma_C} d\omega \frac{i}{\omega^2} = \frac{\Omega^2}{2} \frac{C}{m^2} \left( \frac{1}{g} - \frac{1}{g'} \right) \frac{1}{\Lambda_\omega} \int_{\bar{\epsilon}}^{2\pi - \bar{\epsilon}} dt\, e^{it}$$
$$\overset{\Lambda_\omega \to \infty}{\longrightarrow} 0. \qquad (2.73)$$

The only term left is the $\sim D(\omega)/\omega^2$ piece. Defining the shorthand

$$A = \left( \frac{1}{g} - \frac{1}{g'} \right)^2 \frac{\Omega^2}{2m^2} C \geq 0 \qquad (2.74)$$

and plugging in the form (2.44) of the two-dimensional dimer propagator, the contour integral reads

$$A \int_{\gamma_C} d\omega \frac{-i}{\omega^2} D(\omega) = -\frac{A}{\Lambda_\omega} \int_{\bar{\epsilon}}^{2\pi - \bar{\epsilon}} dt\, \frac{e^{it} 4\pi/m}{\log \left( \frac{\Lambda_\omega e^{i(\pi - t)}}{E_D'} \right)}. \qquad (2.75)$$

The branch cut of the logarithm is indeed never crossed when choosing $-1 = e^{i\pi}$. We will now show that, in the limit of $\Lambda_\omega \to \infty$, the absolute value of the contour

integral is bounded from above by zero. To this end, the triangular inequality $|\int dt f(t)| \leq \int dt |f(t)|$ is used:

$$
\begin{aligned}
\left| A \int_{\gamma_C} d\omega \frac{-i}{\omega^2} D(\omega) \right| &\leq \frac{A}{\Lambda_\omega} \int_{\bar{\epsilon}}^{2\pi - \bar{\epsilon}} dt \left| \frac{4\pi/m}{\log\left(\frac{\Lambda_\omega}{E'_D}\right) + i(\pi - t)} \right| \\
&= \frac{A}{\Lambda_\omega} \mathcal{B}\left(\frac{\Lambda_\omega}{E'_D}\right) \overset{\Lambda_\omega \to \infty}{\longrightarrow} 0,
\end{aligned}
\tag{2.76}
$$

where the integral $\mathcal{B}$ was defined in equation (2.68). Higher order contributions in the OPE have even faster vanishing behavior at infinite frequency. As a reminder: The contour integral along the infinite circle can be equated, as shown in (2.68), with the integral of the RF spectrum over all frequencies. Hence, we have shown that the normalization of the RF spectrum is essentially the product of the Rabi frequency and the number of particles of species 2.

**Sum rule for $f(\omega) = \omega$** In this paragraph, the sum rule for the first moment $\int d\omega \omega \Gamma(\omega)$ of the RF spectrum will be derived. The technique used will be same as in the preceding paragraph. From the known three-dimensional results [52, 50, 48], one expects the sum rule to be proportional to the contact between species 1 and 2. The contour integral of the $\sim 1/\omega$ term in (2.57) evaluates to

$$
\begin{aligned}
\frac{\Omega^2}{2} N_2 \int_{\gamma_C} d\omega \, \omega \frac{i}{\omega} &= \frac{\Omega^2}{2} N_2 \Lambda_\omega \int_{\bar{\epsilon}}^{2\pi - \bar{\epsilon}} dt e^{-it} \\
&= \frac{\Omega^2}{2} N_2 \Lambda_\omega \frac{1}{i} \left[ e^{+i\bar{\epsilon}} - e^{-i\bar{\epsilon}} \right] \\
&\overset{(2.71)}{\approx} \Omega^2 N_2 \Lambda_\omega \frac{\epsilon}{\Lambda_\omega} \overset{\epsilon \to 0}{\longrightarrow} 0,
\end{aligned}
\tag{2.77}
$$

where the small angle $\bar{\epsilon}$ was expanded to first order in terms of the small imaginary part $\epsilon$ of the original contour. Note that the integral is only zero because we are asking for the *imaginary part* of $i\mathcal{O}_{\text{rf}}(\omega + i\epsilon)$. The corresponding real part in fact diverges. This can be understood from the identity (2.59). The integral $\int d\omega \omega \delta(\omega)$, belonging to the imaginary part of $1/\omega + i\epsilon$, indeed vanishes. However, the real part $\int d\omega \omega \mathcal{P} \frac{1}{\omega}$ is infinite.

For the pure $\sim 1/\omega^2$ term, we have

$$
\frac{\Omega^2}{2} \frac{C}{m^2} \left( \frac{1}{g} - \frac{1}{g'} \right) \int_{\gamma_C} d\omega \, \omega \frac{i}{\omega^2} = \pi \Omega^2 \frac{C}{m^2} \left( \frac{1}{g} - \frac{1}{g'} \right).
\tag{2.78}
$$

The contribution is finite and proportional to the contact, as well as to the difference in interaction strengths between the initial and final state. As we will see below, it is the only non-vanishing contribution to the first moment of the RF spectrum. Note that if we would plug in the form (2.45) for the three dimensional coupling constants $g$ and $g'$, the result would be consistent with the sum rule for the three dimensional case [52, 50, 48].

Again using the shorthand $A$ defined in eq. (2.74), we find the contour integral of the $\sim D(\omega)/\omega^2$ piece to be

$$A \int_{\gamma_C} d\omega\, \omega \frac{-i}{\omega^2} D(\omega) \;\; = \;\; -A \int_{\bar\epsilon}^{2\pi-\bar\epsilon} dt \frac{4\pi/m}{\log\left(\frac{\Lambda_\omega e^{i(\pi-t)}}{E'_D}\right)}. \tag{2.79}$$

As before, the form (2.79) avoids crossing the branch cut of the logarithm. The triangle inequality $|\int dt f(t)| \le \int dt |f(t)|$ yields

$$\left| A \int_{\gamma_C} d\omega\, \omega \frac{-i}{\omega^2} D(\omega) \right| \;\; \le \;\; A \int_{\bar\epsilon}^{2\pi-\bar\epsilon} dt \left| \frac{4\pi/m}{\log\left(\frac{\Lambda_\omega}{E'_D}\right) + i(\pi-t)} \right|$$

$$= \;\; A\, \mathcal{B}\left(\frac{\Lambda_\omega}{E'_D}\right) \overset{\Lambda_\omega\to\infty}{\Longrightarrow} 0. \tag{2.80}$$

The integral was again shown to be bounded from above by the integral $\mathcal{B}$ defined in eq. (2.68). Since $\mathcal{B}$ vanishes in the limit of infinite cutoff, the contour integral of the $\sim D(\omega)/\omega^2$ piece has to be zero as well. Higher order terms in the OPE vanish faster for increasing frequencies than the ones we considered so far. Thus, they do not contribute to the sum rule. Note that higher order moments of the RF spectrum will in general be divergent, because the RF spectrum does not decay fast enough to suppress any power of frequency. Another comment concerns the sum rules in three dimensions: They were almost derived here. The only additional ingredient, that needs to be shown explicitly, is that the $\sim D(\omega)/\omega^2$ piece vanishes also in the case of three-dimensional fermions.

**Sum rules for RF spectroscopy**  To summarize the findings on the zeroth and first moments of the radio-frequency spectrum, the explicit form (2.6) for the coupling constants $g$ and $g'$ is plugged into eq. (2.78). From the equality (2.68) of the contour integral with the integral over the imaginary part of $\mathcal{O}_{\rm rf}$, see eqs. (2.64), (2.65), and our results from the preceding paragraphs, we can infer the

**Sum rules for the RF spectrum of the 2D Fermi gas**

The radio-frequency absorbtion spectrum $\Gamma(\omega)$ of the two-dimensional Fermi gas, in the case of an initially empty final state, fulfills the exact relations

$$\int_{-\infty}^{\infty} d\omega\, \Gamma(\omega) = \pi\Omega^2 N_2 \tag{2.81a}$$

$$\int_{-\infty}^{\infty} d\omega\, \omega\Gamma(\omega) = \frac{\Omega^2}{2m} \log\left(\frac{a_2'}{a_2}\right) C. \tag{2.81b}$$

$N_2$ is the number of initially present type-2 atoms. $\Omega$ is the Rabi frequency for the transition from spin state $|2\rangle$ to $|3\rangle$. $a_2'$ and $a_2$ are the two-dimensional scattering lengths with atoms of species 1 in the final and initial state, respectively. The parameter $C$ is the contact between species 1 and 2, defined in (2.13).

For an initially empty final state, these sum rules receive no corrections from final state interactions between states $|2\rangle$ and $|3\rangle$, since the corresponding terms in the OPE are of higher order. The sum rules provide another means for extraction of the contact parameter of the system. In experiment, one usually measures the *clock shift*, defined as the ratio between the two moments (2.81a) and (2.81b):

$$\langle\omega\rangle \;=\; \frac{\int d\omega\,\omega\Gamma(\omega)}{\int d\omega\,\Gamma(\omega)} = \frac{\log\left(\frac{a_2'}{a_2}\right) C}{2\pi m N_2} \tag{2.82}$$

This way, the dependence on the Rabi frequency $\Omega$ of the transition drops out. It is interesting to note that, reminiscent to the three-dimensional case, the first moment of the RF spectrum diverges in the limit of vanishing final state interactions $a_2' \to 0$. This can be understood from the high-frequency asymptotics, given in (2.62). When $a_2' \to 0$, the $\sim 1/\omega^2$ tail results in a logarithmic divergence in the first moment of the spectrum. The presence of final state interactions pushes this behavior "over the edge" to be convergent, since the spectrum decays like $\sim 1/\omega^2 \log^2 \omega$ in this case. In the case of equal interactions in both the initial and final state, the clock shift vanishes. As pointed out earlier in sec. 2.2.3, this is due the fact the RF pulse just applies a rotation in spin space in this case [57]. In particular, the vanishing of the clock shift stays true in the case of non-interacting initial *and* final states.
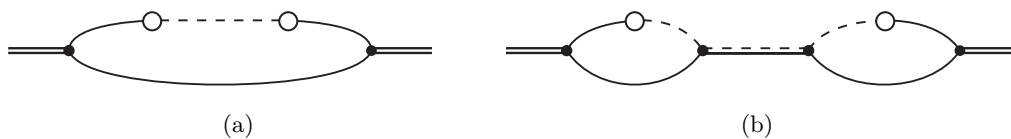
Figure 2.9: Diagrams for the calculation of the RF response of a $1 - 2$ dimer. The double bold lines are the external amputated $1 - 2$ dimer lines. The dashed-bold line stands for the propagation of a $1 - 3$ dimer.

### 2.2.5 RF spectroscopy on the dimer and comparison to experiment

A simple – analytically solvable – case is the one for RF spectroscopy on a single $1 - 2$ dimer at rest. It can be used to test the sum rules (2.81a) and (2.81b), as well as the high frequency asymptotics (2.62). This possibility of a consistency check will be our primary motivation to look at the RF spectrum of the dimer. As it turns out, this case also compares well to experiment when the dimer binding energy is large compared to the Fermi energy. The calculation is performed in the two dimensional case, three dimensional results can be obtained in an analogous manner. For this section, it is useful to introduce the auxiliary dimer fields $d_{12} = \psi_2\psi_1$, $d_{13} = \psi_3\psi_1$ (for details on the auxiliary field trick, see sec. 3.1.2). The propagator of this auxiliary field turns out to be connected to the scattering amplitude (2.7) via

$$G_{d_{12}}(E) \quad = \quad \frac{\mathcal{A}(E)}{(-ig)^2}, \tag{2.83}$$

and completely analogous for $G_{d_{13}}(E)$.

The radio-frequency spectrum of the dimer is determined by the expectation value of the RF correlator $\mathcal{O}_{\mathrm{rf}}$ in the state containing an external dimer of energy $-E_D < 0$, cf. eq. (2.24). This expectation value can be expressed via the diagrams in figure 2.9. The external dimer lines are amputated. This means that, due the LSZ reduction formula [28], we have to include a factor $\sqrt{Z_D}$ for every external dimer leg, where $Z_D$ stands for the residue of the dimer propagator at the bound state pole. It can be identified with the wave function renormalization of the dimer field $d_{12}$. From (2.83), we can infer that the dimer residue for the two-dimensional case is given by

$$Z_D \quad = \quad \frac{4\pi E_D}{mg^2}. \tag{2.84}$$

Hence, the expectation value of the RF operator $\mathcal{O}_{\mathrm{rf}}$ can, using the integrals (2.39) and (2.40), be expressed as

$$i\int d^2 R\langle\mathcal{O}_{\mathrm{rf}}(\omega,\mathbf{R})\rangle \;=\; i(-ig)^2 Z_D\Big[\mathcal{M}(-E_D)$$

$$+(-ig')^2 iG_{d_{13}}(\omega-E_D)\mathcal{K}^2(-E_D)\Big]. \quad (2.85)$$

As you might have noticed, the above expression, when naively evaluated, gets an additional factor of volume from the integration over all positions $\mathbf{R}$. This factor of volume is canceled by the normalization of the center of mass motion part (which, in the present case, carries zero momentum) of the dimer state. Using the identities given in eqs. (2.39) and (2.40), we can express everything in terms of the Lippmann-Schwinger integral $\mathcal{I}$, which, in turn, we can re-express in terms of the scattering amplitudes via eqs. (2.42) and (2.41). The only integral that we need to solve by hand is the term

$$\int_{\mathbf{q}}\left(\frac{i}{-E_D-\frac{q^2}{m}}\right)^2 \;=\; -\frac{m}{4\pi E_D}, \quad (2.86)$$

which can be done with elementary methods. Collecting all the terms yields

$$i\int d^2 R\langle\mathcal{O}_{\mathrm{rf}}(\omega,\mathbf{R})\rangle \;=\; -\frac{E_D}{\omega^2}\left[\frac{\omega}{E_D}+\log\left(1-\frac{\omega}{E_D}\right)-\frac{\log^2\left(1-\frac{\omega}{E_D}\right)}{\log\left(\frac{E_D-\omega}{E_D'}\right)}\right](2.87)$$

for the expectation value of the RF operator in a state with external on-shell dimers. A short comment on the pole and branch cut structure of this expectation value: At first, $\omega=0$ might seem to be a pole in the complex plane, but it is actually not. This can be seen when expanding the logarithms $\log(1-\omega/E_D)\approx-\omega/E_D$ for $\omega\to 0$. The only true pole is the one at $\omega=(E_D-E_D')$, which, as will become more clear below, corresponds to transitions from the initial dimer to a dimer in the final state. For $\omega>E_D$, the expectation value (2.87) has a branch cut. This branch cut corresponds to transitions that break up the dimer in the initial state into two atoms in the final state. The bound-bound pole always lies left of the branch cut that starts at $\omega=E_D$, because $E_D'\geq 0$.

According to eq. (2.24), the RF spectrum for spectroscopy on a single dimer can be obtained from the imaginary part of (2.87) via the replacement $\omega+i\epsilon$ and the limit $\epsilon\to 0$. For $\omega>E_D$, this prescription sets the imaginary part of the logarithms to $-\pi$. For $\omega<E_D$, the logarithmic terms $\sim\log(1-\omega/E_D)$ are real in

the limit $\epsilon \to 0$. Expansion of (2.87) in a Laurent series around the bound-bound pole $\omega = E_D - E'_D$ reveals the following form for the leading term close to the pole:

$$i \int d^2R \langle \mathcal{O}_{\mathrm{rf}}(\omega + i\epsilon, \mathbf{R}) \rangle \approx \frac{E_D E'_D \log^2 \left( \frac{E'_D}{E_D} \right)}{(E_D - E'_D)^2} \frac{-1}{\omega + i\epsilon - (E_D - E'_D)} \quad (2.88)$$

From eqs. (2.59), we can infer that, after taking the imaginary part, this corresponds to a $\delta$ function peak at $\omega = E_D - E'_D$. Collecting all the previous thoughts and performing the limits, we find the RF transition rate for spectroscopy of a single dimer:

$$\begin{aligned} \Gamma_D(\omega) &= \pi\Omega^2 \frac{E_D E'_D \log^2 \left( \frac{E'_D}{E_D} \right)}{(E_D - E'_D)^2} \delta(\omega - (E_D - E'_D)) \\ &+ \pi\Omega^2 \frac{E_D \log^2 \left( \frac{E'_D}{E_D} \right)}{\omega^2 \left[ \log^2 \left( \frac{\omega - E_D}{E'_D} \right) + \pi^2 \right]} \Theta(\omega - E_D) \end{aligned} \quad (2.89)$$

**Plot of the RF transition rate and comparison to experiment**   Figure 2.10 shows a plot of the RF spectrum defined by (2.89). The theory prediction is shown as a black curve, experimental data points are gray. The experimental data, provided to us by Zwierlein and collaborators [61], can be found in [45], figure 1(a), second to lowest plot. The data shown here extend to larger $\omega$ than the ones in ref. [45]. The data in fig. 2.10 were recorded at a magnetic field of 690.7(1) G. The broad Feshbach resonance for the spin states in question lies at a magnetic field of 694.4(5) G [45, 62], which implies that, in three dimensions, the system would be close to unitarity. The ratio of lattice depth to recoil energy was 18.6(7), which implies that the Fermi gas should be well described by two-dimensional physics. $E'_D/E_D = 9.4$ is the ratio of final and initial state binding energies for the given parameters. The binding energy of the initial state dimer is around six times larger than the Fermi energy of the system [61]. The dimer binding energy is thus by far the largest scale in the initial state system. In this so called BEC limit, one expects the system to be well approximated as a gas of structureless dimers. Thus, it makes sense that, at least to leading order, the spectrum is well described by the two-body result (2.89). The only parameter that was adjusted in figure 2.10 is the Rabi frequency $\Omega$, which just redefines the normalization of the spectrum. A least square fit in $\Omega$ was used to fit the height of the experimental data.

As was mentioned before, also the anomalous logarithmic decay $\sim 1/\omega^2 \log^2 \omega$ can be seen in experiment [61, 45, 63].
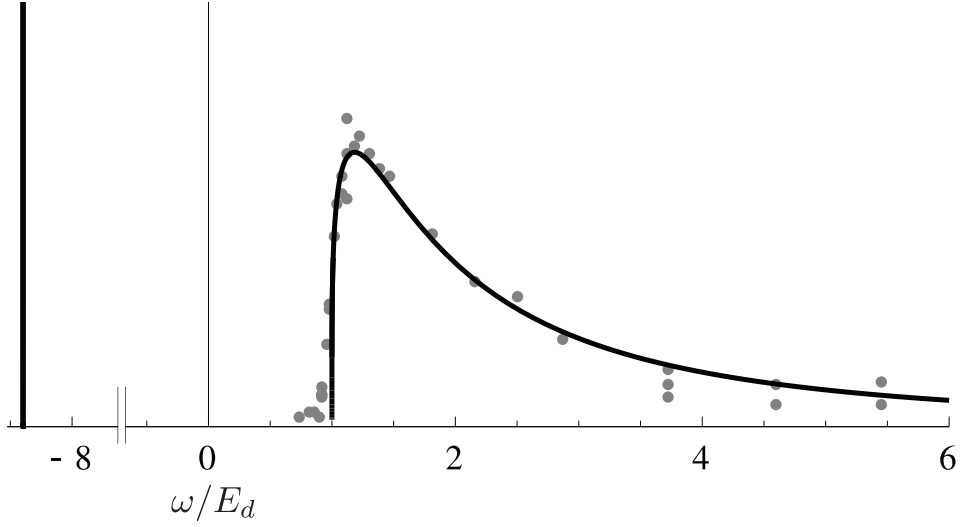
Figure 2.10: Plot of the RF transition rate (2.89) in the case of $E'_D = 9.4E_D$, which was chosen to match the experimental parameters (see text). The height of the theory curve (black) was adjusted by a least square fit to the height of the experimental data (gray points). The $\delta$-peak at $\omega = E_D - E'_D$ corresponds to the transition from a (12)-dimer into a (13)-dimer. The hump starting at $\omega/E_D = 1$ corresponds to transitions that break up the (12)-dimer into a two-atom scattering state.

**Comparing the dimer spectrum to the universal relations**   Extracting the parameters that determine the sum rules (2.81a) and (2.81b), as well as the high-frequency asymptotics (2.62), is straightforward in the case of a single dimer. The number of type-2 atoms in a (12)-dimer is of course $N_2 = 1$. The contact of the dimer can be inferred from the adiabatic theorem, which, for the two-dimensional case, reads [36, 38]

$$C \;=\; 2\pi m a_2 \frac{\partial E}{\partial a_2} \overset{(12)-\text{dimer}}{=} 4\pi m E_D. \tag{2.90}$$

The first test regards the high-frequency asymptotics of the dimer RF spectrum, given in eq. (2.89). Expanding (2.89) in high frequencies $\omega \gg E_D, E'_D$ yields

$$\Gamma_D(\omega) = \pi\Omega^2 \frac{E_D \log^2\left(\frac{E'_D}{E_D}\right)}{\omega^2 \left[\log^2\left(\frac{\omega}{E'_D}\right) + \pi^2\right]} + \dots, \tag{2.91}$$

which equates to (2.62) when using the contact (2.90). The sum rules for the dimer can be derived from the form (2.87) of the RF correlator in case of an initially present dimer. The same contour integration methods as presented in sec. 2.2.4 are used. The result is consistent with (2.81a) and (2.81b) for $N_2 = 1$ and $C = 4\pi m E_D$. The calculation is not presented here. The only slight difference to the one performed in sec. 2.2.4 is that some of the upper bounds are slightly more involved, should you not choose to expand the integrand around $|\omega| = \infty$ first. The sum rules were also tested via numerical integration of the moments of the spectrum (2.89), and are again in agreement with our predictions (2.81a), (2.81b).

### 2.2.6 Summary

In this section, we have treated the problem of radio-frequency spectroscopy for a two-dimensional Fermi gas. Exact relations, that relate the contact to sum rules and high frequency asymptotics of the RF transition rate, were derived. Linear response theory was used to write the transition rate in second quantized form. A short-time operator product expansion of the correlator $\mathcal{O}_{\mathrm{rf}}$, that defines the transition rate, provided the basis for the derivation of the exact relations. The high-frequency asymptotic behavior of the spectrum followed directly from the OPE. This asymptotic behavior will be used, in the special case of vanishing final state interactions, to check the numerical results for the single-particle spectral function in the next section 2.3. For the sum rules, we had to translate the moments of the RF spectrum into weighted contour integrals along an infinite circle, where the OPE becomes exact.

## 2.3 Virial expansion for the spectral function

The picture behind the *three-dimensional* BCS-BEC crossover, in the superfluid regime, is an evolution from weakly bound cooper pairs on the BCS side to strongly bound bosonic molecules on the BEC side. One may ask whether pairing influences physics even above the superfluid transition temperature. On the BEC side of the crossover, the answer is trivially yes, since there exists a two-body bound state. Its occupancy is governed by the ratio $E_D/k_B T$, where $E_D = 1/ma^2$ is the dimer binding energy, and $a$ denotes the three-dimensional scattering length that is tuned through the crossover. On the BCS side, the answer cannot be given so easily. Even though mean-field theory (BCS theory) predicts pairing and condensation to take place at the same temperature, it has been proposed that the true underlying system exhibits pairing at a temperature larger than the critical temperature. A remnant of the pairing gap is expected to influence the physics of the normal phase. This phase is called the *pseudo-gap* phase. A back-bending of the dispersion relation akin to a BCS-type dispersion $\omega(\mathbf{q}) = \sqrt{(\varepsilon_\mathbf{q} - \mu)^2 + \Delta^2}$ is suggested to provide a "smoking gun" sign for the existence of such a pseudo-gap phase. Here, $\varepsilon_\mathbf{q} = \mathbf{q}^2/2m$ is again the free particle dispersion, $\mu$ is the chemical potential and $\Delta$ is a superfluid order parameter. In the pseudogap phase, this superfluid parameter is replaced by a pseudogap parameter $\Delta_{pg} > 0$, which is finite above the superfluid transition temperature. The back-bending should, in addition, result in diminished spectral weight in the density of states. However, one has to be careful about the interpretation of the back-bending, since, as pointed out by Schneider and Randeria [64], back-bending at large momentum is a generic feature of an interacting Fermi gas. In the three-dimensional case, evidence for the existence of the pseudo-gap phase was found in experiments using momentum-resolved radio-frequency spectroscopy [65, 66]. On the theory side, some works find evidence [67, 68], while a self-consistent Luttinger-Ward description [51], which was found to describe the thermodynamic properties of the system well, does not find evidence of a pseudo-gap for the two separate temperature scales for the (pre-)formation of pairs and the pairing instability that leads to the superfluid transition.

Experimental evidence for a pseudo-gap in *two dimensions was* found by Feld *et al.* [69]. They measured the one-particle spectral function using momentum resolved RF spectroscopy and found signs of a back-bending of the dispersion relation on the order of the Fermi momentum at temperatures as high as $T/T_F = 0.45$. One of our main observations in this section will be that back-bending alone cannot be taken as

a clear sign of a pseudo-gap. Even in a high-temperature expansion, a back-bending in the occupied spectral function, which is the one measured experimentally, can be found in the bound state branch of the spectrum. The reason is that the two-dimensional system exhibits a two-body bound state *at all* 2D scattering lengths $a_2$. The spectra thus always have some features of the BEC side of the three-dimensional crossover.

The density of states, which will be formally defined in sec. 2.3.3, might provide a better measure for the existence of a pseudo-gap. The presence of a pseudo-gap implies diminished spectral weight around the Fermi surface. The weight is expected to diminish continuously as $T \to T_c$, and form a true gap for $T < T_c$. Indeed, as shown by Marianne Bauer *et al.* [19] using a self-consistent Luttinger-Ward calculation, such a pseudo gap in the density of states exists on the BCS side of the crossover. In the spectral functions calculated in [19], the lower spectral weight also clearly comes from the quasi particle branch of the spectral function, which is the one that is expected to be responsible for pseudo-gap physics.

As mentioned earlier, bound pairs exist at all temperatures and values of the interaction strength in 2D, in particular also above the superfluid BKT transition temperature $T_c$. However, in the limit of high temperatures, most fermions are unpaired and the system is well described by quasi-particle excitations. Below a temperature which we will call $T^*$, most fermions are in a bound state, giving rise to significant deviations from the simple quasi-particle picture. Indeed, as we will see in 2.3.2, the bound state generates very broad spectral weight in the occupied spectral function of the system. The densities of fermions in a dimer $n_d$ and unbound fermions $n_f$ can be estimated through the assumption of a chemical equilibrium in a gas of non-interacting fermions and non-interacting dimers [70]. The estimate for fixed total density $n = 2n_f + 2n_d$ is given by the two-dimensional version of the so-called Saha formula

$$\frac{n_f^2}{n_d} \;=\; \frac{mk_BT}{4\pi}e^{-E_D/T}.$$ (2.92)

Defining the temperature $T^*$ to be the temperature where the number of fermions in dimers $2n_d$ is equal to the number of unpaired fermions $2n_f$, we obtain

$$\frac{T^*}{T_F} \;=\; \frac{E_D/E_F}{W(E_D/E_F)}$$ (2.93)

for the estimate of $T^*$. $T_F = k_F^2/2m$ is the Fermi temperature and $W$ denotes the Lambert $W$ function. Below $T^*$, the majority of the particles is paired in a

dimer. Thus, we expect the effects of pairing to be dominant for $T \ll T^*$ and less pronounced for $T \gg T^*$.

In the following, our aim will be to establish a virial expansion of the spectral function of the two-dimensional Fermi gas. To this end, the self-energy is calculated to first order in the fugacity. From it, we extract the spectral function and the density of states. Results for the momentum distribution and the (non momentum-resolved) RF spectrum, in the case of a non-interacting final state, are obtained in a similar fashion. Particular emphasis is put on the fact that the Tan relations have to hold order by order within the cluster expansion. A short sketch of proof for this claim will be given. The momentum distribution exhibits the $C/k^4$ tail that is expected from the Tan relations in two dimensions [36, 38, 46]. The tail of the RF spectrum is also found to be compatible with the high-frequency tail derived in sec. 2.2. The quasi-particle properties (such as lifetime and effective mass) of the non-bound branch in the spectral function are analyzed in sec. 2.3.6. The results presented in this section were published in ref. [71], together with Johannes Hofmann. Shortly before the publication of the article [71], ref. [72] appeared, which partly overlaps with the results presented here. Where there is overlap, their findings for the spectral function are consistent with ours, which I checked numerically.

## 2.3.1 Virial expansion and pairing for a two-dimensional gas

The virial expansion provides a tool to analyze the physics of the Fermi gas at high temperatures. In the two-dimensional case, the requirement that the thermal de-Broglie wavelength is small compared to the typical inter-particle spacing reads $\lambda_T \ll n^{-1/2}$, where $n$ is the particle density. Our focus will lie on the two component Fermi gas with balanced population: $n_1 = n_2 = n/2$. The expansion

$$\mathcal{Z} = \sum_N z^N \mathrm{tr}_N e^{-\beta H} \qquad (2.94)$$

of the grand canonical partition function with respect to the fugacity $z = e^{\beta \mu}$ results in the following expression for the density:

$$n = \frac{2}{\lambda_T^2} \left( b_1 z + 2 b_2 z^2 + \dots \right) \qquad (2.95)$$

The prefactor of 2 is present to account for the two spin species in the balanced case. $b_1$ and $b_2$ are the first and second virial coefficients. In the non-interacting case, the $j$-th virial coefficient in two dimensions is given by $b_j^{(0)} = (-1)^{j-1}/j^2$.

This can be easily shown using, for example, the methods presented in chapter 3. The alternating sign is only present for the fermionic case. Since the first virial coefficient involves a "cluster" of only one particle, corrections due to interactions only enter from second order on. The second order correction is the well-known Beth-Uhlenbeck [73] term

$$\Delta b_2 = b_2 - b_2^{(0)} = e^{\beta E_D} + \frac{1}{\pi} \int_0^\infty dk \frac{\partial \delta(k)}{\partial k} e^{-\beta \frac{k^2}{m}}, \qquad (2.96)$$

where the phase shift in two dimensions is given by $\cot \delta(k) = (2/\pi) \ln a_2 k$, cf. eqs. (2.1), (2.7). This result can also be derived diagrammatically using the formalism that was introduced by Leyronas [9] (also see chapter 3 for the 3D case). In contrast to the three-dimensional case, however, the bound state contribution $e^{\beta E_D}$ is present for all scattering lengths, since the existence of the bound state is not restricted to one side of the crossover. For a given chemical potential, the attractive interaction between the particles tends to increase the density with respect to the non-interacting case. A plot of the fugacity as a function of temperature $T/T_F$ for different interaction strengths is shown in figure 2.11(a). The interaction strengths were chosen in order to represent the BEC side ($\ln k_F a_2 = -0.5$, $E_D/E_F = 5.43..$) of the crossover, the "unitary" regime ($\ln k_F a_2 = 0$, $E_D/E_F = 2$), and the BCS side ($\ln k_F a_2 = 1$, $E_D/E_F = 0.27..$) of the crossover. The Saha estimate for the temperature $T^*$, at which the density of paired and unpaired fermions is equal, is also included (as a dashed line) for comparison. For all the different coupling strengths $\ln k_F a_2 = -0.5, 0, 1$, the fugacity has a maximum below $T^*/T_F$ and tends to zero as $T/T_F \to 0$. The small fugacities might suggest that virial expansion is valid even as $T/T_F \to 0$. However, the criterion $z < 1$ is not sufficient in the present case, as can be seen from eq. (2.96). The bound state contribution $\sim e^{\beta E_D}$ contributes an exponentially growing piece for $|a_2| \to 0$. Thus, the better criterion for the validity of the virial expansion is that $z^2 e^{\beta E_D}$ is still smaller than one, which translates to $\mu < -E_D/2$. This is also the criterion used in [72], where the third virial coefficient was extracted using a calculation similar to the one done by Leyronas [9] for the three-dimensional case. From figure 2.11(b), we can infer that, for all three coupling strengths, the chemical potential gets lower than $-E_D/2$ at roughly $T = 0.5 T_F$, which constitutes a lower bound for the extrapolation of the virial expansion. Even though this suggests that the virial expansion in our case might be valid to temperatures as low as $0.5 T_F$, let us take a saver bet and regard the virial expansion to be valid down to $T = T_F$. This way, the series (2.95) can at least in principle have an inversion with respect to $T/T_F$.
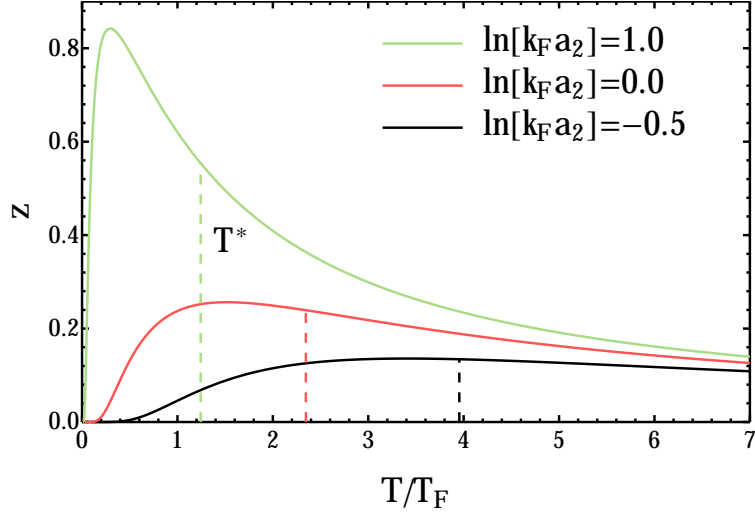
(a)
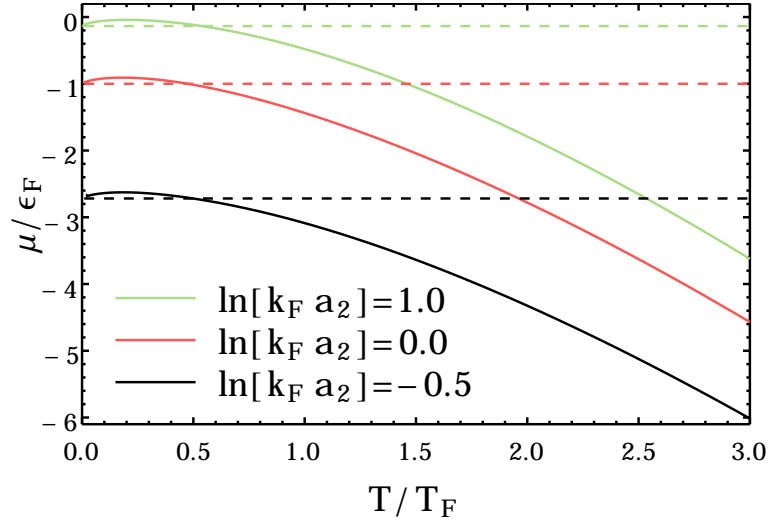


(b)

Figure 2.11: Plots of the fugacity and the chemical potential as functions of temperature. Fig. 2.11(a) shows the fugacity as a function of temperature (at fixed density). The vertical dashed lines are the values of the Saha estimate of the pairing temperature $T^*$, see eq. (2.93). Fig. 2.11(b) shows a plot of the chemical potential as a function of temperature. The horizontal dashed lines indicate half of the dimer binding energy $-E_D/2E_F$. Due to the exponential contribution of the bound state in $b_2$, also see eq. (2.96), the chemical potential needs to be smaller than these values.

It should be noted, that also for thermodynamic quantities like the energy and contact [74, 75] of the harmonically trapped 2D gas, the virial expansion was found to give good results down to remarkably low temperatures $T \approx T_F$. In the 3D case with an harmonic trap, the results were even extrapolated down to temperatures $T \approx 0.5T_F$ [76].

The results that follow in the next subsections describe the experiments conducted in [69] only qualitatively. We will not compare our data quantitatively, since the experiments were conducted in a temperature range $T/T_F = 0.27 - 0.65$, which is lower than the temperature we regard the virial expansion to be valid to. The interaction strengths probed in [69] range from $\ln k_F a_2 = -2$ to $\ln k_F a_2 = 1$. As we see in figure 2.11(b), the chemical potential obtained from a virial expansion is negative. We thus expect the physics to be dominated by the pairing aspect of the system. For $\ln k_F a_2 = 1$, the chemical potential gets close to zero however, so there is a possibility that further corrections might push it over the edge to be positive. As we will see in the following sections however, at least the regime $\ln k_F a_2 \leq 0$ is very well approximated by a first order virial expansion of the self-energy.

### 2.3.2 Virial expansion of the spectral function

In this section, we will extract features of the *single-particle spectral function*, which we mostly refer to as just the *spectral function*, within a virial expansion. The virial expansion presented here will capture one- and two-body physics, in complete analogy to the density expansion (2.95) up to order $z^2$.

#### Definition and examples

Let us start with a comprehensive summary of the spectral function. It is defined as the imaginary part of the *retarded* single-particle Greens function [26, 77]:

$$A_\sigma(\omega, \mathbf{q}) = -2\Im\left[G_\sigma^R(\omega, \mathbf{q})\right], \tag{2.97}$$

where $G_\sigma^R(\omega, \mathbf{q})$ is the Fourier transform of the retarded anti-commutator

$$G_\sigma^R(\omega, \mathbf{q}) = \int dt e^{i\omega t} \int d^d x e^{-i\mathbf{q}\cdot\mathbf{x}} G_\sigma^R(t, \mathbf{x}) \tag{2.98}$$

$$G_\sigma^R(t, \mathbf{x}) = -i\Theta(t)\left\langle\left\{\psi_\sigma(t, \mathbf{x}), \psi_\sigma^\dagger(0, \mathbf{0})\right\}\right\rangle. \tag{2.99}$$

Since we are considering the balanced case of equal densities for both species, $n_1 = n_2 = n/2$, let us drop the indices $\sigma$ from the Greens- and spectral functions, because

$G_1^R(t, \mathbf{x}) = G_2^R(t, \mathbf{x})$ in this case. One can show that $A(\omega, \mathbf{q}) \geq 0$ for all energies and momenta. Together with the normalization property [77]

$$\int \frac{d\omega}{2\pi} A(\omega, \mathbf{q}) = 1, \tag{2.100}$$

one can interpret it as the spectral probability density of creating either a particle or a hole excitation with energy $\omega$ at a given momentum $\mathbf{q}$. In the non-interacting case with dispersion $\varepsilon_{\mathbf{q}}$, the spectral function just reduces to a $\delta$-function peak at $\omega = \varepsilon_{\mathbf{q}}$.

In the experiment [69], momentum resolved RF spectroscopy, which is the analogue of angle resolved photon emission spectroscopy (ARPES) in the condensed matter context [65, 66, 69], was used to measure the spectral function. The momentum resolution is achieved when the final state is non-interacting, since one can then, after the RF-pulse is finished, expand the cloud of final state particles in a ballistic manner to measure the momentum distribution. The experiment of course can only probe (when the final state is initially unpopulated) transitions from occupied states, which is why it in fact measures the *occupied spectral function*

$$\begin{aligned} A_-(\omega, \mathbf{q}) &= n_F(\omega) A(\omega, \mathbf{q}) \\ &= \frac{2\pi}{Z} \sum_{n,m} e^{-\beta E_m} |\langle n|\psi(\mathbf{q})|m\rangle|^2 \delta(\omega - E_m + E_n), \end{aligned} \tag{2.101}$$

where $n_F(\omega) = 1/(e^{\beta\omega} + 1)$ is the Fermi distribution and $Z$ denotes the canonical partition function. That the RF spectrum in this case is indeed proportional to the occupied spectral function (2.101) can be readily shown via the same logic that went into the derivation of the RF correlator (2.21) in sec. 2.2.1. The only difference is that, in eq. (2.17), we are now asking for the rate of change of the occupation of a particle with momentum $\mathbf{q}$, i.e. $\dot{n}_3(\mathbf{q})$, rather than just the rate of change in the total number of particles $\dot{N}_3$. The assumption of a non-interacting final state then simplifies the RF transition rate to the occupied spectral function (2.101) multiplied by a constant (the squared Rabi frequency $\Omega^2$) and evaluated at the arguments $A_-(\varepsilon_{\mathbf{q}} - \omega - \mu, \mathbf{q})$ (also see [51]).

Two instructive cases are the zero-temperature limits of the BCS and BEC regimes, both within mean-field theory. In this approximation, the spectral function for both cases can be calculated analytically. The many-body wave function in these cases corresponds to a product of Cooper pair wave functions in the BCS case [78], and a product of dimer wave functions in the BEC case [79]. Within BCS theory [78], the

spectral function is given by

$$
\begin{aligned}
A(\omega, \mathbf{q}) \;=\; & 2\pi v_{\mathbf{q}}^2 \delta\left(\omega + \sqrt{(\varepsilon_{\mathbf{q}} - \mu)^2 + \Delta^2}\right) \\
& + 2\pi u_{\mathbf{q}}^2 \delta\left(\omega - \sqrt{(\varepsilon_{\mathbf{q}} - \mu)^2 + \Delta^2}\right),
\end{aligned}
\tag{2.102}
$$

where $v_{\mathbf{q}}$ and $u_{\mathbf{q}}$ are the Bogoliubov parameters. They have the normalization property $u_{\mathbf{q}}^2 + v_{\mathbf{q}}^2 = 1$ and are related to the free dispersion and gap via

$$
u_{\mathbf{q}} v_{\mathbf{q}} = \frac{\Delta}{2\sqrt{(\varepsilon_{\mathbf{q}} - \mu)^2 + \Delta^2}}.
\tag{2.103}
$$

In particular, the chemical potential in this case has to be positive in order to produce finite densities. The dispersion relations defined by the $\delta$-peaks of the spectral function (2.102) are *gapped*, with a gap of size $2\Delta$. It is impossible to create a particle or hole excitation in the energy range $-\Delta < \omega < \Delta$ ($\Delta > 0$). The hole excitations are characterized by the $\delta$-function with prefactor $v_{\mathbf{q}}^2$. Their dispersion starts with a parabolic local minimum of the energy around $\mathbf{q} = 0$ and then "bends back" towards negative energies at momenta on the order of the Fermi momentum $q \sim k_F$. When back-bending of the dispersion relation happens in the normal phase, it is often taken as a hallmark sign of a pseudo gap phase (also see the introductory remarks of the section 2.3).

The BEC limit works completely analogously. In the limit where the binding energy of the molecule is much larger than the Fermi energy, $E_D \gg \varepsilon_F$, such that the chemcial potential is approximately given by half of the energy gain to form a molecule, $\mu \approx -E_D/2 < 0$, the spectral function is given by [51, 79]

$$
A(\omega, \mathbf{q}) \;=\; 2\pi Z_{\mathbf{q}} \delta(\omega + \varepsilon_{\mathbf{q}} - \mu) + 2\pi(1 - Z_{\mathbf{q}}) \delta(\omega - \varepsilon_{\mathbf{q}} + \mu).
\tag{2.104}
$$

The factor $Z_{\mathbf{q}} = n|\phi(\mathbf{q})|^2$ is determined by the bound state function of a single molecule in momentum space $\phi(\mathbf{q})$, where $\mathbf{q}$ is the relative momentum between the two Fermions forming the molecule. In the two dimensional case discussed here, $|\phi(\mathbf{q})|^2$ takes the explicit form

$$
|\phi(\mathbf{q})|^2 \;=\; \frac{4\pi a_2^2}{(1 + (qa_2)^2)^2}.
\tag{2.105}
$$

The dispersion relations defined by the spectral function (2.104) are again gapped with a gap of size $E_D$. In contrast to the BCS case (2.102) however, the spectral function (2.104) in the BEC limit does not show any back-bending at finite momentum. In both the BEC and BCS limit, the pairing gap is also visible in the density of states, see sec. 2.3.3.

**Cluster expansion for the spectral function**

To obtain an approximation for the spectral function of the strongly interacting Fermi gas in the non-degenerate regime, we will now expand the self-energy of the single-particle Greens function up to first order in the fugacity. The formalism for the diagrammatic virial expansion, originally proposed by Leyronas in order to calculate the third virial coefficient of an interacting Fermi gas [9], is discussed in detail in chapter 3. For the reader's convenience, I will also give a short summary of the underlying ideas here.

Our starting point is the Dyson equation. It connects the self-energy $\Sigma(\omega, \mathbf{q})$, which corresponds to the one-particle irreducible (1-PI) contribution to the single-particle Green's function, to the Green's function[8]:

$$G(\omega, \mathbf{q}) \quad = \quad \frac{1}{\omega + \mu - \varepsilon_{\mathbf{q}} - \Sigma(\omega, \mathbf{q}) + i0^+} \tag{2.106}$$

At finite temperatures, a Wick rotation of time to the imaginary axis is usually better suited to deal with the problem. This implies that we replace $\omega + i0^+ \to i\omega_n$ in the above equation, where $\omega_n = (2n + 1)\pi/\beta$, $n \in \mathbb{N}$, is a fermionic Matsubara frequency [78]. The key insight underlying the diagrammatic virial expansion is that the free propagator can, when transformed to imaginary time via

$$G_0(\tau, \mathbf{q}) \quad = \quad \frac{1}{\beta} \sum_n \frac{e^{-i\omega_n \tau}}{i\omega_n + \mu - \varepsilon_{\mathbf{q}}}, \tag{2.107}$$

be written as

$$
\begin{aligned}
G_0(\tau, \mathbf{q}) \quad &= \quad e^{-\tau(\varepsilon_{\mathbf{q}} - \mu)} \left( -\Theta(\tau) + n_F(\varepsilon_{\mathbf{q}} - \mu) \right) \\
&= \quad e^{\tau\mu} \left( \underbrace{-\Theta(\tau) e^{-\tau\varepsilon_{\mathbf{q}}}}_{\equiv G^{(0)}(\tau, \mathbf{q})} + \sum_{n=1}^{\infty} \underbrace{(-1)^{n-1} z^n e^{-(n\beta + \tau)\varepsilon_{\mathbf{q}}}}_{\equiv G^{(n)}(\tau, \mathbf{q})} \right).
\end{aligned} \tag{2.108}
$$

Here, $n_F(\varepsilon_{\mathbf{q}} - \mu)$ denotes the Fermi distribution

$$n_F(\varepsilon_{\mathbf{q}} - \mu) \quad = \quad \frac{1}{e^{\beta\varepsilon_{\mathbf{q}}}/z + 1}, \tag{2.109}$$

which was expanded in terms of the fugacity for the case $z = e^{\beta\mu} \ll 1$ in the second line of eq. (2.108). The term $G^{(0)}(\tau, \mathbf{q})$ is purely *retarded*, i.e. it may only run

---

[8]Note that in this section, we are using the conventions in the book of Abrivkosov [26], since they are more suited to deal with problems which are formulated in imaginary time.

(a)                    (b)
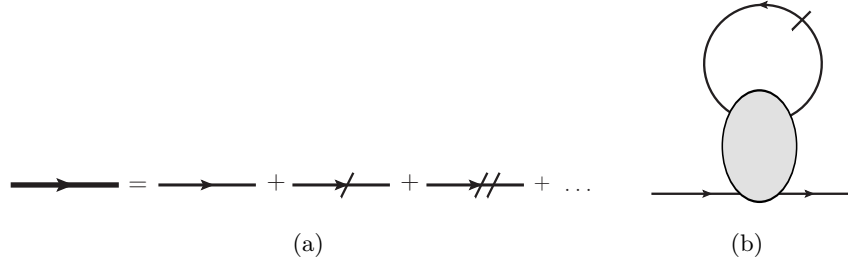
Figure 2.12: Diagrams for the virial expansion of the self-energy. Figure 2.12(a) shows the diagrammatic representation of eq. (2.108). The free propagator is expanded in terms of the propagators $G^{(n)}$, diagrammatically indicated by lines that are slashed $n$ times. Each slash corresponds to a power in the fugacity. To count the order in fugacity of any given diagram, one just needs to count the number of slashes. Lines running backward in imaginary time always require at least one slash. Figure 2.12(b) shows the leading order contribution to the self-energy. The gray blob is the two-particle scattering amplitude.

forward in imaginary time. It is the only term that does not contribute a power in the fugacity to a given diagram. The other terms $G^{(n)}$ (diagrammatically indicated by a line that is slashed $n$-times, see fig. 2.12(a)) contribute a power $z^n$, and every back-running line needs to contribute at least one power in the fugacity. This is what organizes the expansion in increasing powers of the fugacity. The higher we go in powers of the fugacity, the more diagrams we have to include. For the expansion of the self-energy, i.e. the sum of all possible 1PI graphs, it turns out that only the diagram shown in figure 2.12(b) contributes to order $z$. The gray blob indicates repeated scattering of the two fermions running forward, and is thus essentially given by the vacuum scattering matrix $\mathcal{A}$ given in eq. (2.7). There is a single back-running line of a Fermion of the opposite species that comes from the medium. This is the line that makes the diagram of order one in the fugacity. In summary, we have for the first order term in the expansion of the self-energy $\Sigma$ with respect to the fugacity $z$:

$$\Sigma^{(1)}(i\omega_n, \mathbf{q}) \;=\; z \int_0^\beta d\tau \int_{\mathbf{k}} e^{i\omega_n \tau} e^{\mu \tau} e^{-\varepsilon_{\mathbf{q}}(\beta - \tau)} \mathcal{A}(\tau, \mathbf{k} + \mathbf{q}) \qquad (2.110)$$

Thus, up to corrections[9] of order $z^2$ and higher, the self-energy can, after analytic continuation $i\omega_n \to \omega + i\epsilon$, be expressed as a Boltzmann-weighted integral of the vacuum scattering amplitude:

$$
\begin{aligned}
\Sigma^{(1)}(\omega + i\epsilon, \mathbf{q}) &= z \int_{\mathbf{k}} e^{-\beta \varepsilon_{\mathbf{k}}} \mathcal{A}(\omega + i\epsilon + \mu + \varepsilon_{\mathbf{k}} - \varepsilon_{\mathbf{k}+\mathbf{q}}/2) \\
&\underset{\mathbf{k}\to\mathbf{k}+\mathbf{q}}{=} \frac{4\pi z}{m} \int_{\mathbf{k}} \frac{e^{-\beta \varepsilon_{\mathbf{k}+\mathbf{q}}}}{\log\left(-\frac{\omega+\mu+\varepsilon_{\mathbf{k}}/2-\varepsilon_{\mathbf{q}}}{E_D} - i\epsilon\right)} \\
&= 2z \int_0^\infty dk\, k \frac{e^{-\beta \frac{k^2}{2m} - \beta \frac{q^2}{2m}} I_0\left(\frac{\beta k q}{m}\right)}{\log\left(-\frac{\omega+\mu+k^2/4m-q^2/2m}{E_D} - i\epsilon\right)} \quad (2.111)
\end{aligned}
$$

The modified Bessel function $I_0(\beta k q/m)$ is the result of the angular integration. In order to obtain numerical results, the $\epsilon \to 0$ limit is taken via (cf. eq. (2.58))

$$
\Im\left[\frac{1}{\log\left(-\frac{\omega+i\epsilon}{E_D}\right)}\right] = \Theta(\omega)\left[\frac{\pi}{\log^2\left(\frac{\omega}{E_D}\right)+\pi^2}\right] + \pi E_D \delta(\omega + E_D) \quad (2.112\text{a})
$$

$$
\Re\left[\frac{1}{\log\left(-\frac{\omega+i\epsilon}{E_D}\right)}\right] = \Theta(\omega)\left[\frac{\log\left(\frac{\omega}{E_D}\right)}{\log^2\left(\frac{\omega}{E_D}\right)+\pi^2}\right] + \Theta(-\omega)\mathcal{P}\frac{1}{\log\left(\frac{-\omega}{E_D}\right)}, \quad (2.112\text{b})
$$

where $\mathcal{P}$ again denotes the principal part. Alternatively, one can just take the imaginary part, which is numerically well-behaved, and obtain the real part via a Kramers-Kronig transform:

$$
\Re\left[\Sigma(\omega, \mathbf{q})\right] = -\int_{-\infty}^{\infty} \frac{d\omega'}{\pi} \frac{\Im\left[\Sigma(\omega, \mathbf{q})\right]}{\omega' - \omega} \quad (2.113)
$$

The momentum integration can be solved in a numerically very fast fashion when rotating the contour of integration away from the real $k$-axis ($k \to k e^{i\phi}$), which smoothens the integrand. It should be noted that in the imaginary part of the self-energy (2.111), the bound state contribution that comes from evaluation of the $\delta$ function in eq. (2.112a), is restricted to frequencies $\omega + \mu \leq \omega_{\text{th}} + \mu = \varepsilon_{\mathbf{q}} - E_D$. The spectral function $A(\omega, \mathbf{q})$ can now be connected to the expanded self-energy

---

[9]To perform the imaginary time integral in eq. (2.110), one can write the imaginary time integral as a convolution of the scattering amplitude and the free propagator. As it turns out there is a contribution from the pole of the free propagator of order $z$, and a contribution from the scattering amplitude pole and branch cut that goes like $z^2$. The result, truncated at order $z$, thus coincides what one would get from the naive identification $\mathcal{A}(x) = \int_0^\beta d\tau e^{x\tau} \mathcal{A}(\tau)$.

$\Sigma^{(1)}(\omega, \mathbf{q})$ via its definition (2.97) and the Dyson equation (2.106):

$$A(\omega, \mathbf{q}) = -2\frac{\Im\left[\Sigma^{(1)}(\omega, \mathbf{q})\right]}{(\omega + \mu - \varepsilon_\mathbf{q} - \Re\left[\Sigma^{(1)}(\omega, \mathbf{q})\right])^2 + (\Im\left[\Sigma^{(1)}(\omega, \mathbf{q})\right])^2} \tag{2.114}$$

Note that the virial expansion for the self-energy produces a result for the spectral function that still contains all orders of the fugacity. This is because the full Green's function is the sum of all *connected* diagrams, which means that it is the sum of all one-particle-reducible graphs with arbitrarily many 1PI (self-energy) insertions.

**Numerical results**

Let us now turn to the numerical results for the spectral function that is obtained from a leading order virial expansion of the self energy. The spectral functions will be calculated for the three different interaction strengths that we identified as examples for the BEC side ($\ln k_F a_2 = -0.5$), the unitary regime ($\ln k_F a_2 = 0$), and the BCS side ($\ln k_F a_2 = 1$). For $T = T_F$, density plots of the spectral functions at these different interaction strengths are shown in figures 2.13 and 2.14 (left column).

For $\ln k_F a_2 = -0.5$ and $\ln k_F a_2 = 0$, the spectral function exhibits a double peak structure. The upper branch, which will be referred to as the quasi-particle branch, because it follows the quadratic dispersion $\varepsilon_\mathbf{q} = \mathbf{q}^2/2m$ of free particles, is the more pronounced one. At $q = 0$, it is located at $\omega + \mu = 0$. The lower branch, which is associated with the two-particle bound state with binding energy $E_D = 1/ma_2^2$, and therefore starts at the threshold value $-E_D$, extends over a much broader region towards negative frequencies. Its height is also much smaller than the height of the quasi-particle peak, as is also illustrated in figure 2.15 , which shows a cut of the spectral function at zero momentum. Figure 2.15 also shows that the bound state branch is asymmetric. Coming from the threshold value of the energy, it reaches its maximum quickly and then falls of slowly towards negative frequencies. In figure 2.13, the maxima of the two branches were determined numerically with an algorithm that looks for a local maximum above and below the threshold dispersion $\omega_{\text{th}} + \mu = -E_D + \varepsilon_\mathbf{q}$. In most cases, the local maximum found also coincides with the global maximum in the respective data range. For some momentum values at $\ln k_F a_2 = 0$ however, the quasi particle peak is actually still higher than the maximum of the bound state branch even below the threshold, so a global maximum finder would not work in this case. The resulting maxima are indicated by white dashed lines. The same algorithm was also used to find the maxima of the two

(a) $\ln k_F a_2 = -0.5$

(b) $\ln k_F a_2 = -0.5$

(c) $\ln k_F a_2 = 0$

(d) $\ln k_F a_2 = 0$
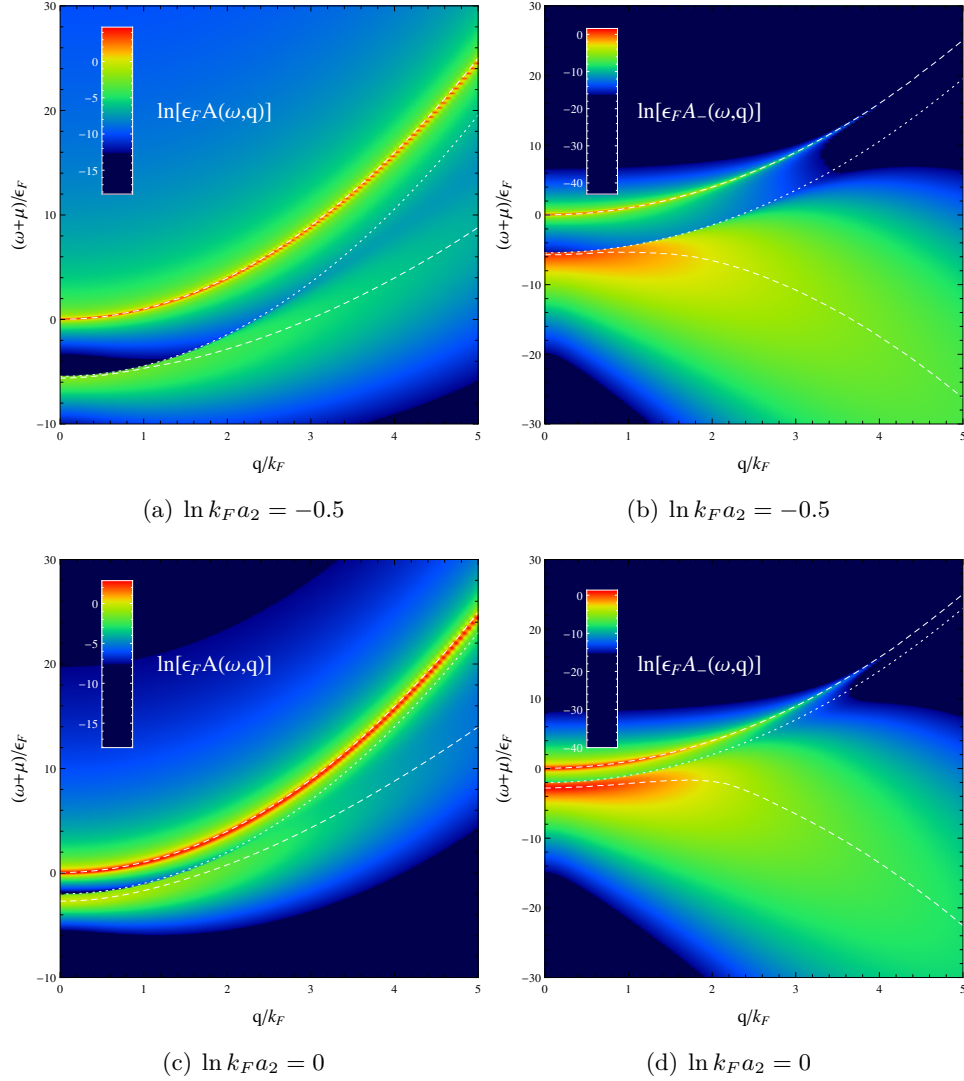
Figure 2.13: Density plots of the spectral function at $T/T_F = 1$. The left column shows the spectral function $A(\omega, \mathbf{q})$, the right column contains the occupied spectral function $A_-(\omega, \mathbf{q})$. The white dotted line indicates the threshold dispersion for the bound state branch: $\omega_{\text{th}} + \mu = -E_D + \varepsilon_{\mathbf{q}}$. The dashed white lines show the maxima of the quasi-particle and bound state branch, respectively.

(a) $\ln k_F a_2 = 1$                    (b) $\ln k_F a_2 = 1$
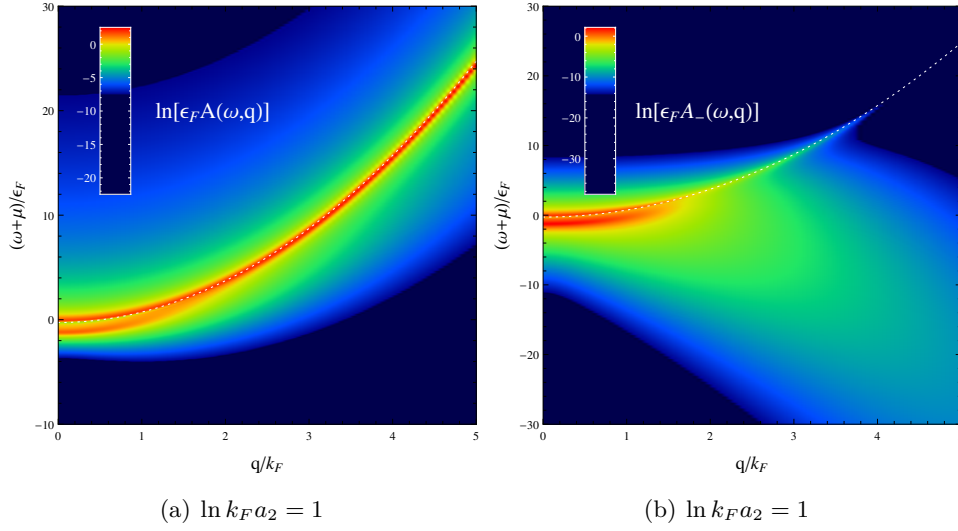
Figure 2.14: Density plots of the spectral function at $T/T_F = 1$ and $\ln k_F a = 1$. Only the threshold dispersion is shown, since for this interaction strength, the bound state maximum is not clearly distinguishable from the quasi-particle peak at all momenta.

branches in the plots for the occupied spectral function (right column in figure 2.13). As the coupling strength is shifted towards the BCS side of the crossover ($\ln k_F a_2 = 1$), the bound-state and quasi-particle branch begin to merge. The well defined local maximum below the bound state threshold also ceases to exist in a certain momentum range, and instead gets deformed to a mere shoulder on the much bigger quasi-particle peak. This is why in figure 2.14, the white dashed lines are not shown.

The occupied spectral function, which is the one measured in experiments, also exhibits a double peak structure. Due to the multiplication with a Fermi function $n_F(\omega + \mu - \mu) \approx z e^{-\beta(\omega+\mu)}$, cf. eq. (2.101), the maximum of the lower branch *bends back* at roughly $2k_F$. This back-bending has nothing to do with the formation of a pseudo-gap however, it is a result of the asymmetric shape of the bound state branch and the reshuffling of weight due to the multiplication with a Fermi distribution. At high momenta, the lower branch is also responsible for the high frequency and momentum tails in the rf-spectrum and momentum distribution of the system (also see secs. 2.3.4 and 2.3.5). It is thus linked to the short range correlations of the
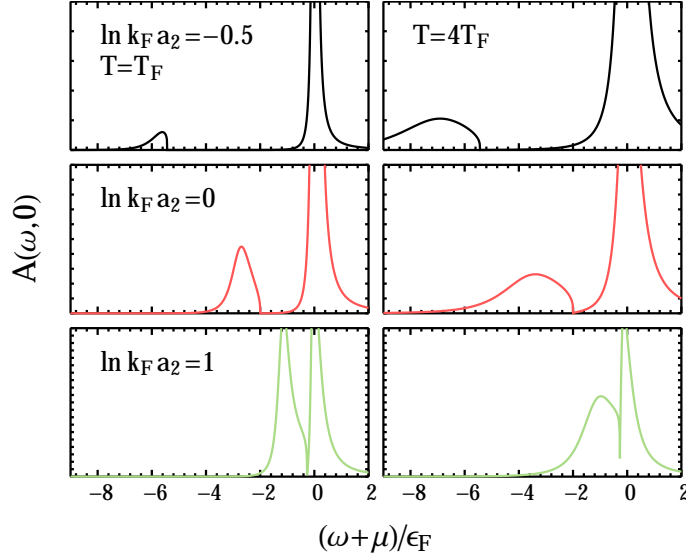
Figure 2.15: Spectral functions $A(\omega, \mathbf{0})$ as functions of frequency at momentum zero. Shown are different interaction strengths (rows) and different temperatures (columns). For increasing temperatures, the peaks get broadened and the maximum of the bound state branch shifts to smaller frequencies.

system, encoded by the *contact*.

Variations in temperature also change the shape of the spectral functions as functions of $\omega + \mu$, as shown in figure 2.15, which shows slices of the spectral function at momentum zero. The spectral functions are plotted for temperatures $T = T_F$ and $T = 4T_F$. At higher temperatures, both the quasi-particle and the bound-state peak get broadened. In addition, the maximum of the bound state branch shifts towards lower frequencies (relative to the chemical potential). Taking into account (2.111), this is to be expected, since a higher range of momenta of the scattering partners becomes accessible at higher temperatures, allowing for more pronounced redistribution of weight. Because of the apparent broadening, it might seem that quasi-particles are not well defined at higher temperatures. It is important to note that this is *not* the case, since, in order to have well defined quasi particles, it is the *ratio* $1/\tau(\mathbf{q})\omega(\mathbf{q})$ of the lifetime (inverse width of the peak) and the quasi particle energy (position of the peak) that needs to be small in comparison to one. The chemical potential, at all given interaction strengths, is much smaller at $T = 4T_F$

than it is at $T = T_F$, see figure 2.11(b). This shifts the starting value of the dispersion $\omega(\mathbf{q})$ higher up and, as it turns out (see sec. 2.3.6 for details), this is more than sufficient to cancel the broadening effects that we see in figure 2.15 (also see [80] for an analogous discussion in 3D).

### 2.3.3 Density of states

The effects of pairing (in the sense of a two-body bound state) should be visible in the density of states $\rho(\omega)$, which, as the name suggests, is a measure for the number of accessible states that exist for an excitation with a given energy $\omega$. The density of states can be obtained from an average of the spectral function over all momenta

$$\rho(\omega) \;\; = \;\; \int_{\mathbf{q}} A(\omega, \mathbf{q}). \tag{2.115}$$

This is intuitively clear, because the spectral function counts the number of excitations that exist for a certain momentum $\mathbf{q}$ and energy $\omega$. The simplest limit where the density of states is known analytically is the non-interacting Fermi gas. In this case, with our normalization of the spectral function, it is given by

$$\rho_{\text{free}}(\omega) \;\; = \;\; m\Theta(\omega + \mu). \tag{2.116}$$

This is the well-known result that the density of states of a non-interacting Fermi gas is a constant in two dimensions. Recalling the two mean-field results (2.102) and (2.104) for the spectral function in the BCS and BEC limit, respectively, we can study the density of states in these limits. This provides qualitative behaviors which we can compare against our results. Keep in mind however, that both of these mean-field results have been calculated for the zero-temperature case. Integrating the spectral functions (2.102) and (2.104) over all momenta, we get the density of states shown in fig. 2.16. The gap is clearly visible in both cases. The gap extends from $\mu_{\text{BEC}} \approx -E_D/2 < 0$ to $-\mu_{\text{BEC}}$ in the limit of tightly bound dimers. In BCS theory, the gap is of size $2\Delta(T = 0)$, centered around the Fermi energy. Beyond the critical temperature $T > T_c$, the gap of course vanishes, since the spectral function (2.102) reduces to the one of a free Fermi gas when the gap vanishes ($v_{\mathbf{k}}^2 = 0$ for $\Delta = 0$). In particular, BCS theory can not predict diminished spectral weight around the Fermi surface for $T > T_c$, because $\Delta(T > T_c) \equiv 0$.
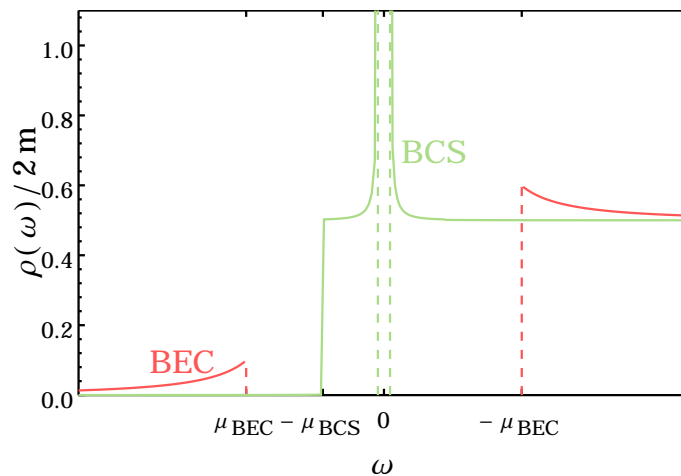
Figure 2.16: Density of states that results from integration of the mean-field spectral
functions (2.102) (green) and (2.104) (red).

## Non-degenerate limit of the density of states

To obtain the density of states within a virial expansion, and thus in the non-degenerate limit, it should be sufficient to integrate the spectral functions shown in figs. 2.14 and 2.13 over all momenta. While true in principle, the two calculations were done separately in practice, because of the strongly peaked nature of the spectral function. The density plots were created using a constant momentum and frequency grid, which was too widely spaced to give an accurate numerically integrated result. Instead, for the calculation of the density of states, the spectral function was sampled very often near the quasi particle and bound branch peaks, which captures the numerical weight of the peaks far more accurately.

The evolution of the density of states with respect to coupling strength and temperature is shown in fig. 2.17. There is a dip in spectral weight around $\omega = -\mu$, which gets washed out at higher temperatures. Beyond our rough estimate $T^*$ for the temperature where the number of "free" fermions equals the number of fermions bound into dimers, cf. eq. (2.93) and fig. 2.11, the dip is no longer clearly visible. The dip is wider for higher binding energies, because the "gap" between the onset of the bound state and quasi-particle branch is roughly of size $E_D$. Over all, the density of states qualitatively resembles the one for the superfluid BEC regime, shown in red in fig. 2.16. The virial expansion does not capture any pseudo-gap features,
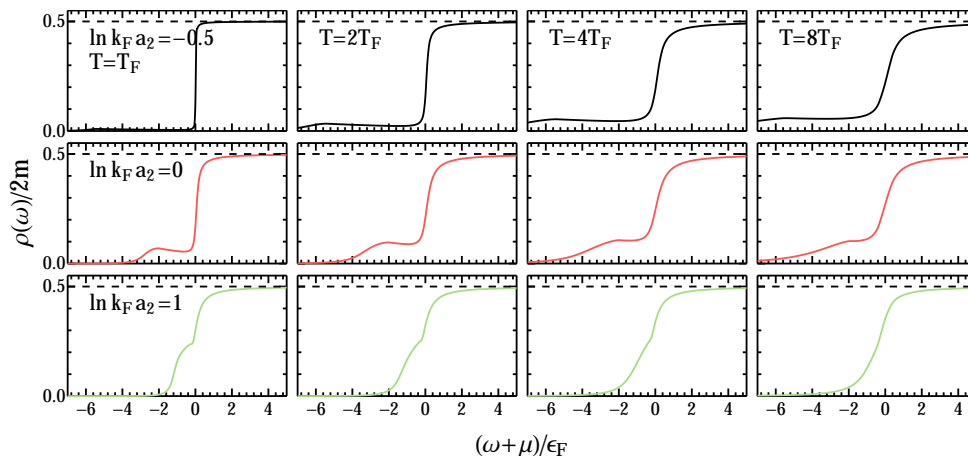
Figure 2.17: Density of states for different coupling strengths $\ln k_F a_2 = -0.5, 0, 1$ (rows) and different temperatures $T = 1, 2, 4, 8T_F$ (columns). For decreasing two-dimensional scattering length $a$, the pairing gap is more pronounced. The black dashed line indicates the value 0.5 for the free Fermi gas (cf. eq. (2.116)).

i.e. diminished spectral weight, around the chemical potential $\omega = \mu$. As noted earlier, a self-consistent Luttinger-Ward calculation [19] has shown clear signs of a pseudo-gap even at $T = 0.45T_F$ and $\log k_F a_2 = 0.8$. Due to the nature of the virial expansion, we can not go to temperatures lower than the Fermi temperature $T_F$ in the present case.

### 2.3.4 Momentum distribution

The spectral function allows for the calculation of other interesting, experimentally observable, quantities. One of them is the momentum distribution, which is given by the integral of the *occupied* spectral function $A_-(\omega, \mathbf{q})$ over all frequencies:

$$n_\sigma(\mathbf{q}) \;\;=\;\; \int \frac{d\omega}{2\pi} A_-(\omega, \mathbf{q}) \tag{2.117}$$

The index $\sigma$ was introduced again to specify that we are not talking about the total momentum distribution $n(\mathbf{q}) = n_1(\mathbf{q}) + n_2(\mathbf{q})$. As mentioned in secs. 2.1 and 2.2, the two-dimensional, contact-interacting Fermi gas fulfills some universal relations, that connect the *contact*, cf. eq. (2.13) with various observables. One of them is the momentum distribution. With our present intensive normalization

$\int_{\mathbf{q}} n_\sigma(\mathbf{q}) = n_\sigma = N_\sigma/V$, the momentum distribution has a tail that vanishes likes $\mathcal{C}/q^4$ as $q \to \infty$. $\mathcal{C} = C/V$ is called the contact density. Via the adiabatic relation (2.12), the contact can be related to the derivative of the grand canonical potential $\Omega$ with respect to the two-dimensional scattering length. Within a virial expansion, its leading order $\sim z^2$ can thus be calculated via

$$
\begin{aligned}
\mathcal{C} &= 2\pi m a_2 \frac{\partial \Omega/V}{\partial a_2} \\
&= -2z^2 m^2 T^2 a_2 \frac{\partial b_2}{\partial a_2} + \mathcal{O}(z^3).
\end{aligned} \tag{2.118}
$$

The leading order is only connected to the second virial coefficient. Higher orders require knowledge of higher virial coefficients $b_n$, which in turn require the solution of the $n$-particle scattering problem.

**Interlude: Are the Tan relations still valid within the virial expansion?**

The question, in the present context, can be rephrased to read: Does the momentum distribution – calculated from a virial expansion – still have a high-momentum tail that vanishes like $\tilde{\mathcal{C}}/q^4$? And is the coefficient in front of that tail still obtainable from the adiabatic theorem? To spoil the answer right away: Yes, and this is where the derivation of the universal relations from an operator product expansion [46, 32] very helpful. The positive answer can be traced back to the fact that the universal relations, as derived from an OPE, are valid for systems with any number of particles. Within the virial expansion approach, we describe expectation values of some quantity, for example the momentum distribution, as a sum of canonical expectation values, and then truncate at some finite power:

$$
\left\langle \psi_\sigma^\dagger \psi_\sigma(\mathbf{q}) \right\rangle = \frac{1}{\mathcal{Z}} \sum_N z^N \underbrace{\mathrm{tr}_N \left[ e^{-\beta H} \psi_\sigma^\dagger \psi_\sigma(\mathbf{q}) \right]}_{\equiv \left\langle \psi_\sigma^\dagger \psi_\sigma(\mathbf{q}) \right\rangle_N}. \tag{2.119}
$$

We know that the Tan relations hold separately in each $N$-particle sector in the canonical ensemble. In the case of the momentum distribution:

$$
\left\langle \psi_\sigma^\dagger \psi_\sigma(\mathbf{q}) \right\rangle_N \to \frac{\mathcal{C}_N}{q^4} = \frac{m^2 g^2 \langle \psi_1^\dagger \psi_2^\dagger \psi_2 \psi_1(0) \rangle_N}{q^4} \tag{2.120}
$$

And we can extract, for each $N$-particle sector, the contact from the adiabatic theorem in a state with $N$ particles:

$$
\mathcal{C}_N = 2\pi m a_2 \frac{\partial E_N/V}{\partial a_2}, \tag{2.121}
$$

where $E_N = \langle H \rangle_N$. Since the universal relations hold in any $N$-particle sector, they have, as a result of the grand canonical expectation values essentially being the sum of canonical ones, also to hold *order by order* in $z$. Note that with our sketchy explanation, we swept under the rug two points. First, normalizing the two particle sector with volume might yield pathological results. Second, the partition function also depends on the two-dimensional scattering length. A more careful treatment reveals that the arguments still hold true, because of the nature of the partial derivate with respect to the scattering length. The adiabatic theorem only holds for the *work* that is needed when changing the scattering length. Effects of re-population of the microscopic states are taken to be zero (hence the term "adiabatic"). A change in the partition function falls into this category. For a more detailed discussion of the matter, see my diploma thesis [27].

**Results for the momentum distribution**

Knowing that our results have to fulfill the adiabatic theorem and the universal $\mathcal{C}/q^4$ tail in the momentum distribution, we can now test our numerical results against these relations. The contact, to leading order $z^2$, as calculated from the adiabatic theorem (2.118) at $T = T_F$, is shown in figure 2.18(a). The dashed orange line indicates the contact for a gas of dimers:

$$\mathcal{C}_{\text{dimergas}} \quad = \quad \frac{4\pi}{a_2^2} n_d \tag{2.122}$$

The three values $\ln k_F a_2 = -0.5, 0, 1$ of the coupling are marked with the corresponding colors. For the momentum distributions, the asymptotic behavior of $q^4 n_\sigma(q)$ is shown in figure 2.18(b). The dashed lines are the predictions of the contact from the adiabatic theorem. They are in perfect agreement with the independently obtained results for $n_\sigma(q)$. In fig. 2.18(b), the momentum distributions saturates the later, the higher the value of the binding energy $E_D$. This is to expected, as the scale for the high momentum tail is generally set by $q \gg \max(1/\lambda_T, 1/k_F, \sqrt{E_D})$. A plot for the momentum distribution itself is not shown, as it almost resembles a Gaussian function (see sec. 3.5.3 for the corresponding three-body calculation in 3D, which looks the same).

It is interesting to note that, at least for our spectral functions, the spectral weight in the lower branch of the spectral function, that was seen to bend back at roughly $2k_F$, is responsible for the $1/q^4$ tail. In order to fulfill the Tan relations, the spectral function had to bend back somewhere. The only other possibility being

(a)



(b)
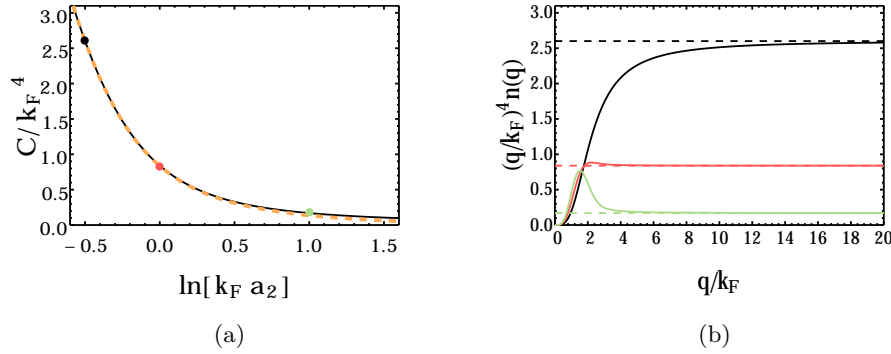
Figure 2.18: Contact at $T = T_F$ and asymptotic behavior of the momentum distri-
bution at $T = T_F$. 2.18(a) shows the contact to order $z^2$, as obtained
from the adiabatic theorem (2.118). The orange dashed line indicates
the contact for a gas that is solely composed of dimers. The three val-
ues of the coupling strengths $\ln k_F a_2 = -0.5$ (black) $\ln k_F a_2 = 0$ (red)
and $\ln k_F a_2 = 1$ (green) are marked separately. In figure 2.18(b), the
dimensionless version of the momentum distribution $q^4 n_\sigma(q)$ is plotted.
The asymptotic behavior agrees perfectly with the dashed lines, which
are the predictions from fig. 2.18(a).

that it starts off as an inverted parabola as in the superfluid BEC case (2.104). As
emphasized before, a back-bending in the occupied spectral function should not be
confused with a pseudo gap.

### 2.3.5 Radio-frequency spectrum

In sec. 2.2.2, we derived the high-frequency asymptotic behavior of the RF transition
rate for a two-dimensional Fermi gas. In the case of vanishing final state interactions,
we can obtain the RF transition rate from the occupied spectral function via [51]

$$\Gamma(\omega) = \Omega^2 \int_{\mathbf{q}} A_-(\varepsilon_{\mathbf{q}} - \omega - \mu, \mathbf{q}), \tag{2.123}$$

where $\Omega$ again denotes the Rabi frequency, which will be set to one in the following.
Our intensive normalization of the RF spectrum thus reads (see the sum rule (2.81a))

$$\int \frac{d\omega}{2\pi} \Gamma(\omega) = \frac{n}{2} \underbrace{=}_{\text{balanced gas}} n_2. \tag{2.124}$$
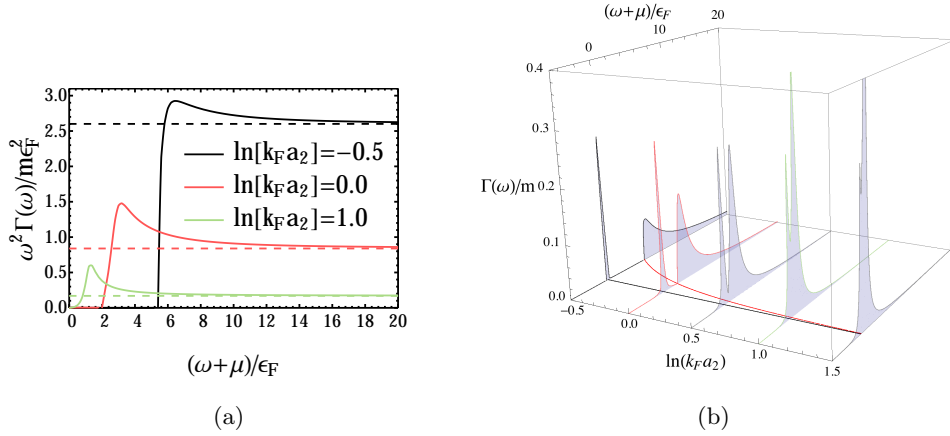
Figure 2.19: RF spectra at $T = T_F$ and for vanishing final state interactions. Fig. 2.19(a) extracts the asymptotic high-frequency tail, given in eq. (2.125) and compares it to the predicted values of the contact from the adiabatic theorem, see fig. 2.18(a). Fig. 2.19(b) shows the evolution of the full rf transition rates with respect to coupling strength. As the dimer binding energy is reduced, the free-free and bound-free peak begin to overlap.

With this normalization, the asymptotic behavior at large frequencies $\omega$, and for vanishing final state interactions, reads

$$\Gamma(\omega) \rightarrow \frac{\mathcal{C}}{4m\omega^2}. \tag{2.125}$$

As we have derived in sec. 2.2.3, final state interactions introduce logarithmic scaling corrections $\sim 1/\omega^2 \ln^2 \omega$ to this tail. A plot of the RF spectra at $T = T_F$, resulting from (2.123) and tested against the universal relation (2.125), is shown in figure 2.19(a). The dashed lines are the predictions of the contact for the three different coupling strengths $\ln k_F a_2 = -0.5; 0; 1$, as obtained from the adiabatic theorem (2.118). The universal relation (2.125) indeed holds true, as is to be expected from the arguments given in the previous subsection 2.3.4.

In figure 2.19(b), the corresponding RF spectra are shown for the parameter values $T = T_F$ and $\ln k_F a_2 = -0.5; 0; 0.5; 1; 1.5$. As a reminder: Due to the vanishing final state interactions in the present case, there are only "free-free" and "bound-free" transitions. The peak at zero frequency belongs to the "free-free" transitions from the quasi-particle branch. The incoherent spectral weight starting at the bound

state energy $E_D$ corresponds to "bound-free" transitions that break up a dimer. Coming from the BEC side ($\ln k_F a_2 = -0.5$) of the crossover and going to smaller binding energies (larger $\ln k_F a_2$), the bump of the dimer-free transitions becomes sharper and finally overlaps with the free-free peak. Because the spectrum needs to reduce to the one of free particles in the limit $E_D \to 0$, a behavior like this is to be expected. Note that we always have a peak of finite width, rather than the $\delta$-function peak mentioned in sec. 2.2.3, because the particles are thermally excited.

### 2.3.6 Analysis of the quasi-particle properties

This section will deal with the properties of the quasi-particle branch of the spectral function. In particular, we will find that quasi-particles are well defined excitations in the limit of high temperatures. The assumption that this is true is of importance when trying to describe the (transport)-properties of the system within a Boltzmann-equation framework.

The quasi-particle dispersion $\omega(\mathbf{q})$ –the energy which the quasi particle peak is centered around– is defined by the position of the pole [81] of the Green's function (2.106):

$$\omega(\mathbf{q}) + \mu - \varepsilon_{\mathbf{q}} - \Re\left[\Sigma(\omega(\mathbf{q}), \mathbf{q})\right] \overset{!}{=} 0 \qquad (2.126)$$

Figure 2.20(a) shows the deviation of the solution $\omega(\mathbf{q})$ from the free particle dispersion at $T = T_F$ and for the three coupling constants $\ln k_F a_2 = -0.5, 0, 1$. The deviations are never really large, even though they are indeed the largest in the BCS limit for momenta of roughly $q/k_F \approx 3$. This might indicate a precursor to the back-bending one expects for a pseudo-gap (compare this to the behavior of the spectral function shown in [19]). The quasi particle dispersion starts at the value

$$\omega(\mathbf{0}) = -\mu + \Re\left[\Sigma(\omega(\mathbf{0}), \mathbf{0})\right], \qquad (2.127)$$

which is a quadratic minimum with an effective mass [81], that can be related to the real part of the self-energy via

$$\frac{m^*}{m} = \frac{1 - \frac{\partial \Re\Sigma}{\partial \omega}}{1 + \frac{\partial \Re\Sigma}{\partial \varepsilon_{\mathbf{q}}}}\bigg|_{\omega=\omega(\mathbf{0}), q=0}. \qquad (2.128)$$

The effective mass obtained from our self-energies is plotted, as a function of temperature, in figure 2.20(b). The effective mass is, for all shown couplings, only slightly enhanced. In the BCS limit, where it gets the largest (when $T \approx T_F$), its maximum
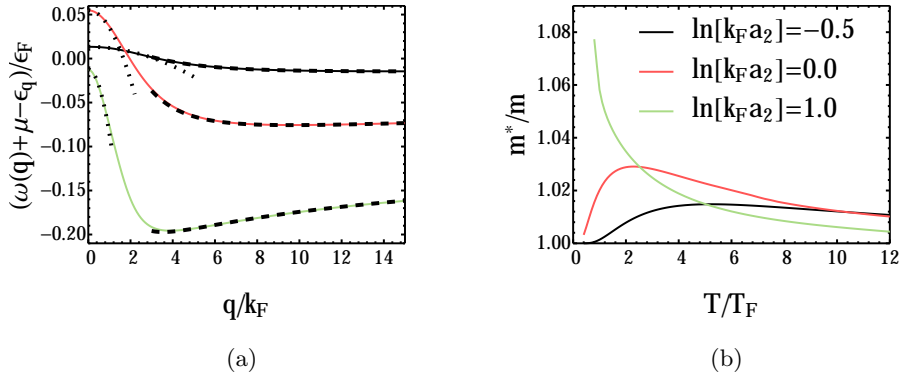
Figure 2.20: Deviation of the quasi-particle energy $\omega(\mathbf{q})$ from the dispersion of free particles at $T = T_F$. Fig. 2.20(a) shows the deviation from the free dispersion relation for different coupling strengths. The dotted lines correspond to the low-momentum dispersion with effective mass $m^*$, see eq. (2.128). The dashed lines correspond to the universal result for high momenta, given by eq. (2.133). Fig. 2.20(b) shows the evolution of the effective mass – again for the typical couplings $\ln k_F a_2 = -0.5, 0, 1$ – with temperature.

value is $m^* \approx 1.08m$. Small effective mass corrections are also found in the strongly interacting Fermi gas in 3D [82]. In the limit of high temperatures, the effective mass approaches the bare mass for all the couplings. Note that in the limit of zero temperature at $\ln k_F a_2 = 0$ for the so-called attractive polaron [83], effective mass corrections are expected to become as large as $m^*/m \approx 1.5$.

The quasi-particle peak can be approximated by a Lorentzian

$$A(\omega, \mathbf{q}) = 2 \frac{-\Im\left[\Sigma(\omega(\mathbf{q}), \mathbf{q})\right]}{\left(\omega + \mu - \varepsilon_{\mathbf{q}} - \Re\left[\Sigma(\omega(\mathbf{q}), \mathbf{q})\right]\right)^2 + \left(-\Im\left[\Sigma(\omega(\mathbf{q}), \mathbf{q})\right]\right)^2} \quad (2.129)$$

in the vicinity of $\omega(\mathbf{q})$. The width of the Lorentzian, given by the imaginary part of the self energy, defines a characteristic inverse lifetime of a state with momentum $\mathbf{q}$:

$$\frac{1}{\tau_{\mathbf{q}}} = -\Im\left[\Sigma(\omega(\mathbf{q}), \mathbf{q})\right] \quad (2.130)$$

For $T = T_F$, the inverse lifetime as a function of momentum is shown in fig. 2.21(a) for the coupling strengths $\ln k_F a_2 = -0.5, 0, 1$. The lifetime is smallest for
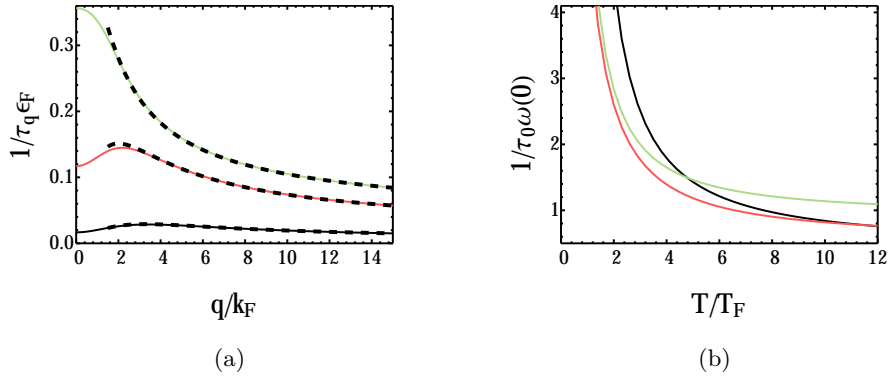
Figure 2.21: Quasi particle lifetime as function of momentum and temperature. Fig. 2.21(a): Inverse quasi particle lifetime as a function of momentum at $T = T_F$ and $\ln k_F a_2 = -0.5, 0, 1$. The dashed line indicates the universal high momentum limit (2.134). Fig. 2.21(b): Evolution of the ratio of inverse quasi particle lifetime and energy $1/\tau_0\omega(\mathbf{0})$ at zero momentum with temperature.

low momenta and $\ln k_F a_2 = 1$. This result might seem counter-intuitive at first, because one would generally expect $\ln k_F a_2 = 1$ to be weakly interacting limit. The important thing to note is that [81, 80], as already shortly discussed in sec. 2.3.2, quasi particles are well defined when the ratio of inverse lifetime to excitation energy becomes small:

$$\frac{1}{\omega(\mathbf{q})\tau_{\mathbf{q}}} \ll 1 \tag{2.131}$$

The ratio $1/\omega(\mathbf{0})\tau_0$ for the state with vanishing momentum is shown as a function of temperature in fig. 2.21(b). The ratio vanishes very weakly, namely logarithmically, at high temperatures. Despite of the slow vanishing, this still shows that quasi-particles are well defined in the limit of high temperatures. As mentioned earlier, this is a basic requirement for a kinetic description of the two-dimensional Fermi gas. Analogous behavior is found for the 3D Fermi gas [80].

Following Nishida [84], an OPE for the Green's function at high momentum and frequency reveals universal behavior of the self-energy in this parameter regime. The leading order term[10] of the self-energy, in the case of a homogeneous gas, is

---

[10]The OPE is not performed here, since Nishida already did the work for us in [84]. All we need to

governed by the density of the other species, which in our case just is given by $n/2$:

$$\Sigma(\omega, \mathbf{q}) = \mathcal{A}(\omega - \varepsilon_\mathbf{q}/2)\frac{n}{2} + \ldots, \tag{2.132}$$

where $\mathcal{A}$ is the two-particle scattering amplitude given in eq. (2.7). From the asymptotic form (2.132) of the self-energy, we can infer the asymptotic forms of the dispersion relation and lifetime. In order to do so, we take the real and imaginary part of (2.132), evaluated at the leading order result $\omega(\mathbf{q}) \approx \varepsilon_\mathbf{q}$ of the dispersion relation:

$$\omega(\mathbf{q}) + \mu = \varepsilon_\mathbf{q} + \frac{2\pi n}{m}\frac{\log\left[\frac{\varepsilon_\mathbf{q}}{2E_D}\right]}{\log^2\left[\frac{\varepsilon_\mathbf{q}}{2E_D}\right] + \pi^2} + \mathcal{O}\left(\frac{1}{q\log^2 q}\right) \tag{2.133}$$

$$\frac{1}{\tau_\mathbf{q}} = \frac{2\pi n}{m}\frac{\pi}{\log^2\left[\frac{\varepsilon_\mathbf{q}}{2E_D}\right] + \pi^2} + \mathcal{O}\left(\frac{1}{q\log^3 q}\right) \tag{2.134}$$

Both relations are indicated by the dashed lines in figures 2.20(a) and 2.21(a). The virial expansion, like is to be expected from the arguments given in sec. 2.3.4, obeys these universal relations. Note that, in particular, the ratio

$$\frac{1}{\tau_\mathbf{q}\omega(\mathbf{q})} \xrightarrow{q\to\infty} \frac{2E_F}{\varepsilon_\mathbf{q}}\frac{\pi}{\log^2\left[\frac{\varepsilon_\mathbf{q}}{2E_D}\right]} \ll 1 \tag{2.135}$$

always gets small at large momenta. Thus, independent of temperature, the excitations of a two-dimensional Fermi gas always have well defined quasi-particle properties in the high-momentum limit.

In conclusion, we have shown that, in the limit of high temperatures, both the low-momentum and high-momentum excitations can be described well as quasi-particles. A kinetic treatment of the two-dimensional Fermi gas, employing a Boltzmann equation ansatz, is thus justified. This allows to study non-equilibrium properties, such as transport and the connected viscosities, of the system.

### 2.3.7 Summary

In this section, we have employed a virial expansion to study the non-degenerate limit of the two-dimensional Fermi gas. The spectral functions turned out to have two branches with spectral weight. The lower branch is connected to the two-atom bound state, which exists for all two-dimensional scattering lengths $a_2$. The upper

---

do is to plug in the two-dimensional scattering amplitude (2.7), instead of the three-dimensional one, into his results.

branch almost resembles the one of free Fermions, but with a finite lifetime (width of the peak) and slightly enhanced effective mass. The density of states exhibits a dip in spectral weight around $\omega = -\mu$, which gets washed out at higher temperatures. The dip is connected to the existence of the two-particle bound state, a pseudo-gap can not be seen in the temperature range that is accessible to the virial expansion. The virial expansion was also shown to fulfill the Tan relations, that connect the contact of the system to various other properties. In particular, the calculation of the contact via the adiabatic relation gave perfect agreement with the high-momentum tail of the momentum distribution, as well as the high-frequency tail of the RF transition rate.

# Chapter 3

# High-temperature expansions for three-dimensional quantum gases

With the possibility to tune the $s$-wave scattering length at will by means of a Feshbach resonance, cold gases have opened the possibility to study a system both in the non-interacting limit, characterized by a vanishing scattering length $a = 0$, as well as the strongly interacting unitary limit $a = \pm\infty$. We will take the approximation of pure contact interactions in the following, such that the interaction strength is solely characterized by the two-particle scattering length $a$. In particular, this means that we neglect effective range corrections in the low-energy expansion of the $s$-wave scattering amplitude:

$$f(k) = \frac{1}{-\frac{1}{a} + \frac{1}{2}r_e k^2 + \cdots - ik} \tag{3.1}$$

When omitting all terms of order $k^2$ and higher in the above equation, one reproduces the scattering amplitude for a pure contact interaction. The approximation of contact interactions (characterized solely by the scattering length) works well in the regime where collision momenta are much smaller than the inverse van-der-Waals length $\ell_{vdW}$, which typically sets the size of the effective range [13, 85]. While the fermionic system is stable at arbitrary scattering lengths, the (unitary) bosonic system is unstable, because the three-particle decay rate, that governs the loss of particles via

$$\frac{dn}{dt} = -\Gamma_3 n \equiv -L_3 n^3 \tag{3.2}$$

scales like $\Gamma_3 \sim n^2 a^4$ (for more details, see below). In addition, the bosonic many-body system suffers from the Thomas collapse [86], which states that the three-body spectrum, even for a contact interaction that just produces an infinitesimally small *two-body* binding energy, is *unbounded* from below. This inevitably leads to a thermodynamic instability of the system, and will be one of our concerns later on, since this unboundedness is in particular also present for the *Efimov effect*.

The Efimov effect, named after its discoverer [10, 11], is the observation that the bosonic three-body problem with contact interactions has a spectrum with infinitely many three-particle bound states. These three-body bound states are called *Efimov trimers*. Within the so called universal theory, which omits short-distance details of the interaction potential, the spectrum has a discrete geometric scaling symmetry in the sense that once one knows the energy of one Efimov trimer at unitarity $(1/a = 0)$, denoted by $E_T^{(0)} = -\kappa_*^2/m$, $\kappa_* \in \mathbb{R}$, one knows the positions of all other three-body bound states [25]:

$$E_T^{(n)} = -\frac{\kappa_*^2}{m} e^{\frac{2\pi}{s_0} n}, \quad n \in \mathbb{Z} \tag{3.3}$$

where $i s_0$ is the first imaginary root of the transcendental equation [25]

$$s \cos\left(\frac{s\pi}{2}\right) - \frac{8}{\sqrt{3}} \sin\left(\frac{s\pi}{6}\right) = 0. \tag{3.4}$$

The above equation can be solved to arbitrary numerical precision, and yields $s_0 = 1.0062378..$ for the first digits of $s_0$. The energies of the geometric spectrum (3.3) are thus separated by powers of $e^{\frac{2\pi}{s_0} n} = 515.035001...$ At unitarity, the spectrum possesses an accumulation point of infinitely shallow trimers at zero energy. Furthermore, it is unbounded from below. This is an artifact of the zero-range approximation, that excludes microscopic short-range details of the interaction. These microscopic details of the interaction potential at short distances, implicitly encoded in the effective range parameter $r_e$, provide a lower cutoff to the spectrum. Within universal theory, one neglects such short-distance non-universal effects for the sake of simplicity. The most important observation for us – as we are going to employ universal theory in order to obtain our results – is that there always exists a lowest lying Efimov trimer in physical reality. We will thus in the following just *specify* one state in the Efimov spectrum to be the deepest one, and implicitly subtract all deeper lying trimer bound states. For an open-channel dominated resonance, for example, refs. [87, 88, 89] find $\kappa_* \ell_{vdW} \approx 0.2$ for the binding wave number of the deepest trimer state at unitarity, where $\ell_{vdW}$ is the van-der-Waals length. Non-universal effects become more important for the lower lying trimers, such that, for
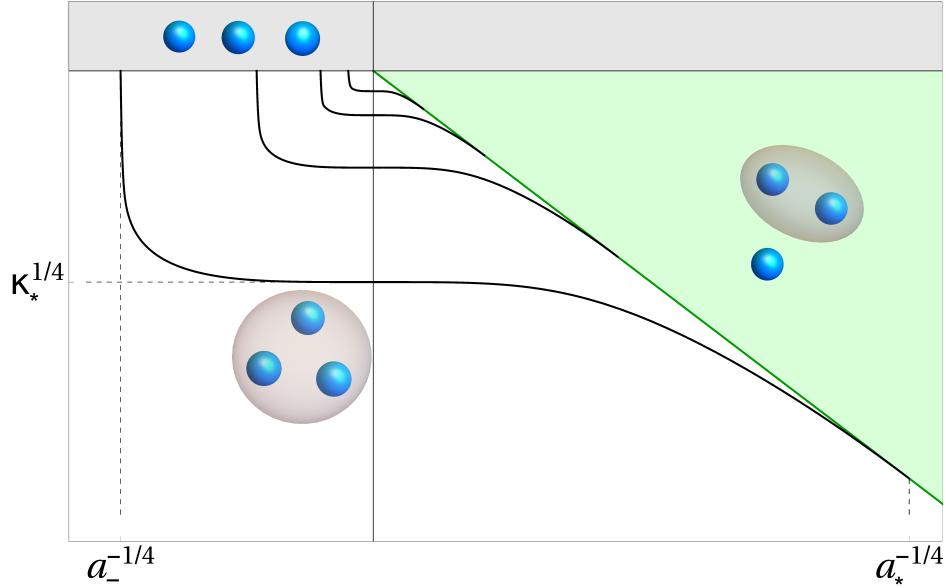
Figure 3.1: Sketch of a typical Efimov spectrum. The energy axis is rescaled with the eighth root $|E|^{1/8}$, while the axis for inverse scattering length is rescaled with the fourth root $1/a^{1/4}$. This reduces the scaling factor between two consecutive Efimov states (black lines) to $(515.035)^{1/8} \approx 2.18$ and allows to see more than just two of them. The gray shaded region indicates the three-atom continuum, the green shaded region is the atom-dimer continuum (see text).

example, the scaling factor between the lowest and second-to lowest Efimov state might no longer be approximately 515 [87, 88, 89], which is the scaling factor in the universal theory.

The Efimov effect is also present away from unitarity, a schematic plot of the full spectrum as a function of scattering length is shown in fig. 3.1. Shown are four of the infinitely many trimer states. The trimer states only exist below the so called three-atom threshold $E = 0$, as well as below the atom-dimer threshold $E = -1/ma^2$. Above these thresholds, the corresponding three-atom (gray shaded region) and atom-dimer (green shaded region) continua start. In these regimes, the system can be viewed as consisting of three unbound atoms, or an atom and a dimer, that scatter off each other, respectively. The energy of the trimer at unitarity defines the three body parameter $\kappa_*$. The scattering length where the trimer hits

the three-atom continuum is labeled by $a_-$, whereas the scattering length where the trimer hits the atom-dimer continuum is called $a_*$. Within universal theory, these quantities are not independent, but related to each other by the relations [25]

$$\frac{1}{a_-} \approx -0.6633\kappa_* \tag{3.5}$$

$$\frac{1}{a_*} \approx 14.132\kappa_*. \tag{3.6}$$

Thus, under the assumption that universal theory can be applied, fixing one of these quantities fixes the other two as well. Experimentally, for example, one usually tries to measure $a_-$ in order to determine the three-body parameter [90, 91, 92, 93]. Here, since we are going to cut off our spectra by choosing a lowest Efimov trimer, the parameters $\kappa_*$, $a_-$ and $a_*$ without an index shall correspond to the deepest trimer. This trimer is implicitly given the index zero, while the infinitely many trimers that lie closer to $E = 0$ shall be labeled by positive integers $n \in \mathbb{N}$, in ascending fashion. Note that the relations (3.5) and (3.6) receive corrections in theories that incorporate non-universal effects. For example, ref. [87] finds $1/a_- = -0.47\kappa_*$ for an open-channel dominated resonance.

In a recent experiment [94], the momentum distribution of a Bose gas was measured after ramping the system to the unitary regime. The three-body loss rate of the resulting strongly interacting Bose gas with a finite temperature was found to take on a finite value [95, 96, 97]. This allows for an experimental study of this system in a quasi-equilibrated state, provided that the experiment is performed over time scales larger than the equilibration time (governed by two-body collisions), but shorter than the timescales for the three-body decay. At first this possibility is surprising, because the three body loss rate at $T = 0$ was found to increase with the fourth power of the scattering length [98, 99]:

$$\Gamma_3 \sim n^2 a^4 C(a), \tag{3.7}$$

where $C(a)$ is a function that encodes loss resonances (at negative scattering lengths) due to the presence of three-body bound states in the Efimov spectrum. In particular, the loss resonances allow to experimentally determine the parameter $a_-$ of the deepest trimer from the (by magnitude) smallest negative scattering length where the loss rate is sharply peaked and follows the $a^4$ trend. Naively, eq. (3.7) suggests that it is impossible to ramp a Bose gas to unitarity without the quick loss of the majority of the particles. However, it was also found in finite temperature calculations [100, 101, 102] that the three-body loss rate of the unitary Bose gas

saturates to $\sim \lambda_T^4 \sim 1/T^2$. This indeed opens a window for the two-body collision rate $\Gamma_2 \sim n\lambda_T$, which equilibrates the gas, to be larger than the three-body collision rate $\Gamma_3 \sim n^2\lambda_T^4$, which is responsible for losses [103, 104]. This window is is exactly the non-degenerate regime $n\lambda_T^3 \ll 1$. Hence, the system ideally suited to be dealt within a high temperature expansion.

As derived by Braaten, Kang and Platter [53] from an OPE approach, the momentum distribution of a contact-interacting Bose gas decays like

$$n(\mathbf{q}) \;\; = \;\; \frac{\mathcal{C}_2}{|\mathbf{q}|^4} + F(|\mathbf{q}|)\frac{\mathcal{C}_3}{|\mathbf{q}|^5} + \ldots \tag{3.8}$$

for large momenta $|\mathbf{q}| \to \infty$. Note that we have chosen an intensive normalization $\int_{\mathbf{q}} n(\mathbf{q}) = n$, where $n$ is the density of the system. The quantities $\mathcal{C}_2$ and $\mathcal{C}_3$ are thus equal to the contacts $C_2$ and $C_3$ in [53], multiplied by a factor of inverse volume. The leading order momentum dependence is, as for the fermionic system [32, 37], of the order $q^{-4}$, with a decay coefficient $\mathcal{C}_2 \sim \langle \psi^\dagger \psi^\dagger \psi \psi \rangle$ that is a measure for two-particle correlations at small distances. As opposed to the fermionic system (with equal masses), however, the next order is not $q^{-6}$. The sub-leading tail is rather of order $q^{-5}$, multiplied by a log-periodic function

$$F(|\mathbf{q}|) \;\; = \;\; A \sin\left(2s_0 \log\left(\frac{q}{\kappa_*}\right) + 2\phi\right), \tag{3.9}$$

where $A = 89.26260$, $\phi = -0.669064$ and $s_0$ again defined by eq. (3.4). The so called three-body contact $\mathcal{C}_3 \sim \langle \psi^\dagger \psi^\dagger \psi^\dagger \psi \psi \psi \rangle$ encodes three-body correlations at short distances, and is, due to the Pauli principle, zero in fermionic systems. For mass-imbalanced Fermi gases with mass ratios $M/m > 13.6$, there exists an analogous operator that contains spatial derivatives, see Nishida and Son in [7]. The three-body parameter shows up in eq. (3.9), which indicates that the sub-leading tail encodes three-body correlations that are connected to the Efimov effect. In the momentum distribution that was measured in ref. [94], no clear $C/q^4$ decay for large momenta could be found. The reason is simply, as we will also see in the following, that the experiment was not able to measure the momentum distribution at high enough momenta. They are probing intermediate momenta which are still dominated by the oscillatory tail defined by eqs. (3.8) and (3.9). This was also pointed out in ref. [105], where the assumption that the asymptotic form (3.8) is valid for $q \gtrsim k_F$ ($k_F = (6\pi^2 n)^{1/3}$ is the Fermi momentum of a single component Fermi gas at the same density $n$ like the bosonic one) was used to extract numerical fits for the quantities $\mathcal{C}_2$ and $\mathcal{C}_3$. Because the momentum distribution of a *single*

Efimov trimer, which was calculated by Werner and Castin [106], was found to saturate very late at values $q > 30\kappa_*$, this assumption might seem a bit dangerous. However, we will see in our numerical results that the error of this assumption is reasonably small in the unitary limit.

The two- and three-body contacts are also related to the energy density $\mathcal{E} = E/V$ of the system via the *adiabatic theorems* [53]

$$\mathcal{C}_2 \ = \ -8\pi m \left. \frac{\partial \mathcal{E}}{\partial \left( \frac{1}{a} \right)} \right|_{\kappa_*} \tag{3.10}$$

$$\mathcal{C}_3 \ = \ -\frac{m}{2} \kappa_* \left. \frac{\partial \mathcal{E}}{\partial \kappa_*} \right|_a , \tag{3.11}$$

where the partial derivatives are supposed to keep all system variables, such as temperature or particle number, fixed. In particular, the energy density can be replaced by other thermodynamic potentials, such as the free energy or the grand potential. We will use the above equations to calculate predictions for the two- and three-body contacts, and then compare them to the high-momentum tails of the momentum distributions that we obtain in an independent fashion. Note that the adiabatic theorem for Fermions [32, 38, 37] is basically given by eq. (3.10), but with the factor of 8 on the right hand side replaced by a factor of 4.

In this chapter, we study the non-degenerate regime of both fermionic and bosonic quantum gases in the approximation of contact interactions. Since we are interested in the non-degenerate regime $n\lambda_T^3 \ll 1$ ($n$ is the density of the system, $\lambda_T = \sqrt{2\pi/mk_BT}$ is the thermal wavelength), we can use a cluster expansion (also see chapter 1) to obtain results for both the momentum distribution and density up to third order in the fugacity $z = e^{\beta\mu}$. Here, $\beta = 1/k_BT$ again denotes the inverse temperature, while $\mu$ is the chemical potential of the gas. A calculation to order $z^3$, which takes into account correlations up to the three-body sector, requires the solution of the three-body scattering problem. In particular, since the Efimov effect requires three or more bosons to be present, the third order in the fugacity is the first order that is sensitive to correlations that are related to Efimov physics, which is our main motivation to not already stop at $z^2$. It should be noted that knowledge of the cluster expansion of the density to $j$-th order is equivalent to the knowledge of the first $j$ virial coefficients $b_1, ..., b_j$:

$$n \ = \ \frac{1}{\lambda_T^3} \left( b_1 z + 2b_2 z^2 + \cdots + j z^j b_j + \dots \right), \tag{3.12}$$

| | Fermions | Bosons |
|---|---|---|
| Grand potential $\Omega/V =$ | $-\dfrac{2k_BT}{\lambda_T^3}\sum_j b_j z^j$ | $-\dfrac{k_BT}{\lambda_T^3}\sum_j b_j z^j$ |
| Density expansion $n =$ | $\dfrac{2}{\lambda_T^3}\sum_j j b_j z^j$ | $\dfrac{1}{\lambda_T^3}\sum_j j b_j z^j$ |
| High $q$ tail $n(q) \to$ | $\dfrac{\mathcal{C}_2}{q^4}$ | $\dfrac{\mathcal{C}_2}{q^4} + F(q)\dfrac{\mathcal{C}_3}{q^5}$ |
| Adiabatic theorem $\mathcal{C}_2 =$ | $-4\pi m\left.\dfrac{\partial \Omega/V}{\partial(\frac{1}{a})}\right|_{T,\mu}$ | $-8\pi m\left.\dfrac{\partial \Omega/V}{\partial(\frac{1}{a})}\right|_{T,\mu,\kappa_*}$ |
| Adiabatic theorem $\mathcal{C}_3 =$ | no analog | $-\dfrac{m}{2}\kappa_*\left.\dfrac{\partial \Omega/V}{\partial\kappa_*}\right|_{T,\mu,a}$ |

Table 3.1: Summary on the different versions of the formulas for two-component fermions and single component bosons in three dimensions.

where we gave the result for bosons. For unpolarized two-component fermions $n_\uparrow = n_\downarrow = n/2$, the density on the left-hand side is replaced by the density $n/2$ of *one* spin species. Since it is hard to keep track of all the different versions of these formulas for fermions and bosons, a summary of the adiabatic theorems, tails etc. is given in table 3.1.

A word about fermions: While our main interest lies certainly with the bosonic system, we will (because we are getting them almost for free) also extract the results for a Fermi gas. For the virial coefficients, this reproduces the known results derived by Leyronas [9]. We will see that our fermionic momentum distributions, when integrated over all momenta, match these known results as well. This gives additional reassurance that the numerical solution of the three-body problem, as well as the integration afterwards, yields correct results. Note that we do *not* consider fermions with unequal masses and, in particular, a mass ratio $m_1/m_2 > 13.6$, for which the existence [107] of three-body bound states might drastically change the results. A study in this direction might be very interesting though, and it should in principle be possible to perform it using the methods that are presented in this chapter.

This chapter is structured as follows: In sec. 3.1 we introduce the models and set up the conventions we will be working with. In sec. 3.2, the three body $T$-

matrix and the Skorniakov–Ter-Martirosian (STM) equation, which is the defining integral equation for the three body $T$-matrix, are introduced. In sec. 3.3, we carefully set up the formalism, as introduced by Leyronas [9], for the diagrammatic virial expansion (which is already used in secs. 2.3 and 4.7.2 of this thesis). We then group the diagrams by orders in the fugacity and evaluate them in an analytic fashion as far as possible. The diagrams will contain the three-body $T$-matrix, and thus have to be evaluated numerically in the end. In sec. 3.4, we shortly discuss the essential ideas for the implementation of the $C++$ code that was used to solve the three-body problem and the integrals that appear in the $z^3$ diagrams. In sec. 3.5, we present the resulting momentum distributions and virial coefficients for two-component fermions. The results for the virial coefficients turn out to be consistent with earlier findings [9]. In addition, the results for the contacts and the momentum distribution are consistent with ref. [108], which appeared shortly before this thesis. Finally, in sec. 3.6 the behavior of the momentum distributions and virial coefficients of the Bose gas is discussed for different scattering lengths and temperatures. Values for the two- and three-body contacts are predicted from the adiabatic theorems, and compared to the tail of the momentum distribution, which shows beautiful agreement with the universal prediction (3.8) for the tail. In sec. 3.7, the results are summarized and an outlook on possible future projects is given. As of the writing of this thesis, Johannes Hofmann and myself have made the bosonic results available as an electronic preprint [109].

## 3.1 Model(s) and conventions

The virial expansion we perform later on will require the solution of the two- and three-body scattering problem in the vacuum. In the following, we introduce the models for contact-interacting bosons and fermions. We also give a short summary on the definitions regarding the imaginary time Green's function, because the virial expansion revolves around expanding this Green's function in a clever way.

### 3.1.1 Bosons

Since we are going to work mostly in the imaginary time formalism later on, which is better suited to deal with finite temperatures, we directly define the theory in imaginary time, i.e. we give the Lagrangian for the *Euclidian* action $S_E$. The action $S_E = \int_0^\beta \int d^d x \mathcal{L}_E(\tau, \mathbf{x})$, where $\mathcal{L}_E$ is the Lagrangian density, defines the (grand

canonical) partition function via the path integral $\mathcal{Z} = \int D\psi D\bar{\psi} e^{-S_E}$. Note that we shall mostly work in the canonical formalism and follow the conventions of [26], but knowing the connections between canonical and path integral formalism is still useful.

As discussed in [25, 23, 24], the three-boson system can be effectively described by the Lagrangian

$$\mathcal{L}_E(\tau, \mathbf{x}) = \bar{\psi}\left(\partial_\tau - \mu\right)\psi + \mathcal{H}(\bar{\psi}, \psi) \tag{3.13}$$

$$\mathcal{H}(\tau, \mathbf{x}) = \bar{\psi}\left(-\frac{\nabla^2}{2m}\right)\psi + \frac{g_2}{4}\bar{\psi}\bar{\psi}\psi\psi + \frac{g_3}{36}\bar{\psi}\bar{\psi}\bar{\psi}\psi\psi\psi, \tag{3.14}$$

where we have rotated the theory to imaginary time and all quantum fields $\bar{\psi}$ and $\psi$ are evaluated at imaginary time $\tau$ and position $\mathbf{x}$. Note that the real-time action looks similar, but with a global minus sign in front of all the non-time derivative terms, while the time derivative gets replaced by $\partial_\tau \to i\partial_t$. The global sign switch can be attributed to the fact that for the real-time problem, the "generating functional" is defined as $\mathcal{Z} \sim \int D\psi D\bar{\psi} e^{iS}$. The Wick rotation changes the meaning of time evolution, and while $\bar{\psi}$ takes the role of $\psi^\dagger$ in the rotated theory, it should not be mistaken as the hermitian conjugate of $\psi$:

$$\psi(\tau, \mathbf{x}) = e^{(H-\mu N)\tau}\psi(\mathbf{x})e^{-(H-\mu N)\tau} \tag{3.15}$$

$$\bar{\psi}(\tau, \mathbf{x}) = e^{(H-\mu N)\tau}\psi^\dagger(\mathbf{x})e^{-(H-\mu N)\tau}, \tag{3.16}$$

where $H = \int d^d x \mathcal{H}(\tau = 0, \mathbf{x})$, with $\mathcal{H}$ defined in (3.14) and $N = \int d^d x \bar{\psi}\psi(\tau = 0, \mathbf{x})$. Note that the symmetry factors in the couplings just turn out to be convenient definitions, they are not strictly necessary. The Lagrangian (3.13), up to the three-body sector [25], is equivalent to the following Lagrangian with an auxiliary field $d$ (that has bosonic commutation relations):

$$\mathcal{L}_E = \bar{\psi}\left(\partial_\tau - \frac{\nabla^2}{2m} - \mu\right)\psi - \frac{g_2}{4}\bar{d}d + \frac{g_2}{4}\bar{d}\psi\psi + \frac{g_2}{4}\bar{\psi}\bar{\psi}d + \frac{g_3}{36}\bar{\psi}\bar{d}d\psi \tag{3.17}$$

We will also call the field $d$ the auxiliary *dimer* field, because the leading order (in $g_3$) of its equation of motion (which can be obtained by varying (3.17) with respect to $\bar{d}$) is $d = \psi\psi + \dots$. The auxiliary field is not necessary for the calculations that will follow, however it makes our life a little easier both diagrammatically and also when calculating symmetry factors of the diagrams that contribute to our virial expansion.

In refs. [24, 23], it was found that in order to make quantities like the two- and three-body scattering amplitudes cutoff-independent, $g_2$ and $g_3$ need a renormalization prescription. We follow [25] and choose

$$g_2(\Lambda) = \frac{8\pi a/m}{1 - \frac{2a\Lambda}{\pi}}, \tag{3.18}$$

in order to reproduce the standard quantum mechanical two-body $s$-wave scattering amplitude with scattering length $a$. $\Lambda$ is a sharp UV-cutoff for the momentum integrals. Regarding renormalization in the three-body sector, it was demonstrated [25, 23, 24] that the choice

$$g_3(\Lambda) = -\frac{9mg_2^2(\Lambda)}{\Lambda^2} H(\Lambda) \tag{3.19}$$

$$H(\Lambda) = \frac{\cos\left(s_0 \log\left(\frac{\Lambda}{\Lambda_*}\right) + \arctan s_0\right)}{\cos\left(s_0 \log\left(\frac{\Lambda}{\Lambda_*}\right) - \arctan s_0\right)} \tag{3.20}$$

makes the three-body scattering amplitude (almost) cutoff-independent. As is emphasized in refs. [110, 53], the choice $\tilde{H}(\Lambda) = 0.879H(\Lambda)$ provides even more numerical accuracy. $\Lambda_*$ can be thought of as the new infrared quantity that characterizes the coupling strength $g_3$, and it can be determined from matching against quantities like the atom-dimer scattering length $a_{AD}$ [23] or the energy $\kappa_*^2/m$ of the lowest Efimov trimer. In fact, we will use the term three-body parameter interchangeably for both $\kappa_*$ and $\Lambda_*$, since one determines the other up to a periodicity that is connected to the periodicities showing up in the Efimov effect. Note that the form (3.20) for $H(\Lambda)$ is only valid at large ratios $\Lambda/\Lambda_* \to \infty$. The renormalization group flow of the coupling constant $g_3$ can be shown to obey a so called limit cycle [25] with diverging values at certain points, which reflects the appearance of new Efimov trimers as one increases the cutoff $\Lambda$. Once we have the form (3.19), we can of course immediately infer that $\Lambda^4 g_3$ is indeed log-periodic in $\Lambda$, since $H(\Lambda)$ is. The RG limit cycle offers one more neat feature, which we will make use of: The possibility of setting $g_3 \equiv 0$ for certain combinations $\Lambda/\Lambda_* = (e^{\pi/s_0})^n e^{\frac{1}{s_0}(\frac{\pi}{2} - \arctan s_0)}$. In most numerical calculations performed later on, typical values were $n = 2, 3$. Doing this is of course not mandatory, and we checked the results against other combinations of $\Lambda/\Lambda_*$.

### 3.1.2 Fermions

In complete analogy to the bosonic case, the Lagrangian that reproduces the quantum mechanical low energy $s$-wave scattering behavior of two fermions of different

species $\sigma = \uparrow, \downarrow$ is defined by

$$\mathcal{L}_E(\tau, \mathbf{x}) = \sum_\sigma \bar{\psi}_\sigma \left( \partial_\tau - \mu \right) \psi_\sigma + \mathcal{H}(\bar{\psi}_\sigma, \psi_\sigma) \tag{3.21}$$

$$\mathcal{H}(\tau, \mathbf{x}) = \sum_\sigma \bar{\psi}_\sigma \left( -\frac{\nabla^2}{2m} \right) \psi_\sigma + g_2 \bar{\psi}_\uparrow \bar{\psi}_\downarrow \psi_\downarrow \psi_\uparrow. \tag{3.22}$$

Due to the Pauli principle, there is no relevant three body operator that has to be taken into account in this effective Lagrangian. In order to describe a system with balanced populations $n_\uparrow = n_\downarrow$, the chemical potential was chosen to be equal for both species. It should be noted that the theory needs (like in the bosonic case) to be renormalized in order to yield finite and cutoff-independent results. We choose the prescription

$$g_2(\Lambda) = \frac{4\pi a/m}{1 - \frac{2a\Lambda}{\pi}}, \tag{3.23}$$

which reproduces the quantum mechanical result for two-body $s$-wave scattering with scattering length $a$. Up to a factor of two, this is the same two-body coupling constant as in the bosonic case, cf. eq. (3.18). This difference has its origin in the distinguishability of the scattering partners in the fermionic case, while two identical bosons are indistinguishable. An non-dynamical auxiliary field $d$ can be introduced via the Lagrangian

$$\mathcal{L}_E = \sum_\sigma \bar{\psi}_\sigma \left( \partial_\tau - \frac{\nabla^2}{2m} - \mu \right) \psi_\sigma - g_2 \bar{d} d + g_2 \bar{d} \psi_\downarrow \psi_\uparrow + g_2 \bar{\psi}_\uparrow \bar{\psi}_\downarrow d \tag{3.24}$$

Varying with respect to $\bar{d}$, we find that the equation of motion is $d = \bar{\psi}_\downarrow \bar{\psi}_\uparrow$. This again motivates the name auxiliary dimer field. The Lagrangian (3.24) is completely equivalent to the Lagrangian (3.21), which can be seen by plugging in the equation of motion for the auxiliary field. In contrast to the bosonic case, since there is no three-body term in the Lagrangian density (3.24), no infrared parameters other than the scattering length $a$ are needed to completely specify our theory.

### 3.1.3 Imaginary time Green's function

This section will give a short review of the definitions that are necessary to define an imaginary-time Green's function, as well as its representation in terms of so called $\mathcal{S}$-matrices. Following the conventions of [26], we define the imaginary-time Green's

function as

$$\mathcal{G}(\mathbf{x} - \mathbf{x}', \tau - \tau') \quad = -\left\langle T_\tau \psi(\mathbf{x}, \tau)\bar{\psi}(\mathbf{x}', \tau')\right\rangle \qquad \text{bosons} \qquad (3.25)$$

$$\mathcal{G}_\sigma(\mathbf{x} - \mathbf{x}', \tau - \tau') = -\left\langle T_\tau \psi_\sigma(\mathbf{x}, \tau)\bar{\psi}_\sigma(\mathbf{x}', \tau')\right\rangle, \qquad \text{fermions} \qquad (3.26)$$

where $T_\tau$ denotes time ordering (in imaginary time $\tau$). The Green's function of an auxiliary field is defined in an analogous fashion. For bosons, the imaginary time ordering just changes the order of fields in such a way that the earlier acting field stands more to the right. For fermions however, due to the anti-commutation rules, there is also a sign change whenever the fields need to be re-ordered. The expectation value is defined by the usual grand-canonical density matrix [1]:

$$\langle ... \rangle \quad = \quad \frac{1}{\mathcal{Z}}\text{Tr}e^{-\beta(H-\mu N)} \qquad (3.27)$$

$$\mathcal{Z} \quad = \quad \text{Tr}e^{-\beta(H-\mu N)} \qquad (3.28)$$

The Green's function can be proven to be (anti-)periodic in imaginary time with period $\beta$, which results in the fact that, in frequency space, energies are replaced by the so-called (fermionic) bosonic Matsubara frequencies: $E \to i\omega_n$, where $\omega_n = 2n\pi/\beta$ in the bosonic case and $\omega_n = (2n+1)\pi/\beta$ in the fermionic case.

We define the time-evolution of an operator in the interaction picture[2] by

$$\psi(\tau, \mathbf{x}) \quad = \quad e^{\tau(H_0-\mu N)}\psi(\mathbf{x})e^{-\tau(H_0-\mu N)} \qquad (3.29)$$

$$\bar{\psi}(\tau, \mathbf{x}) \quad = \quad e^{\tau(H_0-\mu N)}\psi^\dagger(\mathbf{x})e^{-\tau(H_0-\mu N)}, \qquad (3.30)$$

where $H_0$ is the kinetic part of the Hamiltonian. For the fermionic fields, just add a spin index $\sigma$ in the above definition. Furthermore, we define the expectation value $\langle .. \rangle_0$ in the same way as in eqs. (3.27) and (3.28), with the Hamiltonian $H$ replaced by $H_0$. The Green's function (3.25) can then be expressed in terms of the fields in

---

[1] Note that for the two- and three-body problem in the vacuum, this expectation value can get replaced by an actual specification of the incoming and leaving states and the respective momenta and energies.

[2] For the non-interacting system, this definition of course coincides with the Heisenberg time evolution defined in eq. (3.16).

the interaction picture and the non-interacting expectation value [26]:

$$
\mathcal{G}(\mathbf{x} - \mathbf{x}', \tau - \tau') = 
\begin{cases}
-\dfrac{\mathcal{Z}_0}{\mathcal{Z}} \left\langle \mathcal{S}(\beta, \tau)\psi(\mathbf{x}, \tau)\mathcal{S}(\tau, \tau')\bar{\psi}(\mathbf{x}', \tau')\mathcal{S}(\tau', 0) \right\rangle_0 & \tau - \tau' > 0 \\[2ex]
\mp\dfrac{\mathcal{Z}_0}{\mathcal{Z}} \left\langle \mathcal{S}(\beta, \tau)\psi(\mathbf{x}, \tau)\mathcal{S}(\tau, \tau')\bar{\psi}(\mathbf{x}', \tau')\mathcal{S}(\tau', 0) \right\rangle_0 & \tau - \tau' < 0
\end{cases}
$$

$$
=
\begin{cases}
- \left\langle \mathcal{S}(\beta, \tau)\psi(\mathbf{x}, \tau)\mathcal{S}(\tau, \tau')\bar{\psi}(\mathbf{x}', \tau')\mathcal{S}(\tau', 0) \right\rangle_{0,\mathrm{con}} & \tau - \tau' > 0 \\[2ex]
\mp \left\langle \mathcal{S}(\beta, \tau)\psi(\mathbf{x}, \tau)\mathcal{S}(\tau, \tau')\bar{\psi}(\mathbf{x}', \tau')\mathcal{S}(\tau', 0) \right\rangle_{0,\mathrm{con}} & \tau - \tau' < 0
\end{cases},
$$

$$(3.31)$$

where the $+$ for $\tau - \tau' < 0$ corresponds to the fermionic case (add spin indices $\sigma$ for that case, too). The $\mathcal{S}$-matrix is defined as

$$
\begin{aligned}
S(\tau, \tau') &= T_\tau e^{-\int_{\tau'}^{\tau} d\tilde{\tau} H_{\mathrm{int}}(\tilde{\tau})} \\
&= \mathbb{1} - \int_{\tau'}^{\tau} d\tilde{\tau} H_{\mathrm{int}}(\tilde{\tau}) + \int_{\tau'}^{\tau} d\tilde{\tau}_1 H_{\mathrm{int}}(\tilde{\tau}_1) \int_{\tau'}^{\tilde{\tau}_1} d\tilde{\tau}_2 H_{\mathrm{int}}(\tilde{\tau}_2) \\
&\quad + \cdots + (-1)^n \int_{\tau'}^{\tau} d\tilde{\tau}_1 H_{\mathrm{int}}(\tilde{\tau}_1) \ldots \ldots \int_{\tau'}^{\tilde{\tau}_{n-1}} d\tilde{\tau}_n H_{\mathrm{int}}(\tilde{\tau}_n) + \ldots,
\end{aligned}
$$

$$(3.32)$$

where the interaction part $H_{\mathrm{int}}$ contains all the interaction vertices (which are the same as the interaction vertices of the Lagrangian), and its time dependence is defined via the interaction picture in eqs. (3.29) and (3.30). In the second line of eq. (3.31), we implicitly stated that it is possible to express this expectation value as the sum of all *contractions* (Wick's theorem [26, 28]). Furthermore, it was indicated that only the contractions that result in *connected* diagrams contribute (linked cluster theorem [26, 28]).

Note that in most quantum field theory books, eq. (3.32) is just used as a step to get to an end result where the imaginary time integrations all have the same upper and lower bounds, which is then easily translated into momentum and frequency space. Since we are going to work with "mixed" diagrams that are in imaginary time and momentum space, however, the form (3.32) will prove to be the most useful one for us. It allows to associate times $\tau_i$ to a given vertex, such that $0 \leq \tau_i \leq \tau_{i+1}$. Furthermore, the form (3.32) also turns out to be convenient for determining signs (fermionic problem) and symmetry factors (bosonic problem) of a given diagram.

### 3.1.4 Introduction to the diagrammatic virial expansion

The basic ideas on how to turn the virial expansion into an expansion of Feynman diagrams have already been shortly outlined in sec. 2.3 of this thesis, where we have

used this formalism to calculate the spectral function of a two-dimensional Fermi gas in the non-degenerate regime. However, I have also promised a more detailed introduction to the subject, which will be presented here. We define the *free* propagator $G$ like the full Green's function in eq. (3.25), but with a non-interacting expectation value $\langle .. \rangle_0$. The free propagator in momentum and (Matsubara-)frequency space takes the particularly simple form

$$G(i\omega_n, \mathbf{q}) = \frac{1}{i\omega_n + \mu - \varepsilon_{\mathbf{q}}}, \tag{3.33}$$

where $\varepsilon_{\mathbf{q}} = \mathbf{q}^2/2m$ is the free dispersion, and $\mu$ is the chemical potential. The bosonic Matsubara frequencies are even multiples of $\pi/\beta$, while the fermionic (add index $\sigma = \uparrow, \downarrow$ in eq. (3.33)) ones are odd multiples. The corresponding free propagator can be obtained by summation over all Matsubara frequencies:

$$G(\tau, \mathbf{q}) = \frac{1}{\beta} \sum_{\omega_n} e^{-i\omega_n \tau} \frac{1}{i\omega_n + \mu - \varepsilon_{\mathbf{q}}} \tag{3.34}$$

The usual trick [49] to evaluate these sums is to turn the sum into a contour integral and weight the function that is summed over by a Bose- or negative Fermi-distribution, which have poles at the bosonic and fermionic Matsubara frequencies $i\omega_n$, with residue $1/\beta$. Due to the residue theorem, when the function does not have any additional poles enclosed by the contour, the contour integral is then equal to the sum over the Matsubara frequencies. For $\tau < 0$, the contour can be deformed into a large circle with infinite radius, at the cost, however, of including the pole at $z = \varepsilon_{\mathbf{q}} - \mu$ that comes from the Green's function. This yields

$$G(\tau, \mathbf{q}) = -e^{-\tau(\varepsilon_{\mathbf{q}} - \mu)} n_B(\varepsilon_{\mathbf{q}} - \mu) \qquad -\beta < \tau < 0 \tag{3.35}$$

$$G_\sigma(\tau, \mathbf{q}) = e^{-\tau(\varepsilon_{\mathbf{q}} - \mu)} n_F(\varepsilon_{\mathbf{q}} - \mu) \qquad -\beta < \tau < 0, \tag{3.36}$$

where the additional sign change comes from the fact that the small contour around the Green's function pole runs *clockwise*. From the periodicity / anti-periodicity

$$G(\tau) = \mp G(\beta + \tau) \qquad -\beta < \tau < 0 \tag{3.37}$$

of the Green's function, where the minus corresponds to fermions, we can infer its values for $0 < \tau < \beta$:

$$G(\tau, \mathbf{q}) = -e^{-\tau(\varepsilon_{\mathbf{q}} - \mu)} (1 + n_B(\varepsilon_{\mathbf{q}} - \mu)) \qquad 0 < \tau < \beta \tag{3.38}$$

$$G_\sigma(\tau, \mathbf{q}) = e^{-\tau(\varepsilon_{\mathbf{q}} - \mu)} (-1 + n_F(\varepsilon_{\mathbf{q}} - \mu)) \qquad 0 < \tau < \beta. \tag{3.39}$$

For $\tau = 0$, we need to specify from which direction the zero is approached. The usual convention is to interpret $\tau = 0$ as $\tau = 0^-$, such that the Green's function takes the form (3.35) or (3.36). The full result of the bosonic free propagator now reads

$$
\begin{aligned}
G(\tau, \mathbf{q}) &= -e^{-\tau(\varepsilon_{\mathbf{q}} - \mu)} \left[ \Theta(\tau) + n_B(\varepsilon_{\mathbf{q}} - \mu) \right] \\
&= -e^{-\tau(\varepsilon_{\mathbf{q}} - \mu)} \left[ \Theta(\tau) + \sum_{n=1}^{\infty} z^n e^{-n\beta\varepsilon_{\mathbf{q}}} \right] \\
&\equiv \sum_{n=0}^{\infty} z^n G^{(n)}(\tau, \mathbf{q}),
\end{aligned}
\tag{3.40}
$$

where we have expanded the Bose distribution for small fugacities $z = e^{\beta\mu}$ and defined the expanded propagators $G^{(n)}$ by

$$
G^{(n)}(\tau, \mathbf{q}) = \begin{cases} -e^{\tau\mu} e^{-\tau\varepsilon_{\mathbf{q}}} \Theta(\tau) & n = 0 \\ -e^{\tau\mu} e^{-(n\beta + \tau)\varepsilon_{\mathbf{q}}} & n \in \mathbb{N} \end{cases}.
\tag{3.41}
$$

In a similar fashion, the fermionic free propagator can be expanded as

$$
G_\sigma(\tau, \mathbf{q}) = \sum_{n=0}^{\infty} z^n G_\sigma^{(n)}(\tau, \mathbf{q})
\tag{3.42}
$$

$$
G_\sigma^{(n)}(\tau, \mathbf{q}) = \begin{cases} -e^{\tau\mu} e^{-\tau\varepsilon_{\mathbf{q}}} \Theta(\tau) & n = 0 \\ (-1)^{n-1} e^{\tau\mu} e^{-(n\beta + \tau)\varepsilon_{\mathbf{q}}} & n \in \mathbb{N} \end{cases},
\tag{3.43}
$$

where the alternating sign just comes from the expansion of the Fermi distribution with respect to the fugacity. Note that the zeroth order in the fugacity is, up to the factor $e^{\tau\mu}$, the free propagator in the vacuum.

A diagrammatic expansion of the full Green's function will in general contain free propagators that run forward, as well as some that run backward in imaginary time. A backward running line can most often be attributed to a particle coming from the medium and participating in a scattering process (hole scattering). The exception to this is that when $\tau < 0$, the ordering of the external legs enforces one backward running line as well. To expand a given diagram in terms of the fugacity, we can use the expansions (3.42) and (3.42). Diagrammatically, we denote the expanded propagators $G^{(n)}$ by a line that is slashed $n$-times (see fig. 2.12(a) in chapter 2.3). The free propagator is the sum of all these slashed propagators. Since the propagator $G^{(0)}$ is purely retarded, i.e. it may only run forward in imaginary time, a line that
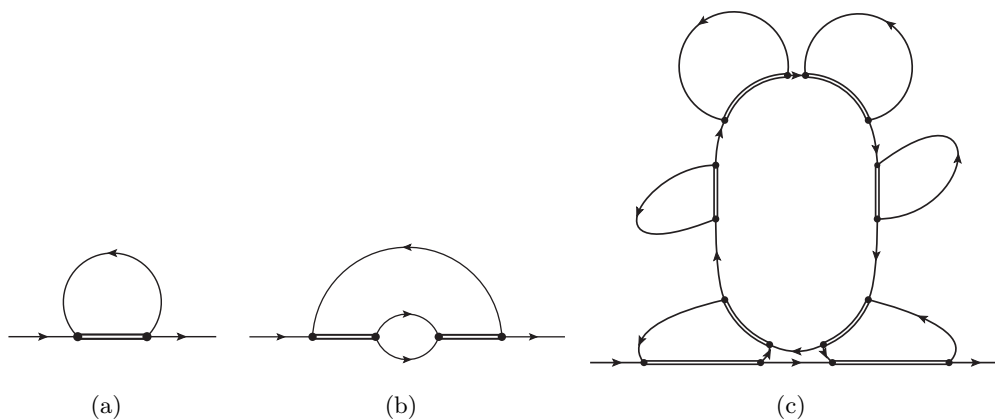
Figure 3.2: Example diagrams for the Green's function that are generated by the perturbative expansion (3.32), written in terms of an auxiliary field. When expanded in terms of fugacity, diagrams 3.2(a) and 3.2(b) are at least $\mathcal{O}(z)$, since the propagator that flows back can only contribute from order $z$ on, cf. eqs. (3.43), (3.41). Diagram 3.2(c) is an exercise for the reader: At which order in $z$ will it first contribute?

runs backwards has to at least be slashed once when expanded. Of course, both forward and backward running lines can be slashed arbitrarily often. To calculate the order of a given diagram in the fugacity, we just need to count the total number of slashes. In sec. 3.3, the big simplification will arise when we truncate the expansion at a given order in the fugacity (as mentioned earlier, we will choose $z^3$ to include three-body correlations). Truncating at any finite order in the fugacity only allows for a finite amount of backward running lines in the "mother"-diagram, which then results in the fact that only certain classes of diagrams contribute to the expansion of the Green's function. This is exemplified in figure 3.2, which shows perturbative diagrams that the are generated by both the bosonic and fermionic Lagrangians (3.17) and (3.24). Note that the bare auxiliary field, since it is non-dynamical, does not have a well defined propagation direction. Since the propagator $G^{(0)}$ does not increase the cost in powers of fugacities, expanded diagrams may always contain a series of ladder diagrams that describe repeated scattering of two or more particles that are already present in the diagram. Diagrams 3.2(a) and 3.2(b) are examples for this statement, since they can in principle contribute at the same order in the fugacity. In fact, they are the first two building blocks of the infinite series that

defines the two-body scattering amplitude, and are thus related to the self-energy diagram 2.12(b) in sec. 2.3. We will show how to sum such series of (forward running) ladder diagrams in the next subsection. Essentially, this amounts to the solution of the scattering problem in the vacuum.

## 3.2 Two- and Three-body $T$-Matrix

The next preparatory step for a virial expansion of the density and momentum distribution to third order in the fugacity is the definition of the two- and three-body $T$-matrices. These scattering matrices, which, as mentioned earlier, describe the repeated scattering of two or three particles, will constitute the non-trivial part in the diagrams that define the cluster expansion of the density and momentum distribution. As we will see in section (3.3), we will be able to rewrite the imaginary time integrations in our diagrams in terms of a Bromwich integration, which is an integration over complex energies. This is the reason why we only will care about the solution of the three-body problem in energy space. We will start with the discussion of the scattering matrices for bosons. For fermions, since the derivations are completely analogous, we will only shortly list the changes (symmetry factors and signs) and give the final expressions.

### 3.2.1 Bosons

Since the two-body scattering problem shows up in the three-body scattering problem, it makes sense to first quickly study the two-body problem. After that, we will introduce the diagrammatic series that defines the three-body problem and the integral equation that has to be solved to sum the series. We will also define the angular momentum decomposition of the the three-body $T$-matrix, which will prove useful for an analytic treatment (as far as possible) of the diagrams in sec. 3.3.

**Two-body scattering matrix**

The example diagrams 3.2(a) and 3.2(a) contain sub-diagrams that resemble the two-body scattering problem in the vacuum. To be more precise, they can be summed to contain the *full* dimer propagator in the vacuum, where we define this quantity by the diagrammatic series shown in fig. 3.3(a). Note that since we want to describe the series that is contained as a sub-diagram, the bosonic lines correspond to the first order propagators $G^{(0)}$, defined in eq. (3.41). We will go into much

(a)



(b)
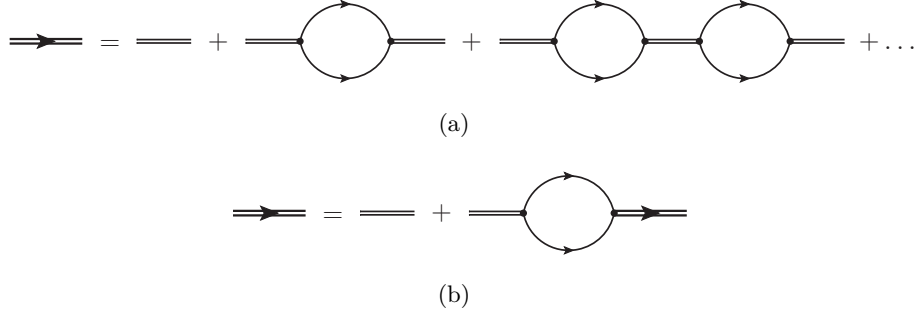
Figure 3.3: Diagrams that define the full dimer propagator.

detail in this section, because understanding the principles of the two-body sector is all it takes to understand the diagrammatic virial expansion. The three-body sector will not offer anything conceptually new. The Feynman-rules that are generated by the Lagrangian (3.17) are summarized in appendix B. Note that while for the bare propagator of the auxiliary field, it does not make sense to talk about a propagation direction, the full dimer propagator will has an energy dependence which allows to define a propagation direction. This is of course just a remnant of the fact that the bosonic atoms in the loop have a propagation direction in time. This is the reason why we will draw the full dimer *with* an arrow. The leading terms of diagram 3.3(a), evaluated in imaginary time and momentum, are given by[3]:

$$
\begin{aligned}
-e^{2\mu(\tau-\tau')}G_{dd}(\tau-\tau',\mathbf{p}) = &-\frac{4}{g_2}\delta(\tau-\tau'-0^+) \\
&+ 2e^{2\mu(\tau-\tau')}\Theta(\tau-\tau')\int_{\mathbf{k}}e^{-(\tau-\tau')(\varepsilon_{\mathbf{k}}+\varepsilon_{\mathbf{p}-\mathbf{k}})} \\
&- g_2 e^{2\mu(\tau-\tau')}\Theta(\tau-\tau')\int_0^{\tau-\tau'}dt\int_{\mathbf{k},\mathbf{k}'}e^{-t(\varepsilon_{\mathbf{k}}+\varepsilon_{\mathbf{p}-\mathbf{k}})}e^{-(\tau-\tau'-t)(\varepsilon_{\mathbf{k}'}+\varepsilon_{\mathbf{p}-\mathbf{k}'})} \\
&+ \dots, \qquad\qquad (3.44)
\end{aligned}
$$

where we included symmetry factors in the following way: Each vertex (that is contributing $-g_2/4$) corresponds to a combination of either $d\bar{\psi}\bar{\psi}$ or $\psi\psi\bar{d}$. For any pair of these vertices, we have two choices for the first contraction, while the second contraction is fixed by our earlier choices. This effectively contributes a symmetry factor of two for each of the loops. We also have defined the dimer Green's function

---

[3]As a reminder: Like in the earlier sections of this thesis, we use the shorthand $\int_{\mathbf{q}} = \int \frac{d^d q}{(2\pi)^d}$ for momentum integrations.

in a way that makes its connection to the real time vacuum dimer propagator clear. The choice of factoring out the $e^{2\mu(\tau-\tau')}$ turns out to be convenient for the diagrams we will encounter in section 3.3. In particular, note that every order in $g_2$ (except the very first term, where, because of the delta function, we can always multiply a term $e^{2\mu(\tau-\tau')}$ by hand) will have the same factor $e^{2\mu(\tau-\tau')}$, because the sum of all propagation times is always $\tau - \tau'$. Note that in eq. (3.44), we have directly written down the series for the negative Green's function, which, comparing to the definition (3.25) of the imaginary time Green's function, corresponds directly to the *contraction* of $d\bar{d}$. While for the bosonic problem, this way seems a little superficial at first, keeping explicit track of signs is needed for determining signs of the *fermionic* diagrams.

One more observation regarding the series in (3.44) is the following: At any order of loops, we can always rearrange the momentum integrations in a way that pulls out a global factor $e^{-(\tau-\tau')\varepsilon_{\mathbf{P}}/2}$. This can be arranged via the substitutions (which have determinant one) of the form $\mathbf{k} \rightarrow \mathbf{k} + \mathbf{p}/2$. The result is that the dimer Green's function is connected to its center of mass counter part via $G_{dd}(\tau - \tau', \mathbf{p}) = e^{-(\tau-\tau')\varepsilon_{\mathbf{P}}/2}G_{dd}(\tau - \tau', \mathbf{0})$. This of course just reflects the fact that our theory is Galilean invariant (in the vacuum).

Taking a closer look at the series (3.44), we see that it can also be brought into the form of an integral equation, where we now concentrate on the center of mass frame:

$$G_{dd}(\tau - \tau', \mathbf{0}) = \frac{4}{g_2}\delta(\tau - \tau' - 0^+) - \frac{g_2}{2}\int_0^{\tau-\tau'} dt \int_{\mathbf{k}} e^{-2t\varepsilon_{\mathbf{k}}}G_{dd}(\tau - \tau', \mathbf{0}) \quad (3.45)$$

Diagrammatically, the integral equation for the dimer propagator is shown in fig. 3.3(b). The integral equation above is, up to constants multiplying, the Lippmann-Schwinger integral equation for the two-body scattering amplitude. As was already mentioned, we will need the Laplace transformed version of this function for later use in our diagrams. $G_{dd}$ is indeed a retarded function, as is apparent from the presence of the $\Theta(\tau-\tau')$ functions in eq. (3.44), which came from expanding the free propagators to order zero in the fugacity. The Laplace transformation is thus well defined, and the convolution theorem[4] for Laplace transforms (which states that the

---

[4] For a short compilation of useful properties regarding the Laplace transform, see appendix C. Note that in contrast to the usual mathematical literature [111], we define the Laplace transform with another sign in the exponent: $f(s) = \int_0^\infty dt e^{st} f(t)$. $s$ thus has to lie (before analytic continuation) in the left half $\Re s < 0$ of the complex plane.
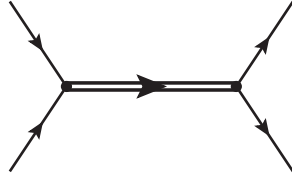
Figure 3.4: Connection between $T_2$-matrix and dimer propagator: The effective Feynman rule for this diagram is $-T_2$.

Laplace transform of a convolution gives the product of Laplace transforms) yields

$$G_{dd}(s, \mathbf{0}) = \frac{4}{g_2} + \frac{g_2}{2} \int_{\mathbf{k}} \frac{1}{s - 2\varepsilon_{\mathbf{k}}} G_{dd}(s, \mathbf{0}), \tag{3.46}$$

where we have applied the convolution theorem to the imaginary time version (3.45) of the integral equation for the dimer propagator. The property that the propagator $G_{dd}$ at finite momentum is related to its center of mass counter part multiplied with $e^{-(\tau - \tau')\varepsilon_{\mathbf{P}}/2}$ translates to

$$G_{dd}(s, \mathbf{p}) = G_{dd}\left(s - \frac{\mathbf{p}^2}{4m}, \mathbf{0}\right) \equiv G_{dd}\left(s - \frac{\mathbf{p}^2}{4m}\right) \tag{3.47}$$

in (complex) energy space. This is the usual Galilean invariant form of the scattering amplitude in momentum and energy space. In order to make comparison to the results of Leyronas [9], let us define the two-body T-matrix

$$T_2(s) = \frac{g_2^2}{4} G_{dd}(s). \tag{3.48}$$

Note that $-T_2(s)$ is the effective Feynman-rule for the vertex shown in fig. 3.4. We already accounted for the symmetry factor of four, that comes from the $2 \cdot 2$ choices to connect the vertices with the external legs. It should also be noted that $T_2(s) = -\mathcal{A}(s)$, where $\mathcal{A}$ is the amplitude used in the other chapters of this thesis. The integral equation for $T_2$, that results from eqs. (3.48) and (3.47), involves a divergent loop-integral. This divergence is exactly canceled by the renormalization prescription (3.18) of the two-body coupling constant $g_2$. The remaining parts yields the standard result

$$T_2(s) = \frac{8\pi}{m} \frac{1}{\frac{1}{a} - \sqrt{-ms}} \tag{3.49}$$
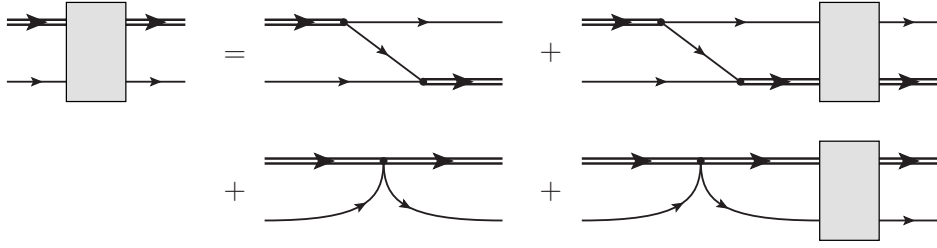
Figure 3.5: STM integral equation for the three-body $T$-matrix $T_3$, which is depicted diagrammatically by a gray box.

for the scattering of two contact-interacting bosons in the vacuum. Note that $T_2$ also inherits the Galilean invariance of the dimer propagator, implying that $T_2(s, \mathbf{p}) = T_2(s - p^2/4m)$. As mentioned earlier, we will always express our diagrams in terms of the $T_2$-matrix, because it makes comparison to the expressions given in [9] straightforward. For the determination of signs (fermions) and symmetry factors (bosons) of a given diagram however, I find it more convenient to work with the full dimer propagator instead.

In summary, we have seen how sub-diagrams that are connected to the scattering problem in the vaccuum appear in our virial expansion. For the three-body sector, we will not go through such a detailed derivation again, and rather just define the series we are going to meet in our diagrams directly in (complex) energy space. The tricks employed here, such as factoring out convenient factors and using Galilean invariance, will of course be implicitly used in the next subsection as well.

**Three-body scattering matrix**

In the three-body sector and in the perturbative expansion that is generated by the $S$-matrices, cf. eqs. (3.31) and (3.32), we are going to meet sub-diagrams that are generated by the diagrammatic integral equation shown in fig. 3.5. This integral equation for the scattering of three particles is called the Skorniakov Ter-Martirosian (STM) equation [112]. Since we already have included the interaction vertices into the $T_2$ matrix, we will exclude them from the three-body $T$-matrix. Let $\mathbf{p}$ and $\mathbf{k}$ be the incoming and outgoing momenta of the *atom*, such that $\mathbf{P} - \mathbf{p}$ and $\mathbf{P} - \mathbf{k}$ are the incoming and leaving momenta of the dimers. Further, let $s$ be the total center of mass energy and $\varepsilon_{\mathbf{p}}$, $\varepsilon_{\mathbf{k}}$ the energies of the incoming and outgoing atoms. The three-body $T$-matrix $T_3$ that we will encounter in our diagrams solves the following

STM equation:

$$T_3(s, \varepsilon_{\mathbf{p}}, \varepsilon_{\mathbf{k}}, \mathbf{P}, \mathbf{p}, \mathbf{k}) = \left[ \frac{1}{s - \varepsilon_{\mathbf{p}} - \varepsilon_{\mathbf{k}} - \varepsilon_{\mathbf{P}-\mathbf{p}-\mathbf{k}}} + \frac{g_3}{9g_2^2} \right]$$
$$+ \int_{\mathbf{q}} \left[ \frac{1}{s - \varepsilon_{\mathbf{p}} - \varepsilon_{\mathbf{q}} - \varepsilon_{\mathbf{P}-\mathbf{p}-\mathbf{q}}} + \frac{g_3}{9g_2^2} \right] T_2 \left( s - \varepsilon_{\mathbf{q}} - \frac{\varepsilon_{\mathbf{P}-\mathbf{q}}}{2} \right) T_3(s, \varepsilon_{\mathbf{q}}, \varepsilon_{\mathbf{k}}, \mathbf{P}, \mathbf{q}, \mathbf{k})$$

$$(3.50)$$

Note that inclusion of the two-body vertices into the externally attached $T_2$-matrix does not yield exactly the same amplitude that one gets from the diagrams in fig. 3.5 by simple amputation of the external legs using the LSZ-reduction formalism [28]. This was done in ref. [25]. This procedure would not prove useful in our case, since, as we will see in sec. 3.3, the external dimer legs of this amplitude are not on-shell. Calling the three-body amplitude in [25] $\mathcal{A}_3(..)$, we have: $\mathcal{A}_3(...) = -16\pi T_3(...)/a$.

From Galilean invariance (or similar arguments to the ones given in the preceding section on the two-body scattering), it follows that the amplitude $T_3$ can be related to its center of mass counterpart $t_3(s, \mathbf{p}, \mathbf{k}) = T_3(s, \varepsilon_{\mathbf{p}}, \varepsilon_{\mathbf{k}}, \mathbf{0}, \mathbf{p}, \mathbf{k})$ via

$$T_3(s, \varepsilon_{\mathbf{p}}, \varepsilon_{\mathbf{k}}, \mathbf{P}, \mathbf{p}, \mathbf{k}) = t_3 \left( s - \frac{\varepsilon_{\mathbf{P}}}{3}, \mathbf{p} - \frac{\mathbf{P}}{3}, \mathbf{k} - \frac{\mathbf{P}}{3} \right). \qquad (3.51)$$

This allows us to concentrate on the solution of the three-body problem in the center of mass frame. The center of mass amplitude $t_3(s, \mathbf{p}, \mathbf{k})$ is a function of the (complex) energy $s$, the magnitudes $p$ and $k$ of the momenta, and the angle $\cos\theta = \hat{\mathbf{p}} \cdot \hat{\mathbf{k}}$, where the hat denotes a unit vector. We now decompose $(l = 0, 1, 2, ..)$ the amplitude into angular momentum components via

$$t_3(s, \mathbf{p}, \mathbf{k}) = \sum_l (2l + 1) P_l(\cos\theta) t_3^{(l)}(s, p, k) \qquad (3.52)$$

$$t_3^{(l)}(s, p, k) = \frac{1}{2} \int_{-1}^{1} d\cos\theta \, P_l(\cos\theta) t_3(s, \mathbf{p}, \mathbf{k}), \qquad (3.53)$$

where the $P_l(\cos\theta)$ are the Legendre polynomials. Appendix D provides details on the projection of the STM equation (3.50) onto angular momentum channels. The key observation is that the resulting effective STM equation for $t_3^{(l)}$ does not mix

different angular momenta:

$$t_3^{(l)}(s, p, k) = \left[ \frac{m}{pk} Q_l \left( \frac{m}{pk} \left[ s - \frac{p^2}{m} - \frac{k^2}{m} \right] \right) - m \frac{H(\Lambda)}{\Lambda^2} \delta_{l0} \right]$$
$$+ \frac{4}{\pi m} \int_0^\Lambda dq \frac{q^2}{\frac{1}{a} - \sqrt{-ms + \frac{3}{4} q^2}}$$
$$\left[ \frac{m}{pq} Q_l \left( \frac{m}{pq} \left[ s - \frac{p^2}{m} - \frac{q^2}{m} \right] \right) - m \frac{H(\Lambda)}{\Lambda^2} \delta_{l0} \right] t_3^{(l)}(s, q, k) \qquad (3.54)$$

The cutoff function $H(\Lambda)$ was defined in eq. (3.20), and takes care of the renormalization of the three-body vertex. The $Q_l(z)$ denote the so called Legendre functions of the second kind, defined by

$$Q_l(z) = \frac{1}{2} \int_{-1}^1 dx \frac{P_l(x)}{z - x}. \qquad (3.55)$$

For integer index, which is the case for us, they can be defined [113, 114] such that they are analytic for $z \in \mathbb{C}/[-1, 1]$, with a branch cut discontinuity ranging from $-1$ to 1. For more details on the Legendre functions of the second kind, see appendix D.

Which bound states does the STM equation (3.54) predict? To answer that, assume that $s \approx -E_B$, $E_B > 0$ is close to a bound state. Near the pole, the amplitude takes the form [25]

$$t_3^{(l)}(s, p, k) \approx \frac{B_{E_B}^{(l)}(p, k)}{s + E_B}, \qquad (3.56)$$

where we have assumed a simple pole. We can now insert (3.56) into the STM equation (3.54), and multiply by $s + E_B \approx 0$, which eliminates the inhomogeneity from the integral equation. Making the factorization ansatz[5] $B_{E_B}^{(l)}(p, k) = B_{E_B}^{(l)}(p) B_{E_B}^{(l)}(k)$, the STM equation near a bound state pole reduces to

$$B_{E_B}^{(l)}(p) = \frac{4}{\pi m} \int_0^\Lambda dq \frac{q^2}{\frac{1}{a} - \sqrt{mE_B + \frac{3}{4} q^2}}$$
$$\left[ \frac{m}{pq} Q_l \left( \frac{m}{pq} \left[ -E_B - \frac{p^2}{m} - \frac{q^2}{m} \right] \right) - m \delta_{0l} \frac{H(\Lambda)}{\Lambda^2} \right] B_{E_B}^{(l)}(q). \qquad (3.57)$$

---

[5]This is justified by two things: mathematically, because the form of the integral equation allows for it. Physically, because $t_3$ is connected to the Green's function of three atoms. The residues of its poles, in turn, are connected to the product of the momentum space wave functions [115] of the atoms in the respective bound state.

Numerically, the usual procedure for the solution of (3.57) is to put the integration onto a discrete grid. The above equation only has solutions when the determinant of the energy dependent kernel matrix is zero. We can thus use a root finder for the determinant to find the bound states. Note that while the above equation also defines the residue, it does so only up to a normalization constant, which is why we use eq. (3.57) only to determine the positions of the poles. It turns out that the amplitude supports infinitely many three-body bound states (poles) in the $l = 0$ channel, while for $l \neq 0$, no bound states are present. The three-body bound states are of course the Efimov trimers (see fig. 3.1, which was created using the above considerations). In practice, we also use equation (3.57) to find $\kappa_*$ (the wavenumber of the Efimov state that we *specify* to be deepest) for a given $\Lambda_*$, where $\Lambda_*$ is the adjustable three-body parameter in eq. (3.20).

### 3.2.2 Fermions

For fermions, both the two- and three-body scattering problem are conceptually the same as for their bosonic counterparts. We will therefore just state the results, and discuss the subtle differences to the bosonic problem. The two-body $T$-matrix $T_2$ for the scattering of an $\uparrow$ and a $\downarrow$ fermion is given by

$$T_2(s) \quad = \quad \frac{4\pi}{m} \frac{1}{\frac{1}{a} - \sqrt{-ms}}. \tag{3.58}$$

It solves the Lippmann-Schwinger equation, but is of course now generated by the Lagrangian (3.24). Since there is, due to the distinguishability of the $\uparrow$ and $\downarrow$ fermions, no need for symmetry factors, the fermionic $T_2$ differs from the bosonic one (see eq. (3.49)) by a factor of two. Diagrammatically, the two-body $T$-matrix is again represented by fig. 3.4, where the external lines have to be labeled with $\uparrow$ and $\downarrow$.

The STM equation for the scattering matrix of three atoms, labeled by $T_{3,\sigma}$ for the scattering of an atom of species $\sigma$ off a dimer (that contains one particle of each species), is diagrammatically represented by fig. 3.5 without the parts that contain a three-body vertex, because the fermionic Lagrangian does not include a three-body term, cf. eq. (3.24). Projection onto angular momentum components

(see the bosonic $T_3$ section and appendix D for details) yields the STM equation

$$t_{3,\sigma}^{(l)}(s,p,k) = \left[ \frac{m}{pk} Q_l \left( \frac{m}{pk} \left[ s - \frac{p^2}{m} - \frac{k^2}{m} \right] \right) \right]$$
$$- \frac{2}{\pi m} \int_0^\Lambda dq \frac{q^2}{\frac{1}{a} - \sqrt{-ms + \frac{3}{4} q^2}}$$
$$\left[ \frac{m}{pq} Q_l \left( \frac{m}{pq} \left[ s - \frac{p^2}{m} - \frac{q^2}{m} \right] \right) \right] t_{3,\sigma}^{(l)}(s,q,k). \qquad (3.59)$$

Like in the bosonic case, we exclude the external interaction vertices from the expression. Comparing the fermionic STM equation (3.59) to the bosonic one, which is given in eq. (3.54), we see that they basically only differ by a factor of $-2$ in the kernel of the integral equation and the missing three-body terms $\sim g_3$. The minus sign comes from a crossing of two fermionic lines, resulting in the fact that the contraction of the fields that act at the vertices contributes a minus sign. This sign change has profound consequences. The fermionic three-body equation does not support any three-body bound states. As a consquence, for example, the ratio $a_{AD}/a$, where $a_{AD}$ is the atom-dimer scattering length, defined via

$$a_{AD} = \frac{8}{3ma} T_{3,\sigma} \left( -\frac{1}{ma^2}, 0, 0, \mathbf{0}, \mathbf{0}, \mathbf{0} \right), \qquad (3.60)$$

is *constant* with respect to variation of the scattering length $a$. I find $a_{AD}/a = 1.179..$, which is consistent with the result $a_{AD}/a = 1.18$ [112, 116]. This is in stark contrast to the bosonic atom dimer scattering length, which shows resonant behavior whenever a trimer-line line hits the atom-dimer continuum at $a_*$ (see fig. 3.1), and variation in between. It should be noted that the fermionic picture will change a lot when introducing a mass-difference for the two-species. It has been shown [107] that for a mass ratio $m_\uparrow/m_\downarrow > 13.6$, the fermionic three-body problem supports three-particle bound states. For a field-theoretic treatment of the problem, see the contribution of Nishida and Son in ref. [7].

Last but not least, note that the transformation properties (3.47) and (3.51) of the two- and three-body $T$-matrices for transformations into the center of mass frame also hold in the fermionic case. This is once again a consequence of the Galilean invariance of the theory defined by the Lagrangian (3.24).

## 3.3 Diagrammatic cluster expansion for momentum distribution and density

With all the preparatory work done, we are now going to aim for the virial expansion of the momentum distribution and the density to third order in the fugacity $z$. The expansion of the density allows for the extraction of the virial coefficients, which define the thermodynamic properties of the system. As mentioned in the introduction, one of the motivations for the calculation of the momentum distribution is the experiment [94], where the momentum distribution of a unitary Bose gas was measured. In sec. 3.3.1, we are going to discuss the bosonic case in great detail. In sec. 3.3.2, we give a less detailed description of the fermionic diagrams, and merely discuss the important changes, as well as the resulting expressions.

### 3.3.1 Bosons

The momentum distribution and density of a bosonic system can, in the translationally invariant case, be related to the imaginary time Green's function $\mathcal{G}$ via

$$
n(\mathbf{q}) = -\lim_{\tau \to 0^-} \mathcal{G}(\mathbf{q}, \tau) = \langle T_\tau \bar{\psi}(\mathbf{q}, 0^+)\psi(\mathbf{q}, 0) \rangle \tag{3.61}
$$

$$
n = -\lim_{\tau \to 0^-} \mathcal{G}(\mathbf{0}, \tau) = \langle T_\tau \bar{\psi}(\mathbf{x}, 0^+)\psi(\mathbf{x}, 0) \rangle, \tag{3.62}
$$

which follows directly from the definition (3.25) of $\mathcal{G}$. Note that since $n = \int_{\mathbf{q}} n(\mathbf{q})$, we can also obtain the density *from* the momentum distribution. I used this in the numerical calculations to test the consistency of the results. As discussed in sec. 3.1.4, we can perform a diagrammatic virial expansion of the full Green's function $\mathcal{G}$ to order $z^3$ via inclusion of all diagrams that have at most three lines that run backward in imaginary time. One of these lines always has to be an external one, since the ordering of the fields in eqs. (3.61) and (3.62) forces an annihilation before the creation of a particle. Diagrammatically, we will indicate the imaginary time $\tau = 0$ by a cross. For the momentum distribution, the external lines will have momentum $\mathbf{q}$, while for the density they are integrated over all possible momenta.

Using our knowledge of the diagrammatic cluster expansion, see sec. 3.1.4, we anticipate that the expansions of the momentum distribution and density can be structured like

$$
\begin{aligned}
n(\mathbf{q}) = {} & z n_1^{(1p)}(\mathbf{q}) + z^2 \left[ n_2^{(1p)}(\mathbf{q}) + n_2^{(2p)}(\mathbf{q}) \right] \\
& + z^3 \left[ n_3^{(1p)}(\mathbf{q}) + n_3^{(2p)}(\mathbf{q}) + n_3^{(3p)}(\mathbf{q}) \right] + \mathcal{O}(z^4),
\end{aligned} \tag{3.63}
$$

(a) $\mathcal{O}(z)$     (b) $\mathcal{O}(z^2)$     (c) $\mathcal{O}(z^3)$
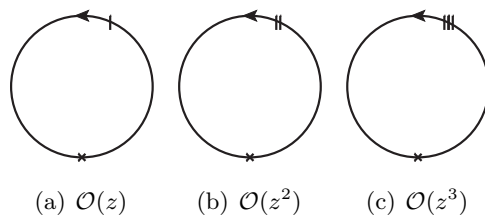
Figure 3.6: Diagrams for the one-particle contributions to the expansion of the density and momentum distribution.

where the density trivially has the analogous structure, because it can be obtained from the momentum distribution by integration over all momenta. The nomenclature was chosen to be suggestive in the sense that $n_i^{jp}$ describes the contribution to order $z^i$ from diagrams that belong to the $j$-particle sector. We are now going to determine these contributions in ascending order in the particle number.

**Momentum distribution**

Except for the one-particle sector, which is simple enough to treat everything at once, we will first only consider the evaluation of the diagrams for the momentum distribution. The diagrams for the density are the same, and thus results for the density can be obtained by integration of the diagrams for the momentum distribution over all external momenta $\mathbf{q}$. In general, it will turn out to be most convenient to integrate an intermediate result over all $\mathbf{q}$, since the end results for the momentum distribution are tailor made for numerical evaluation.

**One-particle diagrams** Since there are no interactions involved, the one-particle sector is very simple. The diagrams that contribute to the density up to order $z^3$ are shown in figure 3.6. The contribution to the momentum distribution from a single closed loop that is slashed $\ell$ times can be directly read off from the definition of the slashed propagator, given in eq. (3.41):

$$n_\ell^{(1p)}(\mathbf{q}) \quad = \quad -\lim_{\tau \to 0^-} G^{(\ell)}(\tau, \mathbf{q}) = e^{-\ell\beta\varepsilon_\mathbf{q}}. \qquad (3.64)$$

A sign convention for later use: Our diagrams are supposed to be diagrams for the Greens function. To obtain the density or momentum distribution, we need to multiply the result of any given diagram by $-1$. The result for the density follows

(a) $\mathcal{O}(z^2)$      (b) $\mathcal{O}(z^3)$      (c) $\mathcal{O}(z^3)$      (d) $\mathcal{O}(z^3)$
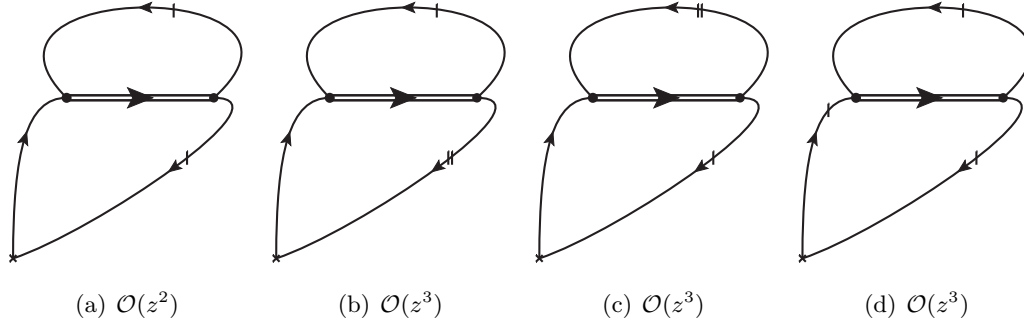
Figure 3.7: Contributions to the cluster expansion of momentum distribution and density from the two-particle sector. The diagrams all originate from the same mother-diagram.

directly from integration of eq. (3.64):

$$n_\ell^{(1p)} \;\; = \;\; \int_{\mathbf{q}} e^{-\ell\beta\varepsilon_{\mathbf{q}}} = \frac{1}{\ell^{3/2}} \frac{1}{\lambda_T^3}. \tag{3.65}$$

Should we make our gas non-interacting by $g_2, g_3 \to 0$, in which case only diagrams of the form 3.6(a)-3.6(c) exist, we can extract the standard result $b_\ell^{(0)} = 1/\ell^{5/2}$ for the virial coefficients of a non-interacting Bose gas from the above formula by comparison with the definition of the density expansion in terms of the virial coefficients (see table 3.1).

**Two-particle diagrams** The contributions from the two-particle sector all come from the same mother-diagram, which contains an infinite series of what can be considered two-particle scattering in the vacuum. The first terms of this series were shown in figs. 3.2(a) and 3.2(b). The resulting diagrams for the two-body sector are shown in figure 3.7.

Before turning to the evaluation of the diagrams, let us pause a moment (maybe even get a coffee?). Didn't we forget a diagram? After all, the effective dimer propagator contains bubbles with two bosons. What keeps us from slashing those lines, too? As it turns out: Nothing. We even have to. However, these diagrams will turn out to belong to the terms that are generated by the three-body $T$-matrix, and thus belong to the three-body sector. We will come back to this issue in the paragraph on the three-particle diagrams, but, to avoid confusion, it was worth mentioning.

**Diagram 3.7(a)**  We will start with the evaluation of the $\sim z^2$ diagram 3.7(a). This will nicely demonstrate how to treat all the other diagrams we are going to meet. Some conventions: The important (imaginary) times in diagram 3.7(a) are, going from left to right:

- The action of the external vertex (cross) at $\tau_0 = 0$

- The action of the first interaction vertex at $\tau_1 \geq 0$

- The action of the second interaction vertex at $\beta \geq \tau_2 \geq \tau_1$

Instead of using the formalism discussed in secs. 3.1.3 and 3.1.4, and expressing the diagrams in terms of these absolute times, we will rather choose to express the diagram in terms of the *time differences*:

- $t_1 = \tau_1 - 0$

- $t_2 = \tau_2 - \tau_1$

- with the constraints $0 < t_1 + t_2 < \beta, 0 < t_1, 0 < t_2$

In the following, we will always define a set of time differences $A$, that fulfills the properties above, even for the case where we need more than two time differences. The precise definition of $A$ can be found in appendix C (with $\tau = \beta$). With these definitions, and labeling the loop momentum $\mathbf{k}$, we can express the contribution of diagram 3.7(a) to the full Green's function as

$$
\begin{aligned}
\mathcal{G}(0^-, \mathbf{q})\Big|_{3.7(a)} &= -z^2 \int_A dt_1 dt_2 \int_{\mathbf{k}} G^{(0)}(t_1, \mathbf{q}) e^{2\mu t_2} T_2(t_2, \mathbf{q} + \mathbf{k}) \\
&\qquad\qquad\qquad G^{(1)}(-t_2, \mathbf{k}) G^{(1)}(-t_1 - t_2, \mathbf{q}) \\
&= z^2 \int_A dt_1 dt_2 \int_{\mathbf{q}} T_2(t_2, \mathbf{q} + \mathbf{k}) e^{-t_1(\varepsilon_{\mathbf{q}} + \varepsilon_{\mathbf{k}})} e^{-(\beta - t_1 - t_2)(\varepsilon_{\mathbf{q}} + \varepsilon_{\mathbf{k}})}.
\end{aligned}
$$
$$(3.66)$$

In the second line, we have plugged in the explicit definitions of the slashed propagators and also inserted a factor of $1 = e^{-t_1 \varepsilon_{\mathbf{k}}} e^{t_1 \varepsilon_{\mathbf{k}}}$. We did this to use the generalized convolution theorem for Laplace transforms, in the form that is given in appendix C. Our integral is now exactly of this form, and we can re-express the two integrations over imaginary times in terms of a Laplace-back-transform of a product of Laplace

transforms[6], such that it only contains a single integration over complex energies:

$$\mathcal{G}(0^-, \mathbf{q})\Big|_{3.7(a)} = z^2 \int_{BW} \frac{ds}{2\pi i} e^{-\beta s} \int_{\mathbf{k}} \frac{T_2(s, \mathbf{k} + \mathbf{q})}{(s - \varepsilon_{\mathbf{k}} - \varepsilon_{\mathbf{q}})^2} \tag{3.67}$$

The Bromwich contour, indicated by $\int_{BW}$, runs parallel to the imaginary axis and to the left of all the singularities. To save space, we shall also indicate the Bromwich integration by

$$\int_s f(s) \equiv \int_{BW} \frac{ds}{2\pi i} f(s) \tag{3.68}$$

$T_2(s, \mathbf{q} + \mathbf{k})$ is the Laplace transform of the two-body $T$-matrix, and is explicitly given in eq. (3.49). We have also used that the Laplace transform of an exponential is given by

$$\int_0^\infty dt e^{st} e^{-t\varepsilon} = -\frac{1}{s - \varepsilon} \qquad \Re s < \varepsilon. \tag{3.69}$$

The Bromwich contour takes care of the condition on the real part. Once we have written down the complete contour integral, we can analytically continue the Laplace transforms and evaluate the Bromwich contour in a conveniently chosen way.

A short comment on symmetry factors: Are we sure that eq. (3.66) contains the right prefactor, as it would be also generated by the perturbative expansion (3.32)? Yes we are. If you are interested in the derivation, please consult appendix E. Here and in the following, let us just state the diagrams together with the right prefactors.

Starting again from eq. (3.67), we perform the substitutions $\mathbf{p} = \mathbf{q} + \mathbf{k}$ and $s' = s - \varepsilon_{\mathbf{p}}$ (afterwards renaming $s' \to s$) in order to perform the angular integrations:

$$\mathcal{G}(0^-, \mathbf{q})\Big|_{3.7(a)} = z^2 \int_s e^{-\beta s} T_2(s) \int_{\mathbf{p}} \frac{e^{-\frac{\beta}{2}\varepsilon_{\mathbf{p}}}}{(s + \frac{\varepsilon_{\mathbf{p}}}{2} - \varepsilon_{\mathbf{q}-\mathbf{p}} - \varepsilon_{\mathbf{q}})^2}$$

$$= \frac{z^2}{(2\pi)^2} \int_s e^{-\beta s} T_2(s) \int_0^\infty dp \frac{2p^2 e^{-\beta \frac{p^2}{4m}}}{\left(\frac{p^2}{4m}\right)^2 + \left(\frac{q^2}{m} - s\right)^2 - \frac{p^2}{2m}\left(\frac{q^2}{m} + s\right)}. \tag{3.70}$$

We have now already (because diagram 3.7(a) is the only diagram (with interactions) that is allowed up to order $z^2$) established the virial expansion of the momentum distribution to order $z^2$! We have

$$n_2^{(2p)}(\mathbf{q}) = -\frac{1}{z^2} \mathcal{G}(0^-, \mathbf{q})\Big|_{3.7(a)}, \tag{3.71}$$

---

[6]For the definitions regarding the Laplace transform and its associated back-transform, see appendix C

where $n_2^{(2p)}(\mathbf{q})$ enters the momentum distribution via eq. (3.63). For the other diagrams, we will proceed with less detailed explanation. The principle ideas are always the same as the ones presented here.

**Diagrams 3.7(b) and 3.7(d)**  The evaluation of these diagrams is grouped together in one paragraph, because they result in the same expression. Using the same tricks as for diagram 3.7(a), we have:

$$
\begin{aligned}
\mathcal{G}(0^-, \mathbf{q})\Big|_{3.7(b)} &= -z^3 \int_A dt_1 dt_2 \int_{\mathbf{k}} G^{(0)}(t_1, \mathbf{q}) e^{2\mu t_2} T_2(t_2, \mathbf{q} + \mathbf{k}) \\
& \qquad\qquad\qquad G^{(2)}(-t_1 - t_2, \mathbf{q}) G^{(1)}(-t_2, \mathbf{k}) \\
&= z e^{-\beta \varepsilon_{\mathbf{q}}} \mathcal{G}(0^-, \mathbf{q})\Big|_{3.7(a)},
\end{aligned}
\tag{3.72}
$$

where the result for diagram 3.7(a) was given in eq. (3.70). Similarly, we get

$$
\begin{aligned}
\mathcal{G}(0^-, \mathbf{q})\Big|_{3.7(d)} &= -z^3 \int_A dt_1 dt_2 \int_{\mathbf{k}} G^{(1)}(t_1, \mathbf{q}) e^{2\mu t_2} T_2(t_2, \mathbf{q} + \mathbf{k}) \\
& \qquad\qquad\qquad G^{(1)}(-t_1 - t_2, \mathbf{q}) G^{(1)}(-t_2, \mathbf{k}) \\
&= z e^{-\beta \varepsilon_{\mathbf{q}}} \mathcal{G}(0^-, \mathbf{q})\Big|_{3.7(a)}
\end{aligned}
\tag{3.73}
$$

**Diagram 3.7(c)**  For the last $\sim z^3$ diagram from the two particle sector, we have:

$$
\begin{aligned}
\mathcal{G}(0^-, \mathbf{q})\Big|_{3.7(c)} &= -z^3 \int_A dt_1 dt_2 \int_{\mathbf{k}} G^{(0)}(t_1, \mathbf{q}) e^{2\mu t_2} T_2(t_2, \mathbf{q} + \mathbf{k}) \\
& \qquad\qquad\qquad G^{(1)}(-t_1 - t_2, \mathbf{q}) G^{(2)}(-t_2, \mathbf{k}) \\
&= z^3 \int_s e^{-\beta s} \int_{\mathbf{k}} \frac{T_2(s, \mathbf{q} + \mathbf{k})}{(s - \varepsilon_{\mathbf{k}} - \varepsilon_{\mathbf{q}})^2},
\end{aligned}
\tag{3.74}
$$

where we have used the generalized convolution theorem for Laplace transforms. The substitutions $s' = s - \varepsilon_{\mathbf{q}+\mathbf{k}}$ ($s' \to s$ afterwards) and $\mathbf{p} = \mathbf{k} + \mathbf{q}/3$ allow to perform the angle integration:

$$
\mathcal{G}(0^-, \mathbf{q})\Big|_{3.7(c)} = \frac{z^3}{2\pi^2} \int_s \int_0^\infty dp \, \frac{p^2 e^{-\beta(s + \frac{3p^2}{4m} + \frac{q^2}{6m})} T_2(s)}{\left(s - \frac{p^2}{4m}\right)^2 - \frac{8}{9}\frac{q^2}{m}\left(s + \frac{p^2}{4m}\right) + \frac{16}{81}\frac{q^4}{m^2}}
\tag{3.75}
$$

Summarizing the results of the $\mathcal{O}(z^3)$ two-particle diagrams, we get:

$$
n_3^{(2p)}(\mathbf{q}) = -\frac{1}{z^3}\left[\mathcal{G}(0^-, \mathbf{q})\Big|_{3.7(c)} + 2z e^{-\beta\varepsilon_{\mathbf{q}}}\mathcal{G}(0^-, \mathbf{q})\Big|_{3.7(a)}\right],
\tag{3.76}
$$

(a) $\mathcal{O}(z^3)$        (b) $\mathcal{O}(z^3)$        (c) $\mathcal{O}(z^3)$

(d) $\mathcal{O}(z^3)$        (e) $\mathcal{O}(z^3)$
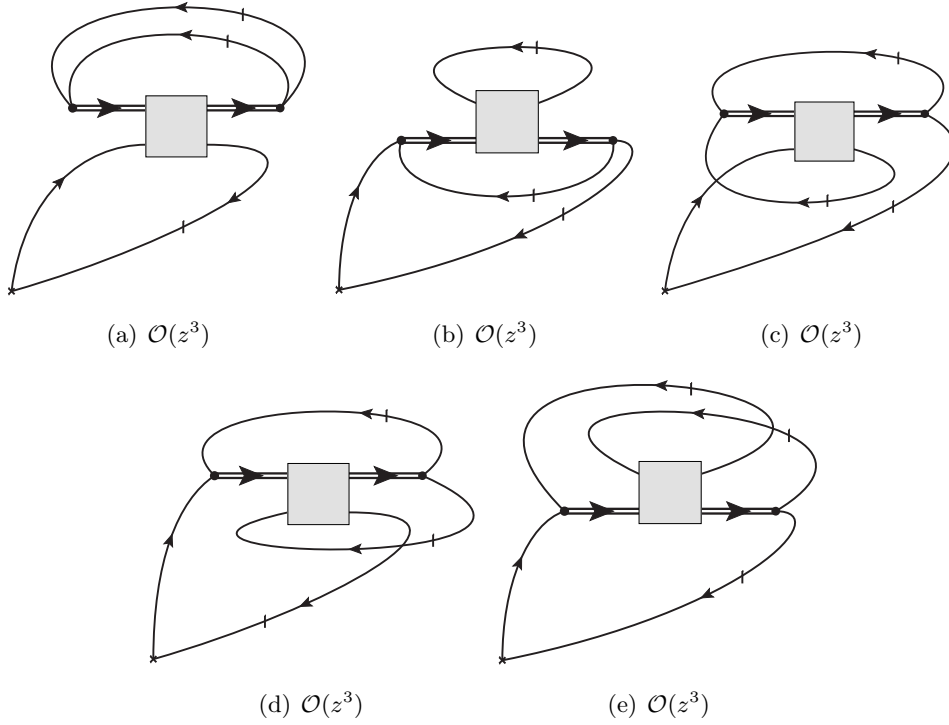
Figure 3.8: Diagrams from the three-particle sector that contribute to the virial expansion of the momentum distribution and density up to order $z^3$. The gray box is the three-body $T$-matrix.

where $\mathcal{G}(0^-, \mathbf{q})\big|_{3.7(a)}$ is given in eq. (3.70).

Note that the results for all the two-particle diagrams of third order in the fugacity decay *exponentially* as $q \to \infty$. This means that these diagrams do not contribute to the universal $C_2/q^4$ asymptotic behavior at large momenta, cf. eq. (3.8).

**Three-particle diagrams**   The only part of the expansion of the momentum distribution that is still left to determine is the one coming from the three-particle sector: $n_3^{(3p)}(\mathbf{q})$. The diagrams that contribute are shown in fig. 3.8. Since these are the first diagrams to contain the three-body $T$-matrix, these are also the first ones to encode true three-body correlations, in particular correlations related to the Efimov effect. The three-body contribution to the momentum distribution can be

(a)



(b)
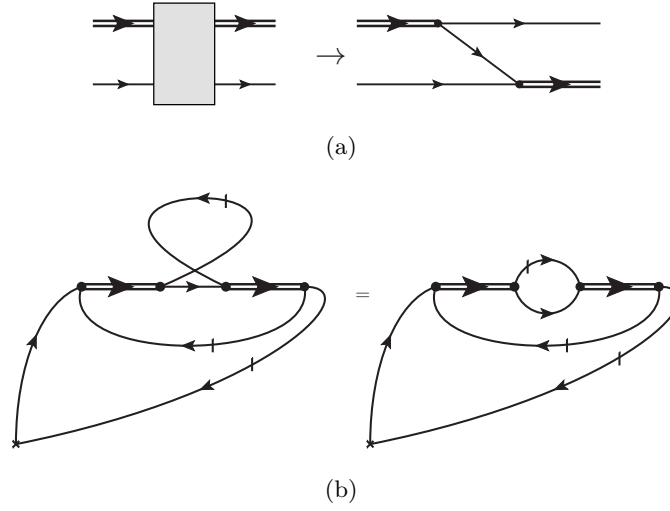
Figure 3.9: The leading order term (we set $g_3 = 0$ for simplicity) in the series that generates the STM equation is shown in 3.8(a). This replacement of the gray box by the leading order term in diagram 3.8(b) generates the missing diagram we were concerned about in the two-particle sector, as shown in figure 3.9(b).

expressed in terms of these diagrams via

$$z^3 n_3^{(3p)}(\mathbf{q}) \;\; = \;\; -\left[\frac{1}{2}\mathcal{G}(0^-, \mathbf{q})\Big|_{3.8(a)} + \mathcal{G}(0^-, \mathbf{q})\Big|_{3.8(b)-3.8(e)}\right], \qquad (3.77)$$

where the last term is a short hand for the sum of the contributions of diagrams 3.8(b)-3.8(e). The calculation of the symmetry factors in presented in appendix E.1.2.

A quick comment on the "missing" slashed diagram from the two-body sector: In the first born approximation, the three-body $T$-matrix is just given by the inhomogeneity of the STM integral equation. Diagrammatically, this corresponds to the replacement shown in fig. 3.9(a). If we make this very replacement in diagram 3.8(b), we are producing the diagram shown in fig. 3.9(b). By untwisting the artificially back-running line, we are generating the very diagram we were concerned about earlier in the beginning of the discussion of the two-body diagrams.

**Diagram 3.8(a)**  The imaginary time differences $t_1, ..., t_4$ are defined in the same spirit as for the two-body diagrams. Their definition can be read off from the

expression that we are going to give for diagram 3.8(a). We will denote the loop momenta by $\mathbf{k}$ and $\mathbf{p}$. The resulting expression for diagram 3.8(a) is

$$
\begin{aligned}
\mathcal{G}(0^-, \mathbf{q})\Big|_{3.8(a)} &= z^3 \int_A \prod_i dt_i \int_{\mathbf{k},\mathbf{p}} G^{(0)}(t_1 + t_2, \mathbf{q}) G^{(1)}(-t_1 - t_2 - t_3, \mathbf{q}) \\
&\quad e^{2\mu t_2} T_2(t_2, \mathbf{k} + \mathbf{p}) e^{3\mu t_3} T_3(t_3, \varepsilon_{\mathbf{q}}, \varepsilon_{\mathbf{q}}, \mathbf{k} + \mathbf{p} + \mathbf{q}, \mathbf{q}, \mathbf{q}) \\
&\quad e^{2\mu t_4} T_2(t_4, \mathbf{k} + \mathbf{p}) G^{(1)}(-t_2 - t_3 - t_4, \mathbf{k}) G^{(1)}(-t_2 - t_3 - t_4, \mathbf{p}) \\
&= z^3 \int_s e^{-\beta s} \int_{\mathbf{k},\mathbf{p}} \frac{T_2^2(s - \varepsilon_{\mathbf{q}}, \mathbf{k} + \mathbf{p}) T_3(s, \varepsilon_{\mathbf{q}}, \varepsilon_{\mathbf{q}}, \mathbf{k} + \mathbf{p} + \mathbf{q}, \mathbf{q}, \mathbf{q})}{(s - \varepsilon_{\mathbf{k}} - \varepsilon_{\mathbf{p}} - \varepsilon_{\mathbf{q}})^2}.
\end{aligned}
\tag{3.78}
$$

For the second equality, we inserted convenient factors of one and used the generalized convolution theorem (C.5) for Laplace transforms. Galilean invariance, cf. eqs. (3.47) and (3.51), implies that the integral can be expressed in terms of the amplitude in the center of mass frame as:

$$
\begin{aligned}
\mathcal{G}(0^-, \mathbf{q})\Big|_{3.8(a)} &= z^3 \int_s e^{-\beta s} \int_{\mathbf{k},\mathbf{p}} \frac{T_2^2\left(s - \varepsilon_{\mathbf{q}} - \frac{\varepsilon_{\mathbf{k}+\mathbf{p}}}{2}\right)}{(s - \varepsilon_{\mathbf{k}} - \varepsilon_{\mathbf{p}} - \varepsilon_{\mathbf{q}})^2} \\
&\quad t_3\left(s - \frac{\varepsilon_{\mathbf{q}+\mathbf{p}+\mathbf{k}}}{3}, \frac{2}{3}\mathbf{q} - \frac{\mathbf{p}}{3} - \frac{\mathbf{k}}{3}, \frac{2}{3}\mathbf{q} - \frac{\mathbf{p}}{3} - \frac{\mathbf{k}}{3}\right)
\end{aligned}
\tag{3.79}
$$

We can reduce the above integral to only two integrations by performing the substitutions

$$
s' = s - \frac{\varepsilon_{\mathbf{q}+\mathbf{p}+\mathbf{k}}}{3}
\tag{3.80}
$$

$$
\begin{pmatrix} \mathbf{p}' \\ \mathbf{k}' \end{pmatrix} = \begin{pmatrix} -\frac{1}{3}\mathbb{1}_3 & -\frac{1}{3}\mathbb{1}_3 \\ -\frac{1}{2}\mathbb{1}_3 & \frac{1}{2}\mathbb{1}_3 \end{pmatrix} \begin{pmatrix} \mathbf{p} - \mathbf{q} \\ \mathbf{k} - \mathbf{q} \end{pmatrix} = \begin{pmatrix} \frac{2}{3}\mathbf{q} - \frac{1}{3}\mathbf{k} - \frac{1}{3}\mathbf{p} \\ \frac{1}{2}\mathbf{k} - \frac{1}{2}\mathbf{p} \end{pmatrix}
\tag{3.81}
$$

The determinant of the transformation contributes a factor $3^3$. Renaming $s' \to s, \mathbf{k}' \to \mathbf{k}, \mathbf{p}' \to \mathbf{p}$, the contribution from diagram 3.8(a) reads

$$
\begin{aligned}
\mathcal{G}(0^-, \mathbf{q})\Big|_{3.8(a)} &= 3^3 z^3 \int_s e^{-\beta s} \int_{\mathbf{k},\mathbf{p}} e^{-3\beta \varepsilon_{\mathbf{q}-\mathbf{p}}} \frac{T_2^2\left(s - \frac{3}{2}\varepsilon_{\mathbf{p}}\right) t_3(s, \mathbf{p}, \mathbf{p})}{(s - \frac{3}{2}\varepsilon_{\mathbf{p}} - 2\varepsilon_{\mathbf{k}})^2} \\
&= \frac{3^2 z^3 m^3}{2q\beta(2\pi)^3} \sum_l (2l+1) \int_s e^{-\beta s} \int_0^\infty dp\, p \frac{T_2^2\left(s - \frac{3p^2}{4m}\right) t_3^{(l)}(s, p, p)}{\sqrt{-ms + \frac{3p^2}{4}}} \\
&\quad e^{-\frac{3\beta}{2m}(q^2 + p^2)} \sinh\left(\frac{3pq\beta}{m}\right)
\end{aligned}
\tag{3.82}
$$

For the last line, we have solved the elementary integral over $\mathbf{k}$ and used that $t_3(s, \mathbf{p}, \mathbf{p}) = \sum_l P_l(\hat{\mathbf{p}} \cdot \hat{\mathbf{p}}) t_3^{(l)}(s, p, p)$ only contains forward scattering, such that all

the Legendre polynomials evaluate to one. Afterwards we have integrated over the angles of **p**.

**Interlude: Cutting off the spectrum**   As you might have noticed, we just trail-blazed ahead and said that we can use the convolution theorem for the Laplace transform in eq. (3.78). But what does the Bromwich contour mean? In principle, the STM equation (3.57) generates infinitely many deep poles that are connected to the presence of the Efimov trimers! To cure this issue, which leads to thermodynamic collapse, we will *choose* one of the bound states branches at unitarity to correspond to the deepest trimer that exists in physical reality. Of course, the deepest to next-to deepest trimer scaling might, because the non-universal influence of short-distance physics provides the cutoff to the spectrum, not have the scaling factor of $22.7^2$. For example, a factor of $\sim 21.0$ is found for the case of $^{133}$Cs [91].

What we are implicitly doing in eq. (3.82) is to define a modified three-body $T$-matrix via subtraction of the deeper lying bound state poles weighted with their residues

$$
\begin{aligned}
\tilde{t}_3^{(0)}(s,p,k) &= t_3^{(0)}(s,p,k) - \sum_{n=-1}^{-\infty} \frac{B_{E_n}^{(0)}(p) B_{E_n}^{(0)}(p)}{s + E_n} \\
\tilde{t}_3^{(0)}(t,p,k) &= t_3^{(0)}(t,p,k) + \sum_{n=-1}^{-\infty} e^{tE_n} B_{E_n}^{(0)}(p) B_{E_n}^{(0)}(p),
\end{aligned}
\tag{3.83}
$$

where $E_n > 0$ defines the bound state energy of the $n$-th Efimov trimer that lies lower than our choice of the deepest branch. This means that in practice, one only includes the infinitely many trimer states above some lowest trimer energy. When connecting to experiment, the scattering length $a_-$ of the deepest trimer branch is matched against the experimentally measured one. Since only the $l = 0$ sector of the three-body $T$-matrix shows the Efimov effect, we have directly regularized this sector. The residues $B^{(0)}(p)$ are the ones defined in eq. (3.56), such that they fulfill the modified STM equation (3.57). To conclude this short interlude: Whenever you see $t_3(s,...)$ in our diagrams, think of $\tilde{t}_3(s,...)$ defined above.

**Diagram 3.8(b)**   We will now proceed with diagram 3.8(b). The game of inserting convenient factors of one, using the convolution theorem, Galilean invariance and some substitutions to solve the integrals will (here and in the following) be same as for diagram 3.8(a). The momentum of the loop that connects to the $T_3$-matrix will be called **k**, the momentum of the loop that connects to the dimer is **p**. We will

suppress the arguments of the $T_3$-matrix in the imaginary time representation here and in the following, these can be inferred from the Bromwich result. We have:

$$
\begin{aligned}
\mathcal{G}(0^-, \mathbf{q})\Big|_{3.8(b)} \ = \ & z^3 \int_A \prod_i dt_i \int_{\mathbf{k}, \mathbf{p}} G^{(0)}(t_1, \mathbf{q}) e^{2\mu t_2} T_2(t_2, \mathbf{q} + \mathbf{p}) e^{3\mu t_3} T_3(t_3, \ldots) \\
& e^{2\mu t_4} T_2(t_4, \mathbf{q} + \mathbf{p}) G^{(1)}(-t_1 - t_2 - t_3 - t_4, \mathbf{q}) G^{(1)}(-t_3, \mathbf{k}) \\
& \qquad\qquad\qquad G^{(1)}(-t_2 - t_3 - t_4, \mathbf{p}) \\
= \ & z^3 \int_s e^{-\beta s} \int_{\mathbf{k}, \mathbf{p}} \frac{T_2^2(s - \varepsilon_{\mathbf{k}}, \mathbf{q} + \mathbf{p}) T_3(s, \varepsilon_{\mathbf{k}}, \varepsilon_{\mathbf{k}}, \mathbf{q} + \mathbf{p} + \mathbf{k}, \mathbf{k}, \mathbf{k})}{(s - \varepsilon_{\mathbf{k}} - \varepsilon_{\mathbf{p}} - \varepsilon_{\mathbf{q}})^2}
\end{aligned}
\tag{3.84}
$$

Expressing this in terms of the center of mass amplitudes and using the substitutions (3.80) for $s$ and

$$
\begin{pmatrix} \mathbf{p}' \\ \mathbf{k}' \end{pmatrix} = \begin{pmatrix} \mathbb{1}_3 & 0 \\ -\frac{1}{3}\mathbb{1}_3 & \frac{2}{3}\mathbb{1}_3 \end{pmatrix} \begin{pmatrix} \mathbf{p} + \mathbf{q} \\ \mathbf{k} \end{pmatrix} = \begin{pmatrix} \mathbf{p} + \mathbf{q} \\ \frac{2}{3}\mathbf{k} - \frac{1}{3}\mathbf{p} - \frac{1}{3}\mathbf{q} \end{pmatrix}
\tag{3.85}
$$

for the momenta, where the determinant of the transformation contributes a factor $(3/2)^3$, the integral can be simplified to

$$
\begin{aligned}
\mathcal{G}(0^-, \mathbf{q})\Big|_{3.8(b)} \ = \ & \frac{3^2 z^3 m}{(2\pi)^4 \beta} \sum_l (2l + 1) \int_s e^{-\beta s} \int_0^\infty dp \int_0^\infty dk\, pk\, t_3^{(l)}(s, k, k) \\
& \frac{\left[ e^{-\frac{3\beta}{8m}(k-p)^2} - e^{-\frac{3\beta}{8m}(p+k)^2} \right] T_2^2 \left( s - \frac{3}{4m} k^2 \right)}{\left[ \frac{3k^2}{4m} + \frac{(p-2q)^2}{4m} - s \right] \left[ \frac{3k^2}{4m} + \frac{(p+2q)^2}{4m} - s \right]},
\end{aligned}
\tag{3.86}
$$

where we again used the fact that for forward scattering, the Legendre polynomials in the angular decomposition of $t_3(s, \mathbf{k}, \mathbf{k})$ all evaluate to one.

**Diagram 3.8(c)**   The loop momentum for the loop that is connected with the two $T_2$-matrices is labeled $\mathbf{p}$, while the other loop shall be $\mathbf{k}$. With these definitions, diagram 3.8(c) reads

$$
\begin{aligned}
\mathcal{G}(0^-, \mathbf{q})\Big|_{3.8(c)} \ = \ & z^3 \int_A \prod_i dt_i \int_{\mathbf{k}, \mathbf{p}} G^{(0)}(t_1 + t_2, \mathbf{q}) e^{2\mu t_2} T_2(t_2, \mathbf{k} + \mathbf{p}) e^{3\mu t_3} T_3(t_3, \ldots) \\
& e^{2\mu t_4} T_2(t_4, \mathbf{q} + \mathbf{p}) G^{(1)}(-t_1 - t_2 - t_3 - t_4, \mathbf{q}) G^{(1)}(-t_2 - t_3, \mathbf{k}) \\
& \qquad\qquad\qquad G^{(1)}(-t_2 - t_3 - t_4, \mathbf{p}) \\
= \ & z^3 \int_s e^{-\beta s} \int_{\mathbf{k}, \mathbf{p}} \frac{T_2(s - \varepsilon_{\mathbf{q}}, \mathbf{k} + \mathbf{p}) T_2(s - \varepsilon_{\mathbf{k}}, \mathbf{q} + \mathbf{p})}{(s - \varepsilon_{\mathbf{k}} - \varepsilon_{\mathbf{p}} - \varepsilon_{\mathbf{q}})^2} \\
& \qquad\qquad T_3(s, \varepsilon_{\mathbf{q}}, \varepsilon_{\mathbf{k}}, \mathbf{q} + \mathbf{p} + \mathbf{k}, \mathbf{q}, \mathbf{k}).
\end{aligned}
\tag{3.87}
$$

Expressing the amplitudes via their respective center of mass versions, together with the usual $s$-substitution (3.80) and the substitution

$$
\begin{pmatrix} \mathbf{p}' \\ \mathbf{k}' \end{pmatrix} = \begin{pmatrix} -\frac{1}{3}\mathbb{1}_3 & -\frac{1}{3}\mathbb{1}_3 \\ -\frac{1}{3}\mathbb{1}_3 & \frac{2}{3}\mathbb{1}_3 \end{pmatrix} \begin{pmatrix} \mathbf{p} - \mathbf{q} \\ \mathbf{k} - \mathbf{q} \end{pmatrix} = \begin{pmatrix} \frac{2}{3}\mathbf{q} - \frac{1}{3}\mathbf{k} - \frac{1}{3}\mathbf{p} \\ \frac{2}{3}\mathbf{k} - \frac{1}{3}\mathbf{p} - \frac{1}{3}\mathbf{q} \end{pmatrix} \tag{3.88}
$$

for the momenta, such that the determinant contributes a factor $3^3$, yields

$$
\begin{aligned}
\mathcal{G}(0^-, \mathbf{q})\Big|_{3.8(c)} &= 3^3 z^3 \int_s e^{-\beta s} \int_{\mathbf{k},\mathbf{p}} e^{-3\beta \varepsilon_{\mathbf{q}-\mathbf{p}}} \frac{T_2(s - \frac{3}{2}\varepsilon_{\mathbf{k}})T_2(s - \frac{3}{2}\varepsilon_{\mathbf{p}})}{(s - 2\varepsilon_{\mathbf{k}} - 2\varepsilon_{\mathbf{p}} - \frac{\mathbf{k}\cdot\mathbf{p}}{m})^2} t_3(s, \mathbf{p}, \mathbf{k}) \\
&= \frac{2m^3}{\beta q} \frac{3^2 z^3}{(2\pi)^4} \sum_l (2l+1) \int_s e^{-\beta s} \int_0^\infty \frac{dp}{p} \int_0^\infty dk\, T_2\left(s - \frac{3}{4m}k^2\right) \\
&\qquad T_2\left(s - \frac{3}{4m}p^2\right)\left[e^{-\frac{3\beta}{2m}(p-q)^2} - e^{-\frac{3\beta}{2m}(p+q)^2}\right] \\
&\qquad \tilde{Q}_l\left(\frac{m}{pk}\left[s - \frac{p^2}{m} - \frac{k^2}{m}\right]\right) t_3^{(l)}(s, p, k). \tag{3.89}
\end{aligned}
$$

For the second equality, we have used the angular momentum decomposition (3.52) of the $t_3$-matrix, set the $z$-axis for the $\mathbf{k}$ integration to be $\hat{\mathbf{p}}$, and then defined $\tilde{Q}_l(z) = -dQ_l(z)/dz$, which, as follows from the definition of the Legendre functions of the second kind in (3.55), is the solution to the angle integration of the $\mathbf{k}$-part. For the angle integration associated with $\mathbf{p}$, we just have taken $\hat{\mathbf{q}}$ as $z$-axis, which makes this angular integration straightforward to solve and yields the usual exponentials.

**Diagram 3.8(d)**  The loop momentum connecting the two $T_2$-matrices is again labeled $\mathbf{p}$, the other one $\mathbf{k}$. We get

$$
\begin{aligned}
\mathcal{G}(0^-, \mathbf{q})\Big|_{3.8(d)} &= z^3 \int_A \prod_i dt_i \int_{\mathbf{k},\mathbf{p}} G^{(0)}(t_1, \mathbf{q}) e^{2\mu t_2} T_2(t_2, \mathbf{q} + \mathbf{p}) T_3(t_3, \ldots) e^{3\mu t_3} \\
&\qquad e^{2\mu t_4} T_2(t_4, \mathbf{k} + \mathbf{p}) G^{(1)}(-t_1 - t_2 - t_3, \mathbf{q}) G^{(1)}(-t_3 - t_4, \mathbf{k}) \\
&\qquad\qquad G^{(1)}(-t_2 - t_3 - t_4, \mathbf{p}) \\
&= z^3 \int_s e^{-\beta s} \int_{\mathbf{k},\mathbf{p}} \frac{T_2(s - \varepsilon_{\mathbf{q}}, \mathbf{k} + \mathbf{p}) T_2(s - \varepsilon_{\mathbf{k}}, \mathbf{q} + \mathbf{p})}{(s - \varepsilon_{\mathbf{k}} - \varepsilon_{\mathbf{p}} - \varepsilon_{\mathbf{q}})^2} \\
&\qquad\qquad T_3(s, \varepsilon_{\mathbf{k}}, \varepsilon_{\mathbf{q}}, \mathbf{k} + \mathbf{p} + \mathbf{q}, \mathbf{k}, \mathbf{q}) \tag{3.90}
\end{aligned}
$$

Comparing this to the expression for diagram 3.8(c), given in eq. (3.87), we see that the two diagrams are almost equal, with the exception that the momenta $\mathbf{q}$ and $\mathbf{k}$ are interchanged in the $T_3$-matrix. This is of course already suggested by the

similarity of the two diagrams. Thus, using the exact same substitutions like for diagram 3.8(c), we can once again eliminate all angle integrations:

$$
\mathcal{G}(0^-, \mathbf{q})\Big|_{3.8(d)} = \frac{2m^3}{\beta q} \frac{3^2 z^3}{(2\pi)^4} \sum_l (2l+1) \int_s e^{-\beta s} \int_0^\infty \frac{dp}{p} \int_0^\infty dk\, T_2\left(s - \frac{3}{4m}k^2\right)
$$
$$
T_2\left(s - \frac{3}{4m}p^2\right)\left[e^{-\frac{3\beta}{2m}(p-q)^2} - e^{-\frac{3\beta}{2m}(p+q)^2}\right]
$$
$$
\tilde{Q}_l\left(\frac{m}{pk}\left[s - \frac{p^2}{m} - \frac{k^2}{m}\right]\right) t_3^{(l)}(s, k, p). \quad (3.91)
$$

**Diagram 3.8(e)** For the last diagram, I was not able to eliminate all the angle integrations, which makes this diagram the by far most expensive one during numerical evaluation. We label the loop momentum that is connected to first $T_2$-vertex $\mathbf{p}$, and the one that leaves the second $T_2$-vertex $\mathbf{k}$. We get the following expression:

$$
\mathcal{G}(0^-, \mathbf{q})\Big|_{3.8(e)} = z^3 \int_A \prod_i dt_i \int_{\mathbf{k}, \mathbf{p}} G^{(0)}(t_1, \mathbf{q}) e^{2\mu t_2} T_2(t_2, \mathbf{q} + \mathbf{p}) T_3(t_3, ...) e^{3\mu t_3}
$$
$$
e^{2\mu t_4} T_2(t_4, \mathbf{k} + \mathbf{q}) G^{(1)}(-t_1 - t_2 - t_3 - t_4, \mathbf{q}) G^{(1)}(-t_3 - t_4, \mathbf{k})
$$
$$
G^{(1)}(-t_2 - t_3, \mathbf{p})
$$
$$
= z^3 \int_s e^{-\beta s} \int_{\mathbf{k}, \mathbf{p}} \frac{T_2(s - \varepsilon_{\mathbf{p}}, \mathbf{k} + \mathbf{q}) T_2(s - \varepsilon_{\mathbf{k}}, \mathbf{q} + \mathbf{p})}{(s - \varepsilon_{\mathbf{k}} - \varepsilon_{\mathbf{p}} - \varepsilon_{\mathbf{q}})^2}
$$
$$
T_3(s, \varepsilon_{\mathbf{k}}, \varepsilon_{\mathbf{p}}, \mathbf{k} + \mathbf{p} + \mathbf{q}, \mathbf{k}, \mathbf{p}) \quad (3.92)
$$

We now express the integral, using eqs. (3.47) and (3.51), in terms of the center of mass amplitudes. Afterwards, we make the substitution (3.80) for the $s$-integration and

$$
\begin{pmatrix} \mathbf{p}' \\ \mathbf{k}' \end{pmatrix} = \begin{pmatrix} \frac{2}{3}\mathbb{1}_3 & -\frac{1}{3}\mathbb{1}_3 \\ -\frac{1}{3}\mathbb{1}_3 & \frac{2}{3}\mathbb{1}_3 \end{pmatrix} \begin{pmatrix} \mathbf{p} - \mathbf{q} \\ \mathbf{k} - \mathbf{q} \end{pmatrix} = \begin{pmatrix} \frac{2}{3}\mathbf{p} - \frac{1}{3}\mathbf{k} - \frac{1}{3}\mathbf{q} \\ \frac{2}{3}\mathbf{k} - \frac{1}{3}\mathbf{p} - \frac{1}{3}\mathbf{q} \end{pmatrix} \quad (3.93)
$$

for the momentum integrations, which yields a factor $3^3$. The resulting expression reads

$$
\mathcal{G}(0^-, \mathbf{q})\Big|_{3.8(e)} = 3^3 z^3 \int_s e^{-\beta s} \int_{\mathbf{k}, \mathbf{p}} e^{-3\beta \varepsilon_{\mathbf{q}+\mathbf{p}+\mathbf{k}}} \frac{T_2(s - \frac{3}{2}\varepsilon_{\mathbf{k}}) T_2(s - \frac{3}{2}\varepsilon_{\mathbf{p}})}{(s - 2\varepsilon_{\mathbf{k}} - 2\varepsilon_{\mathbf{p}} - \frac{\mathbf{k} \cdot \mathbf{p}}{m})^2} t_3(s, \mathbf{k}, \mathbf{p}),
$$
$$
(3.94)
$$

which depends on all three possible angle combinations $\hat{\mathbf{q}} \cdot \hat{\mathbf{k}}, \hat{\mathbf{q}} \cdot \hat{\mathbf{p}}, \hat{\mathbf{k}} \cdot \hat{\mathbf{p}}$. We are now going to employ a trick to get rid of one angle integration. Since our diagrams

never depend on the direction of $\mathbf{q}$, we have:

$$n(\mathbf{q}) = n(|\mathbf{q}|) \quad \Rightarrow \quad n(\mathbf{q}) = \frac{1}{4\pi} \int d\Omega_q n(\mathbf{q}),$$

where $\int d\Omega_q$ means the integration over all directions $\hat{\mathbf{q}}$ on the surface $S^2$ of the unit sphere. Hence, we can rewrite the integral as

$$
\begin{aligned}
\left. \mathcal{G}(0^-, \mathbf{q}) \right|_{3.8(e)} =\; & \frac{3^3 z^3}{(2\pi)^6 4\pi} \int \frac{ds}{2\pi i} e^{-\beta s} \int_0^\infty dk\, k^2 \int_0^\infty dp\, p^2 e^{-\frac{3\beta}{2m}(k^2+p^2+q^2)} \\
& T_2\!\left(s - \frac{3}{4m}k^2\right) T_2\!\left(s - \frac{3}{4m}p^2\right) \sum_l (2l+1) t_3^{(l)}(s,k,p) \\
& \int d\Omega_q \int d\Omega_k \int d\Omega_p\, e^{-\frac{3\beta}{m}(\mathbf{k}\cdot\mathbf{p}+\mathbf{k}\cdot\mathbf{q}+\mathbf{p}\cdot\mathbf{q})} \frac{P_l(\hat{\mathbf{k}}\cdot\hat{\mathbf{p}})}{(s - \frac{k^2}{m} - \frac{p^2}{m} - \frac{\mathbf{k}\cdot\mathbf{p}}{m})^2}.
\end{aligned}
$$

$$(3.95)$$

We first integrate over the direction of $\hat{\mathbf{q}}$, which only appears in the exponential. We choose $\mathbf{k}+\mathbf{p}$ as the $z-$axis for this angular integration so that $\cos\theta_q = \mathbf{q}\cdot(\mathbf{k}+\mathbf{p})/|\mathbf{q}||\mathbf{k}+\mathbf{p}|$. The $\mathbf{q}$-integration now just yields an hyperbolic sine:

$$
\begin{aligned}
\int d\Omega_q e^{-\frac{3\beta}{m}\mathbf{q}\cdot(\mathbf{k}+\mathbf{p})} =\; & 2\pi \int_{-1}^1 d\cos\theta_q\, e^{-\frac{3\beta}{m} q |\mathbf{k}+\mathbf{p}| \cos\theta_q} \\
=\; & \frac{4\pi m}{3\beta q} \frac{\sinh\!\left(\frac{3\beta q}{m} \sqrt{k^2+p^2+2\mathbf{p}\cdot\mathbf{k}}\right)}{\sqrt{k^2+p^2+2\mathbf{p}\cdot\mathbf{k}}}.
\end{aligned}
$$

$$(3.96)$$

The rest of the integral in equation (3.95) now only depends on one angle. We integrate over all angles but this one, which yields

$$
\begin{aligned}
\left. \mathcal{G}(0^-, \mathbf{q}) \right|_{3.8(e)} =\; & \frac{3^3 z^3}{(2\pi)^4} \frac{2m}{3\beta q} \int \frac{ds}{2\pi i} e^{-\beta s} \int_0^\infty dk\, k^2 \int_0^\infty dp\, p^2 \int_{-1}^1 d\cos\theta \\
& e^{-\frac{3\beta}{2m}(k^2+p^2+q^2)} T_2\!\left(s - \frac{3}{4m}k^2\right) T_2\!\left(s - \frac{3}{4m}p^2\right) \sum_l (2l+1) t_3^{(l)}(s,k,p) \\
& \frac{P_l(\cos\theta) e^{-\frac{3\beta}{m} kp\cos\theta}}{(s - \frac{k^2}{m} - \frac{p^2}{m} - \frac{kp}{m}\cos\theta)^2} \frac{\sinh\!\left(\frac{3\beta q}{m}\sqrt{k^2+p^2+2pk\cos\theta}\right)}{\sqrt{k^2+p^2+2pk\cos\theta}}.
\end{aligned}
$$

$$(3.97)$$

This concludes our discussion of the diagrams that contribute to the cluster expansion of the momentum distribution up to third order in the fugacity. Fear not. With the work we invested here, the density and all fermionic diagrams now come almost for free.

**Density**

The density expansion can be obtained from the expansion of the momentum distribution by integration over all momenta. We have already presented the results for the one-particle diagrams in sec. 3.3.1. We will therefore directly start with the two-particle sector.

**Two-particle diagrams**  It will prove useful to not directly integrate the final results for the momentum distribution over all momenta, but rather take an intermediate result where the integrals are straightforward to solve.

**Diagram 3.7(a)**  Integrating the expression (3.67) for diagram 3.7(a) over all momenta, we have:

$$\mathcal{G}(0^-, \mathbf{0})\Big|_{3.7(a)} = z^2 \int_s e^{-\beta s} \int_{\mathbf{q}} \int_{\mathbf{k}} \frac{T_2(s - \varepsilon_{\mathbf{k}+\mathbf{q}}/2)}{(s - \varepsilon_{\mathbf{k}} - \varepsilon_{\mathbf{q}})^2} \tag{3.98}$$

where the $T_2$ matrix is now expressed in the center of mass frame. Via the substitutions

$$s' = s - \frac{\varepsilon_{\mathbf{k}+\mathbf{q}}}{2} \tag{3.99}$$

$$\begin{pmatrix} \mathbf{k}' \\ \mathbf{q}' \end{pmatrix} = \begin{pmatrix} \mathbb{1}_3 & -\mathbb{1}_3 \\ \mathbb{1}_3 & \mathbb{1}_3 \end{pmatrix} \begin{pmatrix} \mathbf{k} \\ \mathbf{q} \end{pmatrix} = \begin{pmatrix} \mathbf{k} - \mathbf{q} \\ \mathbf{k} + \mathbf{q} \end{pmatrix} \tag{3.100}$$

and renaming to the original names afterwards, we can decouple the momentum integrations:

$$\mathcal{G}(0^-, \mathbf{0})\Big|_{3.7(a)} = \frac{z^2}{2^3} \int_s e^{-\beta s} T_2(s) \int_{\mathbf{q}} \int_{\mathbf{k}} \frac{e^{-\beta \frac{\mathbf{q}^2}{4m}}}{(s - \frac{\mathbf{k}^2}{4m})^2}$$

$$= \frac{2z^2}{\lambda_T^3} \underbrace{\frac{m^2}{4\pi\sqrt{2}} \int_s e^{-\beta s} \frac{T_2(s)}{\sqrt{-ms}}}_{=-\Delta b_2 = -(b_2 - b_2^{(0)})} = -z^2 n_2^{(2p)} \tag{3.101}$$

By comparison of the density expansion (see table 3.1) which defines the virial coefficients, we have identified the interaction correction $\Delta b_2$ to the second virial coefficient. Indeed, when we deform the Bromwich contour in the way that is shown in fig. 3.10, such that the contour has a possible contribution from the dimer pole at $a > 0$ and two contours that run infinitesimally close above and below the real axis (with the branchcut of the two-body $T$-matrix in between), we reproduce the

(a) Undeformed Bromwich contour

(b) Deformed Bromwich contour
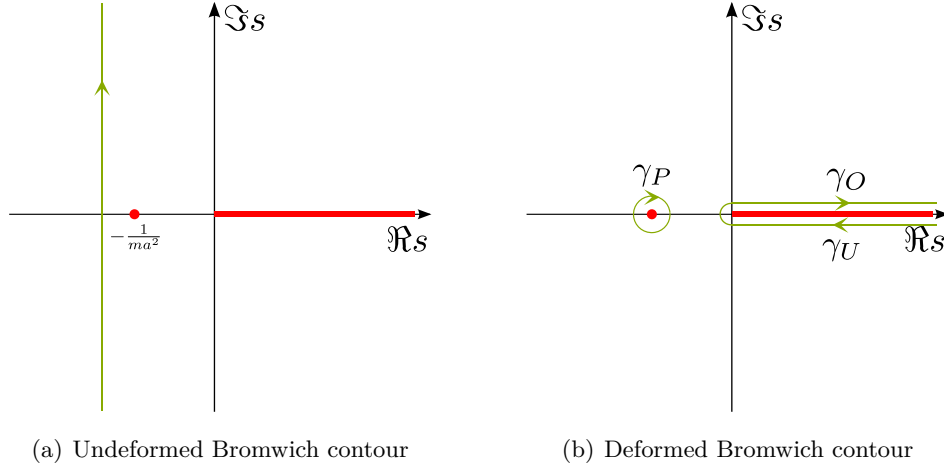
Figure 3.10: Derivation of the Beth-Uhlenbeck result for $\Delta b_2$ via deformation of the Bromwich contour. Red color corresponds to branch cuts or poles (when $a > 0$) of the integrand, green color to the contour of integration. The deformed result can be written in terms of three contours $\gamma_P$, $\gamma_U$, $\gamma_O$. $\gamma_P$ gives the residue at the pole, $\gamma_U$ and $\gamma_O$ give the discontinuity of $T_2(s)/\sqrt{-ms}$ at the branch cut.

well-known Beth-Uhlenbeck result [73] for $\Delta b_2$. To see this, we just use the residue theorem for the contour $\gamma_P$ (which contributes the negative residue because of the winding number). In addition, we parametrize ($k > 0$, $\epsilon > 0$) the other two contours as

$$\gamma_O(k) = \frac{k^2}{m} + i\epsilon \tag{3.102}$$

$$\gamma_U(k) = \frac{k^2}{m} - i\epsilon \tag{3.103}$$

$$\dot{\gamma}_O(k) = \dot{\gamma}_U(k) = \frac{2k}{m}, \tag{3.104}$$

such that $\int_{\gamma_O} .. - \int_{\gamma_U} ..$ is the contribution we need to calculate. Insertion of the above parametrization and evaluating the square roots and the residue yields

$$\Delta b_2 = 2^{3/2}\left[\Theta(a)e^{\frac{\beta}{ma^2}} + \frac{1}{\pi}\int_0^\infty dk e^{-\beta\frac{k^2}{m}} \underbrace{\frac{-a}{1+a^2k^2}}_{=\frac{\partial\delta_0}{\partial k}}\right], \tag{3.105}$$

where the $s$-wave phase shift is obtained from $\cot \delta_0(k) = -1/ka$. This is indeed the result found by Beth and Uhlenbeck [73, 117].

**Diagrams 3.7(b)-3.7(d)**  All two-particle diagrams to order $z^3$ turn out to give the same contribution to the density. Starting from equation (3.67) and multiplying the integrand by $ze^{-\beta\varepsilon_\mathbf{q}}$ to get the expression for diagram 3.7(b), we have:

$$\mathcal{G}(0^-, \mathbf{0})\bigg|_{3.7(b)} = z^3 \int_s e^{-\beta s} \int_\mathbf{q} \int_\mathbf{k} e^{-\beta\varepsilon_\mathbf{q}} \frac{T_2(s - \varepsilon_{\mathbf{k+q}}/2)}{(s - \varepsilon_\mathbf{k} - \varepsilon_\mathbf{q})^2} \tag{3.106}$$

We eliminate the dependence on the angle via the substitutions (3.99) for $s$ and

$$\begin{pmatrix} \mathbf{k}' \\ \mathbf{q}' \end{pmatrix} = \begin{pmatrix} \frac{1}{2}\mathbb{1}_3 & -\frac{1}{2}\mathbb{1}_3 \\ \frac{1}{3}\mathbb{1}_3 & \frac{2}{3}\mathbb{1}_3 \end{pmatrix} \begin{pmatrix} \mathbf{k} \\ \mathbf{q} \end{pmatrix} = \begin{pmatrix} \frac{1}{2}\mathbf{k} - \frac{1}{2}\mathbf{q} \\ \frac{1}{3}\mathbf{k} + \frac{2}{3}\mathbf{q} \end{pmatrix} \tag{3.107}$$

for the momenta. The determinant of the substitution contributes a factor $2^3$. The $\mathbf{q}$-integration is now a Gaussian integral without angle dependence and can be performed as well. The result is:

$$\mathcal{G}(0^-, \mathbf{0})\bigg|_{3.7(b)} = \frac{z^3}{\lambda_T^3} \frac{2^3}{3^{\frac{3}{2}}} \int_s e^{-\beta s} T_2(s) \int_0^\infty \frac{dk\, k^2}{2\pi^2} \frac{e^{-\frac{\beta}{3m}k^2}}{(s - \frac{k^2}{m})^2} \tag{3.108}$$

Diagram 3.7(d) trivially yields the same contribution, because diagrams 3.7(b) and 3.7(d) also have the same contribution to the momentum distribution, cf. eqs. (3.73), (3.73).

Integrating (3.74) for diagram 3.7(c) over all momenta $\mathbf{q}$ yields

$$\mathcal{G}(0^-, \mathbf{0})\bigg|_{3.7(c)} = z^3 \int_s e^{-\beta s} \int_\mathbf{q} \int_\mathbf{k} e^{-\beta\varepsilon_\mathbf{k}} \frac{T_2(s - \varepsilon_{\mathbf{k+q}}/2)}{(s - \varepsilon_\mathbf{k} - \varepsilon_\mathbf{q})^2}, \tag{3.109}$$

which is just the same as (see eq. (3.106)) the expression for diagram 3.7(b) with $\mathbf{k}$ and $\mathbf{q}$ interchanged. Therefore, all three diagrams contribute equally to the third order in the density, and we have:

$$n_3^{(2p)} = -\frac{3}{z^3} \mathcal{G}(0^-, \mathbf{0})\bigg|_{3.7(b)}, \tag{3.110}$$

with $\mathcal{G}(0^-, \mathbf{0})\bigg|_{3.7(b)}$ given by eq. (3.108).

**Three-particle diagrams**  The three-body sector will turn out to only have two independent contributions to the density at order $z^3$.

**Diagrams 3.8(a) and 3.8(b)** Starting from the first line of eq. (3.82), we make, since we are now integrating over all $\mathbf{q}$, the substitution $\mathbf{q}' = \mathbf{q} - \mathbf{p}$ and rename $\mathbf{q}' \to \mathbf{q}$ afterwards, which yields

$$
\mathcal{G}(0^-, \mathbf{0})\Big|_{3.8(a)} = \quad 3^3 z^3 \int_s e^{-\beta s} \int_{\mathbf{q},\mathbf{k},\mathbf{p}} e^{-3\beta \varepsilon_{\mathbf{q}}} \frac{T_2^2(s - \frac{3}{2}\varepsilon_{\mathbf{p}})}{(s - \frac{3}{2}\varepsilon_{\mathbf{p}} - 2\varepsilon_{\mathbf{k}})^2} t_3(s, \mathbf{p}, \mathbf{p}) \quad (3.111)
$$

$$
= \quad \frac{3^{\frac{3}{2}} z^3}{\lambda_T^3} \int_s e^{-\beta s} \int_{\mathbf{k},\mathbf{p}} \frac{T_2^2(s - \frac{3}{2}\varepsilon_{\mathbf{p}})}{(s - \frac{3}{2}\varepsilon_{\mathbf{p}} - 2\varepsilon_{\mathbf{k}})^2} t_3(s, \mathbf{p}, \mathbf{p})
$$

$$
= \quad \frac{3^{\frac{3}{2}} z^3}{\lambda_T^3} \frac{m^2}{8\pi} \int_s e^{-\beta s} \int_0^\infty \frac{dp\, p^2}{2\pi^2} \frac{\left[T_2(s - \frac{3}{4m}p^2)\right]^2}{\sqrt{-ms + \frac{3}{4}p^2}}
$$

$$
\sum_l (2l + 1) t_3^{(l)}(s, p, p), \quad (3.112)
$$

where we have again used $P_l(0) = 1$ for the forward scattering in $t_3(s, \mathbf{p}, \mathbf{p})$. For diagram 3.8(b), we just compare the two equations (3.78) and (3.84) for the contributions of diagram 3.8(a) and 3.8(b). After integration over all $\mathbf{q}$, they differ only by the name of the integration variables. It follows that diagram 3.8(b) gives the same contribution to the density as diagram 3.8(a).

**Diagrams 3.8(c) - 3.8(e)** For the contribution of diagram 3.8(c), we integrate the first line of eq. (3.89) over all $\mathbf{q}$ and make the substitution $\mathbf{q}' = \mathbf{q} - \mathbf{p}$, which yields, after renaming $\mathbf{q}' \to \mathbf{q}$:

$$
\mathcal{G}(0^-, \mathbf{0})\Big|_{3.8(c)} = 3^3 z^3 \int_s e^{-\beta s} \int_{\mathbf{q},\mathbf{k},\mathbf{p}} e^{-3\beta \varepsilon_{\mathbf{q}}} \frac{T_2(s - \frac{3}{2}\varepsilon_{\mathbf{k}}) T_2(s - \frac{3}{2}\varepsilon_{\mathbf{p}})}{(s - 2\varepsilon_{\mathbf{k}} - 2\varepsilon_{\mathbf{p}} - \frac{\mathbf{k}\cdot\mathbf{p}}{m})^2} t_3(s, \mathbf{p}, \mathbf{k}) \quad (3.113)
$$

$$
= \frac{3^{\frac{3}{2}} z^3}{\lambda_T^3} \int_s e^{-\beta s} \int_0^\infty \frac{dk}{2\pi^2} k^2 \int_0^\infty \frac{dp}{2\pi^2} p^2 T_2\Big(s - \frac{3k^2}{4m}\Big) T_2\Big(s - \frac{3p^2}{4m}\Big)
$$

$$
\frac{1}{2} \int_{-1}^1 d\cos\theta_k \frac{\sum_l (2l + 1) P_l(\cos\theta_k) t_3^{(l)}(s, p, k)}{(s - \frac{k^2}{m} - \frac{p^2}{m} - \frac{kp}{m}\cos\theta_k)^2}
$$

$$
= \frac{3^{\frac{3}{2}} z^3 m^2}{\lambda_T^3} \int_s e^{-\beta s} \int_0^\infty \frac{dk}{2\pi^2} \int_0^\infty \frac{dp}{2\pi^2} T_2\Big(s - \frac{3k^2}{4m}\Big) T_2\Big(s - \frac{3p^2}{4m}\Big)
$$

$$
\sum_l (2l + 1) \tilde{Q}_l\Big(\frac{m}{pk}\Big(s - \frac{p^2}{m} - \frac{k^2}{m}\Big)\Big) t_3^{(l)}(s, p, k), \quad (3.114)
$$

For the third equality, we have again used the shorthand $\tilde{Q}_l(z) = -dQ_l(z)/dz$ together with the representation (3.55) of the Legendre functions of the second kind.

By comparison of eqs. (3.87) and (3.90) (the contributions of diagrams 3.8(c) and 3.8(d) before substitutions) we see that they are the same but with $\mathbf{q}$ and $\mathbf{k}$ interchanged in the $T_3$-matrix. We can thus, using all the substitutions we used for diagram 3.8(c), bring 3.8(d) into the form (3.113) with $\mathbf{p}$ and $\mathbf{k}$ interchanged. The contribution of diagram 3.8(d) to the density is hence given by (3.114).

For diagram 3.8(e), we start from eq. (3.94) and make the substitution $\mathbf{q}' = \mathbf{q} + \mathbf{k} + \mathbf{p}$, which, after renaming, yields

$$\mathcal{G}(0^-, \mathbf{0})\Big|_{3.8(e)} = 3^3 z^3 \int_s e^{-\beta s} \int_{\mathbf{q},\mathbf{k},\mathbf{p}} e^{-3\beta\varepsilon_{\mathbf{q}}} \frac{T_2(s - \frac{3}{2}\varepsilon_{\mathbf{k}})T_2(s - \frac{3}{2}\varepsilon_{\mathbf{p}})}{(s - 2\varepsilon_{\mathbf{k}} - 2\varepsilon_{\mathbf{p}} - \frac{\mathbf{k}\cdot\mathbf{p}}{m})^2} t_3(s, \mathbf{k}, \mathbf{p}), \quad (3.115)$$

which is just (3.113) with $\mathbf{p}$ and $\mathbf{k}$ interchanged. Hence, also diagram 3.8(e) contributes the same to the density like diagram 3.8(c).

In summary, the three-particle contributions to the density are given by

$$n_3^{(3p)} = -\frac{1}{z^3}\left[\frac{3}{2}\mathcal{G}(0^-, \mathbf{0})\Big|_{3.8(a)} + 3\mathcal{G}(0^-, \mathbf{0})\Big|_{3.8(c)}\right], \quad (3.116)$$

where the contribution 3.8(a) is given by eq. (3.112) and the contribution 3.8(c) by eq. (3.114). We have thus established the virial expansion of the density of a bosonic gas up to third order in the fugacity. As you might have noticed, our derivation did not really depend on the details of $T_2$ and $t_3$. This is why the calculations here could be easily extended to cases that include, for example, effective range corrections in the two-body sector. In fact, since we never really specified the definitions of $T_2$ and $T_3$, all we need is Galilean invariance and a three-body $T$-matrix that, in the center of mass frame, depends on one angle.

### 3.3.2 Fermions

With the exception of the signs of the diagrams, which are calculated in appendix E, the virial expansion of both the momentum distribution and the density of the contact-interacting Fermi system comes for free. The only thing that changes is that we need to use the definitions (3.58) and (3.59) of the fermionic $T_2$ and $t_3$ matrices. We will establish the virial expansion for $n_\uparrow(\mathbf{q}) = n(\mathbf{q})/2$ (population balanced system) and draw the diagrams for $n_\uparrow(\mathbf{q})$, and likewise for the density. Note that due to the anti-commuting nature of the fermions, we now have

$$n_\uparrow(\mathbf{q}) = \lim_{\tau \to 0^-} \mathcal{G}_\uparrow(\tau, \mathbf{q}) = \lim_{\tau \to 0^-} \langle T_\tau \bar{\psi}(0, \mathbf{q})\psi(\tau, \mathbf{q})\rangle. \quad (3.117)$$

As was the case for bosons, cf. eq. (3.63), we decompose the cluster expansion of the fermionic momentum distribution like

$$
\begin{aligned}
n_\uparrow(\mathbf{q}) \;=\;& z n_{\uparrow,1}^{(1p)}(\mathbf{q}) + z^2 \left[ n_{\uparrow,2}^{(1p)}(\mathbf{q}) + n_{\uparrow,2}^{(2p)}(\mathbf{q}) \right] \\
&+ z^3 \left[ n_{\uparrow,3}^{(1p)}(\mathbf{q}) + n_{\uparrow,3}^{(2p)}(\mathbf{q}) + n_{\uparrow,3}^{(3p)}(\mathbf{q}) \right] + \mathcal{O}(z^4),
\end{aligned}
\tag{3.118}
$$

where the same suggestive naming scheme applies. Since the density can be obtained from the momentum distribution by integration over all momenta, the same decomposition holds for the density.

**Momentum distribution**

For the fermionic system, there are only very slight diagrammatic changes. The external line now is always an ↑-fermion. The dimer line always needs a particle of each spin-species at each vertex.

**One-particle diagrams**   Up to order $z^3$, the one particle diagrams are given by figs. 3.6(a)-3.6(c). More generally, we have for the contribution $n_{\uparrow,\ell}^{(1p)}(\mathbf{q})$:

$$
n_{\uparrow,\ell}^{(1p)}(\mathbf{q}) \;=\; \lim_{\tau \to 0^-} G^{(\ell)}(\tau,\mathbf{q}) \overset{(3.43)}{=} (-1)^{\ell-1} e^{-\ell\beta\varepsilon_\mathbf{q}}
\tag{3.119}
$$

In complete analogy to the bosonic case, when integrated over all $\mathbf{q}$, this yields $b_\ell^{(0)} = (-1)^{\ell-1}/\ell^{5/2}$ for the virial coefficients (set $2n_\uparrow = n$, and compare to table 3.1) of the non-interacting Fermi gas.

**Two-particle diagrams**   The two-particle diagrams are given by diagrams 3.7(a)-3.7(d), where the loop carries a ↓-fermion. The calculation of the signs in appendix yields

$$
\left. \mathcal{G}_\uparrow(0^-,\mathbf{q}) \right|_{3.7(a)} \;=\; -(3.70) = z^2 n_{\uparrow,2}^{(2p)}(\mathbf{q})
\tag{3.120}
$$

$$
\left. \mathcal{G}_\uparrow(0^-,\mathbf{q}) \right|_{3.7(b)} \;=\; (3.72) = \left. \mathcal{G}_\uparrow(0^-,\mathbf{q}) \right|_{3.7(d)}
\tag{3.121}
$$

$$
\left. \mathcal{G}_\uparrow(0^-,\mathbf{q}) \right|_{3.7(c)} \;=\; (3.75)
\tag{3.122}
$$

where the equation numbers refer to the expressions that we would obtain in the bosonic case. Of course, we have to perform the replacement $T_{2,\text{Bose}} \to T_{2,\text{Fermi}}$ in these formulas. For the contribution $n_{\uparrow,3}^{(2p)}(\mathbf{q})$, just sum over the three Green's functions of diagrams 3.7(b)-3.7(d) above.

(a) $\mathcal{O}(z^3)$      (b) $\mathcal{O}(z^3)$      (c) $\mathcal{O}(z^3)$

(d) $\mathcal{O}(z^3)$      (e) $\mathcal{O}(z^3)$      (f) $\mathcal{O}(z^3)$
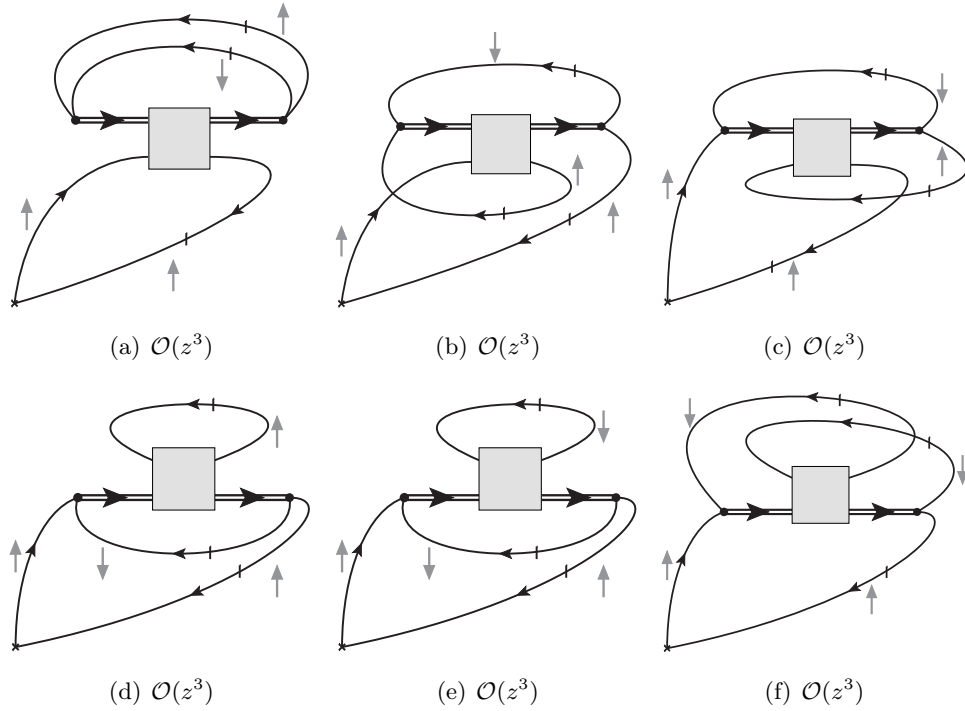
Figure 3.11: Diagrams from the three-particle sector that contribute to the virial expansion of the momentum distribution and density of the fermionic system up to order $z^3$. The gray box is the three-body $T$-matrix. We have ordered the diagrams so that they correspond to the labeling of Leyronas [9].

**Three-particle diagrams** The three-body sector contains six diagrams in the fermionic case, which we show in fig. 3.11. With the signs that we obtain from the calculation in appendix E, we get:

$$
\begin{aligned}
n_{\uparrow,3}^{(3p)}(\mathbf{q}) = \quad & \frac{1}{z^3}\Bigg[ -\mathcal{G}(0^-,\mathbf{q})\Big|_{3.8(a)} + \mathcal{G}(0^-,\mathbf{q})\Big|_{3.8(c)} + \mathcal{G}(0^-,\mathbf{q})\Big|_{3.8(d)} \\
& -\mathcal{G}(0^-,\mathbf{q})\Big|_{3.8(b)} - \mathcal{G}(0^-,\mathbf{q})\Big|_{3.8(b)} + \mathcal{G}(0^-,\mathbf{q})\Big|_{3.8(e)} \Bigg] \\
= \quad & \frac{1}{z^3}\left[ -(3.82) + (3.89) + (3.91) - (3.86) - (3.86) + (3.97) \right] (3.123)
\end{aligned}
$$

where the Green's function without a spin index denote the corresponding results for bosons, and we ordered to terms so that they correspond to 3.11(a), 3.11(b),.., 3.11(f). In the second line, we give the references to the relevant equations for

convenience. Like before, we have to use the fermionic two- and three-body $T$-matrices in these equations. The sign switches between the diagrams are related to the diagrammatic structure: An even and an uneven amount of crossings of fermionic lines has to give a different prefactor, since the related contraction needs an uneven or even amount of anti-commutations to be untangled. This is explained in more detail in appendix E, where also the global sign is fixed.

**Density**

The results for the density are obtained – analogous to the bosonic results – via integration of (intermediate) steps for the momentum distribution. We already have obtained the one-particle results. The two- and three-body results can be read off from eqs. (3.120)-(3.122) and (3.123) by comparison to the corresponding bosonic (see sec. 3.3.1) results for the density. We get

$$
\begin{aligned}
n_{\uparrow,2}^{(2p)} &= -\frac{1}{z^2}(3.101) & (3.124) \\
n_{\uparrow,3}^{(2p)} &= \frac{3}{z^3}(3.108) & (3.125)
\end{aligned}
$$

for the two-particle contributions to the density. The numbers on the right hand side refer to the expressions for the bosonic case. Similarly, we also give the final result for the fermionic three-body contribution in terms of the equations for the bosonic contributions to the density:

$$
n_{\uparrow,3}^{(3p)} = \frac{3}{z^3}\left[-(3.112) + (3.114)\right] \tag{3.126}
$$

## 3.4 Comments on numerical implementation

This is a short outline on how the code that performs the momentum and Bromwich integrations is implemented. We will only outline key ideas, for details on the implementation of a Gauss-Legendre quadrature and the numerical solution of linear integral equations, see the book "Numerical Recipes" [118].

The key observation for the momentum distribution is the following: We have brought the integrands of diagrams 3.8(a)-3.8(e) into a form, where the three-body $T$-matrix only depends on the momenta that are integrated over. We now put the integrations (also the $s$-integration!) on a Gauss-Legendre grid (for convenience a quadratic one in momentum), and calculate the three-body $T$-matrix *once* for

every energy (on the grid) and angular momentum we want, i.e. we solve the STM equation

$$\mathbf{t}_{s_i}^{(l)} = \left[ \mathbb{1} - \mathbf{K}_{s_i}^{(l)} \right]^{-1} \mathbf{g}_{s_i}^{(l)} \tag{3.127}$$

in matrix form, where the matrix means $\mathbf{t}_{s_i,mn}^{(l)} = t_3^{(l)}(s_i, p_m, k_n)$ element-wise, and similarly for the kernel matrix $\mathbf{K}$ and the inhomogeneity $\mathbf{g}$. This means that for an energy grid of size $n$, we need to solve $n \times l_{max}$ STM equations, where $l_{max}$ means the highest angular momentum we want to include. In practice, I chose $l_{max} = 10$, from $l_{max} = 7$ on, I could not really see any deviations by including higher $l$. When we want to evaluate the momentum distribution, do we need to invert the matrix STM equations now over and over? No, the $t_3$ matrix never depends on $q$ in the integrand. So we invert once, save the solutions to the memory and can evaluate the momentum distributions for many different $q$.

The bound states (Efimov trimers) are found by putting the integral equation (3.57) on a grid and solving

$$\det \left[ \mathbb{1} - K_E^{(0)} \right] \overset{!}{=} 0 \tag{3.128}$$

with a simple rootfinder.

The residues of the three-body $t_3$-matrix are *not* calculated similarly. We rather use a numerical integration on a contour around the pole. This is very precise and has the advantage that it is stable against errors in the position of the bound state energy. When the bound state energies lie numerically too deep, we move the Bromwich integration to the right of the pole, and rather include the residue(-matrix) calculated in the formerly described way.

Last but not least, to extract the two- and three-body contacts, we use a numerical derivative (in practice a so-called four-point rule) with respect to $1/a$ or $\kappa_*$ on the virial coefficients that are extracted from the density diagrams.

## 3.5 Results for fermions

For comparison to the behavior of the bosonic case, on which the main focus lies, let us shortly discuss the fermionic case as well. We will discuss the behavior of the third virial coefficient and the contact as functions of the scattering length. We will not discuss the second virial coefficient, since, up to a factor of two, it is the same as the bosonic one [119, 120]. Regarding the third virial coefficient, we
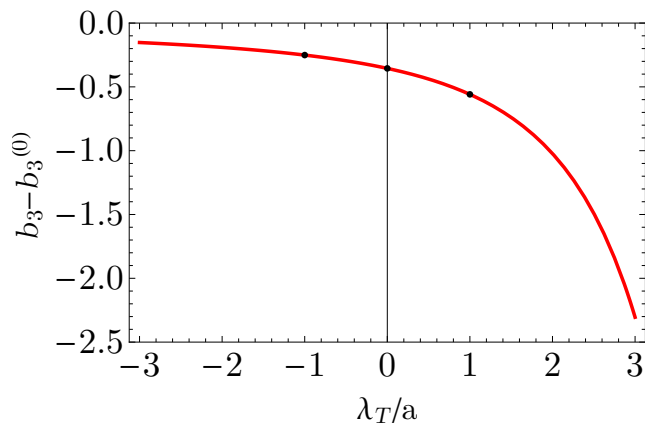
Figure 3.12: Interaction contribution to the third virial coefficient of the fermionic system. We obtain the exact same results as Leyronas [9]. Black dots indicate the values of the virial coefficient as obtained from the integrating the $\mathcal{O}(z^3)$ parts of the momentum distributions that are shown in fig. 3.14, over all $q$.

reproduce the results obtained by Leyronas [9], which is a nice test for the numerical implementation. We will then turn to the discussion of the fermionic momentum distribution at different scattering lengths. Our results for the contacts are indeed compatible with the tails we see in the momentum distribution. Our results for the contacts are also compatible with the findings of ref. [108], which calculates the momentum distribution and contacts from the spectral function of the Fermi gas, expanded to second order in the fugacity. This provides a strong test for our numerics.

### 3.5.1 Third virial coefficient

The interaction correction $\Delta b_3 = b_3 - b_3^{(0)}$ to the third virial coefficient comes from the diagrams 3.7(b)-3.7(d) in the two-particle sector and 3.11(a)-3.11(f) in the three-body sector. Its behavior as a function of inverse scattering length is shown in fig. 3.12. In particular, including angular momenta up to $l = 10$, we obtain the result

$$\Delta b_3 \left( \frac{\lambda_T}{a} = 0 \right) = -0.355103 \tag{3.129}$$

for the third virial coefficient of the unitary Fermi gas, in complete accordance with earlier findings [9, 121, 122]. At all scattering lengths, the third virial coefficient is

negative, which means it tends to *reduce* the density at given chemical potential. This behavior can be seen as a consequence of the Pauli principle.

### 3.5.2 Contact parameter

Having established the behavior of the third virial coefficient as a function of scattering length, we can immediately ask for the behavior of the contact parameter, which dominates the short-time and -distance correlations of the system. From the adiabatic theorem, cf. table 3.1, we have for the contact density $\mathcal{C} = C/V$:

$$
\begin{aligned}
\mathcal{C} &= \frac{16\pi^2}{\lambda_T^4}\left[\frac{\partial b_2}{\partial\left(\frac{\lambda_T}{a}\right)}z^2 + \frac{\partial b_3}{\partial\left(\frac{\lambda_T}{a}\right)}z^3 + \mathcal{O}(z^4)\right]\\
&\equiv \left[C^{(2)}z^2 + C^{(3)}z^3 + \mathcal{O}(z^4)\right],
\end{aligned}
\tag{3.130}
$$

where the contribution from $b_1$ was annihilated by the derivative, because $b_1$ does not depend on the scattering length. The same implicitly holds for the one-particle contributions to $b_2$ and $b_3$. In the second line, we have the defined the order $z^n$ contributions $C^{(n)}$ to the contact. Because we know the behavior of the virial coefficients as functions of scattering length (for $b_2$, see sec. 3.6.1 and divide by a factor of 2), we can now, by differentiation with respect to the scattering length, infer the contacts $C^{(2)}$ and $C^{(3)}$. The resulting behavior is shown in figure 3.13. As is to be expected from the negativity of the third virial coefficient, $C^{(3)}$ (red line) is negative throughout the crossover. In contrast, the contribution $C^{(2)}$ (green line) is positive (and larger in value). The cancellation of these terms to a finite and positive result is illustrated by the black line, which is the sum of the two contributions for $z = 0.4$. The value of the fugacity has been chosen such that $z^2 e^{\beta E_D} < 1$ for the values of scattering length we are going to use in our plots of the momentum distribution in the next subsection. This requirement is in complete analogy to one for the virial expansion of the two-dimensional Fermi gas in sec. 2.3.

### 3.5.3 Momentum distribution

In figure 3.14(a), the momentum distribution of a particle of species $\uparrow$ is shown at three different scattering lengths. They correspond to the BCS-side (red), the unitary limit (green) and the BEC-side (blue) of the crossover. The momentum variable $\zeta = \lambda_T q$ is made dimensionless via multiplication with the thermal wavelength, which is the natural scale for the virial expansion. As mentioned in the
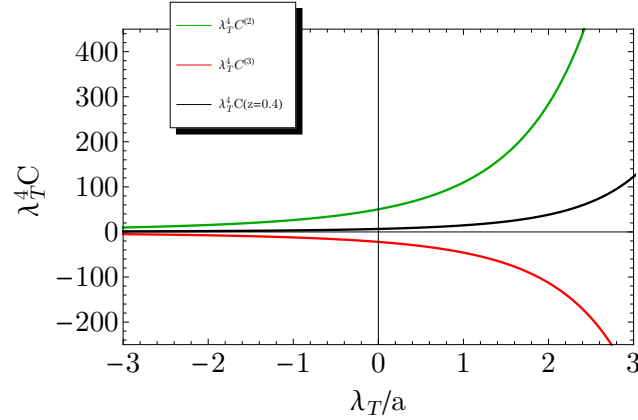
Figure 3.13: Contact contributions of order $z^2$ (green line) and $z^3$ (red line) as obtained from differentiation of the virial coefficients. The black line shows the full contact up to order $z^3$ at fugacity $z = 0.4$.

preceding section, we chose a fugacity of $z = 0.4$, which makes the virial expansion well defined for all of the values $\lambda_T/a = -1, 0, 1$. The momentum distributions all look more or less like a Gaussian function, with the height increasing from the BCS to the BEC side. Since our momentum distributions are normalized to give the density after integration over all $q$, this just reflects the fact that attractive interactions tend to increase the density at given chemical potential. It should be noted that these momentum distributions are of course not pure Gaussian functions, because they exhibit a power-law tail at high momenta.

In figure 3.14(b), due to multiplication with $\zeta^4$, the high-momentum tail $\sim C/q^4$ becomes visible. The straight lines indicate the predictions of the contacts as obtained from the adiabatic theorem (3.130), and correspond to the values of the black line in fig. 3.13 at the corresponding scattering lengths. The prediction agrees perfectly with the tails we find. Notice the general behavior of the saturation: The multiplied momentum distribution always swings above its asymptotic value once, and then approaches it slowly from above. In the regime $\lambda_T/|a| < 1$, the saturation to the universal tail always happens around $q\lambda_T \approx 10$. For large inverse scattering lengths, we expect the saturation to occur later, also see sec. 2.3.4 for the corresponding discussion in the two-dimensional case. The high-momentum behavior will qualitatively change for the bosonic case, due to the presence of the log-periodic sub-leading tail that is connected to three-body correlations at short distances, cf.
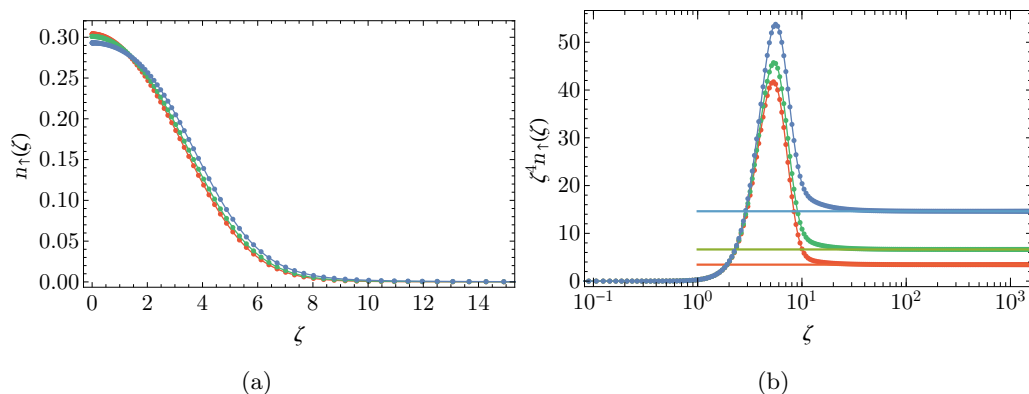
Figure 3.14: 3.14(a): Fermionic momentum distributions at fugacity $z = 0.4$ and scattering lengths $\frac{\lambda_T}{a} = -1(\text{red}), 0(\text{green}), 1(\text{blue})$, as a function of dimensionless momentum $\zeta = q\lambda_T$. Points indicate numerical results, the line in between is a cubic spline interpolation to guide the eye. 3.14(b) makes – via multiplication with $\zeta^4$ – the $C/q^4$ tail visible. The straight lines are the predictions for the contacts from the adiabatic theorem.

eqs. (3.8) and (3.9).

## 3.6 Results for bosons

The bosonic system has an additional parameter compared to the fermionic system: The binding wave number $\kappa_*$ of the deepest Efimov trimer at unitarity, which is connected to our choice of the lowest trimer branch in eq. (3.83). The product $\lambda_T \kappa_*$, which encodes the ratio between the temperature and this trimer binding energy, indeed strongly determines the behavior of the system. This is to be expected, since an attractive force that leads to bound states tends to increase the density at given chemical potential. Compared to fermions, the new aspect about the bosonic system is that the bound states even exist at unitarity and on the negative $a$-side, where no two-body bound states exist. Since in the limit of large trimer binding energies, the virial coefficients will contain exponentially large terms $\sim e^{\beta|E_T|}$, we talk about *reduced* quantities instead. This means, we multiply the quantities by an

exponential reduction factor that contains the largest binding energy of the system:

$$e^{-\beta\Xi} \;\;=\;\; \begin{cases} 1 & a < a_- \\ e^{-\beta|E_T|} & a_- \leq a \leq a_* \\ e^{-\beta|E_D|} & a_* < a \end{cases} \qquad (3.131)$$

Of course, the validity of the virial expansion is very limited in the regime $\kappa_*\lambda_T \gg 1$, because we need exponentially small fugacities to produce finite densities. This is completely analogous to the case of the Fermi gas we have studied in the preceding section, as well as in section 2.3, where the presence of the two-body bound state on the BEC side also sets upper bounds for the fugacity. We will still show results for the trimer dominated limit, but keep in mind that this has to be understood as an extrapolation.

In the scattering dominated limit $\kappa_*\lambda_T \ll 1$, we expect corrections from the effective range to become important. This can be understood from connection $\kappa_* \approx 0.2/\ell_{vdW}$ [87, 89], where $\ell_{vdW}$ is the van-der-Waals length. The size of the effective range is typically also set by the van-der-Waals length. This means that for momenta $k \approx \ell_{vdW}^{-1}$, $s$-wave scattering no longer is dominant. Hence, for too large temperatures, our description of the system via the universal Lagrangian (3.17), which only includes $s$-wave scattering, becomes questionable. We will come back to this point during the discussion of the third virial coefficient. However, it should be noted that due to the relation $\kappa_* \approx 0.2/\ell_{vdW}$ [87, 89], there indeed *exists* a broad regime where $\kappa_* < \lambda_T^{-1} < \ell_{vdW}^{-1}$, and hence the discussion of this limit is justified.

### 3.6.1 Virial coefficient

We begin by discussing the second virial coefficient. Its interaction contribution is given by the Beth-Uhlenbeck result [73] in eq. (3.105), and can be brought into the analytic form [120, 119]

$$\Delta b_2 \;\;=\;\; \sqrt{2}e^{\frac{\beta}{ma^2}}\left[1 + \mathrm{erf}\left(\frac{1}{a\sqrt{mk_BT}}\right)\right], \qquad (3.132)$$

where erf is the error function. The result above is valid for both $a > 0$ and $a < 0$. The reduced second virial coefficient of a Bose gas is shown in fig. 3.15(a), where the axis of the scattering length is rescaled with the fourth square root. This is convenient for comparison to the third virial coefficient over the Efimov spectrum, which is usually rescaled by a fourth square root as well. In the dimer
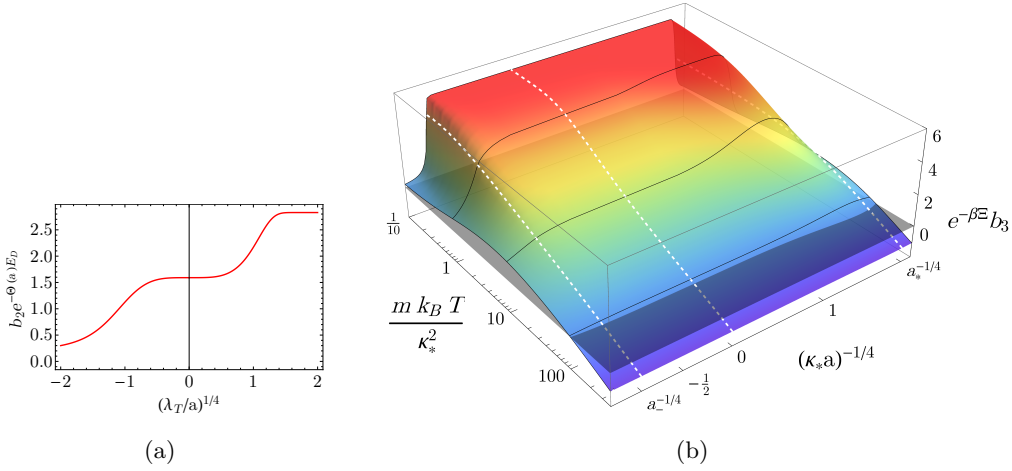
Figure 3.15: 3.15(a): Second virial coefficient of the Bose gas, as obtained from eq. (3.132). 3.15(b): Third virial coefficient of the Bose gas. Black lines indicate cuts at $mk_BT/\kappa_*^2 = 10^n, n \in \mathbb{Z}$. White dashed lines indicate cuts at unitarity, the three-atom threshold $1/\kappa_*a_-$ and the atom-dimer threshold $1/\kappa_*a_*$.

dominated regime, the reduced second virial coefficient saturates to $2^{3/2}$, which of course implies that the full virial coefficient $\approx 2^{3/2}e^{\beta E_D}$ becomes exponentially large. It is important to note that the lack of variation around unitarity is a consequence of the rescaling, the second virial coefficient has finite slope at unitarity (which is important for the contact!).

A plot of the reduced third virial coefficient is shown in fig. 3.15(b). This virial coefficient is obtained via numeric evaluation of diagrams 3.7(b)-3.8(e) for the density, cf. sec. 3.3.1. Angular momenta up to $l = 10$ were included in the calculation. The axes where chosen such that on the $mk_BT/\kappa_*^2$ axis, we can think of varying temperature. On the $1/\kappa_*a$ axis, we are probing different regions of vacuum physics, and do not vary temperature. The three white dashed lines indicate the three-atom threshold, unitarity, and the atom-dimer threshold. It should be noted that following the white dashed line at unitarity produces a plot that is consistent with the results of Werner and Castin [123]. The black transparent plane at zero was inserted to aid the eye to see the zero crossing of the third virial coefficient, which happens in the regime $\kappa_*\lambda_T \ll 1$ ($mk_BT/\kappa_*^2 \gg 1$). As already mentioned earlier, this is the regime where effective range corrections might become important, and those may

even keep the third virial coefficient from becoming negative. This is only speculative though, one would need to perform a calculation similar to the one presented here and compare the results. One could use the effective field theory developed in [124], or the model that was used in [87, 88]. In the limit of small effective range, those two theories become equivalent.

In the trimer dominated regime $mk_BT/\kappa_*^2 \ll 1$, the reduced third virial coefficient varies rapidly at the scattering lengths that define the atom-dimer and three-atom thresholds. It jumps from almost zero values to the trimer dominated result $e^{-\beta|E_T|}b_3 = 3\sqrt{3}$, which was analytically derived by Pais and Uhlenbeck [117] (see the section regarding strong binding) and recently re-derived by Werner and Castin for the unitary Bose gas [123].

In the regime $mk_BT/\kappa_*^2 = \mathcal{O}(1)$, the virial coefficient still varies notably around the scattering and atom-dimer thresholds $1/a_-$ and $1/a_*$, although not as intensely as in the trimer dominated regime.

### 3.6.2 Contact parameters

By the adiabatic theorems given in eqs. (3.10) and (3.11), the knowledge of the third virial coefficient implies the knowledge of the two- and three-body contacts that determine the magnitudes of the leading and sub-leading high momentum tails given in eq. (3.8). The contacts measure short-distance correlations and are connected to the probability that two or three bosons can be found at the same point in space [53]. In complete analogy to the fermionic case (see eq. (3.130)), we define

$$
\begin{aligned}
\mathcal{C}_2 &= \frac{C_2}{V} = \frac{16\pi^2}{\lambda_T^4}\left[\frac{\partial b_2}{\partial\left(\frac{\lambda_T}{a}\right)}z^2 + \frac{\partial b_3}{\partial\left(\frac{\lambda_T}{a}\right)}z^3 + \mathcal{O}(z^4)\right] \\
&\equiv \left[C_2^{(2)}z^2 + C_2^{(3)}z^3 + \mathcal{O}(z^4)\right]
\end{aligned}
\tag{3.133}
$$

for the two-body contact, and likewise for the three-body contact:

$$
\mathcal{C}_3 = \frac{C_3}{V} = \frac{\pi}{\lambda_T^5}(\lambda_T\kappa_*)\frac{\partial b_3}{\partial(\lambda_T\kappa_*)}z^3 + \mathcal{O}(z^4) \equiv C_3^{(3)}z^3 + \mathcal{O}(z^4)
\tag{3.134}
$$

The second order contribution $C_2^{(2)}$ can be obtained analytically from the use of the adiabatic theorem on eq. (3.132). The result is

$$
C_2^{(2)} = 8\pi\frac{2^{3/2}}{\lambda_T^3}\left[\sqrt{\frac{m}{\pi\beta}} + \frac{e^{\frac{\beta}{ma^2}}}{a}\mathrm{erfc}\left(-\frac{1}{a\sqrt{mk_BT}}\right)\right],
\tag{3.135}
$$

where erfc is the complementary error function. In the dimer dominated limit $1/a \to \infty$, this simplifies to

$$z^2 C_2^{(2)} \xrightarrow{a \to 0^+} \frac{16\pi}{a} \frac{2^{3/2} e^{\beta E_D} z^2}{\lambda_T^3} = C_{2,\text{Dimer}} n_D, \tag{3.136}$$

where we used the fact that the contact of a single dimer is given by $16\pi/a$ and the density of dimers in the dimer dominated limit can be obtained from the second virial coefficient (3.132) and the assumption that every atom is bound in a dimer in this limit: $n = 2n_D$. The last assumption of course only makes sense if the system is not dominated by trimers, i.e. at $a < a_*$. The result (3.136) could also have been obtained from a simple meanfield-ansatz $E = -E_D n_D$, together with the adiabatic theorem (3.10).

The behavior of the the reduced dimensionless second $(C_2^{(2)})$ and third order $(C_2^{(3)})$ contributions to the two-body contact $\mathcal{C}_2$ is shown in figure 3.16. In the trimer dominated limit $\kappa_* \lambda_T \gg 1$ $(mk_B T/\kappa_*^2 \ll 1)$, the second order contribution only becomes comparable to (or dominant over) the third order contribution when the trimer state is non-existent. It should be noted that the second order contributions, on the positive $a$ side, is exponentially large itself $\sim e^{\beta|E_D|}$. It is just the even larger trimer energy that pushes the reduced contact to zero when multiplying by $e^{-\beta\Xi}$. It is clear from eq. (3.135), that the second virial coefficient never explicitly depends on $\kappa_*$, hence, in figure (3.16(a)), what we are seeing is mainly the interplay between the reduction exponent $\Xi$ and the dimer binding energy $E_D$.

The reduced third order contribution $C_2^{(3)}$ rises to large values in the trimer limit, getting larger as the scattering length is increased. This reflects the fact that the trimer energy gets larger (in magnitude) as the scattering length is increased. As can be already inferred from the behavior of the third virial coefficient, it then drops to almost zero when the atom-dimer threshold is crossed. This is the regime where the second order contribution starts to dominate. From the negative slope of the third virial coefficient with respect to $\kappa_*$, it is clear that also $C_2^{(3)}$ must have a zero crossing, which is located in the scattering dominated limit $\kappa_* \lambda_T \ll 1$ $(mk_B T/\kappa_*^2 \gg 1)$. As mentioned before, these results have to be taken with a grain of salt, since effective range corrections might change the picture. Note that the *full* two-body contact in our theory always stays positive, when we choose fugacities such that the density stays positive (otherwise the virial expansion breaks down anyway). We will come back to this in a moment.

The qualitative behavior of the leading order contribution to the three-body con-

(a) $\lambda_T^4 C_2^2$
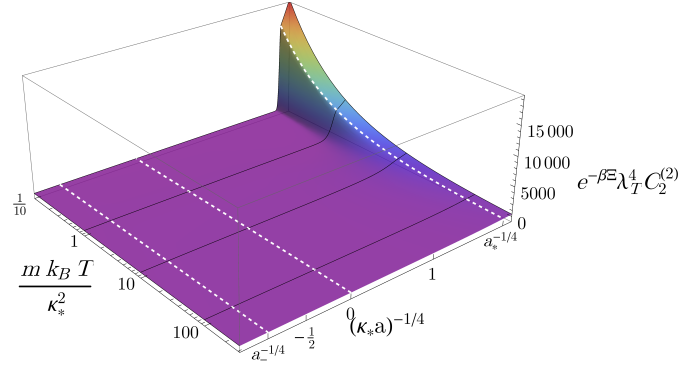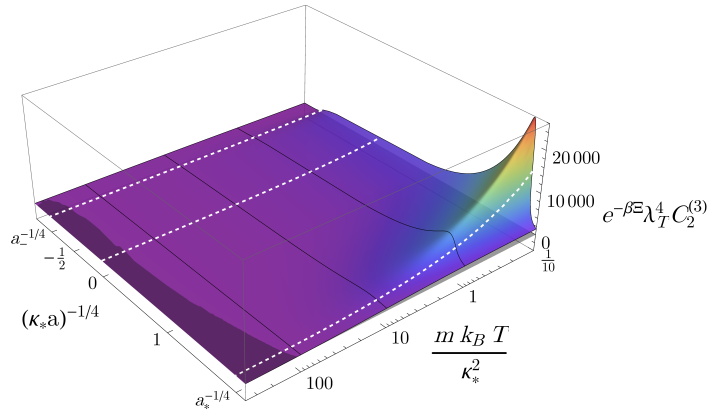


(b) $\lambda_T^4 C_2^3$

Figure 3.16: General behavior of the reduced two-body contact of the Bose gas. Fig. 3.16(a) shows the second order contribution in fugacity. Fig. 3.16(b) shows the third order contribution. White dashed lines again indicate the three-atom threshold, unitarity, and the atom-dimer threshold. Black lines are cuts at $mk_BT/\kappa_*^2 = 10^n, n \in \mathbb{Z}$.
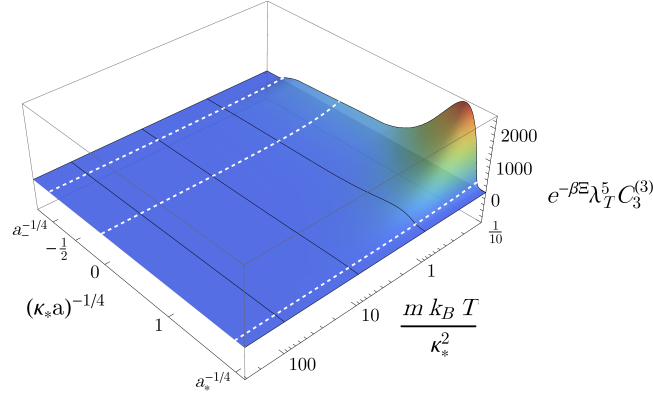
Figure 3.17: Reduced third order contribution to the three-body contact of the Bose gas. Black and dashed white lines mean the same as in figure 3.16.

tact is shown in figure 3.17. Its dependence with respect to $mk_BT/\kappa_*^2$ always looks similar for different scattering lengths (only scaled). For positive scattering lengths, the reduced three-body contact decreases, which reflects the fact that the trimer binding energy gets closer to the dimer binding energy, which then dominates the form of spectrum (but multiplication with $e^{-\beta\Xi}$ suppresses this dependence again). In contrast to the two-body body contact, the three-body contact never changes sign. From the viewpoint of the tail of the momentum distribution, this is plausible since the three-body contact just describes sub-dominant oscillations around the $C_2/q^4$ tail of the momentum distribution, and thus doesn't determine the overall sign of the virial coefficient. One could also derive it from the fact that the three-body contact, like the *full* two-body contact, is a positive definite quantity, as can be inferred from its operator definition [53]. While sub- leading corrections are allowed to have a different sign, the leading order term needs to be positive in order to ensure this property.

In order to understand the interplay between the second and third order terms of the two-body contact better, we show the behavior of the full contact $C_2$ in the third order of the virial expansion, at unitarity and as a function of $T/T_F$, in figure 3.18. The contact is now made dimensionless with respect to $k_F = (6\pi^2 n)^{1/3}$, and made intensive via division of $N$. These are the units used in experiment [94]. Exactly like in section 2.3, the chemical potential, and hence the fugacity, is determined by fixing the ratio $T/T_F$ in the density expansion (3.12). For completeness, fig. 3.18(b)
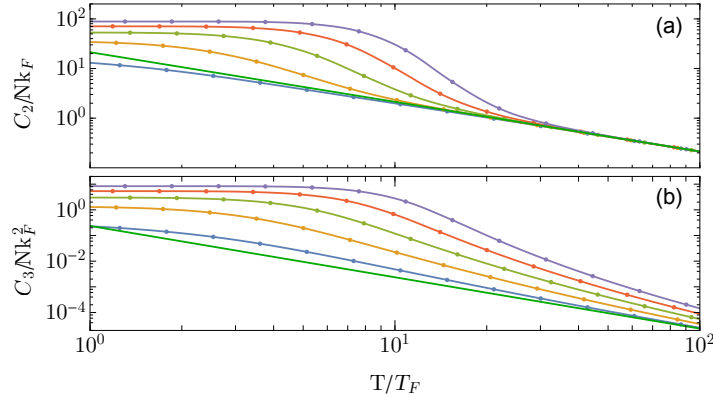
Figure 3.18: Full Contacts of the Bose at unitarity, truncated after the third order in the cluster expansion. (a): Two-body contact as a function of $T/T_F$ for different values of $\kappa_*$. (b): Three-body contact as a function of $T/T_F$ for different values of $\kappa_*$. The green lines denote asymptotic high temperature results, see text. Other colors, from lowest to largest values in both figures: $\kappa_*/k_F = 1, 2, 3, 4, 5$.

shows the corresponding three-body contact at unitarity and as function of $T/T_F$. The green lines correspond to the asymptotic high temperature results

$$\frac{C_2}{Nk_F} \xrightarrow{T \to \infty} \frac{64}{3} \frac{T_F}{T} \tag{3.137}$$

$$\frac{C_3}{Nk_F^2} \xrightarrow{T \to \infty} \frac{4s_0}{\sqrt{3}\pi^2} \left(\frac{T_F}{T}\right)^2. \tag{3.138}$$

The result for the two-body contact can be readily derived from the use of the analytic result (3.135) in the limit $T \to \infty$, which yields $\lambda_T^4 \mathcal{C}_2^{(2)} = 32\pi z^2$. Re-expressing this in terms of $T/T_F$ (using the leading order $n\lambda_T^3 \approx z$ of the density expansion (3.12)) yields (3.137). For (3.138), we have used the analytic result $b_3 \approx 3\sqrt{3}\frac{s_0}{2\pi} \log \left( e^{\gamma_E + 2\pi C/s_0} \frac{\kappa_*^2}{mk_B T} \right)$, given by Werner and Castin [123] for the high temperature limit of the third virial coefficient of the unitary bose gas. $\gamma_E$ is the Euler-gamma and $C = 0.648$. After the use of the adiabatic theorem, this yields $\mathcal{C}_3 \lambda_T^5 = z^3 3\sqrt{3}s_0$, which can again be re-expressed in terms of $T/T_F$. As is apparent from fig. 3.18, the contacts increase by several orders of magnitude when the temperature is lowered, and then saturate near $T/T_F = 1$.

### 3.6.3 Momentum distribution

Having completed our discussion of the two- and three-body contacts, we can now turn to the results for the momentum distribution. In particular, our aim is to study the asymptotic behavior at high momenta, and compare it to the universal relations (3.8) and (3.9). We will see that while the saturation to the log-periodic tail is very slow, the assumption of relatively early saturation, that was made in [105] in order to fit $C_2$ and $C_3$ is not *too* far off. In the end, we will compare the numerical results to experiment, which will yield a surprising result.

For our theory curves, we parametrize

$$n(\mathbf{q}) \;=\; e^{\beta\Xi}\left[zn_1(\mathbf{q}) + z^2 n_2(\mathbf{q}) + z^3 n_3(\mathbf{q}) + \mathcal{O}(z^4)\right]. \qquad (3.139)$$

This has the advantage that we can directly discuss the behavior of the non-trivial $n_3(q)$ part, which encodes the three-body correlations. For the high momentum tails, $n_1(q)$ does not contribute because it is a Gaussian. $n_2(q)$ gives the leading order tail $\sim C_2^{(2)}/q^4$, but does not encode the three-body correlations we are interested in. If required, it can always be obtained from eq. (3.70). As a reminder: The third order diagrams we need to solve, in order to obtain $n_3(q)$, are 3.6(c), 3.7(b)-3.7(d), and 3.8(a)-3.8(e).

**Momentum distribution at different scattering lengths**

Figure 3.19 shows the third order part of the momentum distribution at different scattering lengths and as function of dimensionless momentum $\zeta = \lambda_T q$ at $\kappa_* \lambda_T = 3$ , which implies that the binding energy of the deepest trimer at unitarity and the temperature are roughly the same. $\lambda_T/a = -6.55$ (fig. 3.19(a)) was chosen to represent the negative $a$-side, and $\lambda_T/a = 6.55$ (fig. 3.19(c)) represents the positive side. As in the fermionic case, the third order parts $n_3(q)$ resemble a Gaussian function. The qualitative behavior of the momentum distribution multiplied by $q^4$, however, is vastly different to the fermionic case, because the log-periodic subleading tail makes the momentum distributions oscillate around the asymptotic value of the two-body contact. The momentum distributions match perfectly with our predictions for the contacts $e^{-\beta\Xi}C_2^{(3)}$ and $e^{-\beta\Xi}C_3^{(3)}$ from the adiabatic theorem, as well as the resulting tail (3.8). It is interesting to note that the fastest saturation to the tail happens at unitarity (fig. 3.19(b)), where $1/a$ does not provide a scale for the asymptotic behavior of the OPE. For finite $a$, the behavior at intermediate momenta differs a lot from the unitary case.

(a) $\lambda_T/a = -6.55$

(b) $\lambda_T/a = 0$

(c) $\lambda_T/a = 6.55$
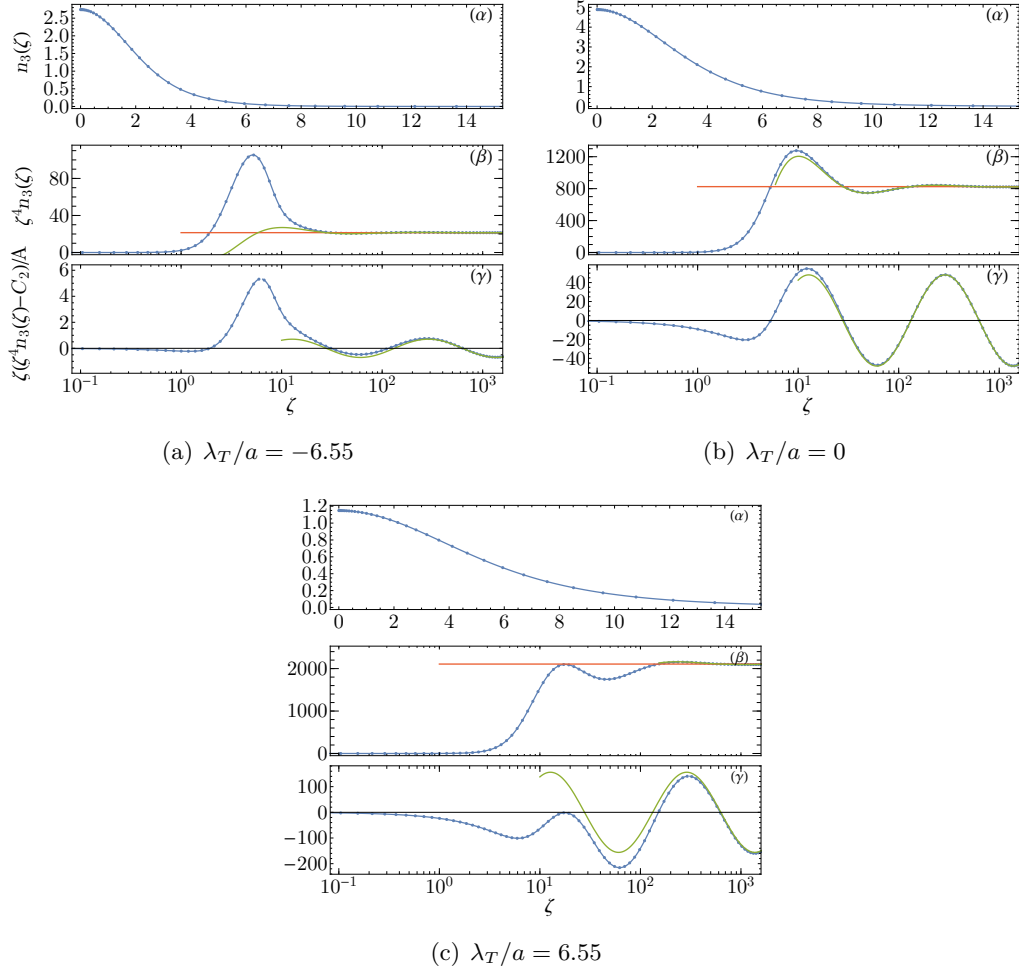
Figure 3.19: Momentum distributions at $\lambda_T \kappa_* = 3$ and different scattering lengths as functions of dimensionless momentum $\zeta = q\lambda_T$. Figures $(\alpha)$ show $n_3(q)$. Figures$(\beta)$ enhance the high momentum tail via multiplication of $\zeta^4$. The orange line denotes the $C_2^{(3)}/q^4$ prediction, the green line the full prediction (3.8). Figures $(\gamma)$ extract the sub-leading log-periodic high momentum tail, divided by $A$ (see (3.8)).

**Momentum distribution at unitarity**

Figure 3.20 illustrates the variation of the momentum distribution with $\kappa_* \lambda_T$. The dimensionless momentum is again $\zeta = q\lambda_T$. The reference momentum distribution at $\kappa_* \lambda_T = 3$ from fig. 3.19(b) was again included for convenience. The different values of $\kappa_* \lambda_T$ were chosen to represent the scattering dominated regime ($\kappa_* \lambda_T = 1$), the balanced regime ($\kappa_* \lambda_T = 3$), and the trimer dominated regime ($\kappa_* \lambda_T = 6.42$). At unitarity, the scales of saturation barely change with temperature, and are an order of magnitude smaller than in the case of finite scattering lengths. In particular, as shown in the figures $(\beta)$, the $q^4 n(q)$ momentum distribution always swings over the asymptotic value defined by the two-body contact $e^{-\beta\Xi} C_2^{(3)}$, and then oscillates around this value in a decaying manner. We also see that the assumption that the momentum distribution is almost saturated at the first hump, that was used in ref. [105] to fit the two- and three-body contacts to experiment, is reasonably justified in the trimer dominated limit, where the error is on the order of five percent. In the scattering dominated limit, this assumption becomes more dangerous, as can be inferred from figure 3.20(a)$(\beta)$. Here, the error will be larger, because both the position of the first hump, as well as its height show a pronounced deviation from the universal prediction (green line). It should be noted that fig. 3.20 over-pronounces this effect, because the scattering limit is the one where the second order corrections become comparable to the third order result. Hence, while the position of the first minimum still gives an error, the error in the height of the first peak is smaller.

**Comparison to experiment**

As a final application of the calculations done in this chapter, we will compare the momentum distributions from the virial expansion to the experiment [94], where the momentum distribution of the unitary Bose gas was measured after a ramp to unitarity. Instead of averaging our results over the trap using the local density approximation, like we did in our article [109], we are going to use the average densities in experiment and compare to directly to our calculation for the homogeneous system. For comparison, we will also show the trap-averaged results (for details, consult appendix F).

Table 3.2 shows the experimental parameters for the two momentum distributions that were measured in [94]. It has to be emphasized that the temperature in the experiment is *unknown*[7], and hence we can not directly insert the ratio $T/T_F$. To

---

[7]More specifically: The experimental temperature is unknown *after* the ramp. Before the ramp,

(a) $\kappa_*\lambda_T = 1$

(b) $\kappa_*\lambda_T = 3$

(c) $\kappa_*\lambda_T = 6.42$
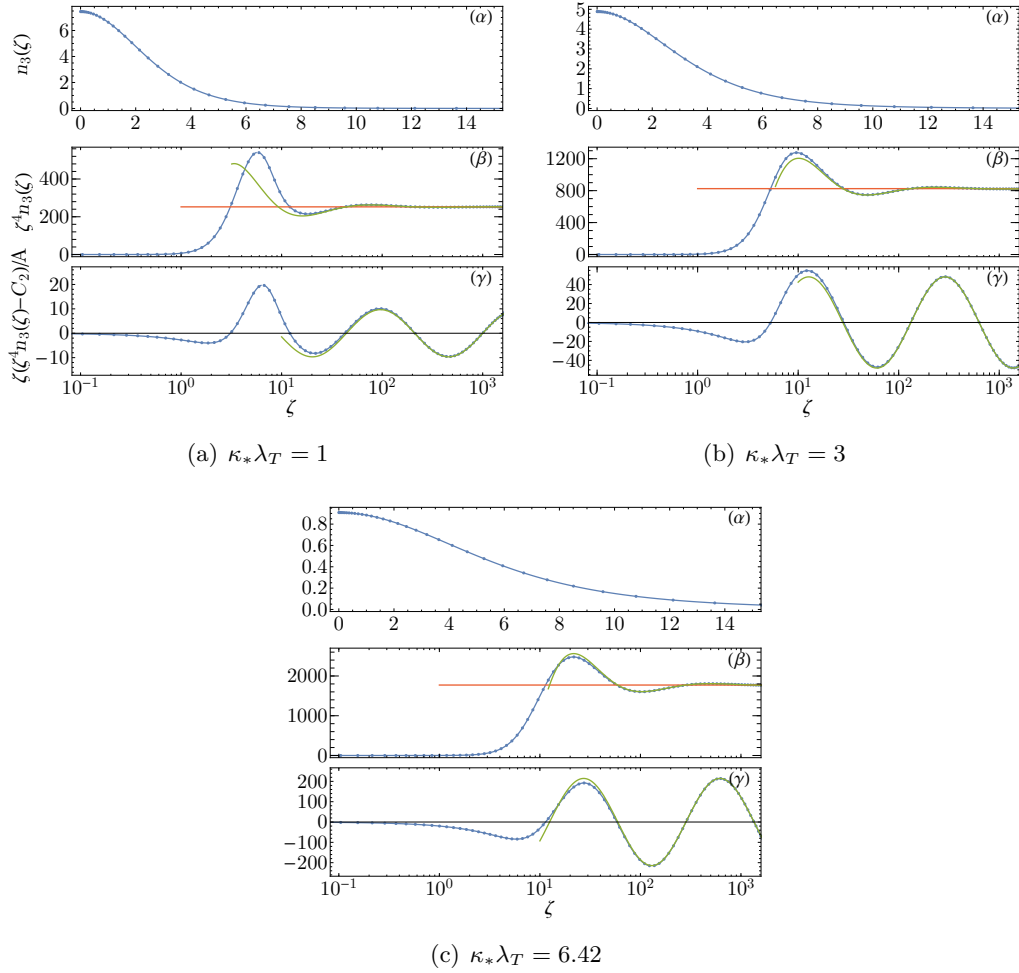
Figure 3.20: Third order contribution to the momentum distribution as function of dimensionless momentum $\zeta = q\lambda_T$. Green and orange lines as in fig. 3.19. The different values of $\kappa_*\lambda_T$ represent the scattering dominated regime ($\kappa_*\lambda_T = 1$), the regime where collision momenta are on average equal to the trimer binding energy ($\kappa_*\lambda_T = 3$), and the trimer dominated limit ($\kappa_*\lambda_T = 6.42$).

| $\langle n \rangle \ (cm^{-3})$ | $T_F \ (nK)$ | $\kappa_*/k_F$ |
|---|---|---|
| $5.5 \times 10^{12}$ | 135.2 | 5.52 |
| $1.6 \times 10^{12}$ | 59.4 | 8.33 |

Table 3.2: Experimental parameters in [94]. $\kappa_*/k_F$ is inferred from the values of the density, together with the known value [90] of $a_- = 759(6)a_0$, where $a_0$ is the Bohr radius. The universal relation $\kappa_* a_- = -1.50763$ (see eq. (3.5)) then yields $\kappa_* = 38 \mu m^{-1}$.

cure this issue, we calculate the momentum distributions at various values of $\kappa_* \lambda_T$. Then, via the relations $\lambda_T k_F = 2\sqrt{\pi T_F/T}$ and $\kappa_*/k_F = \lambda_T \kappa_*/k_F \lambda_T$, we can infer the value $T/T_F$ (because we have fixed $\kappa_*/k_F$ and $\lambda_T \kappa_*$). Inversion of eq. (3.12) then yields the fugacity $z$, and we can calculate the momentum distributions by summing the contributions from all the diagrams.

To compare the momentum distributions to experiment, we normalize both the experimental and the numerically obtained momentum distributions, as functions of the dimensionless momentum $\kappa = q/k_F$, to unity:

$$\int \frac{d^3\kappa}{(2\pi)^3} n(\kappa) = 1. \tag{3.140}$$

We then plot all the numerically obtained momentum distributions and compare them against the ones obtained from experiment. In practice, numerical data between $\lambda_T \kappa_* = 0.125$ (scattering dominated limit) and $\lambda_T \kappa_* = 44.8$ (extreme trimer limit) was created, ranging over fifty different momentum distributions. No momentum distribution in the given range, when using the values of $\kappa_*/k_F$ given in table 3.2, seems to fit the experimental data well. Remarkably, when *reducing* these values by a factor of 22.7 however, and hence setting $\kappa_*'/k_F = \kappa_*/22.7 k_F$, we find agreement for the momentum distributions with $\kappa_*' \lambda_T = 1$ (for $\kappa_*'/k_F = 5.52/22.7$) and $\kappa_*' \lambda_T = 1.4$ (for $\kappa_*'/k_F = 8.33/22.7$). These values correspond to $T/T_F = 0.9$ ($\kappa_*'/k_F = 8.33/22.7$) and $T/T_F = 0.75$ ($\kappa_*'/k_F = 5.52/22.7$), and hence the virial

---

[94] states temperatures of around $10nK$, meaning $T/T_F \approx 0.1(n = 5.5 \times 10^{12} cm^{-3}) - 0.2(n = 1.6 \times 10^{12} cm^{-3})$ before the ramp.

(a) homogeneous



(b) trap averaged
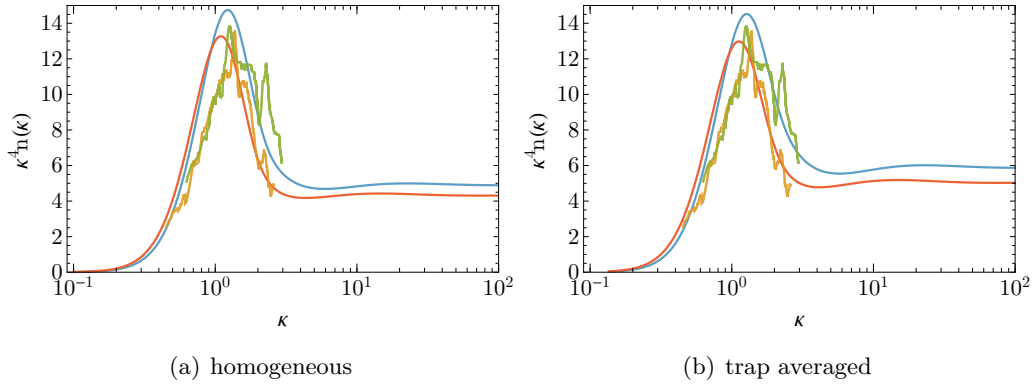
Figure 3.21: (a) Momentum distributions of the homogeneous unitary Bose gas in comparison to the measurements of ref. [94] for the densities $\langle n \rangle = 5.5 \times 10^{12} cm^{-3}$ (orange line) and $\langle n \rangle = 1.6 \times 10^{12} cm^{-3}$ (green line). The dimensionless momentum is $\kappa = q/k_F$. The continuous red line denotes a momentum distribution at $\kappa'_* \lambda_T = 1$ and fugacity $z = 0.35$. The blue line is a momentum distribution at $\kappa'_* \lambda_T = 1.38$ and fugacity $z = 0.29$. (b) Momentum distributions after trap-averaging. Color coding as in (a), however the fugacities are now $z = 0.44$ (blue line) and $z = 0.54$ (red line). The values of $\kappa_* \lambda_T$ are the same, but for the trap center.

expansion in this regime has to be understood as an extrapolation. The temperatures extracted in this way are much larger than the ones before the ramp. The data given in ref. [94] implies $T/T_F = 0.17$ ($\kappa'_*/k_F = 8.33/22.7$) and $T/T_F = 0.07$ ($\kappa'_*/k_F = 5.52/22.7$) for the temperatures before the ramp to unitarity.

In fig. 3.21(a), the resulting momentum distributions are shown. It should be noted that a trap-averaging procedure fits the experimental values even a little better, but changes the picture only slightly, as can be seen from fig. 3.21(b), which shows the momentum distributions after the trap averaging process. However, the values of the fugacity and $T/T_F$ turn out to be different. In table 3.3, our findings for $T/T_F$, $n\lambda_T^3$, and the fugacity $z$ are shown. For completeness, also the trap-averaged[8]

---

[8]The trap averaging procedure assumes that the system only is in local equilibrium [102], as well as the local density approximation. The biggest weakness in this scheme right now is that we have to assume a constant value of $\kappa_* \lambda_T$ throughout the trap, which is certainly violated when

| $\kappa'_*/k_F$ | $\kappa_* \lambda_T$ | $T/T_F$ | $n\lambda_T^3$ | $z$ |
|---|---|---|---|---|
| 5.52/22.7 | 1.0 | 0.74 | 1.18 | 0.35 |
| 5.52/22.7 trap | 1.0 | 0.55 | 2.93 | 0.54 |
| 8.33/22.7 | 1.38 | 0.9 | 0.89 | 0.29 |
| 8.33/22.7 trap | 1.38 | 0.66 | 2.22 | 0.44 |

Table 3.3: Experimental quantities involving temperature. For the trap averaged results read: $\kappa_* \lambda_T$ is the value in the trap center, $T/T_F$ and $n\lambda_T^3$ are trap averages over the Thomas Fermi profile. $z$ is the fugacity, that is assumed to be constant throughout the trap (assumption of only local equilibrium [102]).

values are given, for details on the calculation see appendix F. One could improve upon the results given here by refining the grid in $\kappa_* \lambda_T$, which could yield even nicer fitting curves, and more precise values for $T/T_F$. Another possibility would be to develop a code that actually can take into account a local dependence of $\kappa_* \lambda_T$ over the trap.

Turning to the interpretation of our results, our findings might mean two things: Either the virial expansion is not a good approximation in the experimental regime. Even though this turns out to be true mathematically, the virial expansion for Fermi gases has proven to be a good extrapolation to values as low as $T/T_F \approx 0.5$ [76]. Figure 3.22 supports this further: It shows the fugacity of the homogeneous system as a function of $T/T_F$ for both experimental values of $\kappa_*/k_F$. In both cases, the extracted value of $T/T_F$ is still far away from the maximum, which we can interpret as lower bound for the validity of the virial expansion (also see the discussion in sec. 2.3.1). Another possible explanation is that the experiment is not populating the deepest trimer branch during the ramp and in the time where the momentum distribution is recorded. This might have to do with the ramp times, which are roughly $5\mu s$. Investigating this matter more closely would be interesting. Last,

---

the gas only equilibrates locally.
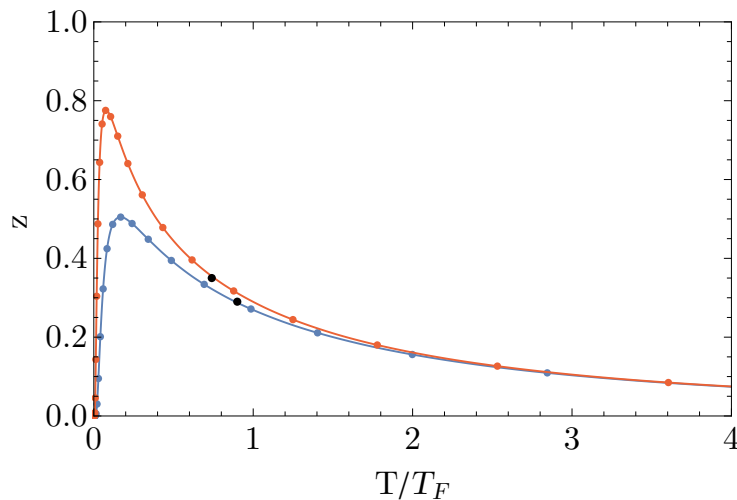
Figure 3.22: Fugacity $z$ as function of $T/T_F$, as obtained from the inversion of the density expansion in eq. (3.12) in the homogeneous case. Black dots denote the values we extract from the (homogeneous) momentum distributions that fit the experiment the best. The red line corresponds to $\kappa_*/k_F = 5.22/22.7$, while the blue line is for $\kappa_*/k_F = 8.33/22.7$.

but not least, note that the fitting procedure employed in [105] can *not* distinguish between the trimer branches, and hence our results do not contradict any existing work.

## 3.7 Outlook

In summary, we have performed a virial expansion of both a fermionic and a bosonic quantum gas with large scattering length. The virial expansion has allowed us to calculate virial coeffcients, contact parameters, and the momentum distribution in the non-degenerate regime. We have presented the formalism that is necessary to solve, as far as possible, all the diagrams up to third order in the fugacity. The fermionic case was studied for comparison with the bosonic case and to test our numerical routines.

In the bosonic case, we have calculated the third virial coefficient as a function of scattering length and temperature, and we observe a rapid variation around the three-atom and atom-dimer thresholds. The third virial coefficient of the bosonic gas

becomes negative in the scattering dominated limit. In order to prevent the system from collapsing, we have assumed that the spectrum is bounded from below, even though we are using universal theory for the calculations. It would be interesting to see if theories that incorporate an effective range, and hence have no need for such an artifical cutoff-procedure, still produce a negative third virial coefficient at large temperatures. In principle, the formalism for such a calculation would be the same as the one presented here. From the adiabatic theorems, we have predicted values for the two- and three-body contacts and compared them to the bosonic momentum distribution. We see beautiful agreement with the universal predictions of the tails. Saturation to the tails happens fastest at unitarity.

Last, but not least, we have compared our calculations to the experiment [94]. Since the temperature after the ramp to unitarity is unknown, we had to guess the temperature by looking at the predicted momentum distributions for different values of $\kappa_* \lambda_T$. We found good agreement under the assumption that the relevant three-body parameter in experiment is scaled down by a factor of $1/22.7$. This could possibly indicate that the experiment does not populate the lowest trimer branch. Since the virial expansion assumes thermodynamic equilibrium, it is not capable of explaining why or how this would happen. Further investigation in this direction, using time dependent methods, might provide understanding if our assertion is correct, and if yes why.

One could extend the calculations presented here to the fermionic case with two species of different mass, such that the ratio is bigger than 13.6. In this case, we also expect Efimov-like behavior [107, 7], and it is worthwhile to not already truncate the expansion at $z^2$, because the $z^3$ sector is by definition the first one to include three-particle correlations in an exact manner.

# Chapter 4

# Short-distance properties of Coulomb systems

> "Something unknown is doing
> we don't know what."
>
> *(Sir Arthur Eddington)*

In the following, let us switch gears completely and discuss short-distance / high-momentum properties of the Coulomb system. In particular, we will study the short-distance behavior of the one-particle density matrix and the density-density correlator. The short-distance singularities in these correlation functions give rise to power law tails of the associated Fourier transforms, namely the momentum distribution and the static structure factor. The motivation to study this problem came from the contact-interacting Fermi gases, where the operator product expansion (OPE) was successfully employed to (re-)derive and extend a set of formulas that are known as the "Tan universal relations" [32, 27]. These universal relations were used extensively in the preceding chapters. They relate the quantity known as the contact, which is connected (see eq. (2.13)) to the zero-distance pair correlation function $\sim \psi_1\psi_2\psi_2\psi_1(\mathbf{R})$, to various high-momentum / high-frequency tails of the system. Via the adiabatic theorem (see (2.12) for the 2D case), these tails can also be connected to the *thermodynamics* of the system (see my diploma thesis for a detailed derivation in the 1D case [27]). Since the proof of the adiabatic theorem relies on the contact-interacting nature of the system, we will not be able to connect the high-momentum tails of the Coulomb-interacting system, the nature of which is extremely long ranged, to its thermodynamics.

The Coulomb problem is inherently interesting, because it describes the physics of the basic (in a non-relativistic picture) constituents of matter, such as electron-electron, nucleus-nucleus, as well as nucleus-electron interactions. The long ranged

Coulomb potential $\sim e^2/r$, where $-e$ is the charge of an electron, and $r$ is the distance between the two interaction partners, acts *instantaneously*[1]. The Coulomb problem has been the subject of extensive study [125] regarding the stability of ordinary matter. Stability requires the (neutral) systems energy to scale *extensively*, i.e. linearly with the number of constituents. Super-linear scaling would lead to a collapse, sub-linear scaling would destroy the possibility that charged matter can accumulate in the form of liquids or solids. The proof of the linear scaling, and, in consequence, the stability of matter, relies on the Pauli-principle, i.e. the fermionic nature of the electrons. The exact mass and statistics of the nuclei does not play a role in this proof.

The *jellium model* approximates a metal as a gas of freely moving electrons, together with a smeared out positively charged background that ensures the charge neutrality of the system. In the ground state, the relevant dimensionless coupling strength is $r_s = r_0/a_0$, where[2] $a_0 = \hbar^2/me^2$ is the Bohr radius and $r_0$ is the average distance between the electrons. In three dimensions, $r_0$ is connected to the electronic density via $r_0 = (3/4\pi n)^{\frac{1}{3}}$. In two dimensions, we have $r_0 = (1/\pi n)^{\frac{1}{2}}$. The jellium model predicts cohesion energy and compressibility of some metals reasonably well [78, 126, 47]. Despite its simplicity however, very few exact results are known even for this highly simplified problem. Because of the long-ranged nature of the Coulomb potential, perturbation theory works in the opposite regime, where one would usually (at least from the cold gases viewpoint) expect it to work: It is the *high-density* limit $r_s \ll 1$, where perturbation around a non-interacting Fermi gas works. This can be understood by writing the Hamiltonian of the jellium model, in units of $\mathrm{Ry} = e^2/2a_0$ (distances in units $r_0$), as

$$H \;\; = \;\; -\frac{1}{r_s^2}\sum_i \nabla_i^2 + \frac{1}{r_s}\sum_{i<j}\frac{2}{|\mathbf{r}_i - \mathbf{r}_j|} + H_b, \tag{4.1}$$

where the sums label the electrons. $H_b$ accounts for both, the energy of the homogeneous background, as well as its interactions with the electrons. For the jellium model, this results in $H_b$ being a constant (but, to cancel the mutual Coulomb repulsion of the electrons, infinite) shift of the energy, which is why we do not give

---

[1]In the Maxwell equations when using the Coulomb gauge, causality is still valid because the components of the electric field that result from the gauge field via $\sim \partial_t \mathbf{A}(\mathbf{x})$ travel with the speed of light $c$ and the instantaneous part gets canceled out as well.

[2]In most of this chapter, $\hbar$ will still, like in the preceding chapters, be set to one. When discussing the classical limit, however, $\hbar$ needs to be restored. It is thus useful to keep the dependence of the defining quantities of the system on $\hbar$ explicit.

its form explicitly. In the high density limit $r_s \to 0$, the kinetic energy in the Hamiltonian (4.1) dominates. As a result, the Coulomb interaction can indeed be treated perturbatively in this limit, which makes a Fermi liquid description applicable (except for the Kohn-Luttinger effect [127], which is a mechanism that can cause superfluidity even for purely repulsive fermions). This implies, for example, a jump in the momentum distribution at $|\mathbf{q}| = k_F$, where the height of the jump is given by the quasi particle residue $0 < Z < 1$. Typical values for metals are, however, in the range of $1 < r_s < 5$, and perturbation theory has to be understood as an extrapolation. Despite this fact, the qualitative features of electrons in metals are still captured correctly in this picture. In the low-density limit $r_s \to \infty$, the interaction energy in the Hamiltonian (4.1) becomes dominant. Minimization of the interaction term leads to the expectation that the electron liquid forms a *Wigner crystal* at sufficiently low densities. Intermediate phases are expected to show up as well, in fact, in two dimensions, a direct transition from the liquid to the Wigner crystal was ruled out by thermodynamic arguments [128]. The precise nature of the intermediate phases, however, stays an open topic even today.

The experimental realization of two-dimensional electron gases (2DEG) using "quantum wells" [129], has also made the two-dimensional jellium problem relevant. In particular, note that we do not discuss the Coulomb problem in two-dimensional space, i.e. we do *not* solve the Helmholtz equation of a point charge in two dimensions to obtain the potential. We are rather thinking about the experimental situation, where the electrons are confined to two-dimensional motion, while the electric field can still permeate all three spatial dimensions. Hence, we still have a $\sim e^2/r$ potential in the 2D case.

In view of the complexity of the – already highly simplified – jellium problem, any exact relation one can derive may prove useful. As mentioned above, we will employ an OPE to (re-)derive such exact relations for the high-momentum tails of the static structure factor and the momentum distribution of the electron in the approximation given by the jellium model. It should be noted that Kimball [130, 131, 132] derived this behavior in the seventies, using an assumption of factorization of the many-body wave function when two electrons come close together. Previous work on the subject was done by Kato [133], and the behavior of the wave function at small relative distances was generalized in refs. [134, 135]. Since the derivation presented below only involves operator identities, we can extend the validity of these relations to all temperatures and phases, regardless of particle number. The only possibility for the system to avoid tails of the form we will derive, is, as we will see below, a

vanishing of the pair correlation function at zero distance. This is in close analogy to the case of contact-interacting Fermi gases, where a vanishing contact is the only possibility to avoid the $C/k^4$ tail in the momentum distribution. The contact indeed vanishes, for example, in the non-interacting system, consistent with the expectation that the momentum distribution is given by a Fermi function, which decays exponentially. The derivation given here also offers the advantage that we can even prove the factorization of the wave functions, as assumed by Kimball [130, 131, 132]. Moreover, even though his results are correct, part of the proof, being pedantic, relied on an infinite recursion [130], and no clear criterion to break out of this recursion was offered. Furthermore, even though the OPE itself is quite involved, the connection to the tails is straight forward once the OPE is established. The calculation of the tails from a wave function approach is more involved, because one needs to take into account all the possibilities that different particle coordinates come close together. All the results which are derived here can be readily extended to the attractive case via the replacement $e \to -e$. In particular, this would allow for the inclusion of the nuclei.

The chapter is structured as follows: in sec. 4.1, we will see that the hydrogen atom provides the simplest example for the high momentum tails in the electronic momentum distribution and structure factor. These tails are of the exact form that we will discover in later sections. In sec. 4.2, the jellium model is introduced in a field theoretic language. Correlation functions that are relevant later on are defined. In sec. 4.3, a comprehensive summary of the two-body scattering problem with $\sim 1/r$ interactions in two and three dimensions is given. Essentially, solving the two-particle scattering problem amounts to solving the continuous part of the spectrum of the hydrogen Hamiltonian, which is rarely discussed in quantum mechanics courses. In sec. 4.4, we establish the short-distance OPE for the density-density correlator, which is then connected to the static structure factor. In sec. 4.5, the (quite involved) OPE for the one-particle density matrix is established, and is then connected to the momentum distribution. In sec. 4.6, we will prove the approximate factorization of the ground state wave function when the coordinates of two particles are close by. Finally, since the high-momentum tails contain the zero-distance value $g(0)$ of the pair-correlation function, sec. 4.7.2 will study its behavior in the analytically solvable limits of high temperatures and in the classical limit. While those are typically taken to be equivalent, we will learn that in the case of Coulomb interactions, the limits $T \to \infty$ and $\hbar \to 0$ do *not* commute.

## 4.1 Hydrogen atom as the simplest example

The hydrogen atom provides an analytically solvable example for the exact relations that we are about to derive. The only difference to the relations that will follow is that the reduced mass of the system is $m$, rather than $m/2$, and that the interaction is attractive rather than repulsive. This can be accounted for by the replacement $1/a_0 \to -2/a_0$ in the asymptotic relations (4.44) and (4.77) that are given in secs. 4.4 and 4.5. The wave functions of the relative motion, that are part of the discrete (bound) spectrum of the Hamiltonian (in the approximation of infinite proton mass) are, in spherical coordinates $\mathbf{r} = (r\cos\varphi\sin\theta, r\sin\varphi\sin\theta, r\cos\theta)$, given by [136]

$$\psi_{nlm}(\mathbf{r}) = \left(\frac{2}{a_0 n}\right)^{\frac{3}{2}} \sqrt{\frac{(n-l-1)!}{2n(n+l)!}} Y_{lm}(\theta,\varphi) \left(\frac{2r}{a_0 n}\right)^l e^{-\frac{r}{a_0 n}} L_{n-l-1}^{2l+1}\left(\frac{2r}{a_0 n}\right), \quad (4.2)$$

where $n$ is the principal quantum number, $l$ is the angular quantum number and $m$ denotes the magnetic quantum number. $Y_{lm}(\theta,\varphi)$ denotes the spherical harmonics and $L_{n-l-1}^{2l+1}(z)$ stands for the generalized Laguerre polynomials [113]. The Fourier transform

$$\Upsilon_{nlm}(\mathbf{q}) = \int d^3 r\, e^{-i\mathbf{q}\cdot\mathbf{r}} \psi_{nlm}(\mathbf{r}) \tag{4.3}$$

was first calculated by Podolski and Pauling [137]. In spherical coordinates $\mathbf{q} = (q\cos\phi\sin\vartheta, q\sin\phi\sin\vartheta, q\cos\vartheta)$, the momentum space wave functions are given by

$$\begin{aligned}
\Upsilon_{nlm}(\mathbf{q}) = {}& 2^{2l+4}\pi(a_0 n)^{\frac{3}{2}}(-i)^l l! \sqrt{\frac{n(n-l-1)!}{(n+l)!}} Y_{lm}(\vartheta,\phi) \\
& \times \frac{\zeta^l}{(\zeta^2+1)^{l+2}} C_{n-l-1}^{l+1}\left(\frac{\zeta^2-1}{\zeta^2+1}\right),
\end{aligned} \tag{4.4}$$

where $\zeta = q a_0 n$ and $C_{n-l-1}^{l+1}(z)$ is a Gegenbauer polynomial [113] (sometimes called "ultra-spherical function", because it can be viewed as the natural generalization of the spherical harmonics to higher dimensions). The absolute square of the momentum space wave function (4.4) defines the momentum distribution of the electron. Expansion of $|\Upsilon_{nlm}(\mathbf{q})|^2$ in a series around $q = \infty$ reveals that it decays asymptotically like $1/q^{8+2l}$. Thus, $l = 0$ ($s$-wave states) constitute the slowest decaying contribution. For the $s$-wave states, the leading term in the series reads

$$n_{e^-}(\mathbf{q}) = |\Upsilon_{n00}(\mathbf{q})|^2 = \left(\frac{8\pi}{a_0}\right)^2 \frac{|\psi_{n00}(\mathbf{0})|^2}{q^8} + \mathcal{O}\left(\frac{1}{q^{10}}\right). \tag{4.5}$$

The *s*-wave states are the only ones where the electron has a non-vanishing probability density $|\psi_{nlm}(\mathbf{0})|^2 = 1/\pi(a_0 n)^3$ at the origin (proton).

The same – using terminology from cold atoms – "contact density" also shows up in the atomic form factor $\rho_{nlm}(\mathbf{q})$, which is defined as the Fourier transform of the electronic density distribution $|\psi_{nlm}(\mathbf{r})|^2$. For *s*-wave states, the leading order term in a series around $q = \infty$, which can be extracted from the Fourier transform of a short-distance expansion [138] of the density distribution defined by the wave function (4.2), is given by

$$\rho_{n00}(\mathbf{q}) \quad = \quad \frac{16\pi}{a_0} \frac{|\psi_{n00}(\mathbf{0})|^2}{q^4} + \mathcal{O}\left(\frac{1}{q^6}\right). \tag{4.6}$$

Higher angular momentum states contribute only at higher orders $1/q^{4+2l}$ in the momentum tail. As was the case for the momentum distribution, the coefficient of the leading order tail is associated with the probability density for the electron and proton to sit at the same spot. Since the leading orders in both cases come from $l = 0$ states, the tails are spherically symmetric.

In the following sections, we will see that the many-body systems exhibits similar behavior. The "contact" probability density $|\psi_{n00}(\mathbf{0})|^2$ will be replaced by the contact value $g(0)$ of the pair correlation function. In addition, the leading order short-range contributions will also be found to spherically symmetric.

## 4.2 Model and conventions

To study the problem within the OPE framework, we will now set up the model and define the correlators in second quantized form. The Hamiltonian of the jellium model is, in second quantized form, given by [78]

$$\begin{aligned}
H \quad = \quad & H_b + \sum_\sigma \int d^d x \, \psi_\sigma^\dagger \left[ \frac{-\hbar^2 \nabla^2}{2m} \right] \psi_\sigma(\mathbf{x}) \\
& + \frac{1}{2} \sum_{\sigma,\sigma'} \int d^d x d^d x' \, \psi_\sigma^\dagger(\mathbf{x}) \psi_{\sigma'}^\dagger(\mathbf{x}') \frac{e^2}{|\mathbf{x} - \mathbf{x}'|} \psi_{\sigma'}(\mathbf{x}') \psi_\sigma(\mathbf{x}),
\end{aligned} \tag{4.7}$$

where the summation over $\sigma, \sigma' = \uparrow, \downarrow$ sums over the two possible electronic spins. The factor $1/2$ in front of the interaction term accounts for a double counting, and $H_b$, as mentioned earlier, accounts for the homogeneous, positively charged background [78]. Since the Hamiltonian is only given by one- and two-particle terms, the energy it defines can be rewritten in terms of the one- and two-particle reduced

density matrices $\gamma^{(1)}$ and $\gamma^{(2)}$ [125]. The one-body density matrix, in position and spin-resolved form, reads

$$\gamma_\sigma^{(1)}(\mathbf{x}, \mathbf{x}') \;=\; \left\langle \psi_\sigma^\dagger(\mathbf{x}) \psi_\sigma(\mathbf{x}') \right\rangle. \tag{4.8}$$

Because the Hamiltonian (4.7) does not contain any spin flip processes, we have simplified the one-body density matrix to the diagonal form in spin space $\sim \delta_{\sigma\sigma'}$. The one-body density matrix defines the momentum distribution of the system via

$$
\begin{aligned}
n_\sigma(\mathbf{q}) &= \frac{1}{V} \int d^d x\, d^d x'\, e^{-i\mathbf{q}\cdot(\mathbf{x}'-\mathbf{x})} \left\langle \gamma_\sigma(\mathbf{x},\mathbf{x}') \right\rangle \\
&= \frac{1}{V} \int d^d R\, d^d r\, e^{-i\mathbf{q}\cdot\mathbf{r}} \left\langle \psi_\sigma^\dagger\left(\mathbf{R}-\frac{\mathbf{r}}{2}\right)\psi_\sigma\left(\mathbf{R}+\frac{\mathbf{r}}{2}\right)\right\rangle,
\end{aligned} \tag{4.9}
$$

where the intensive normalization $\int_\mathbf{q} n_\sigma(\mathbf{q}) = n_\sigma$, that gives the density $n_\sigma$ of species $\sigma$ after integration over all momenta, was chosen. In the second line, we have, via the substitution $[\mathbf{R} = (\mathbf{x} + \mathbf{x}')/2;\ \mathbf{r} = \mathbf{x}' - \mathbf{x}]$, already brought the correlation function into a form that will convenient for the OPE in sec. 4.5. The substitution has determinant one and does not change the prefactor.

In order to characterize the interaction energy in the Hamiltonian (4.7), the "diagonal" elements $\gamma_{\sigma\sigma,\sigma'\sigma'}^{(2)}(\mathbf{x},\mathbf{x};\mathbf{x}',\mathbf{x}')$ are sufficient. They define the dimensionless, spin-resolved pair distribution function $g_{\sigma\sigma'}(\mathbf{x},\mathbf{x}')$:

$$n_\sigma(\mathbf{x})n_{\sigma'}(\mathbf{x}')g_{\sigma,\sigma'}(\mathbf{x},\mathbf{x}') \;=\; \left\langle \psi_\sigma^\dagger(\mathbf{x})\psi_{\sigma'}^\dagger(\mathbf{x}')\psi_{\sigma'}(\mathbf{x}')\psi_\sigma(\mathbf{x}) \right\rangle \tag{4.10}$$

The pair distribution function $g_{\sigma,\sigma'}(\mathbf{x},\mathbf{x}')$ is a measure for the probability that a particle with spin projection $\sigma'$ can be found at location $\mathbf{x}'$, given that there is a particle with spin projection $\sigma$ sitting at location $\mathbf{x}$. We say that the system is completely uncorrelated, when $g_{\sigma\sigma'}(\mathbf{x},\mathbf{x}') \equiv 1\ \forall \mathbf{x},\mathbf{x}' \in \mathbb{R}^d$. Note that, in order to stay as general as possible, we did not use any assumptions about translational invariance. The assumption of translational invariance will be violated in, for example, a Wigner crystallized phase. For non-crystallized homogeneous phases, the pair correlation function approaches unity for large enough separations $|\mathbf{x} - \mathbf{x}'| \to \infty$: $g(\mathbf{x},\mathbf{x}') \to 1$, which reflects the fact there exists a finite correlation length in a liquid or gaseous phase. The *total pair distribution function*, defined as

$$g(\mathbf{x},\mathbf{x}') \;=\; \sum_{\sigma\sigma'} \frac{n_\sigma(\mathbf{x})n_{\sigma'}(\mathbf{x}')}{n(\mathbf{x})n(\mathbf{x}')} g_{\sigma\sigma'}(\mathbf{x},\mathbf{x}'), \tag{4.11}$$

also approaches unity in this limit. It is the sum of the spin-resolved pair distribution functions, weighted by the according densities. The static structure factor $S(\mathbf{q})$ of

the system is defined as the Fourier transform of the density-density correlator [126]:

$$S(\mathbf{q}) = \frac{1}{N} \int d^dx d^dx' \, e^{-i\mathbf{q}\cdot(\mathbf{x}'-\mathbf{x})} \langle n(\mathbf{x}) n(\mathbf{x}') \rangle - (2\pi)^d n\delta(\mathbf{q})$$
$$= \frac{1}{N} \int d^dR d^dr \, e^{-i\mathbf{q}\cdot\mathbf{r}} \left\langle n\left(\mathbf{R} - \frac{\mathbf{r}}{2}\right) n\left(\mathbf{R} + \frac{\mathbf{r}}{2}\right) \right\rangle - (2\pi)^d n\delta(\mathbf{q}). \qquad (4.12)$$

We have again used the substitution $[\mathbf{R} = (\mathbf{x} + \mathbf{x}')/2; \, \mathbf{r} = \mathbf{x}' - \mathbf{x}]$, that will be convenient for the OPE in sec. 4.4. The $\delta$-function ensures that $S(\mathbf{q} = \mathbf{0})$ is finite and comes from the fact the static structure factor only encodes density *fluctuations* around the average density. At $\mathbf{q} \neq 0$, this contribution can obviously be neglected. In the translational invariant case $g(\mathbf{x}, \mathbf{x}') = g(\mathbf{x}' - \mathbf{x})$, the static structure factor $S(\mathbf{q})$ simplifies further to give

$$S(\mathbf{q}) = 1 + n \int d^dr e^{-i\mathbf{q}\cdot\mathbf{r}}(g(\mathbf{r}) - 1). \qquad (4.13)$$

The one outside the integral comes from the self correlation term, i.e. the $\delta$ function of the fields when we anti-commute them into the order given in (4.10).

The behavior of the pair correlation function at small separations $|\mathbf{x} - \mathbf{x}'| \to 0$ discriminates between the contributions from equal and opposite spins. For equal spins, because of the Pauli principle, $g_{\sigma\sigma}(\mathbf{x}, \mathbf{x}')$ vanishes quadratically as $|\mathbf{x}-\mathbf{x}'| \to 0$. For particles of opposite species, the behavior at vanishing separation is, as we will see in sec. 4.4, dominated by the Coulomb interaction. Allowing for a finite spin polarization $\zeta = (n_\uparrow - n_\downarrow)/n$, the contact value $g(\mathbf{0})$ of the total pair distribution function can be written as

$$g(\mathbf{0}) = \frac{1}{2}(1 - \zeta^2)g_{\uparrow\downarrow}(\mathbf{0}), \qquad (4.14)$$

where we have simplified the expression to the translational invariant case. In the case of no translational invariance, here and in the following, one should read $g(\mathbf{0}, \mathbf{R})$ instead. The dependence on the "center of mass" coordinate (see eq. (4.12)) $\mathbf{R} = (\mathbf{x} + \mathbf{x}')/2$ will be suppressed from now on.

## 4.3 Two-body scattering

Having concluded our section on the model itself, as well as the correlators of interest, let us study the two-electron scattering problem next. The two-body scattering matrix will be needed for the matching process performed in sections 4.4 and 4.5. We will not go into full detail, but rather shortly test the validity of the results of
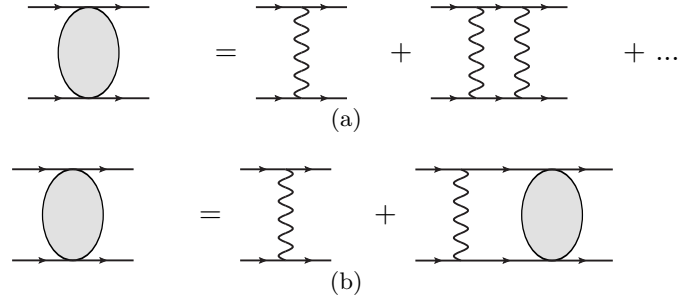
Figure 4.1: Different ways to obtain the two-electron scattering amplitude. 4.1(a) shows the series that has been summed in refs. [139, 140, 141] (3D) and [142] (2D). 4.1(b) shows the Lippmann-Schwinger integral equation. A wavy line with momentum transfer $\mathbf{q}$ contributes a factor $-iV(\mathbf{q})$, where $V(\mathbf{q})$ is defined in eq. (4.16).

refs. [139, 140, 141] (3D case) and [142] (2D case), which derive a one parameter representation of the Coulomb Green's function. This is instructive, as we get to know the functions $H_2$ and $H_3$, as well as their important "reduction property" (see eqs. (4.19) and (4.26) below). We will use these functions and, implicitly, the reproduction property during the matching process in sections 4.4 and 4.5.

The two-body scattering amplitude in the center of mass frame can be expressed diagrammatically as an infinite series (see diagram 4.1(a)) of re-scattering between the two interaction partners. Re-summing the series on the right-hand side yields the well-known Lippmann-Schwinger integral equation for the scattering amplitude $i\mathcal{A}$ (which is connected to the $T$ matrix by $T = -\mathcal{A}$), shown in fig. 4.1(b). For the Coulomb problem with center of mass energy $E = k_0^2/m$, the Lippmann-Schwinger equation reads

$$i\mathcal{A}(k_0, \mathbf{p}, \mathbf{p}') \;=\; -iV(\mathbf{p} - \mathbf{p}') + \int_{\mathbf{q}} \frac{V(\mathbf{p} - \mathbf{q})}{\frac{k_0^2}{m} - \frac{\mathbf{q}^2}{m} + i\epsilon} i\mathcal{A}(k_0, \mathbf{q}, \mathbf{p}'), \qquad (4.15)$$

where, using the residue theorem, the integration over the undetermined loop energy $q_0$ was already performed. $V(\mathbf{q})$ denotes the Fourier transform of the Coulomb

potential. It is given by

$$V(\mathbf{q}) = \int d^dx e^{-i\mathbf{q}\cdot\mathbf{x}} \frac{e^2}{|\mathbf{x}|} = \begin{cases} \dfrac{2\pi e^2}{|\mathbf{q}|} & \text{(2D)} \\[3mm] \dfrac{4\pi e^2}{|\mathbf{q}|^2} & \text{(3D)}, \end{cases} \tag{4.16}$$

where have explicitly chosen the repulsive version of the potential to account for electron-electron scattering. As noted earlier, just replace $e^2 \to -e^2$ in the attractive case. Diagrammatically, the action of the potential is indicated by a wavy line that contributes $-iV(\mathbf{q})$. All the other Feynman rules are the same as in chapter 2.2, also see appendix A.

### 4.3.1 Three-dimensional scattering problem

In order to solve the Lippmann-Schwinger equation in the three-dimensional case, let us define the auxiliary function ($x \in [0, 1]$)

$$H_3(k_0, \mathbf{p}, \mathbf{p}', x) = (1-x)^2(k_0^2 - p^2)(k_0^2 - p'^2) - 4xk_0^2(\mathbf{p} - \mathbf{p}')^2 \tag{4.17}$$

$$\Rightarrow \frac{d}{dx}\frac{x}{H_3(k_0, \mathbf{p}, \mathbf{p}', x)} = \frac{(1-x^2)(k_0^2 - p^2)(k_0^2 - p'^2)}{H_3^2(k_0, \mathbf{p}, \mathbf{p}', x)}. \tag{4.18}$$

The key property of $H_3$, which allows, using an inductive proof [139, 141], for re-summation of the scattering series in fig. 4.1(a), is

$$\int_{\mathbf{q}} \frac{1}{(\mathbf{p} - \mathbf{q})^2} \frac{-4k_0^2}{q^2 - k_0^2 - i\epsilon} \frac{d}{dx}\frac{x}{H_3(k_0, \mathbf{q}, \mathbf{p}', x)} = -\frac{ik_0}{2\pi} \frac{1}{H_3(k_0, \mathbf{p}, \mathbf{p}', x)}, \tag{4.19}$$

together with the observation that one can rewrite

$$\frac{1}{(\mathbf{p} - \mathbf{p}')^2} = -4k_0^2 \int_0^1 dx \frac{d}{dx}\frac{x}{H_3(k_0, \mathbf{p}, \mathbf{p}', x)} = -\frac{4k_0^2}{H_3(k_0, \mathbf{p}, \mathbf{p}', 1)}. \tag{4.20}$$

The above equalities can be shown using elementary integration methods. The $\epsilon > 0$ is important to determine the sign of the final expression in eq. (4.19). We will call (4.19) the *reduction property*. With the definition of $H_3$ at hand, we can now define the scattering amplitude in the three dimensional case as

$$i\mathcal{A}(k_0, \mathbf{p}, \mathbf{p}') = 16\pi ie^2 k_0^2 \int_0^1 dx\, x^{i\xi} \frac{d}{dx}\frac{x}{H_3(k_0, \mathbf{p}, \mathbf{p}', x)}, \tag{4.21}$$

where $\xi = me^2/2k_0$. To test if this truly is the solution to the Lippmann-Schwinger equation (4.15), we just plug it into the former, together with the 3D version (4.16)

of the Fourier-transformed Coulomb potential:

$$
\begin{aligned}
i\mathcal{A}(k_0, \mathbf{p}, \mathbf{p}') \quad &= \quad -i\frac{4\pi e^2}{(\mathbf{p}-\mathbf{p}')^2} \\
&\quad + \int_0^1 dx\, x^{i\xi} \int_{\mathbf{q}} \frac{4\pi e^2}{(\mathbf{p}-\mathbf{q})^2} \frac{16\pi i e^2 k_0^2}{\frac{k_0^2}{m}-\frac{\mathbf{q}^2}{m}+i\epsilon} \frac{d}{dx}\frac{x}{H_3(k_0,\mathbf{q},\mathbf{p}',x)} \\
\overset{(4.20),(4.19)}{=} \quad & i\frac{16\pi e^2 k_0^2}{H_3(k_0,\mathbf{p},\mathbf{p}',1)} \\
&\quad -i16\pi e^2 k_0^2 i\xi \int_0^1 dx\, x^{i\xi-1}\frac{x}{H_3(k_0,\mathbf{p}.\mathbf{p}',x)} \\
\overset{\text{PI}}{=} \quad & i16\pi e^2 k_0^2 \int_0^1 dx\, x^{i\xi}\frac{d}{dx}\frac{x}{H_3(k_0,\mathbf{p},\mathbf{p}',x)} = (4.21) \qquad (4.22)
\end{aligned}
$$

The last equality can be readily shown by partial integration. The anti-derivative of the integrand vanishes at $x = 0$, and the $x = 1$ term cancels against the bare Coulomb potential. This concludes the section on scattering of two electrons in three dimensions. The integral representation (4.21) of the scattering amplitude will lead to the fact that most two-particle matrix elements are, in secs. 4.4 and 4.5, also written in terms of an integral representation.

### 4.3.2 Two-dimensional scattering problem

The two-dimensional case can be treated in a completely analogous manner (see refs. [142, 143, 144] for a detailed derivation), we just have to come up with the right function $H_2$ that fulfills the two-dimensional analogue of the reduction property (4.19), as well as eq. (4.20) in order to re-express the Coulomb potential. To this end, define

$$
H_2(k_0, \mathbf{p}, \mathbf{p}', x) \quad = \quad \sqrt{-H_3(k_0, \mathbf{p}, \mathbf{p}', x)} \qquad (4.23)
$$

$$
\Rightarrow \frac{d}{dx}\frac{x^{\frac{1}{2}}}{H_2(k_0, \mathbf{p}, \mathbf{p}', x)} \quad = \quad -\frac{1}{2\sqrt{x}}\frac{(1-x^2)(k_0^2-p^2)(k_0^2-p'^2)}{H_2^3(k_0, \mathbf{p}, \mathbf{p}', x)}, \qquad (4.24)
$$

where $H_3$ is given in equation (4.17). Like in the 3D case, we can easily express the Coulomb potential in terms of the auxiliary function $H_2$:

$$
\frac{1}{|\mathbf{p}-\mathbf{p}'|} \quad = \quad 2k_0 \int_0^1 dx \frac{d}{dx}\frac{x^{\frac{1}{2}}}{H_2(k_0, \mathbf{p}, \mathbf{p}', x)} = \frac{2k_0}{H_2(k_0, \mathbf{p}, \mathbf{p}', 1)} \qquad (4.25)
$$

Setting $k_0^2 \to k_0^2 + i\epsilon$, in order to make the square roots that appear in the problem well defined, we can also show that $H_2$ indeed possesses the convenient reduction

property

$$\int_{\mathbf{q}} \frac{1}{|\mathbf{p}-\mathbf{q}|} \frac{2k_0}{q^2-k_0^2-i\epsilon} \frac{d}{dx} \frac{x^{\frac{1}{2}}}{H_2(k_0,\mathbf{q},\mathbf{p}',x)} = \frac{i}{2\pi} \frac{x^{-\frac{1}{2}}}{H_2(k_0,\mathbf{p},\mathbf{p}',x)}. \tag{4.26}$$

We follow the same path as in the three-dimensional case, and define the two-dimensional amplitude $i\mathcal{A}$ in terms of $H_2$ via

$$i\mathcal{A}(k_0,\mathbf{p},\mathbf{p}') = -4\pi i e^2 k_0 \int_0^1 dx\, x^{i\xi} \frac{d}{dx} \frac{x^{\frac{1}{2}}}{H_2(k_0,\mathbf{p},\mathbf{p}',x)}, \tag{4.27}$$

where $\xi = me^2/2k_0$ is the same as in the three-dimensional case. Insertion of the above amplitude into the Lippmann-Schwinger equation (4.15), this time with the 2D form (4.16) of the Coulomb potential, yields

$$
\begin{aligned}
i\mathcal{A}(k_0,\mathbf{p},\mathbf{p}') \quad &= \quad -i\frac{2\pi e^2}{|\mathbf{p}-\mathbf{p}'|} \\
&\quad + \int_0^1 dx\, x^{i\xi} \int_{\mathbf{q}} \frac{2\pi e^2}{|\mathbf{p}-\mathbf{q}|} \frac{-4\pi i e^2 k_0}{\frac{k_0^2}{m}-\frac{\mathbf{q}^2}{m}+i\epsilon} \frac{d}{dx} \frac{x^{\frac{1}{2}}}{H_2(k_0,\mathbf{q},\mathbf{p}',x)} \\
&\overset{(4.25),(4.26)}{=} \frac{-4\pi i e^2 k_0}{H_2(k_0,\mathbf{p},\mathbf{p}',1)} + 4\pi i e^2 k_0 i\xi \int_0^1 dx\, x^{i\xi-1} \frac{x^{\frac{1}{2}}}{H_2(k_0,\mathbf{p},\mathbf{p}',x)} \\
&\overset{\text{PI}}{=} \quad -4\pi i e^2 k_0 \int_0^1 dx\, x^{i\xi} \frac{d}{dx} \frac{x^{\frac{1}{2}}}{H_2(k_0,\mathbf{p},\mathbf{p}',x)} = (4.27). \tag{4.28}
\end{aligned}
$$

For the last equality, we have again used partial integration. Like in the 3D case, the anti-derivative vanishes at $x = 0$, and the $x = 1$ piece cancels against the bare Coulomb potential.

Armed with the two-body scattering amplitudes for both two and three dimensions, we are prepared to perform the OPE for the correlators of interest up to the two-electron sector. In particular, the trick of expressing the amplitudes as single parameter integrals will be applied to the two-particle matrix elements during the matching process in secs. 4.4 and 4.5.

## 4.4 Operator Product Expansion for the static structure factor

The static structure factor was already introduced in sec. 4.2. It is the Fourier transform of the density-density correlator, cf. (4.12), and thus measures fluctuations in the electronic density distribution. The aim in the following will be to make

exact statements about its asymptotic behavior at high momenta $|\mathbf{q}| \to \infty$. Before proceeding, we define the spin-resolved static structure factor as

$$S_{\sigma\sigma'} = \frac{1}{N} \int d^d R d^d r \, e^{-i\mathbf{q}\cdot\mathbf{r}} \left\langle n_\sigma \left( \mathbf{R} - \frac{\mathbf{r}}{2} \right) n_{\sigma'} \left( \mathbf{R} + \frac{\mathbf{r}}{2} \right) \right\rangle$$
$$- (2\pi)^d \frac{n_\sigma n_{\sigma'}}{n} \delta(\mathbf{q}). \qquad (4.29)$$

For $\sigma \neq \sigma'$, we call it the inter-species structure factor. Correspondingly, for $\sigma = \sigma'$, it is the intra-species structure factor. The sum of the spin resolved structure factors gives the static structure factor defined in eq. (4.12):

$$S(\mathbf{q}) = \sum_{\sigma,\sigma'} S_{\sigma\sigma'}(\mathbf{q}) \qquad (4.30)$$

Since the static structure factor $S(\mathbf{q})$ is given as the Fourier transform of the density-density correlator, its asymptotic behavior at high momenta is governed by short-distance singularities of the density-density correlator. This mapping of singularities is a generic property of the Fourier transform [138]. The short-distance singular behavior of the density-density correlator, in turn, is – in a state-independent fashion – encoded in its OPE. Establishing the OPE will be the aim in the following. Note that we will focus on the OPE of the *inter-species* density-density correlator $n_\uparrow(\mathbf{R} - \mathbf{r}/2)n_\downarrow(\mathbf{R}+\mathbf{r}/2)$, since, because of the Pauli principle, the density-density correlator for equal species only contains sub-leading singularities as $|\mathbf{r}| \to 0$. Hence, the high-momentum corrections for $S_{\uparrow\uparrow}(\mathbf{q})$ only come in at higher order in $1/|\mathbf{q}|$.

For the jellium problem, by dimensional analysis, the OPE for operators $\mathcal{O}_a$ and $\mathcal{O}_b$, which are separated by a small distance and have scaling dimensions $\Delta_a$ and $\Delta_b$, has to look like

$$\mathcal{O}_a \left( \mathbf{R} - \frac{\mathbf{r}}{2} \right) \mathcal{O}_b \left( \mathbf{R} + \frac{\mathbf{r}}{2} \right) = \sum_n r^{\Delta_n - \Delta_a - \Delta_b} f_n \left( \frac{r}{a_0}, \hat{\mathbf{e}}_\mathbf{r} \right) \mathcal{O}_n(\mathbf{R}), \quad (4.31)$$

where $\Delta_n$ denotes the scaling dimension of the operator $\mathcal{O}_n$. The Wilson coefficient $c_n(\mathbf{r})$ was split into a naive scaling part and a dimensionless function $f_n$. The function $f_n(r/a_0, \hat{\mathbf{e}}_\mathbf{r})$ only depends on the dimensionless combination $r/a_0$, and possibly the direction of $\mathbf{r} = r\hat{\mathbf{e}}_\mathbf{r}$. The operators with the lowest scaling dimensions are again expected to contribute at the lowest orders. These remarks apply both to the OPE of the density-density correlator, as well as to one of the one-particle density matrix, which is discussed in sec. 4.5.

For the inter-species density-density correlator, the OPE with operators up to scaling dimension $2d + 1$ (length dimension $L^{-2d-1}$) takes the form

$$\psi_\uparrow^\dagger\psi_\uparrow\left(\mathbf{R} - \frac{\mathbf{r}}{2}\right)\psi_\downarrow^\dagger\psi_\downarrow\left(\mathbf{R} + \frac{\mathbf{r}}{2}\right) = c_{\uparrow\dagger\downarrow\dagger\downarrow\uparrow}(\mathbf{r})\,\psi_\uparrow^\dagger\psi_\downarrow^\dagger\psi_\downarrow\psi_\uparrow(\mathbf{R})$$

$$+ \sum_{A,i} c_{A_i}(\mathbf{r})\partial_{A_i}\psi_\uparrow^\dagger(\mathbf{R}_1)\psi_\downarrow^\dagger(\mathbf{R}_2)\psi_\downarrow(\mathbf{R}_3)\psi_\uparrow(\mathbf{R}_4)\Bigg|_{\mathbf{R}_A=\mathbf{R}} + \dots, \quad (4.32)$$

where $A = 1, .., 4$ labels the vectors $\mathbf{R}_A$ and $i$ its components. For both two and three dimensions, the Wilson coefficients of the first order derivative operators combine in such a way that they reproduce the result that would be obtained from a Taylor expansion:

$$\psi_\uparrow^\dagger\psi_\uparrow\left(\mathbf{R} - \frac{\mathbf{r}}{2}\right)\psi_\downarrow^\dagger\psi_\downarrow\left(\mathbf{R} + \frac{\mathbf{r}}{2}\right) = c_{\uparrow\dagger\downarrow\dagger\downarrow\uparrow}(\mathbf{r})\,\psi_\uparrow^\dagger\psi_\downarrow^\dagger\psi_\downarrow\psi_\uparrow(\mathbf{R})$$

$$+ \frac{\mathbf{r}}{2}\cdot\left[\psi_\uparrow^\dagger\psi_\uparrow\nabla\psi_\downarrow^\dagger\psi_\downarrow - \left(\nabla\psi_\uparrow^\dagger\psi_\uparrow\right)\psi_\downarrow^\dagger\psi_\downarrow\right](\mathbf{R}) + \dots, \quad (4.33)$$

which can be inferred from diagrams 4.2(a) and 4.3(a) that we will meet in the matching process in the following. The derivation of these analytic terms will thus not be given explicitly. After Fourier transform, the analytic terms will not contribute to the high-momentum tail of the static structure factor. All one-particle operators are of course trivially matched to zero, because the matrix elements of the left-hand side of (4.33) require the presence of at least one particle of each spin-species to be non-zero.

### 4.4.1 Matching

We will now determine the Wilson coefficient of the contact operator $\psi_\uparrow^\dagger\psi_\downarrow^\dagger\psi_\downarrow\psi_\uparrow$. To this end, we first calculate the matrix elements of the interspecies density-density correlator in (off-shell) scattering states $|k_0, \pm\mathbf{0}\rangle$, which contain one $\uparrow$ and one $\downarrow$ electron with relative momentum zero and total off-shell energy $k_0$. We expand the result with respect to small $k_0$ (or small $r$) and match it against the matrix elements of the contact. The Feynman rules of the operators can be derived following the same logic that is presented in appendix A.2. For two particles with incoming
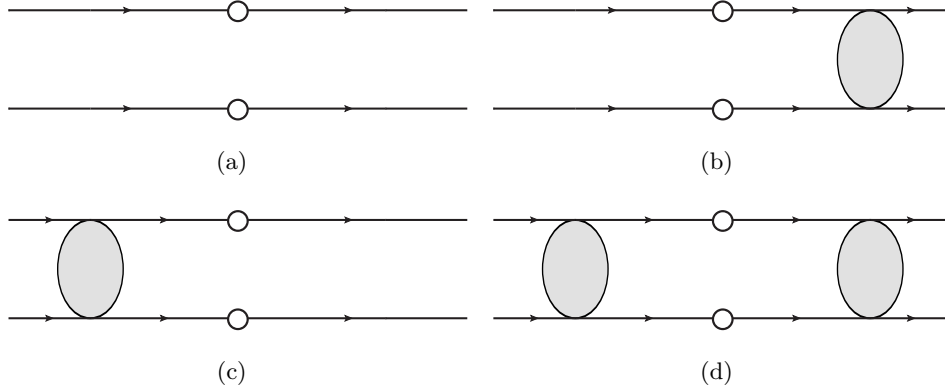
Figure 4.2: Diagrams for the matrix element of $\psi_\uparrow^\dagger \psi_\uparrow (\mathbf{R} - \mathbf{r}/2)\psi_\downarrow^\dagger \psi_\downarrow (\mathbf{R} + \mathbf{r}/2)$.

momenta $\mathbf{p}_\uparrow, \mathbf{p}_\downarrow$ and outgoing momenta $\mathbf{p}'_\uparrow, \mathbf{p}'_\downarrow$, the resulting rules are:

$$
\begin{aligned}
\psi_\uparrow^\dagger \psi_\uparrow (\mathbf{R} - \mathbf{r}/2)\psi_\downarrow^\dagger \psi_\downarrow (\mathbf{R} + \mathbf{r}/2) : & \qquad e^{i\mathbf{R}\cdot(\mathbf{p}_\uparrow + \mathbf{p}_\downarrow - \mathbf{p}'_\uparrow - \mathbf{p}'_\downarrow) + i\frac{\mathbf{r}}{2}\cdot(\mathbf{p}_\downarrow - \mathbf{p}'_\downarrow + \mathbf{p}'_\uparrow - \mathbf{p}_\uparrow)} \\
\psi_\uparrow^\dagger \psi_\downarrow^\dagger \psi_\downarrow \psi_\uparrow (\mathbf{R}) : & \qquad e^{i\mathbf{R}\cdot(\mathbf{p}_\uparrow + \mathbf{p}_\downarrow - \mathbf{p}'_\uparrow - \mathbf{p}'_\downarrow)} \\
\psi_\uparrow^\dagger \psi_\uparrow \nabla \psi_\downarrow^\dagger \psi_\downarrow (\mathbf{R}) : & \qquad i(\mathbf{p}_\downarrow - \mathbf{p}'_\downarrow)e^{i\mathbf{R}\cdot(\mathbf{p}_\uparrow + \mathbf{p}_\downarrow - \mathbf{p}'_\uparrow - \mathbf{p}'_\downarrow)} \\
\left(\nabla\psi_\uparrow^\dagger \psi_\uparrow\right) \psi_\downarrow^\dagger \psi_\downarrow (\mathbf{R}) : & \qquad i(\mathbf{p}_\uparrow - \mathbf{p}'_\uparrow)e^{i\mathbf{R}\cdot(\mathbf{p}_\uparrow + \mathbf{p}_\downarrow - \mathbf{p}'_\uparrow - \mathbf{p}'_\downarrow)} \qquad (4.34)
\end{aligned}
$$

**Matrix element of the density-density correlator**

The matrix element of the inter-species density-density correlator $n_\uparrow(\mathbf{R} - \mathbf{r}/2)n_\downarrow(\mathbf{R} + \mathbf{r}/2)$ is the sum of the four diagrams 4.2(a) - 4.2(d). In order to keep the formulas short, it is useful to define an auxiliary integral

$$
\mathcal{Z}_d(\mathbf{r}, k_0) = \int_{\mathbf{q}} e^{i\mathbf{q}\cdot\mathbf{r}} \frac{i}{\frac{k_0^2}{m} - \frac{\mathbf{q}^2}{m} + i\epsilon} i\mathcal{A}(k_0, \mathbf{q}, \mathbf{0}), \qquad (4.35)
$$

where the index $d = 2, 3$ stands for the dimensionality of the momentum integration and the form of the scattering amplitude $i\mathcal{A}$ [in $d = 2$: (4.27), in $d = 3$ : (4.21)]. To linear order in $k_0|\mathbf{r}|$, the integral evaluates to

$$
\mathcal{Z}_d(\mathbf{r}, k_0) = \begin{cases} -2i\xi \int_0^1 dx\, \frac{x^{i\xi - 1/2}}{1 + x} + 4\xi k_0|\mathbf{r}| \int_0^1 dx\, x^{i\xi} \frac{d}{dx}\frac{x^{1/2}}{1 + x} + \mathcal{O}(|\mathbf{r}|^2) & \text{(2D)} \\[2ex] -4i\xi \int_0^1 dx\, \frac{x^{i\xi}}{(1 + x)^2} + 4\xi k_0|\mathbf{r}| \int_0^1 dx\, x^{i\xi} \frac{d}{dx}\frac{x}{(1 + x)^2} + \mathcal{O}(|\mathbf{r}|^2) & \text{(3D)} \end{cases}
$$
$$(4.36)$$

For more details on the evaluation of the integral $\mathcal{Z}_d(\mathbf{r}, k_0)$, see appendix G.1.

Using the Feynman rule (4.34), the sum of the four diagrams in fig. 4.2 can now be expressed in the compact form

$$\left\langle k_0, \pm\mathbf{0} \left| \psi_\uparrow^\dagger \psi_\uparrow (\mathbf{R} - \mathbf{r}/2) \psi_\downarrow^\dagger \psi_\downarrow (\mathbf{R} + \mathbf{r}/2) \right| k_0, \pm\mathbf{0} \right\rangle = (1 + \mathcal{Z}_d(\mathbf{r}, k_0))^2. \quad (4.37)$$

Expansion of the result to linear order in $|\mathbf{r}|$ yields

$$\left\langle k_0, \pm\mathbf{0} \left| \psi_\uparrow^\dagger \psi_\uparrow (\mathbf{R} - \mathbf{r}/2) \psi_\downarrow^\dagger \psi_\downarrow (\mathbf{R} + \mathbf{r}/2) \right| k_0, \pm\mathbf{0} \right\rangle$$

$$= \begin{cases} \left( 1 - 2i\xi \int_0^1 dx \, \dfrac{x^{i\xi - 1/2}}{1 + x} \right)^2 \\ \quad + 8\xi k_0 |\mathbf{r}| \int_0^1 dx' \, x'^{\,i\xi} \dfrac{d}{dx'} \dfrac{x'^{1/2}}{1 + x'} \left( 1 - 2i\xi \int_0^1 dx \, \dfrac{x^{i\xi - 1/2}}{1 + x} \right) + \mathcal{O}(|\mathbf{r}|^2) \end{cases} \quad (2\text{D})$$

$$\qquad \begin{cases} \left( 1 - 4i\xi \int_0^1 dx \, \dfrac{x^{i\xi - 1} x}{(1 + x)^2} \right)^2 \\ \quad + 8\xi k_0 |\mathbf{r}| \int_0^1 dx' \, x'^{\,i\xi} \dfrac{d}{dx'} \dfrac{x'}{(1 + x')^2} \left( 1 - 4i\xi \int_0^1 dx \, \dfrac{x^{i\xi - 1} x}{(1 + x)^2} \right) + \mathcal{O}(|\mathbf{r}|^2) \end{cases} \quad (3\text{D})$$

$$\overset{\text{PI}}{=} \begin{cases} \left[ 1 + \dfrac{2|\mathbf{r}|}{a_0} \right] \left( 2 \int_0^1 dx \, x^{i\xi} \dfrac{d}{dx} \dfrac{x^{1/2}}{1 + x} \right)^2 + \mathcal{O}(|\mathbf{r}|^2) & (2\text{D}) \\[4mm] \left[ 1 + \dfrac{|\mathbf{r}|}{a_0} \right] \left( 4 \int_0^1 dx \, x^{i\xi} \dfrac{d}{dx} \dfrac{x}{(1 + x)^2} \right)^2 + \mathcal{O}(|\mathbf{r}|^2) & (3\text{D}) \end{cases}$$

$$(4.38)$$

For the third part of the equation, partial integration was used to compactify the expressions. $\xi = me^2/2k_0$ was plugged in to make the dependence on $|\mathbf{r}|/a_0$ apparent. The off-shell energy $k_0$ carries information about the specifics of the state and can not be part of a Wilson coefficient. The small $|\mathbf{r}|$ expansion of the matrix element was factorized into a part that indeed is independent of $k_0$, and a part that carries information about the state. As we will see, the latter is exactly the matrix element of the contact operator.

### 4.4.2 Matrix element of the contact operator

The matrix element of the contact operator $\psi_\uparrow^\dagger \psi_\downarrow^\dagger \psi_\downarrow \psi_\uparrow (\mathbf{R})$ in the states $|k_0, \pm\mathbf{0}\rangle$ is given by the sum of the four diagrams shown in fig. 4.3. Due to the fact that incoming and outgoing total momentum of the vertex vanish in the states $|k_0, \pm\mathbf{0}\rangle$
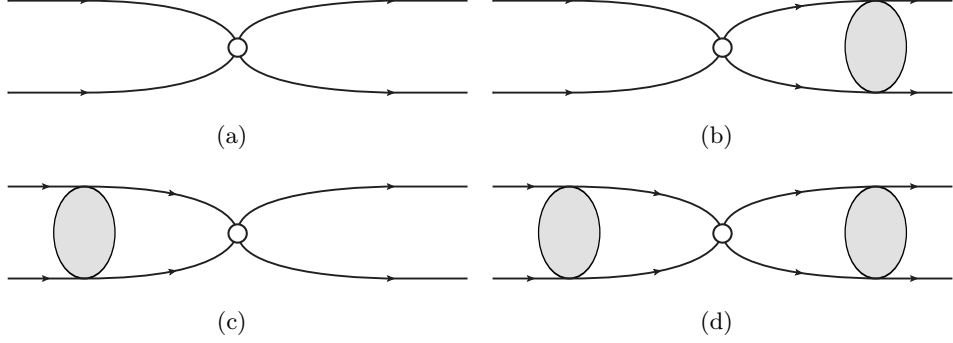
Figure 4.3: Diagrams for the matrix element of $\psi_\uparrow^\dagger \psi_\downarrow^\dagger \psi_\downarrow \psi_\uparrow(\mathbf{R})$.

(see the Feynman rule (4.34)), the matrix element of the contact simplifies to

$$\left\langle k_0, \pm\mathbf{0} \left| \psi_\uparrow^\dagger \psi_\downarrow^\dagger \psi_\downarrow \psi_\uparrow(\mathbf{R}) \right| k_0, \pm\mathbf{0} \right\rangle \;=\; (1 + \mathcal{Z}_d(\mathbf{0}, k_0))^2, \tag{4.39}$$

where the auxiliary integral $\mathcal{Z}(\mathbf{0}, k_0)$ is given by eq. (4.36) with $|\mathbf{r}| = 0$. Following the same path as in equation (4.38), we can simplify the sum of the four diagrams 4.3(a)-4.3(d) via partial integration to:

$$\begin{aligned}
&\langle k_0, \pm\mathbf{0} | \psi_\uparrow^\dagger \psi_\downarrow^\dagger \psi_\downarrow \psi_\uparrow(\mathbf{R}) | k_0, \pm\mathbf{0} \rangle \\
&= \begin{cases}
\left( 2 \displaystyle\int_0^1 dx\, x^{i\xi} \frac{d}{dx} \frac{x^{1/2}}{1+x} \right)^2 &=\; \dfrac{1}{16\xi^4} + \mathcal{O}(k_0^6) \quad \text{(2D)} \\[4mm]
\left( 4 \displaystyle\int_0^1 dx\, x^{i\xi} \frac{d}{dx} \frac{x}{(1+x)^2} \right)^2 &=\; \dfrac{1}{4\xi^4} + \mathcal{O}(k_0^6) \quad \text{(3D)}
\end{cases}
\end{aligned} \tag{4.40}$$

The leading order term of a series expansion around $k_0 = 0$ ($\xi = \infty$) will prove useful when matching the matrix elements of the contact for the OPE of the momentum distribution. For details on how to perform the series expansion, see appendix G.2.1, where we expand the scattering amplitudes in an analogous fashion. Note that in the states with zero external momenta, diagrams 4.3(a)-4.3(d) vanish for the first order derivative operators given in 4.33. Because of this, by comparison of eqs. (4.40) and (4.38), the Wilson coefficient of the contact (up to order $|\mathbf{r}|$) is determined:

$$c_{\uparrow\downarrow\uparrow\downarrow\uparrow}(\mathbf{r}) = \begin{cases}
1 + \dfrac{2|\mathbf{r}|}{a_0} + \mathcal{O}(|\mathbf{r}|^2) & \text{(2D)} \\[4mm]
1 + \dfrac{|\mathbf{r}|}{a_0} + \mathcal{O}(|\mathbf{r}|^2) & \text{(3D)}
\end{cases} \tag{4.41}$$

We have thus successfully established the OPE (4.33) of the density-density correlator to order $|\mathbf{r}|$.

### 4.4.3 Results for the OPE and correlation functions

In the previous subsections, we have proven that the OPE of the interspecies density-density correlator takes the explicit form

$$
\psi_\uparrow^\dagger \psi_\uparrow \left( \mathbf{R} - \frac{\mathbf{r}}{2} \right) \psi_\downarrow^\dagger \psi_\downarrow \left( \mathbf{R} + \frac{\mathbf{r}}{2} \right) =
$$
$$
+ \left( 1 + 2^{3-d} \frac{|\mathbf{r}|}{a_0} \right) \psi_\uparrow^\dagger \psi_\downarrow^\dagger \psi_\downarrow \psi_\uparrow (\mathbf{R})
$$
$$
+ \frac{\mathbf{r}}{2} \cdot \left[ \psi_\uparrow^\dagger \psi_\uparrow \nabla \psi_\downarrow^\dagger \psi_\downarrow - \left( \nabla \psi_\uparrow^\dagger \psi_\uparrow \right) \psi_\downarrow^\dagger \psi_\downarrow \right] (\mathbf{R}) + \mathcal{O}(|\mathbf{r}|^2), \qquad (4.42)
$$

where $d = 2$ corresponds to the two-dimensional, and $d = 3$ to the three-dimensional case. By definition (4.10), the OPE (4.42) results in the

> **Universal short-distance expansion of the pair correlation function**
>
> The homogeneous electron gas displays the following universal short-distance behavior in its pair-correlation function:
>
> $$
> g(|\mathbf{r}|) = \begin{cases} \left( 1 + \dfrac{2|\mathbf{r}|}{a_0} + \dots \right) g(0) & \text{(2D)} \\ \left( 1 + \dfrac{|\mathbf{r}|}{a_0} + \dots \right) g(0) & \text{(3D)} \end{cases}, \qquad (4.43)
> $$
>
> Using the terminology of ref. [145], we call this the *cusp* condition.

In the mathematical literature, this condition is also often called the Kato-cusp condition [133, 135]. The result was restricted to the rotational invariant and homogeneous case. Both the two- and three-dimensional result agree with the results obtained by Kimball [130, 131, 132]. Due the Pauli principle, the contact value $g(0)$ of the pair correlation function only receives contributions from $g_{\uparrow\downarrow}(0)$ and $g_{\downarrow\uparrow}(0)$. Equation (4.43) implies that the pair correlation function of electrons at short distances exhibits a dip, and then *rises* with slope $2^{d-3} g(0)/a_0$. For the case of an attractive Coulomb interaction, we have to replace $a_0 \to -a_0$ (and possibly a numerical factor to take into account a different reduced mass). From the fact that the Coulomb attraction is strongest near the origin, we expect that the value of $g(0)$ is greater than one. Thus, in the attractive case, eq. (4.43) implies that the

pair correlation function has a maximum at $|\mathbf{r}| = 0$ and then *falls* off with slope $\sim -g(0)/a_0$. For simplicity, the name *cusp condition* is also be used in the repulsive case. It is interesting to note that one observes (see [27, 34]) a similar behavior for a one-dimensional, contact-interacting Fermi gas, with the Bohr radius $a_0$ being replaced by the one dimensional scattering length $a_1$.

The cusp condition (4.43) is violated by various approximations that have been used for the jellium problem. The most renowned one is the random phase approximation (RPA) [146], which becomes exact in the long wavelength limit. Of course, the inadequacy of the RPA at short distances arises from the fact that the RPA was designed to probe the opposite momentum regime that is probed here. However, since (4.43) constitutes an exact result, various extensions of RPA [147] that obey the cusp condition have been developed. These extensions include so-called local field corrections [147]. Within these schemes however, the price for capturing the correct short-range physics is the violation [148] of the "compressibility sum rule" $S(\mathbf{q}) \sim \mathbf{q}^2$ as $|\mathbf{q}| \to 0$.

As we have seen in sec. 4.2, the static structure factor is the Fourier transform of the density-density correlator, cf. eqs. (4.12),(4.29). The short-distance singularity $\sim |\mathbf{r}|$ in the pair correlation function implies[3] the following

---

**Asymptotic behavior of the static structure factor at large momenta**

The static structure factor of the homogeneous electron gas decays like

$$
S(\mathbf{q}) - 1 =
\begin{cases}
-\dfrac{4\pi}{a_0}\dfrac{ng(0)}{|\mathbf{q}|^3} + \mathcal{O}\left(|\mathbf{q}|^{-4}\right) & \text{(2D)} \\[2em]
-\dfrac{8\pi}{a_0}\dfrac{ng(0)}{|\mathbf{q}|^4} + \mathcal{O}\left(|\mathbf{q}|^{-5}\right) & \text{(3D)}
\end{cases}
\tag{4.44}
$$

at large momenta. The leading order correction comes solely from the inter-species part $S_{\uparrow\downarrow}(\mathbf{q})$ of the static structure factor, whereas the dominant 1 comes from the self-correlation part of the intra-species static structure factor $S_{\uparrow\uparrow}(\mathbf{q})$.

---

[3]The Fourier transform (in the sense of distributions [56]) of $|\mathbf{r}|$ is $-2\pi/|\mathbf{q}|^3$ and $-8\pi/|\mathbf{q}|^4$ in two and three dimensions, respectively. This can be shown by applying $\nabla_{\mathbf{q}}^2$ to eq. (4.16).

In the *inhomogeneous* system (with equal populations $n_\uparrow = n_\downarrow$), as can be seen from eq. (4.42), we have to replace

$$n_\uparrow n_\downarrow g_{\uparrow\downarrow}(0) \quad \rightarrow \quad \frac{1}{V} \int d^d R \left\langle \psi_\uparrow^\dagger \psi_\downarrow^\dagger \psi_\downarrow \psi_\uparrow (\mathbf{R}) \right\rangle \tag{4.45}$$

$$\frac{n}{2} g(0) \quad \rightarrow \quad \frac{1}{N} \int d^d R \left\langle \psi_\uparrow^\dagger \psi_\downarrow^\dagger \psi_\downarrow \psi_\uparrow (\mathbf{R}) \right\rangle \tag{4.46}$$

in eq. (4.44). The Wigner crystal phase would be an example where we indeed need the general, non-translation invariant, form above.

Another example is the case of hydrogen (see sec. 4.1): the absolute square of the relative wave function is indeed the analogue of the pair correlation function, as it describes the probability of finding the electron at position $\mathbf{r}$, given that the proton sits at the origin. In this case, we have

$$\int d^3 R \left\langle \psi_\uparrow^\dagger \psi_\downarrow^\dagger \psi_\downarrow \psi_\uparrow (\mathbf{R}) \right\rangle = |\psi_{n00}(0)|^2, \tag{4.47}$$

and our results (4.43) and (4.44) indeed reproduce the behavior observed in hydrogen, provided we replace $1/a_0 \rightarrow -2/a_0$. This replacement takes into account both the different reduced mass ($m_r = m$ instead of $m/2$) and the different sign for the attractive interaction.

## 4.5 Operator Product Expansion for the momentum distribution

The study of the hydrogen problem in sec. 4.1 already strongly suggests that there is also a universal high-momentum tail in the momentum distribution of the electron gas. Indeed, as found by Kimball [130, 131, 132], such a tail exists. In this section, we will establish an OPE for the one-particle density matrix, that proves this behavior in a *state-independent* fashion. The short-distance singularities of the one-particle density matrix define the large-momentum asymptotic behavior of the momentum distribution $n_\sigma(\mathbf{q})$, which is the Fourier transform of the former, cf. eq. (4.9). As is the case for cold Fermi gases, the leading order tail of the momentum distribution will be the same for both species $\sigma = \uparrow, \downarrow$.

Regarding the general structure of the OPE and its Wilson coefficients, the same remarks as in sec. 4.4 apply. In particular, the Wilson coefficients are again expected to be powers of $|\mathbf{r}|$, possibly multiplied by dimensionless functions of $|\mathbf{r}|/a_0$. The one-particle sector will, as shown below, contribute terms that look like a Taylor

expansion of the fields. With this in mind, we can write the OPE of the one-body density matrix as

$$
\psi_\sigma^\dagger \left(\mathbf{R} - \frac{\mathbf{r}}{2}\right) \psi_\sigma \left(\mathbf{R} + \frac{\mathbf{r}}{2}\right) = \left[e^{-i\frac{\mathbf{r}}{2}\cdot\nabla}\psi_\sigma^\dagger(\mathbf{R})\right]\left[e^{i\frac{\mathbf{r}}{2}\cdot\nabla}\psi_\sigma(\mathbf{R})\right]
$$
$$
+ c_{\uparrow\dagger\downarrow\dagger\downarrow\uparrow}(\mathbf{r})\psi_\uparrow^\dagger\psi_\downarrow^\dagger\psi_\downarrow\psi_\uparrow(\mathbf{R}) + \ldots, \quad (4.48)
$$

where we indicate the analytic terms as the product of the two fields with translation operators acting on them.

## 4.5.1 Matching

In this section, we will prove the form (4.48) of the OPE of the one particle density matrix. In particular, the explicit form of the Wilson coefficient of the contact operator is calculated. The postulated form of the bilinear field combinations with derivatives acting on them is proven first, via the matching between states that contain a single particle. These derivative terms will also be grouped together in a convenient way. This makes the evaluation of the diagrams that appear in the two-body sector more straightforward.

To determine the Wilson coefficient of the contact operator, we will then perform the matching in states that contain a single ↑- and a single ↓-electron. For both the two- and three-dimensional case, a calculation involving the full matrix elements like in sec. 4.4 is in principle possible. However, the calculations are, in both dimensions, extremely long. Great simplification arises when we only determine the leading orders of the matrix elements in $k_0$, at the cost however, that we have to introduce a somewhat artificial infrared cutoff. Since this procedure still allows to determine the Wilson coefficient of the contact uniquely, it is sufficient for our purpose.

**One-particle sector**

The simplest states with non-vanishing matrix elements of the one-particle density matrix $\psi_\sigma^\dagger \left(\mathbf{R} - \frac{\mathbf{r}}{2}\right) \psi_\sigma \left(\mathbf{R} + \frac{\mathbf{r}}{2}\right)$ are states that contain an electron of species $\sigma$. The incoming energy and momentum are called $E, \mathbf{p}$, the outgoing ones are $E', \mathbf{p}'$. The Feynman rules for the bilocal and local vertices are:

$$
\psi_\sigma^\dagger \left(\mathbf{R} - \frac{\mathbf{r}}{2}\right) \psi_\sigma \left(\mathbf{R} + \frac{\mathbf{r}}{2}\right) : \qquad e^{i\mathbf{p}\cdot\left(\mathbf{R}+\frac{\mathbf{r}}{2}\right)}e^{-i\mathbf{p}'\cdot\left(\mathbf{R}-\frac{\mathbf{r}}{2}\right)} \qquad (4.49)
$$

$$
\left(\partial_i^m \psi_\sigma^\dagger\right) \partial_j^n \psi_\sigma(\mathbf{R}) : \qquad (-ip_i')^m(ip_j)^n e^{i\mathbf{R}\cdot(\mathbf{p}-\mathbf{p}')} \qquad (4.50)
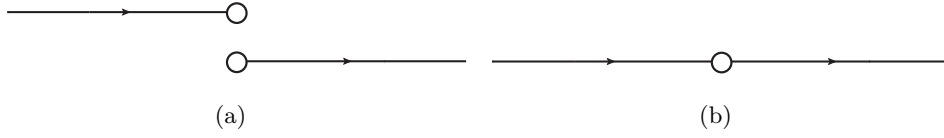$$

(a)                                    (b)

Figure 4.4: Diagrams for the matching of the one-particle sector. 4.4(a) represents the diagram for $\psi_\sigma^\dagger \left(\mathbf{R} - \frac{\mathbf{r}}{2}\right) \psi_\sigma \left(\mathbf{R} + \frac{\mathbf{r}}{2}\right)$. 4.4(b) is the diagram for all the local one particle operators on the right-hand side. Incoming energy and momentum are $E, \mathbf{p}$, outgoing energy and momentum are $E', \mathbf{p}'$.

The partial derivatives $\partial_i^m$ denote the derivative with respect to the coordinate $R_i$, $m$ times. Note that neither the vertex of the one-particle density matrix, nor the local one-body terms conserve energy or momentum, since they are not integrated over in time or space, cf. appendix A.2.

**Left-hand side**  The matrix element of the one-particle density matrix in the states $|E, \mathbf{p}\rangle$ and $|E', \mathbf{p}'\rangle$ is diagrammatically depicted in fig. 4.4(a). Its (amputated) value

$$
\left\langle E', \mathbf{p}' \left| \psi_\sigma^\dagger \left(\mathbf{R} - \frac{\mathbf{r}}{2}\right) \psi_\sigma \left(\mathbf{R} + \frac{\mathbf{r}}{2}\right) \right| E, \mathbf{p} \right\rangle
$$

$$
= e^{i\mathbf{p}\cdot\left(\mathbf{R}+\frac{\mathbf{r}}{2}\right)} e^{-i\mathbf{p}'\cdot\left(\mathbf{R}-\frac{\mathbf{r}}{2}\right)} = e^{i\mathbf{R}\cdot(\mathbf{p}-\mathbf{p}')} \left[ \sum_{m=0}^\infty \frac{\left(\frac{i}{2}\mathbf{r}^T\mathbf{p}\right)^m}{m!} \right] \left[ \sum_{u=0}^\infty \frac{\left(\frac{i}{2}\mathbf{r}^T\mathbf{p}'\right)^u}{u!} \right]
$$

$$
= e^{i\mathbf{R}\cdot(\mathbf{p}-\mathbf{p}')} \left[ \sum_{n=0}^\infty \left(\frac{i}{2}\right)^n \sum_{k=0}^n \frac{\left(\mathbf{r}^T\mathbf{p}\right)^{n-k} \left(\mathbf{r}^T\mathbf{p}'\right)^k}{(n-k)! \; k!} \right] \tag{4.51}
$$

can be directly inferred from the Feynman rule (4.49). In the second and third line, the scalar products were expressed in terms of the standard matrix multiplication. The matrix element was brought into a form that will be convenient for the matching of the local one-body operators. In particular, this form avoids –as best as possible– an index battle for all the different derivatives.

**Right-hand side**  In order to keep the calculation short, let us directly match derivative operators with ansatz-Wilson coefficients that are constructed to fit the result (4.51). Diagrammatically, the matrix elements are all given by fig. 4.4(b).

We are asking for the matrix element of the operators

$$
\left(\mathbf{r}^T \nabla_{\mathbf{x}'}\right)^k \psi_\sigma^\dagger(\mathbf{x}') \left(\mathbf{r}^T \nabla_{\mathbf{x}}\right)^{n-k} \psi_\sigma(\mathbf{x})\Big|_{\mathbf{x}=\mathbf{x}'=\mathbf{R}}, \tag{4.52}
$$

where $n$ and $k$ are positive integers such that $n - k > 0$. The Feynman-rule (4.50) implies that the matrix element in the states with incoming momentum $\mathbf{p}$ and outgoing momentum $\mathbf{p}'$ is given by

$$
\left\langle E', \mathbf{p}' \left| \left[ \left(\mathbf{r}^T \nabla_{\mathbf{x}'}\right)^k \psi_\sigma^\dagger(\mathbf{x}') \left(\mathbf{r}^T \nabla_{\mathbf{x}}\right)^{n-k} \psi_\sigma(\mathbf{x}) \right]\Big|_{\mathbf{x}=\mathbf{x}'=\mathbf{R}} \right| E, \mathbf{p} \right\rangle
$$
$$
= i^n(-1)^k \left(\mathbf{r}^T \mathbf{p}'\right)^k \left(\mathbf{r}^T \mathbf{p}\right)^{n-k} e^{i\mathbf{R}\cdot(\mathbf{p}-\mathbf{p}')}, \tag{4.53}
$$

which matches eq. (4.51) with coefficient $(-1)^k/2^n k!(n-k)!$. This shows that the OPE of the one-particle density matrix, in the one-particle sector, can indeed be written as

$$
\psi_\sigma^\dagger \left(\mathbf{R} - \frac{\mathbf{r}}{2}\right) \psi_\sigma \left(\mathbf{R} + \frac{\mathbf{r}}{2}\right) = \left[e^{-i\frac{\mathbf{r}}{2}\cdot\nabla} \psi_\sigma^\dagger(\mathbf{R})\right] \left[e^{i\frac{\mathbf{r}}{2}\cdot\nabla} \psi_\sigma(\mathbf{R})\right]
$$
$$
= \sum_{n=0}^\infty \frac{1}{2^n} \sum_{k=0}^n \frac{(-1)^k}{k!(n-k)!} \left[ \left(\mathbf{r}^T \nabla_{\mathbf{x}'}\right)^k \psi_\sigma^\dagger(\mathbf{x}') \left(\mathbf{r}^T \nabla_{\mathbf{x}}\right)^{n-k} \psi_\sigma(\mathbf{x}) \right]_{\mathbf{x}=\mathbf{x}'=\mathbf{R}}
$$
$$
\equiv \sum_{n=0}^\infty \mathcal{D}_n^\sigma(\mathbf{r}, \mathbf{R}). \tag{4.54}
$$

In the last line, we have defined operators $\mathcal{D}_n^\sigma(\mathbf{r}, \mathbf{R})$ that are the sum of all $n$-th order derivatives that contribute, together with their Wilson coefficients. This definition will turn out to be convenient during the matching in the two-particle sector.

### 4.5.2 Two-particle sector

In this section, we will perform the matching in the two-body sector. As mentioned earlier, we expand the matrix elements in a series around $k_0 = 0$ ($\xi = \infty$), which greatly simplifies the matching process. In order to get the leading order behavior of the matrix elements, we need to find the leading order term of the two-body scattering amplitudes $i\mathcal{A}$, given by eqs. (4.27) and (4.21), for the two- and three-dimensional case, respectively. We will be using states with vanishing external momentum, and the important amplitudes in the following will be

$$
i\mathcal{A}(k_0, \mathbf{q}, \mathbf{0}) = \begin{cases} \dfrac{2\pi i e^2}{4q\xi^2} + \mathcal{O}\left(\dfrac{1}{\xi^4}\right) & \text{(2D)} \\[3mm] \dfrac{4\pi i e^2}{2q^2\xi^2} + \mathcal{O}\left(\dfrac{1}{\xi^4}\right) & \text{(3D)} \end{cases} \tag{4.55}
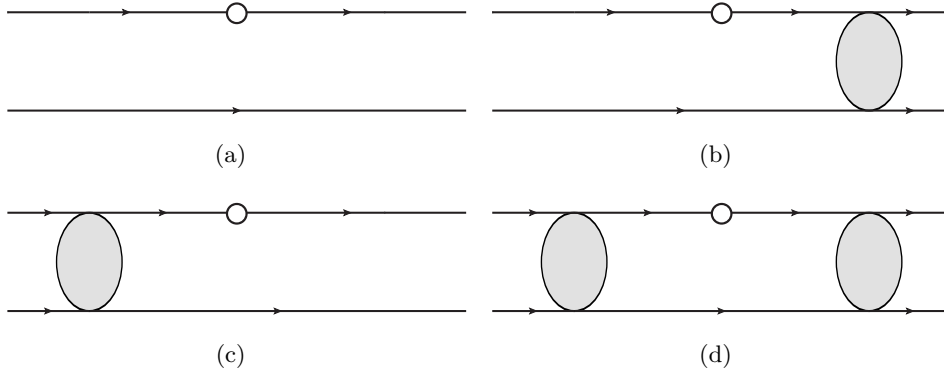$$

Figure 4.5: Diagrams for the matrix elements of the local one-body operators. We set the external and leaving momenta of the particles to $\pm\mathbf{0}$, which greatly simplifies the expressions. The center of mass energy of the entering and leaving particles is $k_0^2/m$.

For details on the expansion around $\xi = \infty$, please consult appendix G.2.1. The propagators $(q^2 - k_0^2)^{-1} \approx q^{-2}$ that appear in the diagrams will also be only taken at leading order in $k_0$. Note that this procedure introduces infrared divergences, which we regulate via the replacement $1/q \to 1/\sqrt{q^2 + \mu^2}$, where $\mu > 0$.

**Matrix elements of the local one-particle operators**

Before considering the actual matrix elements of the one-particle operators on the right-hand side of the OPE, we will derive an effective Feynman-rule for the operators $\mathcal{D}_n^\sigma(\mathbf{r}, \mathbf{R})$ that were defined in eq. (4.54). Due to the nature of the states we will be using, we only need the Feynman rule for equal incoming and outgoing momentum $\mathbf{p}$. Using the Feynman rule (4.50), we get the simple result

$$\mathcal{D}_n^\sigma(\mathbf{r}, \mathbf{R}): \qquad \frac{1}{2^n} \sum_{k=0}^n \frac{(-1)^k \left(-i\mathbf{r}^T\mathbf{p}\right)^k \left(i\mathbf{r}^T\mathbf{p}\right)^{n-k}}{k!(n-k)!} = \frac{(i\mathbf{p} \cdot \mathbf{r})^n}{n!}. \qquad (4.56)$$

In particular, for $n > 0$ and vanishing leaving and entering momenta at the vertex, $D_n^\sigma$ sets the diagram to zero.

The matrix elements of the operators $\mathcal{D}_n^\sigma(\mathbf{r}, \mathbf{R})$ in states $|k_0^2/m, \pm\mathbf{0}\rangle$ with zero relative momentum are given by the sum of the four diagrams shown in fig. 4.5. Using the Feynman rule (4.56), we get, for a given operator $\mathcal{D}_n^\sigma(\mathbf{r}, \mathbf{R})$, the following

expressions:

$$4.5(a) \quad = \quad \delta_{0,n}\delta_{(0,\mathbf{0})} \tag{4.57}$$

$$4.5(b) \quad = \quad \delta_{0,n}\frac{i}{\frac{k_0^2}{m}+i\epsilon}i\mathcal{A}(k_0,\mathbf{0},\mathbf{0}) \tag{4.58}$$

$$4.5(c) \quad = \quad \delta_{0,n}\frac{i}{\frac{k_0^2}{m}+i\epsilon}i\mathcal{A}(k_0,\mathbf{0},\mathbf{0}) \tag{4.59}$$

$$4.5(d) \quad = \quad \int_{\mathbf{q}}\frac{(i\mathbf{q}\cdot\mathbf{r})^n}{n!}\left(\frac{i}{\frac{k_0^2}{m}-\frac{q^2}{m}+i\epsilon}\right)^2(i\mathcal{A}(k_0,\mathbf{q},\mathbf{0}))^2, \tag{4.60}$$

where we have used the symmetry of the scattering amplitude $i\mathcal{A}(k_0,\mathbf{p},\mathbf{p}') = i\mathcal{A}(k_0,\mathbf{p}',\mathbf{p})$. For diagram 4.5(d), the integration over the loop energy was also already evaluated. Diagrams 4.5(a)-4.5(c) vanish for $n \geq 1$. Note that diagrams 4.5(a)-4.5(c) have to trivially match the corresponding diagrams 4.6(a)-4.6(c) of the bilocal operators, since there is no loop integration. As we will see below, this is indeed what happens, so let us now concentrate on the non-trivial diagram 4.5(d). The first observation regarding this diagram is that is vanishes for odd $n$, since the $\mathbf{q}$-integration is odd in this case. Let us denote the contribution of diagram 4.5(d) to the matrix element of $\mathcal{D}_n^\sigma(\mathbf{r},\mathbf{R})$ by $\mathcal{D}_n^\sigma|_{4.5(d)}$ in the following. In preparation for sec. 4.5.2, we have to calculate this contribution up to $n = 4$.

The – with respect to $k_0$ – expanded version of the $n = 0$ contribution is given by (also see eq. (4.55))

$$\mathcal{D}_0^\sigma|_{4.5(d)} = \begin{cases} \dfrac{\pi^2}{4a_0^2\xi^4}\displaystyle\int\frac{d^2q}{(2\pi)^2}\frac{1}{(q^2+\mu^2)^3} = \dfrac{\pi}{16a_0^2\xi^4}\dfrac{1}{2\mu^4} & \text{(2D)} \\[4mm] \dfrac{4\pi^2}{a_0^2\xi^4}\displaystyle\int\frac{d^3q}{(2\pi)^3}\frac{1}{(q^2+\mu^2)^4} = \dfrac{\pi}{48a_0^2\xi^4}\dfrac{3}{\mu^5} & \text{(3D)} \end{cases}, \tag{4.61}$$

where we grouped the result in a way that will allow for easy comparison to the bilocal diagram in section 4.5.2. The big advantage of the expansion technique is, as you can see, that the appearing integrals become solvable with elementary methods. Proceeding in the same way for $n = 2$, we get

$$\mathcal{D}_2^\sigma|_{4.5(d)} = \begin{cases} -\dfrac{1}{2}\dfrac{\pi^2}{4a_0^2\xi^4}\displaystyle\int\frac{d^2q}{(2\pi)^2}\frac{(\mathbf{q}\cdot\mathbf{r})^2}{(q^2+\mu^2)^3} = \dfrac{\pi}{16a_0^2\xi^4}\left(\dfrac{-r^2}{8\mu^2}\right) & \text{(2D)} \\[4mm] -\dfrac{1}{2}\dfrac{4\pi^2}{a_0^2\xi^4}\displaystyle\int\frac{d^3q}{(2\pi)^3}\frac{(\mathbf{q}\cdot\mathbf{r})^2}{(q^2+\mu^2)^4} = \dfrac{\pi}{48a_0^2\xi^4}\left(\dfrac{-r^2}{2\mu^3}\right) & \text{(3D)} \end{cases}. \tag{4.62}$$

For $n = 4$, a small complication arises in the two-dimensional case:

$$\mathcal{D}_4^\sigma|_{4.5(d)} = \begin{cases} \dfrac{1}{4!}\dfrac{\pi^2}{4a_0^2\xi^4}\displaystyle\int \dfrac{d^2q}{(2\pi)^2}\dfrac{(\mathbf{q}\cdot\mathbf{r})^4}{(q^2+\mu^2)^3} = \dfrac{\pi}{16a_0^2\xi^4}\left(-\dfrac{r^4}{32}\left(\dfrac{3}{4}+\log\dfrac{\mu}{\Lambda}\right)\right) & \text{(2D)} \\[4ex] \dfrac{1}{4!}\dfrac{4\pi^2}{a_0^2\xi^4}\displaystyle\int \dfrac{d^3q}{(2\pi)^3}\dfrac{(\mathbf{q}\cdot\mathbf{r})^4}{(q^2+\mu^2)^4} = \dfrac{\pi}{48a_0^2\xi^4}\left(\dfrac{r^4}{8\mu}\right) & \text{(3D)} \end{cases}$$

$$(4.63)$$

While the three-dimensional integral can be solved directly, we have to introduce a ultraviolet cutoff $\Lambda$ in order to regulate the diagram in the two-dimensional case. The equal sign for 2D is not exact, but the neglected terms are of order $\mu^2/\Lambda^2$ and higher. Since these terms vanish in the limit $\Lambda \to \infty$, we can safely omit them. In contrast to the artificial infrared cutoff $\mu$ that we had to introduce because we wanted to make our life easer, the ultraviolet cutoff $\Lambda$ is needed for *all* values of $k_0$. As will become clear in sec. 4.5.2 – since the matrix elements of the one-particle density matrix are *finite* – this is a case of so called *operator mixing* [35]. We mentioned this phenomenon already shortly in sec. 2.1, because the OPE for the one-particle density matrix of a contact-interacting Fermi gas shows similar behavior. In this case, the operator of the kinetic energy mixes with the contact, resulting in finite matrix elements for both of them. For our electronic case here, it is only the fourth derivative operator that needs renormalization, while the matrix elements of the contact given in eq. (4.40) are finite. Let us postpone the rest of this discussion until the calculation of the matrix elements of the left-hand side.

**Matrix element of the one-particle density matrix**

The matrix element of the one-particle density matrix is given by the sum of the diagrams shown in figure 4.6. The external lines still have the same incoming and outgoing momenta ($\pm\mathbf{0}$) and center of mass energies ($k_0^2/m$) as before. Bringing the diagrams into a form where incoming and outgoing momenta at the bilocal vertex are equal, and hence simplifying the Feynman rule (4.49) to $e^{i\mathbf{p}\cdot\mathbf{r}}$, we get the
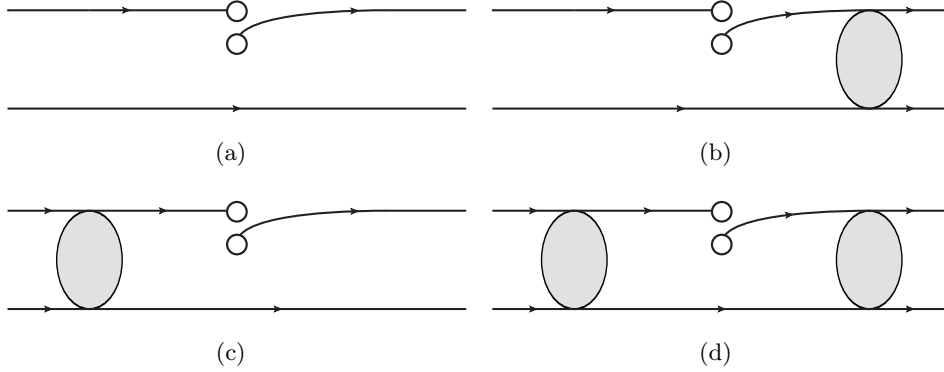
Figure 4.6: Diagrams for the matrix element of the bilocal one-particle density matrix. We again set the external incoming and outgoing momenta of the particles to $\pm\mathbf{0}$, and the center of mass energy of the entering and leaving particles to $k_0^2/m$.

following contributions:

$$4.6(a) \;=\; \delta_{(0,\mathbf{0})} \tag{4.64}$$

$$4.6(b) \;=\; \frac{i}{\frac{k_0^2}{m} + i\epsilon} i\mathcal{A}(k_0, \mathbf{0}, \mathbf{0}) \tag{4.65}$$

$$4.6(c) \;=\; \frac{i}{\frac{k_0^2}{m} + i\epsilon} i\mathcal{A}(k_0, \mathbf{0}, \mathbf{0}) \tag{4.66}$$

$$4.6(d) \;=\; \int_{\mathbf{q}} e^{i\mathbf{q}\cdot\mathbf{r}} \left( \frac{i}{\frac{k_0^2}{m} - \frac{q^2}{m} + i\epsilon} \right)^2 (i\mathcal{A}(k_0, \mathbf{q}, \mathbf{0}))^2, \tag{4.67}$$

Diagrams 4.6(a) - 4.6(c) exactly match the contribution of diagrams 4.5(a)-4.5(c) for $\mathcal{D}_0^\sigma = \psi_\sigma^\dagger \psi_\sigma$. Thus, the only piece we have left to determine is the loop integral in diagram 4.6(d). The three-dimensional integration can be solved straightforwardly using the residue theorem. The two-dimensional case[4] is tabulated in [149] and

---

[4]The integral is tabulated only indirectly, however they have: $I_{\text{aux}} = \int_0^\infty dq\, q J_0(qr) \cos(aq)(q^2 + \mu^2)^{-1} = \cosh(a) K_0(\mu r)$ for $a < r < \infty$. We see that we can produce our 2D integral $I_{2\text{D}}$ by $a \to 0$ and the combination $I_{2\text{D}} \sim \left[ \partial_\mu^2 I_{\text{aux}} - \partial_\mu I_{\text{aux}} \right]/\mu^2$. Filling in the constants and usage of recurrence relations [113] for the modified bessel functions $K_n(r\mu)$ yields the result.

yields a modified Bessel function. The loop integration results in

$$
4.6(d) = \begin{cases} \dfrac{\pi^2}{4a_0^2\xi^4} \displaystyle\int \dfrac{d^2q}{(2\pi)^2} \dfrac{e^{i\mathbf{q}\cdot\mathbf{r}}}{(q^2+\mu^2)^3} = \dfrac{\pi}{16a_0^2\xi^4} \dfrac{r^2 K_2(\mu r)}{4\mu^2} & \text{(2D)} \\[3ex]
\dfrac{4\pi^2}{a_0^2\xi^4} \displaystyle\int \dfrac{d^3q}{(2\pi)^3} \dfrac{e^{i\mathbf{q}\cdot\mathbf{r}}}{(q^2+\mu^2)^4} = \dfrac{\pi}{48a_0^2\xi^4} \dfrac{3+3\mu r+(\mu r)^2}{\mu^5} e^{-\mu r} & \text{(3D)} \end{cases}
$$

$$
= \begin{cases} \dfrac{\pi}{16a_0^2\xi^4} \left[ \dfrac{1}{2\mu^4} - \dfrac{r^2}{8\mu^2} + \dfrac{r^4}{32}\left(\dfrac{3}{4} - \log\mu - \log\dfrac{re^{\gamma_E}}{2}\right) \right] + \mathcal{O}(r^6) & \text{(2D)} \\[3ex]
\dfrac{\pi}{48a_0^2\xi^4} \left[ \dfrac{3}{\mu^5} - \dfrac{r^2}{2\mu^3} + \dfrac{r^4}{8\mu} - \dfrac{r^5}{15} \right] + \mathcal{O}(r^6), & \text{(3D)} \end{cases}
$$

$$(4.68)$$

where $\gamma_E = 0.577216..$ is the Euler-Mascheroni constant. The part that is still left to match, denoted by $A$, is given by the difference of (4.68) and the sum of the contributions of the local one-body operators $\mathcal{D}_n^\sigma|_{4.5(d)}$, cf. eqs. (4.61), (4.62) and (4.63):

$$
A = (4.68) - \sum_{n=0}^{4} \mathcal{D}_n^\sigma|_{4.5(d)}
$$

$$
= \begin{cases} -\left(\dfrac{2\pi}{a_0}\right)^2 \dfrac{r^4}{128\pi} \left(\gamma_E - \dfrac{3}{2} - \log 2 + \log r + \log\Lambda\right) \underbrace{\dfrac{1}{16\xi^4}}_{\text{Contact}} & \text{(2D)} \\[4ex]
-\left(\dfrac{4\pi}{a_0}\right)^2 \dfrac{r^5}{2880\pi} \underbrace{\dfrac{1}{4\xi^4}}_{\text{Contact}} & \text{(3D)} \end{cases}
$$

$$(4.69)$$

We have grouped the result in a way that allows easy comparison with the matrix elements of the contact operator (see eq. (4.40)). It will also allow straightforward comparison to the results of Kimball [130, 131, 132] once we Fourier-transform – in order to get the results for momentum distribution – the OPE back to momentum space. From (4.69), we can immediately infer the Wilson coefficients (up to order $r^6$) of the contact operator $\psi_\uparrow^\dagger \psi_\downarrow^\dagger \psi_\downarrow \psi_\uparrow(\mathbf{R})$:

$$
\tilde{c}_{\uparrow\uparrow\downarrow\downarrow\downarrow\uparrow}(\mathbf{r}) = \begin{cases} -\left(\dfrac{2\pi}{a_0}\right)^2 \dfrac{|\mathbf{r}|^4}{128\pi} \left(\gamma_E - \dfrac{3}{2} - \log 2 + \log|\mathbf{r}| + \log\Lambda\right) & \text{(2D)} \\[4ex]
-\left(\dfrac{4\pi}{a_0}\right)^2 \dfrac{|\mathbf{r}|^5}{2880\pi} & \text{(3D)}, \end{cases}
$$

$$(4.70)$$

where symbol $\tilde{c}$ shall indicate that this is the "bare" Wilson coefficient.

**A comment on operator mixing** What about the cutoff dependence of the Wilson coefficient in the two-dimensional case? We see that, by construction, the cutoff dependent term cancels the divergence of the operator $\mathcal{D}_4^\sigma$, such that the matrix elements of the *sum*

$$D_4^\sigma(\mathbf{r}, \mathbf{R}) + \tilde{c}_{\uparrow\dagger\downarrow\dagger\downarrow\uparrow}(\mathbf{r})\psi_\uparrow^\dagger\psi_\downarrow^\dagger\psi_\downarrow\psi_\uparrow(\mathbf{R}) \qquad (4.71)$$

are *finite*. That this is indeed true for all matrix elements, and not just a pathologic result we are getting from our expansion around $k_0 = 0$, is shown in more detail in appendix G.2.2. Of course, in principle we would need to renormalize (which means subtract the appropriate parts proportional to the contact) all the operators that are part of the sum $\mathcal{D}_4^\sigma$ separately and find their respective Wilson coefficients to see that the result indeed coincides with what we have. This is just a technical complication, and we will avoid this way because it doesn't deliver any insight. If anything, we would get buried under an avalanche of indices.

Following Collins [35], we will denote the renormalized version of an operator $\mathcal{O}_A$ by $[\mathcal{O}_A]$. Studying the sum (4.71) more closely, we realize that we can define a renormalized version of the operator $D_4^\sigma(\mathbf{r}, \mathbf{R})$ by

$$[D_4^\sigma(\mathbf{r}, \mathbf{R})] \quad = \quad D_4^\sigma(\mathbf{r}, \mathbf{R}) - \left(\frac{2\pi}{a_0}\right)^2 \frac{|\mathbf{r}|^4}{128\pi} \log \Lambda \psi_\uparrow^\dagger\psi_\downarrow^\dagger\psi_\downarrow\psi_\uparrow(\mathbf{R}). \qquad (4.72)$$

In the above definition, we subtracted the bare minimum that is needed to make the operator finite. This procedure is usually called *minimal subtraction* [35]. This is the scheme we are going to use. Note however, that we could also over-subtract a little. For example, we could also put all parts of (4.71) except the $\sim |\mathbf{r}|^4 \log |\mathbf{r}|$ term into the renormalized version of $D_4^\sigma$. Equation (4.72) nicely illustrates why the phenomenon is called operator mixing: The operator $D_4^\sigma$ mixes with the contact operator $\psi_\uparrow^\dagger\psi_\downarrow^\dagger\psi_\downarrow\psi_\uparrow(\mathbf{R})$ in order to have finite matrix elements. Note that since the contact operator itself has finite matrix elements (which is different from contact-interacting Fermi gases in two and three dimensions), its renormalized version is equal to the bare version:

$$[\psi_\uparrow^\dagger\psi_\downarrow^\dagger\psi_\downarrow\psi_\uparrow(\mathbf{R})] \quad = \quad \psi_\uparrow^\dagger\psi_\downarrow^\dagger\psi_\downarrow\psi_\uparrow(\mathbf{R}) \qquad (4.73)$$

The definition (4.72) of course just shifts the $\log \Lambda$ term away from the bare Wilson coefficient (4.70) into the definition of the operator that represents all contributing quartic derivatives.

### 4.5.3 OPE of the one-particle density matrix

Putting together the results of the previous subsection, we can now infer that the OPE of the one-particle density matrix, in the case of an electron gas, is given by

$$\psi_\sigma^\dagger \left( \mathbf{R} - \frac{\mathbf{r}}{2} \right) \psi_\sigma \left( \mathbf{R} + \frac{\mathbf{r}}{2} \right) = \left[ e^{-i\frac{\mathbf{r}}{2}\cdot\nabla} \psi_\sigma^\dagger(\mathbf{R}) \right] \left[ e^{i\frac{\mathbf{r}}{2}\cdot\nabla} \psi_\sigma(\mathbf{R}) \right]$$

$$- \psi_\uparrow^\dagger \psi_\downarrow^\dagger \psi_\downarrow \psi_\uparrow (\mathbf{R}) \left\{ \begin{array}{ll} \left( \dfrac{2\pi}{a_0} \right)^2 \dfrac{|\mathbf{r}|^4}{128\pi} \left( \log |\mathbf{r}| - \log 2e^{-\gamma_E} - \dfrac{3}{2} \right) & \text{(2D)} \\ \left( \dfrac{4\pi}{a_0} \right)^2 \dfrac{|\mathbf{r}|^5}{2880\pi} & \text{(3D)} \end{array} \right\}$$

$$+ \mathcal{O}(|\mathbf{r}|^{d+3}), \qquad (4.74)$$

where the one-body term is a suggestive short-hand for the sum of the operators $D_n^\sigma$ up to order $n = d+2$. In the case of two dimensions, the operator $D_4^\sigma$ is replaced by its minimally subtracted version (4.72). The leading order non-analytic terms are, in both dimensions, given by the contact operator. When taking the expectation value of (4.74), this will give a term proportional to the $\uparrow - \downarrow$ pair correlation function at zero distance.

### 4.5.4 Momentum distribution at large momenta

The momentum distribution is, by eq. (4.9), just the Fourier transform of the one-particle density matrix. The Fourier transforms of the non-analytic terms are given by [56]

$$\int d^2r \, e^{-i\mathbf{q}\cdot\mathbf{r}} |\mathbf{r}|^4 \log |\mathbf{r}| = -\frac{128\pi}{|\mathbf{q}|^6} \qquad (4.75)$$

$$\int d^3r \, e^{-i\mathbf{q}\cdot\mathbf{r}} |\mathbf{r}|^5 = -\frac{2880\pi}{|\mathbf{q}|^8}. \qquad (4.76)$$

The Fourier transforms of the analytic terms will not contribute [138] in the limit of large $|\mathbf{q}|$, which is the one we are interested in, since they give gradients of the delta function. In particular, the $\sim |\mathbf{r}|^4 \psi_\uparrow^\dagger \psi_\downarrow^\dagger \psi_\downarrow \psi_\uparrow (\mathbf{R})$ terms in the two-dimensional case also count as analytic contributions under Fourier transform. Taking the expectation value of (4.74) and Fourier transforming, we have the following result for the

---

**Momentum distribution at large momenta**

The momentum distribution $n_\sigma(\mathbf{q})$ of the electron species with spin $\sigma$ asymptotically vanishes like

$$n_\sigma(\mathbf{q}) \stackrel{|\mathbf{q}|\to\infty}{\longrightarrow} \begin{cases} \left(\dfrac{2\pi}{a_0}\right)^2 \dfrac{C}{|\mathbf{q}|^6} & \text{(2D)} \\[3mm] \left(\dfrac{4\pi}{a_0}\right)^2 \dfrac{C}{|\mathbf{q}|^8} & \text{(3D),} \end{cases} \tag{4.77}$$

where $a_0$ is the Bohr radius and $C = \int d^d R \langle \psi_\uparrow^\dagger \psi_\downarrow^\dagger \psi_\downarrow \psi_\uparrow(\mathbf{R})\rangle/V$ is an intensive integral that contains the pair correlation function of an $\uparrow$ and an $\downarrow$ electron at zero distance. The decay coefficient $C$ is the same regardless of the spin species $\sigma$.

---

The big advantage of our derivation is the fact that (4.77) holds for any state, and thus both in the plasma and possible crystallized phases. The only possibility for the system to avoid the tails given in (4.77) is a vanishing pair correlator at zero distance. In the translational invariant case, the tails simplify to

$$n_\sigma(\mathbf{q}) \to \begin{cases} \left(\dfrac{2\pi}{a_0}\right)^2 \dfrac{n_\uparrow n_\downarrow g_{\uparrow\downarrow}(0)}{|\mathbf{q}|^6} & \text{(2D)} \\[3mm] \left(\dfrac{4\pi}{a_0}\right)^2 \dfrac{n_\uparrow n_\downarrow g_{\uparrow\downarrow}(0)}{|\mathbf{q}|^8} & \text{(3D).} \end{cases} \tag{4.78}$$

From the form (4.78), it is immediately clear that our results reproduce the ones given by Kimball [130, 131, 132].

In the case of hydrogen, we have to normalize the momentum distribution in an extensive fashion. As mentioned in sec. 4.4, we also have to replace $1/a_0 \to -2/a_0$ because of the attractive interaction and the different reduced mass. The coefficient $C$ of the tail is given by eq. (4.47), which is the analogue of the pair correlation function at zero distance in the case of hydrogen. With these definitions, the results (4.77) and (4.5) for the momentum distribution of the hydrogen atom at high momenta are indeed equivalent.

Our calculation does of course not yield any numerical values for the size of the coefficients of the tails. To answer this question, one still needs to solve a many-body problem in order to get the contact value $g(0)$ of the pair correlation function. For a discussion of known numerical limits, see sec. 4.7.1. Furthermore, we will employ

a virial expansion to obtain some analytic results for the behavior of $g(0)$ in the classical and high-temperature limits in sec. 4.7.2.

## 4.6 Short-distance properties of the Many Body Wave function

The fundamental insight that was already implicitly used by Kimball [130, 131, 132] during the proof of the tails of both the static structure factor and the momentum distribution is the following: The many-body wave function, when two of its coordinates are much closer together than the average inter-particle distance, factorizes into a two-body contribution and a remainder. This is somewhat intuitively clear, as the mutual Coulomb repulsion of the two particles dominates the physics in this limit. In the following, our aim will be to prove this intuitive assumption by the means of a short-distance OPE. The factorization was also discussed by Lepage [150], using the language of effective field theories. Bogner and Roscher [151] used an approach similar to an OPE to derive the tails of both the Coulomb gas the contact-interacting Fermi gas. Note that a similar proof as the one given below should also work in the context of contact-interacting Fermi gases, resulting in the factorization condition that Werner and Castin [38] used during their derivation of the Tan relations.

To illustrate the idea of our proof, assume we know the the OPE of the operator

$$\psi_\uparrow\left(-\frac{\mathbf{r}}{2}\right)\psi_\downarrow\left(\frac{\mathbf{r}}{2}\right) \;=\; \sum_n c_n(\mathbf{r})\mathcal{O}_n(\mathbf{0}), \tag{4.79}$$

where, for simplicity, we have chosen to ignore the usual dependence on the center coordinate $\mathbf{R}$ and set $\mathbf{R} = \mathbf{0}$. The $N$-body wave function $\Psi$, in an arbitrary state $|\Psi_N\rangle$, can, when two coordinates of an $\uparrow-$ and a $\downarrow-$electron come sufficiently close together, be written as

$$\Psi\left(-\frac{\mathbf{r}}{2},\uparrow;\frac{\mathbf{r}}{2},\downarrow;\mathbf{r}_3,\sigma_3;\dots\right) = \frac{1}{\sqrt{N_\uparrow!N_\downarrow!}}\left\langle 0\left|\psi_\uparrow\left(-\frac{\mathbf{r}}{2}\right)\psi_\downarrow\left(\frac{\mathbf{r}}{2}\right)\prod_{l=3}^N \psi_{\sigma_l}(\mathbf{r}_l)\right|\Psi_N\right\rangle$$

$$= \sum_n \frac{c_n(\mathbf{r})}{\sqrt{N_\uparrow!N_\downarrow!}}\left\langle 0\left|\mathcal{O}_n(\mathbf{0})\prod_{l=3}^N \psi_{\sigma_l}(\mathbf{r}_l)\right|\Psi_N\right\rangle, \tag{4.80}$$

where the first equality is just the defining projection to position space. For the second equality, we have plugged in the short-distance OPE (4.79) for the operator that annihilates two fermions of type $\uparrow$ and $\downarrow$ that are close by. In the limit of
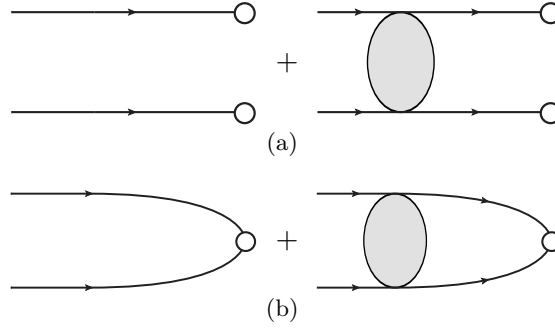
(a)

(b)

Figure 4.7: Diagrams for the matching of the spin singlet operator. The incoming momenta are $\pm\mathbf{p}$ and the center of mass energy is $p^2/m$. The outgoing state is the vacuum.

$|\mathbf{r}| \to 0$, and assuming that there is only one leading order operator, eq. (4.80) indeed implies factorization of the wave function! To study the precise form of both the remainder and the short-distance part, we need an explicit expression for the leading order term and its Wilson coefficient.

In order to proceed, we rewrite $\psi_\uparrow (-\mathbf{r}/2)\, \psi_\downarrow (\mathbf{r}/2)$ as the sum of a singlet term

$$\psi\left(-\frac{\mathbf{r}}{2}\right)\psi\left(\frac{\mathbf{r}}{2}\right) \;\equiv\; \frac{1}{2}\left[\psi_\uparrow\left(-\frac{\mathbf{r}}{2}\right)\psi_\downarrow\left(\frac{\mathbf{r}}{2}\right) - \psi_\downarrow\left(-\frac{\mathbf{r}}{2}\right)\psi_\uparrow\left(\frac{\mathbf{r}}{2}\right)\right] \qquad (4.81)$$

and a triplet term that has a relative plus sign between the two operators. The triplet combination is symmetric under exchange of the spin indices. Since the fermion fields anti-commute, the leading order term in its OPE is suppressed by an order in $|\mathbf{r}|$. We thus only need to consider the OPE of the spin-singlet part. As we will see below, the leading order term in the OPE of the singlet part is just the singlet operator $\psi\psi(0)$ evaluated at zero distance. To prove this, we take the matrix element of the operators $\psi(-\mathbf{r}/2)\psi(\mathbf{r}/2)$ and $\psi\psi(0)$ between the vacuum and a state with particles of incoming momenta $\pm\mathbf{p}$, and (on-shell) center of mass energy $p^2/m$. Diagrammatically, the matrix elements are shown in fig. 4.7. By the Lippmann-Schwinger equation for the scattering wave function (see [136] or [115] for details), we can turn the matrix element into the scattering wave function:

$$\langle 0|\psi\left(-\frac{\mathbf{r}}{2}\right)\psi\left(\frac{\mathbf{r}}{2}\right)|\mathbf{p},\uparrow;-\mathbf{p},\downarrow\rangle = \langle \mathbf{r}|1 + G_0 T|\mathbf{p},\uparrow;-\mathbf{p},\downarrow\rangle = \psi_p(\mathbf{r}) \qquad (4.82)$$

It follows trivially that the matrix element of the local singlet operator is just given by scattering wave function $\psi_p(0)$ at zero separation. We can determine the Wilson

coefficient of the singlet operator by matching this in the zero-energy limit. From this procedure, it follows that the Wilson coefficient solves the (zero-energy) two-body $s$-wave Schrödinger equation

$$\left[-\Delta + \frac{1}{a_0 r}\right] c_{\psi\psi}(\mathbf{r}) = 0. \tag{4.83}$$

The boundary condition, because of the matching procedure, is $c_{\psi\psi}(0) = 1$. The solution of this differential equation can be expanded to leading order in $|\mathbf{r}|$:

$$c_{\psi\psi}(\mathbf{r}) = \begin{cases} 1 + \dfrac{|\mathbf{r}|}{a_0} + \mathcal{O}(|\mathbf{r}|^2) & \text{(2D)} \\[2mm] 1 + \dfrac{|\mathbf{r}|}{2a_0} + \mathcal{O}(|\mathbf{r}|^2) & \text{(3D)} \end{cases} \tag{4.84}$$

We have thus found the leading order term in the OPE of the singlet operator. From the arguments given below eq. (4.80), this leads to the approximate factorization

$$\lim_{|\mathbf{r}|\to 0} \Psi\left(-\frac{\mathbf{r}}{2},\uparrow;\frac{\mathbf{r}}{2},\downarrow;\dots\right) = c_{\psi\psi}(\mathbf{r})\Psi(\mathbf{0},\uparrow;\mathbf{0},\downarrow;\dots) \tag{4.85}$$

in the limit of small separation of a $\uparrow$ and a $\downarrow$-electron. In particular, $c_{\psi\psi}$ is determined by the solution of the two-body problem at small distances. This is indeed the crucial insight, that Kimball used to prove the tails of the momentum distribution (see eq. (4.78)) and the static structure factor (see eq. (4.44)). For the derivation of the tails from the factorization of the wave function, please consult the papers of Kimball [130, 131, 132]. For the structure factor, the derivation is quite straightforward. For the momentum distribution, the counting of coordinates that come close together is a bit involved.

Using the idea of the factorization of the wave function, detailed derivations of the high-momentum tails of the contact-interacting Fermi gas were given by Werner and Castin [38] and Zhang [152]. Of course, the two-body part (coming from the Wilson coefficient) in this case solves another Schrödinger equation, namely the free one with Bethe-Peierls boundary conditions.

## 4.7 The pair distribution function at zero distance

In the preceding sections, we have established that the high-momentum tails of both, the static structure factor and the momentum distribution, are governed by the contact value $g(0)$ of the pair distribution function. The aim of this section will

be to study the behavior of this value. In sec. 4.7.1, its known behavior as a function of the parameter $r_s$ is summarized. In sec. 4.7.2, we will derive its high-temperature $(T \to \infty)$ and classical limits $(\hbar \to 0)$ from a virial expansion. While they are very often taken to be same, since the thermal de-Broglie wavelength

$$\lambda_T \;\; = \;\; \hbar\sqrt{\frac{2\pi}{mk_BT}} \tag{4.86}$$

vanishes in either of the two limits, we will see that in the case of the Coulomb gas, those limits are *not* identical. We have restored $\hbar$ in order to be able to discuss the classical limit in the following.

### 4.7.1 Known results for the tails

As was emphasized before, the big advantage of our OPE derivation of the high-momentum tails (4.78) and (4.44) is that, since the OPE is an operator identity, it holds for arbitrary states of the system. This, in particular, implies the presence of the tails (as long as $g(0) \neq 0$) at all temperatures. Let us focus on the zero-temperature case first, and the regime of moderate $r_s$ values, where the system is in a uniform Fermi liquid phase. The momentum scale for the validity of the tails is then set by the Fermi wave vector $k_F = 1/\alpha r_0$, where $r_0$ is the average inter-particle spacing and $\alpha = (4/9\pi)^{1/3} \approx 0.521$ in three dimensions and $\alpha = 1/\sqrt{2}$ in two dimensions.

Let us define a dimensionless strength $s$ of the tails of the momentum distribution via $n_\sigma(\mathbf{q}) \to s(k_F/|\mathbf{q}|)^{2d+2}$ as $|\mathbf{q}| \to \infty$. We have [153]

$$s(r_s) = \begin{cases} 2\alpha^6 g(0)r_s^2 & \text{(2D)} \\[2mm] \dfrac{9}{2}\alpha^8 g(0)r_s^2 & \text{(3D)} \end{cases} \tag{4.87}$$

The dimensionless strength of the tail, as a (continuous) function of $r_s$, vanishes in both the limit $r_s \to 0$ and $r_s \to \infty$. In particular, as long as the system is not fully spin-polarized (because in this case $g(0)$ is trivially zero due to the Pauli principle), even the Wigner crystal shows the power law tails in the momentum distribution and static structure factor. The contact value $g(0)$ in this low-density regime is expected to vanish exponentially with $r_s$. In the opposite limit of high densities, one has $g(0) = 1/2 + \mathcal{O}(r_s)$ [154], and thus the dimensionless strength of the tails vanishes quadratically in $r_s$. From these two limits, we can conjecture that $s(r_s)$ must have a maximum somewhere in between the two limits.

Recent Quantum Monte Carlo simulations indicate that the size of the dimensionless strength is surprisingly small. In ref. [155], they found $s(r_s = 10) \approx 0.006$ for the two-dimensional case. In the three-dimensional case, studied in ref. [156], the value is of the same order $s(r_s = 10) \approx 0.009$. This is in stark contrast to strongly interacting cold Fermi gases. For example, the dimensionless strength of the tail of a one-dimensional Fermi gas [34, 27], at infinite short range repulsion, $s(\infty) = 32 \log 2/(3\pi^2) \approx 0.749$ exceeds those values by roughly two orders of magnitude.

### 4.7.2 Classical and high-temperature limits

In this section, we will derive analytical results for the contact value $g(0)$ of the pair distribution function of a homogeneous and non spin-polarized system. A virial expansion technique will our tool to extract these results. Note that one can also obtain one of the results we are about to derive from a diagrammatic virial expansion like the ones performed in section 2.3 and chapter 3 of this thesis. This diagrammatic method reproduces the result of the high-temperature limit of $g(0)$ given below. We will not go into detail on the diagrammatic method, however, and merely show the contributing diagrams. For details, I refer you to our article [157].

In the remainder of this section, we will consider the Coulomb gas in the non-degenerate regime

$$
\begin{aligned}
k_B T &\gg \frac{\hbar^2 n^{2/d}}{m} \\
\Rightarrow n^{1/d} \lambda_T &\ll 1.
\end{aligned}
\tag{4.88}
$$

Within this regime, we can approximate observables of the system with an expansion in fugacity $z = e^{\beta\mu} \approx n\lambda_T^d/2 \ll 1$. Note that while, due to the long ranged nature of the Coulomb potential, a virial expansion is not well-defined for all observables, we will see that the expansion of the contact value $g(0)$ is well behaved. The non-degeneracy condition in eq. (4.88) does *not* contain any information about the coupling strength $e^2$ of the Coulomb system. Furthermore, it is satisfied both the high-temperature limit $T \to \infty$, as well as the classical limit $\hbar \to 0$. A purely classical scale for Coulomb systems that weighs temperature against the interaction strength is the so called *Bjerrum length* $\ell_B$:

$$
\ell_B = \frac{e^2}{k_B T}
\tag{4.89}
$$

The Bjerrum length, when increasing temperature and keeping $\hbar$ finite, becomes eventually shorter than the thermal wavelength. Thus, when taking $T \to \infty$ before $\hbar \to 0$, one has

$$n^{-1/d} \gg a_0 \gg \lambda_T \gg \ell_B \tag{4.90}$$

for the hierarchy of length scales in the non-degenerate regime. However, if we take $\hbar \to 0$ before $T \to \infty$, we instead get

$$n^{-1/d} \gg \ell_B \gg \lambda_T \gg a_0. \tag{4.91}$$

This is a result of the fact that the Bjerrum length is independent of $\hbar$. The contact value of the pair correlation function will turn out to yield different values in these two regimes, proving that the classical and the high-temperature limit do not commute in the case of a Coulomb system.

**Virial expansion for the Contact value of the pair correlation function**

In the following, we will establish the form of the contact value $g(0)$ of the pair correlation function within a virial expansion. To this end, we will consider the inter-species value $g_{\uparrow\downarrow}(0)$, because the contribution from the equal species part vanishes due to the Pauli principle. Rewriting the definition (4.10) of the spin-resolved pair correlation function more explicitly in terms of a grand-canonical trace, we have

$$
\begin{aligned}
\frac{n^2}{4} g_{\uparrow\downarrow}(\mathbf{x}, \mathbf{x}') &= \frac{1}{\mathcal{Z}} \sum_{N_\uparrow, N_\downarrow} z^{N_\uparrow} z^{N_\downarrow} \mathrm{tr}_{N_\uparrow, N_\downarrow} \left[ e^{-\beta H} \psi_\uparrow^\dagger(\mathbf{x}) \psi_\downarrow^\dagger(\mathbf{x}') \psi_\downarrow(\mathbf{x}') \psi_\uparrow(\mathbf{x}) \right] \\
&= z^2 \mathrm{tr}_{1,1} \left[ e^{-\beta H} \psi_\uparrow^\dagger(\mathbf{x}) \psi_\downarrow^\dagger(\mathbf{x}') \psi_\downarrow(\mathbf{x}') \psi_\uparrow(\mathbf{x}) \right] + \mathcal{O}(z^3), \tag{4.92}
\end{aligned}
$$

where the first equality is completely general (when summing over states with well-defined particle number), and the second equality is the leading order result in an expansion with respect to the fugacity. Since we want to consider the non-spin polarized case, we set the chemical potentials, and hence the fugacities, of the two electronic species to be the same: $z_\uparrow = z_\downarrow = z$. The canonical trace in the second line of eq. (4.92) runs over all two-particle eigenstates that contain an $\uparrow -$ and a $\downarrow -$electron. Because we are considering the repulsive Coulomb problem, there are no bound states and the trace only runs over the continuous part of the spectrum. Before we completely specify the quantum numbers the trace depends on, let us label the eigen-energies $E_\alpha$ by a symbolic quantum number index $\alpha$, and take a

closer look at the trace:

$$\sum_\alpha e^{-\beta E_\alpha} \langle \alpha | \psi_\uparrow^\dagger(\mathbf{x}) \psi_\downarrow^\dagger(\mathbf{x}') \psi_\downarrow(\mathbf{x}') \psi_\uparrow(\mathbf{x}) | \alpha \rangle = \sum_\alpha e^{-\beta E_\alpha} |\psi_\alpha(\mathbf{x},\uparrow;\mathbf{x}',\downarrow)|^2$$

$$= \sum_\alpha e^{-\beta E_\alpha} |\psi_\alpha(\mathbf{R},\mathbf{r})|^2 \qquad (4.93)$$

We are just summing over the two-particle wave function at $\mathbf{x}$ and $\mathbf{x}'$. In the second line, we switched to the coordinates $\mathbf{R} = (\mathbf{x}+\mathbf{x}')/2$ and $\mathbf{r} = \mathbf{x}-\mathbf{x}'$. Thus, the contact value of the pair correlation function is just determined by the value $|\psi_\alpha(\mathbf{R},\mathbf{0})|$ of the wave function when the two electrons sit on top of each other.

**Contact value of the wave function and conversion of sums into integrals**
The solutions of the two-particle problem factorize into a center of mass piece $\chi_{\mathrm{CMS}}$ and a relative wave function $\psi$, where $\chi_{\mathrm{CMS}}(\mathbf{R}) = e^{i\mathbf{P}\cdot\mathbf{R}}/\sqrt{V}$. We enclose the system into a large box of volume $V$, and the factor $1/\sqrt{V}$ ensures normalization of the center of mass wave function. We now turn the sum over $\alpha$ into a sum over center of mass momenta $\mathbf{P}$ (to be more precise $\mathbf{P}$ is a wave number, but we will use loose nomenclature). In addition, we sum over the energies $\hbar^2 p^2/m$ in the center of mass frame, as well as a complete set of eigenfunctions of the Laplace operator $\Delta_{S^{d-1}}$ on the surface of the sphere. Like in the standard hydrogen problem, the relative wave function $\psi$ factorizes into the pure angular part $Y$, and a radial part $\chi$:

$$\psi_{pm}(r) = \mathcal{N} Y_m(\varphi) \chi_{pm}(r) \qquad \text{(2D)} \qquad (4.94)$$

$$\psi_{plm}(r) = \mathcal{N} Y_{lm}(\theta,\varphi) \chi_{pl}(r), \qquad \text{(3D)} \qquad (4.95)$$

where the constant $\mathcal{N}$ was introduced to ensure normalization. $Y_{lm}$ denotes the spherical harmonics. In two dimensions, the magnetic quantum number is all that is left of the angular momentum, and we have $Y_m(\varphi) = e^{im\varphi}/\sqrt{2\pi}$ for the normalized eigenfunctions of the Laplace operator $\Delta_{S^1}$. With these definitions, the leading order contact value of the pair correlation function reads

$$\frac{n^2}{4} g_{\uparrow\downarrow}(0) = z^2 \underbrace{\int_\mathbf{P} e^{-\beta \frac{\hbar^2 P^2}{4m}} |\chi_{\mathrm{CMS},\mathbf{P}}(\mathbf{R})|^2}_{= \frac{2^{d/2}}{\lambda_T^d}} \begin{cases} \sum\limits_{pm} e^{-\beta \frac{\hbar^2 p^2}{m}} |\psi_{pm}(0)|^2 & \text{(2D)} \\ \sum\limits_{plm} e^{-\beta \frac{\hbar^2 p^2}{m}} |\psi_{plm}(0)|^2 & \text{(3D)} \end{cases} \qquad (4.96)$$

The summation over the center of mass momenta was turned into an integral. We will treat the relative motion more carefully in the following, in order to ensure that

the long range nature of the Coulomb potential has no subtle effects that would render the standard treatment of these sums wrong.

We will now follow a procedure that is outlined in [70], in order to turn the momentum (implicitly: energy) sum into an integral. The advantage of this procedure is that it provides a concise scaling of the normalization of the relative wave function with volume. The radial parts solve the Schödinger equations

$$p^2 \chi_{pm}(r) = \left[ \partial_r^2 - \frac{1}{r}\partial_r + \frac{m^2}{r^2} + \frac{1}{a_0 r} \right] \chi_{pm}(r) \qquad \text{(2D)} \qquad (4.97)$$

$$p^2 \chi_{pl}(r) = \left[ -\frac{1}{r^2}\partial_r r^2 \partial_r + \frac{l(l+1)}{r^2} + \frac{1}{a_0 r} \right] \chi_{pl}(r). \qquad \text{(3D)} \qquad (4.98)$$

In both two and three dimensions [113, 136], the solution can be expressed in terms of Kummer's hypergeometric function $_1F_1(a, b; z)$. There is a second linearly independent solution which is proportional to a confluent hypergeometric function. However, since this solution diverges at the origin in a non-normalizable fashion, we set its coefficient to zero. Explicitly, with the help of the Sommerfeld parameter $\xi = me^2/2\hbar^2 p$, the solutions read

$$\chi_{pm}(r) = e^{-ipr} \frac{(2ipr)^m}{\Gamma(1 + 2m)} \, _1F_1\left(\frac{1}{2} - i\xi + m, 1 + 2m; 2ipr\right) \qquad \text{(2D)} \qquad (4.99)$$

$$\chi_{pl}(r) = e^{-ipr} \frac{(2ipr)^{l+1}}{r} \, _1F_1(1 - i\xi + l, 2l + 2; 2ipr) \qquad \text{(3D)} \qquad (4.100)$$

In the 2D case, we kept the $\Gamma$-function to ensure that the result is well defined when $m$ takes on negative values $-1, -2, \ldots$ The first thing to note is that, as was already implicitly mentioned for the case of 3D hydrogen, only the solutions with vanishing angular momentum have a finite value at the origin:

$$\chi_{pm}(0) \quad \sim \quad \delta_{0m} \qquad \qquad (4.101)$$

$$\chi_{pl}(0) \quad \sim \quad \delta_{0l} \qquad \qquad (4.102)$$

This means that the summation over angular momenta in eq. (4.96) is trivially evaluated, and we will focus purely on vanishing angular momenta in the following. We now demand the solution to vanish at the boundary $r = R$ of our large spherical box: $\chi_{p0}(r = R) \overset{!}{=} 0$. We will send $R \to \infty$ in the end of the calculation. A series expansion of the solutions (4.99) and (4.100) around $r = \infty$ reveals that the

condition $\chi_{p0}(r = R) = 0$ implies

$$pR \underbrace{-\xi \log 2pR + \arg \Gamma \left( \frac{1}{2} + i\xi \right) - \frac{3\pi}{4}}_{\equiv \sigma_2(p)} = n\pi \quad \text{(2D)} \qquad (4.103)$$

$$pR \underbrace{-\xi \log 2pR + \arg \Gamma(1 + i\xi)}_{\equiv \sigma_3(p)} = n\pi \quad \text{(3D)}, \qquad (4.104)$$

where $n$ is an integer. Note that the "phase shifts" $\sigma_d$ diverge logarithmically when $R \to \infty$, which reflects the fact that, because of the long ranged nature of the Coulomb potential, we can never talk about "free" incoming and outgoing scattering states. Using the above equations for two successive integers, and taking the limit of large $R$, we see that the distance $dp$

$$dp = \frac{\pi}{R + \partial_p \sigma_d(p)} \qquad (4.105)$$

of two consecutive values of $p$ goes to zero as $R \to \infty$. Now, let $g(p)$ be the number of states in $[p, p + dp]$, such that $g(p)dp = 1$. This *density of states* provides us with a clear prescription on how to replace the sum over the discrete values of $p$ with an integral: $\sum_p .. \approx \int_0^\infty dp \, g(p)...$

To ensure proper normalization $\int_0^R dr \, r^{d-1} |\mathcal{N}|^2 |\chi_{p0}(r)|^2 = 1$ of the radial wave functions, it is enough to study the large $r$ part of the integrand, since this is what dominates the integral. Indeed, we have [113]

$$r|\chi_{p0}(r)|^2 = \frac{e^{2\pi\xi} + 1}{2p\pi} + \text{osc.} + \mathcal{O}\left( \frac{1}{r} \right) \qquad \text{(2D)} \qquad (4.106)$$

$$r^2|\chi_{p0}(r)|^2 = \frac{e^{2\pi\xi} - 1}{\pi\xi} + \text{osc.} + \mathcal{O}\left( \frac{1}{r} \right) \qquad \text{(3D)}, \qquad (4.107)$$

where the presence of some rapidly oscillating (as $r \to \infty$) terms, that will average to zero when integrating over the large $r$ region, is indicated in plain text. Since the integral should be normalized to one, we have

$$|\mathcal{N}|^2 = \begin{cases} \dfrac{1}{R} \dfrac{2p\pi}{e^{2\pi\xi} + 1} + \mathcal{O}\left( \dfrac{1}{R^2} \right) & \text{(2D)} \\ \dfrac{1}{R} \dfrac{\pi\xi}{e^{2\pi\xi} - 1} + \mathcal{O}\left( \dfrac{1}{R^2} \right) & \text{(3D)}, \end{cases} \qquad (4.108)$$

where we indicated that this formula receives corrections of the order $1/R^2$. Using the solutions (4.99) and (4.100), we are now in the position to give the contact values

$$|\psi_{p0}(0)|^2 = \frac{1}{R} \frac{p}{e^{2\pi\xi} + 1} \qquad \text{(2D)} \qquad (4.109)$$

$$|\psi_{p00}(0)|^2 = \frac{1}{R} \frac{\xi p^2}{e^{2\pi\xi} - 1} \qquad \text{(3D)} \qquad (4.110)$$

of the relative function. The angular terms $Y_{00}(\theta, \varphi) = 1/\sqrt{4\pi}$ and $Y_0(\phi) = 1/\sqrt{2\pi}$ were also already included. Using the density of states $g(p)$, where $g^{-1}(p)$ is given by eq. (4.105), and the replacement $\sum_p \to \int_0^\infty dp\, g(p)$, the virial expansion (4.96) for the contact value of the pair correlation function can be rewritten as

$$
\frac{n^2}{4} g_{\uparrow\downarrow}(0) = z^2 \frac{2^{d/2}}{\lambda_T^d} \begin{cases} \int_0^\infty dp \left[ \frac{R}{\pi} + \frac{\partial_p \sigma_2(p)}{\pi} \right] e^{-\beta \frac{\hbar^2 p^2}{m}} |\psi_{p0}(0)|^2 & \text{(2D)} \\[2mm] \int_0^\infty dp \left[ \frac{R}{\pi} + \frac{\partial_p \sigma_3(p)}{\pi} \right] e^{-\beta \frac{\hbar^2 p^2}{m}} |\psi_{plm}(0)|^2 & \text{(3D)} \end{cases}
$$

$$
= \frac{z^2}{\pi} \frac{2^{d/2}}{\lambda_T^d} \begin{cases} \int_0^\infty dp\, e^{-\beta \frac{\hbar^2 p^2}{m}} \frac{p}{e^{2\pi\xi} + 1} + \mathcal{O}\left( \frac{\log R}{R} \right) & \text{(2D)} \\[2mm] \int_0^\infty dp\, e^{-\beta \frac{\hbar^2 p^2}{m}} \frac{\xi p^2}{e^{2\pi\xi} - 1} + \mathcal{O}\left( \frac{\log R}{R} \right), & \text{(3D)} \end{cases}
\tag{4.111}
$$

where the corrections of order $\log R/R$ come from the derivatives of the "phase shifts" $\sigma_d(p)$, and vanish in the limit of infinite volume. As a reminder: $\xi = me^2/2\hbar^2 p$ is the Sommerfeld parameter, and depends on the integration variable $p$.

**Evaluation of the integral and results for the contact value**   The integrals in eq. (4.111) can be brought, via the substitution $x = \beta \hbar^2 p^2/m$ and using $\lambda_T/a_0 = 2\pi \ell_B/\lambda_T$, into the form

$$
\frac{n^2}{4} g_{\uparrow\downarrow}(0) = z^2 \frac{2^{d/2}}{\lambda_T^{2d}} \int_0^\infty dx \begin{cases} \dfrac{e^{-x}}{e^{\frac{\sqrt{2}\pi^{3/2}\ell_B}{\sqrt{x}\lambda_T}} + 1} & \text{(2D)} \\[4mm] \dfrac{\pi \ell_B}{\lambda_T} \dfrac{e^{-x}}{e^{\frac{\sqrt{2}\pi^{3/2}\ell_B}{\sqrt{x}\lambda_T}} - 1} & \text{(3D)} \end{cases}
\tag{4.112}
$$

This form is advantageous, because it makes the dependence on the dimensionless quantity $\ell_B/\lambda_T$ evident. Note that for the $T \to \infty$ limit, we have $\ell_B/\lambda_T \to 0$. In the classical limit $\hbar \to 0$ however, we have $\ell_B/\lambda_T \to \infty$.

Let us treat the limit $T \to \infty$ first (implying the hierarchy of length scales given in eq. (4.90)). The integrand has the series expansion

$$
\frac{e^{-x}}{e^{\frac{2\pi^{3/2}\ell_B}{\lambda_T\sqrt{x}}} + 1} = e^{-x} \left[ \frac{1}{2} - \frac{\pi^{3/2}}{2^{3/2}\sqrt{x}} \frac{\ell_B}{\lambda_T} + \mathcal{O}\left( \frac{\ell_B^2}{\lambda_T^2} \right) \right]
\tag{4.113}
$$

$$
\frac{\pi \ell_B}{\lambda_T} \frac{e^{-x}}{e^{\frac{2\pi^{3/2}\ell_B}{\lambda_T\sqrt{x}}} - 1} = e^{-x} \left[ \frac{\sqrt{x}}{\sqrt{2\pi}} - \frac{\pi}{2} \frac{\ell_B}{\lambda_T} + \mathcal{O}\left( \frac{\ell_B^2}{\lambda_T^2} \right) \right].
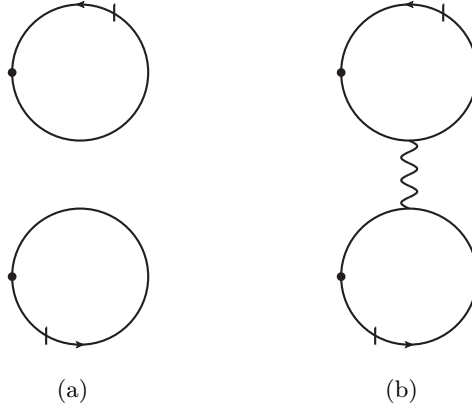\tag{4.114}
$$

Figure 4.8: Diagrams that contribute to the contact value $g(0)$ in a virial and perturbative expansion. The propagators of the bubble have to run back, since all the fields act at imaginary time $\tau = 0$. As a consequence, they need to be slashed at least once, making the leading order diagram order $z^2$. For details on the formalism, see chapter 3.

Performing the $x$-integration term by term, and plugging in the leading order virial result $z = n\lambda_T^d/2$ for the fugacity in terms of the density, we get the following result for the contact value $g(0) = g_{\uparrow\downarrow}(0)/2$:

$$g(0) = \begin{cases} \dfrac{1}{2}\left(1 - \dfrac{\pi^2}{\sqrt{2}}\dfrac{\ell_B}{\lambda_T} + \dots\right) & \text{(2D)} \\[2ex] \dfrac{1}{2}\left(1 - \sqrt{2}\pi\dfrac{\ell_B}{\lambda_T} + \dots\right) & \text{(3D)} \end{cases} \tag{4.115}$$

The leading order term is the same result as for a classical non-interacting gas. The first correction vanishes at large temperatures like $\sim 1/\sqrt{T}$. Note that the tails in the OPE are expected to occur at momenta $q \gg \lambda_T^{-1}$, and thus get pushed very far out. The prefactor of the tails, however, is of order one in this regime. Note that we can also obtain the result (4.115) using the same diagrammatic virial expansion technique that was used extensively in chapter 3 and sec. 2.3. Also performing an expansion in the coupling strength $e^2$, the diagrams that contribute are shown in fig. 4.8. After evaluation of the loop integrals, this exactly yields (4.115) for the contact value $g(0)$, which is a nice reassurance that we did not make any mistake during our discussion of the normalization of the wave function.

The classical limit $\hbar \to 0$, where the Rydberg dominates over temperature $\mathrm{Ry} \gg k_B T$, describes non-degenerate plasmas at relatively low temperatures. Charged dust particles [158] in space are, for example, described by this limit. The exponential term in the denominator of the integrand in eq. (4.112) now dominates, so we can just omit the one. The result of this integration is a Meier-$G$ function, which, after again using $z = n\lambda_T^d/2$ and $g(0) = g_{\uparrow\downarrow}(0)/2$, results in the following leading order behavior of the pair correlation function at zero distance:

$$g(0) = \begin{cases} \dfrac{2\pi 2^{1/3}}{3^{1/2}} \left(\dfrac{\ell_B}{\lambda_T}\right)^{1/3} e^{-\frac{3\pi}{2^{1/3}}(\frac{\ell_B}{\lambda_T})^{2/3}} + \dots & \text{(2D)} \\ \dfrac{4\pi^2 2^{1/3}}{3^{1/2}} \left(\dfrac{\ell_B}{\lambda_T}\right)^{4/3} e^{-\frac{3\pi}{2^{1/3}}(\frac{\ell_B}{\lambda_T})^{2/3}} + \dots & \text{(3D)} \end{cases} \qquad (4.116)$$

In the limit $\hbar \to 0$, the contact value vanishes exponentially! Note that the high-momentum tails of both the momentum distribution (4.78) and the static structure factor (4.44) contain the inverse Bohr radius, which diverges as $\hbar \to 0$. However, once again, the typical scale $q \gg \lambda_T^{-1}$ where the tails appear is pushed out to infinity. Furthermore, since the contact value $g(0)$ vanishes exponentially, the total weight of the tails vanishes. This is the explanation why a purely classical calculation leads to different tails [159] than the ones observed in eqs. (4.78) and (4.44). For example, the static structure factor of the classical electron gas decays like $1/q^2$ for momenta $\kappa < q < \ell_B$, where $\kappa = \sqrt{n\ell_B}$ is the so called Debye-Hückel length [159].

A little discussion is in order. Why do we have contradictory findings for the classical limit and the high-temperature limit? In fact, the path that lead us to discover the difference of those limits was Prof. Zwerger asking for the classical limit of $g(0)$. Since $\lambda_T \to 0$ both in the classical and high-temperature limit, I actually assumed those limits to be the same. I got the result (4.115), while his calculation predicted the contact value to vanish exponentially. This was puzzling at first, but if we think about the meaning of the results (4.115) and (4.116), we can indeed understand this paradox. In the limit (4.115), we are asking for the infinite temperature limit of a quantum mechanical gas. The typical energies of the colliding particles are thus extremely large, and hence they barely feel the Coulomb repulsion, even while passing through each other. In the limit (4.116) however, we are asking for the classical limit of the probability of two particles sitting on top of each other. The Coulomb potential is infinitely repulsive at short distances, and while that does not concern a quantum particle, classical particles can *never* enter the point where the energy would actually be infinite! This is all the non-commuting limits boil down to.

## 4.8 Summary

In this chapter, we have discussed the high-momentum tails of the momentum distribution and the static structure factor in the repulsive Coulomb problem, i.e. for an electron gas. The momentum distribution $n_\sigma(\mathbf{q})$ was shown to decay like $\sim 1/|\mathbf{q}|^6$ in two dimensions and $\sim 1/|\mathbf{q}|^8$ in three dimensions. The leading contribution is rotationally invariant and the prefactor of the tails is proportional to the contact value $g(0)$ of the pair correlation function, which is a measure for the probability that two electrons occupy the same point in space. A generalized version of this statement even holds true in the non-translational invariant case. The contact value $g(0)$ was also found to be the prefactor of the tails of the static structure factor $S(\mathbf{q})$, which scales like $S(\mathbf{q}) - 1 \sim 1/|\mathbf{q}|^3$ in two dimensions, and $S(\mathbf{q}) - 1 \sim 1/|\mathbf{q}|^4$ in three dimensions. Our derivation has the advantage that, due to the OPE being a relation for operators, it holds for any state. The results are all compatible with the results already known from Kimball's work [130, 131, 132].

We also derived, by means of an OPE of the operator $\psi_\uparrow(\mathbf{x})\psi_\downarrow(\mathbf{y})$, the factorization of the wave function when two of the coordinates come close together. This is a nice justification of the Ansatz that Kimball used to prove the tails.

In the last part, we studied the classical and high-temperature limits of the contact value $g(0)$ of the pair correlation function. It turned out that these limits are not identical. An intuitive explanation on why this is the case was given.

In conclusion, the maybe most important message of this chapter is that the OPE is indeed applicable to a non-relativistic system with Coulomb interactions. Besides the advantage that the OPE offers relations at the operator level, the OPE opens the opportunity to also study dynamical correlators. For this problem, an approach relying on the factorization of the wave function is not sufficient. One could, for example, think about studying the frequency and momentum dependence of the spectral function or the dielectric constant. Possible sum rules could also be derived, using methods analogous to the ones used in sec. 2.2 of this thesis. I have to admit, however, that the complexity of the scattering amplitude and the associated loop integrals will make such calculations quite involved.

# Chapter 5

# Conclusion

> "No electron was harmed in the making of this thesis."
>
> *(I hope so, at least.)*

In this thesis, methods of quantum field theory were used to study the behavior of various systems in regimes where few-body correlations are important. For the two-dimensional, contact-interacting Fermi gas, we have used an operator product expansion to derive exact asymptotic relations and sum rules for RF-spectroscopy. Subsequently, a quantum cluster (virial-) expansion was used to extract the behavior of the spectral function in the non-degenerate limit. Various quantities that are connected to the spectral function were obtained, and the virial expansion was shown to fulfill the universal Tan relations.

We then changed our focus away from the two-dimensional case, and studied three-dimensional quantum gases in the approximation of contact-interactions. We again employed a virial expansion to extract three-body correlations in both the fermionic and the bosonic case. Due to the novelty of the formalism, the calculation of the momentum distribution, the contact parameters and the virial coefficients was meticulously presented. The results are in excellent agreement with known universal relations. For bosons at unitarity, comparison to experiment revealed that in order to reproduce the experimentally measured momentum distributions, we need to assume that only the next-to deepest trimer state is populated.

In the last part, we have re-derived asymptotic relations for the momentum distribution and the static structure factor of the Coulomb gas. We have shown that the wave-function at short distances indeed factorizes, and have calculated the pair correlation function at zero distance for the classical and high-temperature limits. They were shown not to commute, which can be understood even intuitively.

# Appendix A

# Feynman rules for two-dimensional Fermions

## A.1 Feynman rules of the theory

This appendix contains a compilation of the Feynman rules for the theory of two-dimensional contact interacting fermions defined by the Lagrangian (2.5). The conventions are for the real-time formalism. Since we are working in the equal mass case $m_\sigma = m \ \forall \sigma$, the *bare propagator* is the same for all the particles, independent of their species quantum number $\sigma$. Furthermore, since we will in practice only ever set $g_{12} \equiv g$ and $g_{13} \equiv g'$ to nonzero, we will just give the Feynman rules for the case $\sigma = 1, 2$. For the third species, everything is completely analogous. To each bare fermion line, like the one in figure A.1(a), associate a Green's function

$$G(q_0, \mathbf{q}) \;\; = \;\; \frac{i}{q_0 - \frac{\mathbf{q}^2}{2m} + i\epsilon} \tag{A.1}$$

To each two body vertex between particles of species $\sigma$ and $\sigma'$, an example of which is depicted in figure A.1(b), attach a factor $-ig$. Note that $g_{\sigma\sigma} = 0$ for all $\sigma$, since fermions of the same species can not, due to the Pauli exclusion principle, have contact interactions. Finally, integrate over each momentum that is not determined from energy and momentum conservation at each vertex with the measure $\int dq_0/2\pi \int d^2q/(2\pi)^2$. We often have to sum a series of loop diagrams that, when summed to all orders in the interaction, gives the solution to the Lippmann-Schwinger equation (see figure 2.1). For the resulting amplitude, we have the following effective Feynman rule: To each gray blob, like the one depicted in figure A.1(c), that stands for an infinite series of ladder diagrams, associate an amplitude

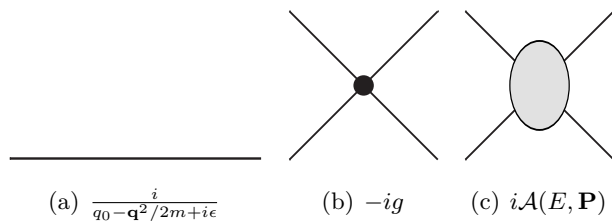(a) $\frac{i}{q_0 - \mathbf{q}^2/2m + i\epsilon}$      (b) $-ig$      (c) $i\mathcal{A}(E, \mathbf{P})$

Figure A.1: Feynman rules for the theory defined by the Lagrangian 2.5 for two species $\sigma = 1, 2$. The amplitude $\mathcal{A}$ is given by equations (A.2) and (A.3).

$i\mathcal{A}$. In the center of mass frame, we have

$$\mathcal{A}(E) \;\; = \;\; \frac{4\pi}{m} \frac{1}{\log(-ma_2^2 E)}. \tag{A.2}$$

We can use Galilean invariance to show that the general amplitude $\mathcal{A}(E, \mathbf{P})$ with center of mass momentum $\mathbf{P}$ and energy $E$ is connected to its center of mass counterpart via

$$\mathcal{A}(E, \mathbf{P}) \;\; = \;\; \mathcal{A}\!\left(E - \frac{\mathbf{P}^2}{4m}\right). \tag{A.3}$$

## A.2 Feynman rules for operator vertices

In sec. 2.2.2, it is important to know which operators contribute which factors to the amplitudes that are matched against each other. A sketch of the derivation of these Feynman rules will be given here for the case of the RF operator $\mathcal{O}_{\mathrm{rf}}(\omega + i\epsilon, \mathbf{R})$. Quite generally, a vertex is only momentum- and/or energy-conserving when it is being integrated over in space and/or time. This is also the reason why the interaction vertices that appear in the Feynman diagrams are momentum- and energy-conserving. The local operators on the right hand side of the OPE (2.28) are not integrated over in time or space, thus they neither conserve energy nor momentum. The matter is a little more subtle for the RF operator, because one of its vertices is integrated over all times, and both vertices are integrated over their relative distance. As we will see below, this results in a specific rule relating incoming and outgoing momenta. The essential ingredient for the derivation of the Feynman rules of the operator vertices

is the Fourier decomposition of the quantum fields $\psi_\sigma(\mathbf{x}, t)$:

$$\psi_\sigma(\mathbf{x}, t) = \int_{\omega, \mathbf{k}} e^{-i(\omega t - \mathbf{k} \cdot \mathbf{x})} \psi_\sigma(\mathbf{k}, \omega) \tag{A.4}$$

$$\psi_\sigma(\mathbf{k}, \omega) = \int dt \int d^d x \, e^{i(\omega t - \mathbf{k} \cdot \mathbf{x})} \psi_\sigma(\mathbf{x}, t) \tag{A.5}$$

Corresponding formulas for the adjoint fields $\psi_\sigma^\dagger$ can be obtained from the above formulas via complex and hermitian conjugation. The derivation of the Feynman rules of the one-body operators is completely analogous. They can be read off from eqs. (2.33), (2.34) and (2.35), that contain their matrix elements in one body states. The two-body operator $\psi_1^\dagger \psi_2^\dagger \psi_2 \psi_1$ that defines the contact density has the following Feynman rule: Let the momenta of the incoming lines, that are connected to the vertex, be $\mathbf{p}_1$, $\mathbf{p}_2$. The corresponding outgoing momenta shall be denoted by $\mathbf{p}_1'$, $\mathbf{p}_2'$. Under these conditions, the vertex $\psi_1^\dagger \psi_2^\dagger \psi_2 \psi_1(\mathbf{R})$ contributes a factor $e^{i(\mathbf{p}_1 + \mathbf{p}_2 - \mathbf{p}_1' - \mathbf{p}_2') \cdot \mathbf{R}}$.

For the derivation of the Feynman rule of the RF operator, we insert the Fourier decomposition (A.4) into the defining equation (2.23):

$$
\begin{aligned}
\mathcal{O}_{\mathrm{rf}}(\omega, \mathbf{R}) &= \int dt \, e^{i\omega t} \int d^d r \int_{(\eta, \mathbf{u}), (\eta', \mathbf{u}'), (\nu, \mathbf{v}), (\nu', \mathbf{v}')} e^{-it(\nu - \nu')} \\
&\quad e^{i\mathbf{R} \cdot (\mathbf{v} - \mathbf{v}' - \mathbf{u}' + \mathbf{u})} e^{i\frac{\mathbf{r}}{2} \cdot (\mathbf{v} - \mathbf{v}' + \mathbf{u}' - \mathbf{u})} \\
&\quad \psi_2^\dagger(\mathbf{v}', \nu') \psi_3(\mathbf{v}, \nu) \psi_3^\dagger(\mathbf{u}', \eta') \psi_2(\mathbf{u}, \eta) \\
&= 2\pi \delta(\omega - (\nu - \nu'))(2\pi)^d \delta\left(\frac{1}{2}\left[(\mathbf{u}' + \mathbf{v}) - (\mathbf{v}' + \mathbf{u})\right]\right) \\
&\quad e^{-i\mathbf{R} \cdot (\mathbf{v}' - \mathbf{v} + \mathbf{u}' - \mathbf{u})} \times \int_{(\eta, \mathbf{u}), (\eta', \mathbf{u}'), (\nu, \mathbf{v}), (\nu', \mathbf{v}')} \\
&\quad \psi_2^\dagger(\mathbf{v}', \nu') \psi_3(\mathbf{v}, \nu) \psi_3^\dagger(\mathbf{u}', \eta') \psi_2(\mathbf{u}, \eta) \tag{A.6}
\end{aligned}
$$

From the expression above, the Feynman rule in momentum space can be read off:

- Make sure that the outgoing energy of the second vertex is $\omega$ lower than the energy entering the vertex: $\nu = \nu' + \omega$

- Make the sum of momenta of the inner 3-lines equal to the sum of the momenta of the outer 2-lines: $(\mathbf{u}' + \mathbf{v}) = (\mathbf{v}' + \mathbf{u})$. This is what I referred to as "half momentum conserving" in sec. 2.2.2.

- Multiply by a factor $e^{-i\mathbf{R} \cdot (\mathbf{v}' - \mathbf{v} + \mathbf{u}' - \mathbf{u})}$

*Appendix A Feynman rules for two-dimensional Fermions*

Of course, when fields of different momentum and energy are contracted with the fields above, this sets their four momenta equal. A small subtlety is the following: The factor $1/2$ in the $\delta$ function in eq. (A.6) might contribute a factor $2^d$. However, this factor $1/2$ never really contributes in our diagrams. In the one particle diagrams, this is very easy to see, because $\mathbf{u}' = \mathbf{v}$ implies $2\mathbf{v} = \mathbf{u} + \mathbf{v}'$, which cancels the $1/2$ inside the delta function. For the two particle diagrams, it is either the same reason as given before, or another momentum conserving $\delta$-function, for example the one of the vertex $iD$, contributes in a way that cancels the two again. This involved treatment of momenta at the vertices is the price for symmetrizing the RF correlator in the distance $\mathbf{r}$ of the two vertices. The physical advantage of this procedure is that this yields current densities rather than derivatives like $(\nabla \psi_2^\dagger)\psi_2$ in the OPE.

# Appendix B

# Feynman rules in imaginary time

This appendix gives a short compilation of the Feynman rules that follow from the Lagrangian densities (3.17) (bosonic case) and (3.24) (fermionic case). In principle, the Feynman-rules are the same as in ref. [25], except for the omission of the various factors of $i$. In fig. B.1, we state the Feynman rules for the (bare) contractios and vertices. Except for the Feynman rule of the slashed propagator, all rules are given in Matsubara-frequency and momentum space.



(a) $\frac{1}{i\omega_n + \mu - \varepsilon_{\mathbf{q}}}$

(b) $G^{(1)}_{(\sigma)}(\tau, \mathbf{q})$, cf. eqs. (3.41) (Bose) and (3.43) (Fermi)

(c) $-4/g_2$ (Bose), $-1/g_2$ (Fermi)

(d) $-2 \cdot g_2/4$ (Bose), $-g_2$ (Fermi)

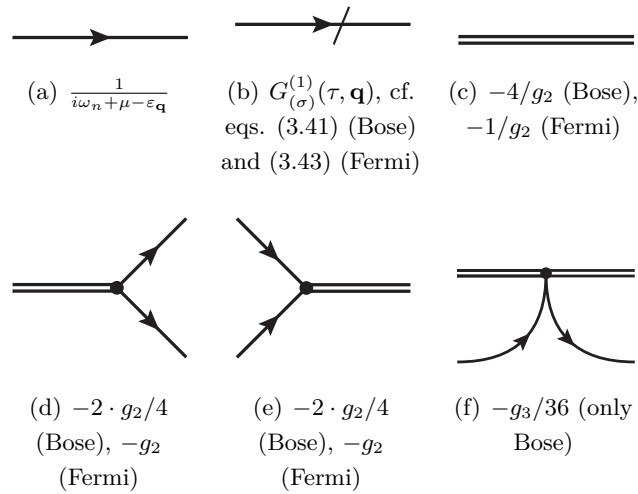(e) $-2 \cdot g_2/4$ (Bose), $-g_2$ (Fermi)

(f) $-g_3/36$ (only Bose)

Figure B.1: Feynman rules defined by the imaginary time actions in eqs. (3.17) (Bose) and (3.24) (Fermi). Symmetry factors have not been made explicit. All Feynman rules, except for (B.1(b)), are given in momentum space. We will only encounter the slashed propagators in the imaginary time / momentum representation, which is why we gave this Feynman-rule in the mixed representation.

*Appendix B Feynman rules in imaginary time*

The Feynman rule for the auxiliary field is most easily derived from the path integral formalism, in the canonical formalism one needs a little additional care, because the auxiliary field is non-dynamical.

# Appendix C

# Some properties of the Laplace transform

This appendix is a compilation of definitions and properties regarding the Laplace transform. All of the properties and the proofs regarding those can be found in the book [111]. We define the Laplace transform of a function $f(t)$, that is only non-zero for $t > 0$, by

$$f(s) \quad = \quad \int_0^\infty dt e^{st} f(t) \tag{C.1}$$

$$f(t) \quad = \quad \int_{BW} \frac{ds}{2\pi i} e^{-ts} f(s), \tag{C.2}$$

where in (C.1), we need to choose $s$ such that the integral exists. Afterwards, we can analytically continue the result to other $s$. The inverse formula (C.2) only holds true if the Bromwich integral exists. Note that our definition of the Laplace transform has the opposite sign as in [111]. For our convention, the Bromwich integral in (C.2) runs parallel to the imaginary axis, to the left of all non-analyticities of $f(s)$. Depending on the analytic structure of $f(s)$, one can also deform the contour into a convenient other contour, as long as the integral is still well-defined.

In the sections on the two- and (implicitly) three-body scattering problem, as well as during the study of the diagrams that contribute to the virial expansion up to third order in the fugacity, we make frequent use of the convolution theorem for the Laplace transform:

$$h(\tau) \quad = \quad \int_0^\tau dt g(t - \tau) f(t)$$
$$\Rightarrow h(s) \quad = \quad f(s) g(s) \tag{C.3}$$

We can also generalize this convolution theorem to the case of more than a single

function. To this end, we define the set

$$A = \left\{ (t_1, ..., t_n) : t_i \geq 0 \, \forall i \in \{1, ..., n\} \text{ and } \sum_{i=1}^{n} t_i \leq \tau \right\} \qquad (C.4)$$

as a shorthand. Repeated application of the convolution theorem for two functions yields

$$\int_A \prod_i dt_i \, g\left(\tau - \sum_i t_i\right) f_1(t_1)...f_n(t_n) = \int_{BW} \frac{ds}{2\pi i} e^{-\tau s} g(s) f_1(s)...f_n(s), \qquad (C.5)$$

where we have written the convolution theorem in the back-transformed way. Setting $\tau = \beta$, the above form is tailor-made for the imaginary time integrations that show up in the diagrams of the virial expansion, cf. sec. 3.3. This, as realized by Leyronas [9], allows us to express all the imaginary time integrations in terms of a single contour integration.

# Appendix D

# Projection of the STM equation onto angular momenta

In this appendix, we will perform the projection of the STM equation (3.50) (in the center of mass frame $\mathbf{P} = \mathbf{0}$), and show that it indeed yields (3.54). In particular, different angular momentum channels do not mix, which simplifies the numerical treatment of the problem by a great deal.

## D.1 Legendre functions of the second kind

In order to perform the angular projection, let us first review (for details, see [113]) some properties of the Legendre functions of the second kind $Q_l(z)$, defined in eq. (3.55), which we repeat here for convenience:

$$Q_l(z) \;\; = \;\; \frac{1}{2} \int_{-1}^{1} dx \frac{P_l(x)}{z - x}. \tag{D.1}$$

We will focus on integer indices, since the $P_l(x)$ have integer indices in our problem (one can, in principle, generalize the above formula to non-integer ones, such that the Legendre polynomials are replaced by Legendre functions [113]). From the definition (D.1) and the completeness of the Legendre polynomials on the interval $[-1, 1]$, it follows that

$$\frac{1}{z - x} = \sum_{l=0}^{\infty} (2l + 1) P_l(x) Q_l(z), \tag{D.2}$$

where $-1 \leq x \leq 1$ and $z \in \mathbb{C}/[-1, 1]$. We use the above form to eliminate the propagators containing an angle in the denominator. Similar to the Legendre polynomials $P_l(x)$, the Legendre functions of the second kind can be obtained from a

recursion relation [113]. For integer indices, this recursion relation is solved by [114]

$$Q_l(z) \;=\; \frac{1}{2}P_l(z)\log\left(\frac{z+1}{z-1}\right) - W_{l-1}(z) \tag{D.3}$$

$$W_{l-1}(z) \;=\; \sum_{k=1}^{l}\frac{1}{k}P_{l-k}(z)P_{k-1}(z) \tag{D.4}$$

$$W_{-1}(z) \;=\; 0, \tag{D.5}$$

which is how I generated the Legendre functions for numerical evaluation in my $C++$ code. For example, the first two Legendre functions are

$$Q_0(z) \;=\; \frac{1}{2}\log\left(\frac{z+1}{z-1}\right) \tag{D.6}$$

$$Q_1(z) \;=\; \frac{1}{2}z\log\left(\frac{z+1}{z-1}\right) - 1 \tag{D.7}$$

For analytic evaluation of the angle integrations that appear in the three-body sector of the virial expansion, we define

$$\tilde{Q}_l(z) \;=\; -\frac{d}{dz}Q_l(z) = \frac{1}{2}\int_{-1}^{1}dx\,\frac{P_l(x)}{(z-x)^2} \tag{D.8}$$

## D.2 Projecting the STM equation onto angular momentum channels

Equation (3.53) defines the angular projection $t_3^{(l)}(s,p,k)$ of the three-body $T$-matrix. We now want to derive a reduced STM equation for these angular momentum components $t_3^{(l)}$. Defining $\hat{\mathbf{p}}\cdot\hat{\mathbf{k}} = \cos\theta_{pk}$, we project the STM equation (3.50) (with vanishing center of mass momentum $\mathbf{P}=\mathbf{0}$) onto angular momentum $l$ by multiplying both sides by $P_l(\cos\theta_{pk})/2$ and integrating over $\int_{-1}^{1}d\cos\theta_{pk}$. The resulting equation reads

$$
\begin{aligned}
t_3^{(l)}(s,p,k) =& \frac{1}{2}\int_{-1}^{1}d\cos\theta_{pk}\,P_l(\cos\theta_{pk})\left[\frac{\frac{m}{pk}}{\frac{m}{pk}\left(s-\frac{p^2}{m}-\frac{k^2}{m}\right)-\cos\theta_{pk}} + \frac{g_3}{9g_2^2}\right] \\
&+ \frac{1}{2}\int_{-1}^{1}d\cos\theta_{pk}\,P_l(\cos\theta_{pk})\int_0^{\infty}\frac{dq}{(2\pi)^3}q^2\int_{-1}^{1}d\cos\theta_{qk}\int_0^{2\pi}d\phi \\
&\left[\frac{\frac{m}{pq}}{\frac{m}{pq}\left(s-\frac{p^2}{m}-\frac{q^2}{m}\right)-\cos\theta_{pq}} + \frac{g_3}{9g_2^2}\right]T_2\left(s-\frac{3q^2}{4m}\right) \\
&\sum_{L=0}^{\infty}(2L+1)P_L(\cos\theta_{qk})t_3^{(L)}(s,q,k), \tag{D.9}
\end{aligned}
$$

where we imply the suggestive definitions $\cos\theta_{qk} = \hat{\mathbf{q}} \cdot \hat{\mathbf{k}}$ and $\cos\theta_{pq} = \hat{\mathbf{p}} \cdot \hat{\mathbf{q}}$. We also used the angular decomposition (3.52) to expand $T_3$ in terms of Legendre polynomials on the right-hand side. Note that the three cosines are *not* independent of each other, since the unit vectors $\hat{\mathbf{q}}, \hat{\mathbf{p}}, \hat{\mathbf{k}}$ form a spherical triangle. We have chosen $\hat{\mathbf{k}}$ as the $z$-axis for the $\mathbf{q}$-integration, and we choose $\phi$ to be the angle between the projection of $\hat{\mathbf{p}}$ onto the plane perpendicular to $\hat{\mathbf{k}}$ and the same projection of $\hat{\mathbf{q}}$. This means that we choose the projected $\hat{\mathbf{p}}$ as the $x$-axis for the $\mathbf{q}$-integration. The law of cosines for spherical triangles (easily derived from $\hat{\mathbf{x}} \cdot \hat{\mathbf{y}}$ for two general unit vectors in spherical coordinates) allows us to re-express $\cos\theta_{pq}$ in terms of the other angles:

$$\cos\theta_{pq} = \cos\theta_{qk}\cos\theta_{pk} + \sin\theta_{qk}\sin\theta_{pk}\cos\phi \qquad (D.10)$$

Furthermore, eqs. (D.2) and (D.1) allow us to rewrite the propagators in the inhomogeneity and the $q$-integral in eq. (D.9) in terms of the Legendre functions of the second kind. The propagator in the $q$-integral contains a series of Legendre polynomials $P_n(\cos\theta_{pq})$. We can re-express these via the addition theorem [113]

$$P_n(\cos\theta_{qk}\cos\theta_{pk} + \sin\theta_{qk}\sin\theta_{pk}\cos\phi) = P_n(\cos\theta_{qk})P_n(\cos\theta_{pk})$$
$$+ 2\sum_{m=1}^{n}\frac{(n-m)!}{(n+m)!}P_n^m(\cos\theta_{qk})P_n^m(\cos\theta_{pk})\cos m\phi \qquad (D.11)$$

for Legendre polynomials. The $P_n^m(x)$ are associated Legendre functions. The first important simplification now arises from the integration $\int_0^{2\pi} d\phi$: Since $m \geq 1$ is integer in the above formula, the second term of the addition theorem will always vanish when integrated over $\phi$. Using all of the above considerations, we can simplify the integral equation to

$$t_3^{(l)}(s,p,k) = \left[\frac{m}{pk}Q_l\left(\frac{m}{pk}\left[s - \frac{p^2}{m} - \frac{k^2}{m}\right]\right) + \frac{g_3}{9g_2^2}\delta_{0l}\right]$$
$$+ \frac{1}{2}\int_{-1}^{1}d\cos\theta_{pk}P_l(\cos\theta_{pk})\int_0^{\infty}\frac{dq}{(2\pi)^2}q^2\int_{-1}^{1}d\cos\theta_{qk}$$
$$\left[\sum_n(2n+1)P_n(\cos\theta_{pk})P_n(\cos\theta_{qk})\frac{m}{pq}Q_l\left(\frac{m}{pq}\left[s - \frac{p^2}{m} - \frac{q^2}{m}\right]\right) + \frac{g_3}{9g_2^2}\right]$$
$$T_2\left(s - \frac{3q^2}{4m}\right)\sum_{L=0}^{\infty}(2L+1)P_L(\cos\theta_{qk})t_3^{(L)}(s,q,k), \qquad (D.12)$$

where we have already used the orthogonality relation

$$\int_{-1}^{1}dx P_l(x)P_m(x) = \frac{2\delta_{lm}}{2l+1} \qquad (D.13)$$

for the Legendre polynomials to simplify the inhomogeneity. We can now use the same orthogonality relation on the $\cos\theta_{pk}$ integration, which collapses the sum over $n$ and yields a Kronecker delta $\delta_{0l}$ in front of the $g_3$ term under the integral. Afterwards, we integrate over $\cos\theta_{qk}$, which collapses the remaining sum over $L$. Plugging in the definition (3.19) of $g_3$ in terms of $H(\Lambda)$ then yields the reduced STM equation (3.54) for the angular component $t_3^{(l)}$ of the three-body $T$-matrix. For fermions, the procedure is completely the same as the one presented here.

# Appendix E

# Symmetry factors and signs for chapter 3

This appendix presents the calculation of symmetry factors and signs for the diagrams that show up in the virial expansion.

## E.1  Bosons

The one particle sector of course does not yield any symmetry factors. We will directly start with the two-particle sector. To obtain the symmetry factors, it is, in my opinion, useful to not directly express the diagrams in terms of the two-body $T$-matrix $T_2$, but to rather take the dimer propagator $G_{dd}$, defined by the integral equation (3.46), and in the end plug in the definition (3.48) of $T_2$ in terms of $G_{dd}$. The advantage of this procedure is that we do not need to worry about the effective symmetry factors that are contained in $T_2$. The procedure will always be to determine the symmetry factors for the mother diagrams that are generated by the perturbative expansion (3.32). The expansion in terms of the fugacity ("slashing" the lines) is done in sec. 3.3.1.

### E.1.1  Two-Particle Diagrams

We will start out with the mother diagram of diagrams 3.7(a)-3.7(d). It is shown in fig. E.1, together with a suggestion for the counting of the symmetry factor. The logic behind the counting is the following: The two interaction vertices correspond $-g_2 \bar{d} \psi \psi / 4$ and $-g_2 d \bar{\psi} \bar{\psi} / 4$, while the external vertex is $\psi \bar{\psi}$. The contraction of the two dimer fields yields the vacuum dimer propagator (times $e^{2\mu t_2}$), when we already
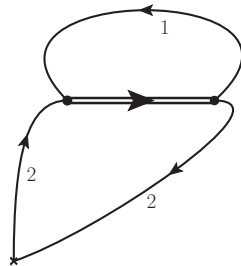
Figure E.1: Calculating the symmetry factor for the diagram that defines the two-
particle sector. For the logic, see the text.

insert[1] the expanded propagators $G^{(0)}$ for the loops contained in this contraction. For each of the external legs, we have two choices with which $\psi$ or $\bar\psi$ of the vertices we want to contract. The inner loop is then fixed by our earlier choices and does not contribute anything else. We thus get:

$$
\begin{aligned}
\mathcal{G}(0^-,\mathbf{q}) \quad &= \quad -4\left(\frac{g_2}{4}\right)^2 \int_A \int_{\mathbf{k}} G(t_1,\mathbf{q})G(-t_1-t_2,\mathbf{q})e^{2\mu t_2}G_{dd}(t_2,\mathbf{k}+\mathbf{q})G(-t_2,\mathbf{k}) \\
&\overset{(3.48)}{=} \quad -\int_A \int_{\mathbf{k}} G(t_1,\mathbf{q}))G(-t_1-t_2,\mathbf{q})e^{2\mu t_2}T_2(t_2,\mathbf{k}+\mathbf{q})G(-t_2,\mathbf{k}) \quad\quad \text{(E.1)}
\end{aligned}
$$

Expanding the propagators yields diagrams 3.7(a)-3.7(d).

### E.1.2 Three-Particle Diagrams

We will determine the prefactors of the three-body diagrams 3.8(a)-3.8(e) by using the "born approximation" for the $T_3$-matrix. This means that we replace the gray box in diagrams 3.8(a)-3.8(e) by the two leading order terms in diagram 3.5. This indeed generates all the mother diagrams for the approximated $T_3$ amplitude. Of course you could now say: But I can just directly read off symmetry factors from the diagrams when treating the $T_3$ vertex like $d\psi t_3(...)\bar{d}\bar\psi$! Very observant of you. But while this procedure is capable of producing relative symmetry factors, we can not prove that it is indeed the $T_3$ matrix defined by eq. (3.50) that enters in our diagrams. To fix the global prefactor, we still need to look at the mother-diagrams. The reason of course that our logic in truth is reversed: We look at all diagrams

---

[1] If your are not comfortable with that, please view the diagrams here and in the following as containing the bare dimer propagator. If you do the math, this of course works out to give the same symmetry factors as the ones obtained here.
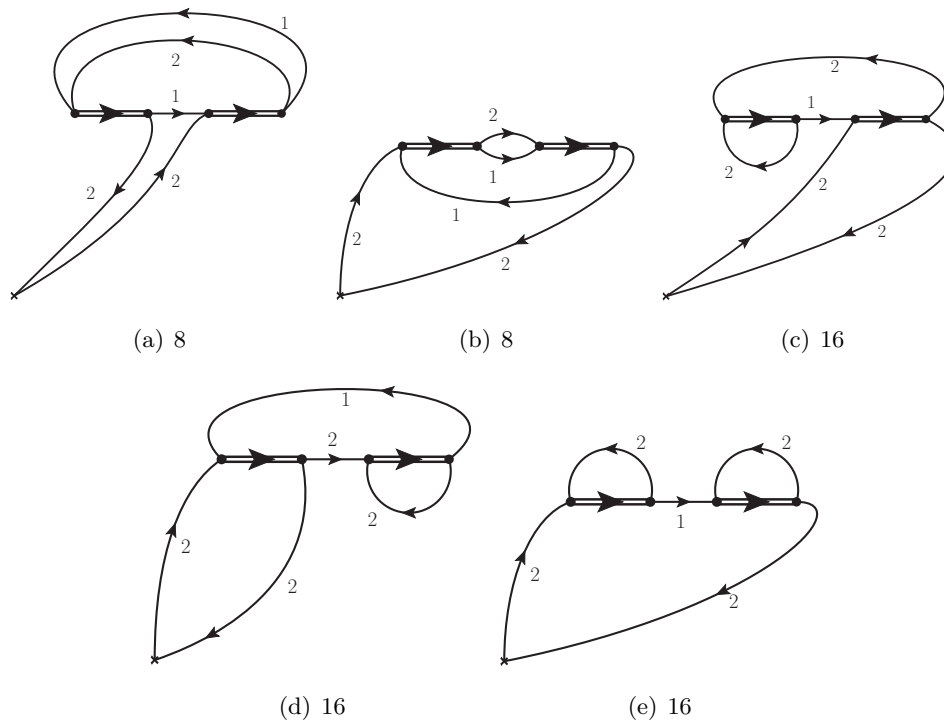
Figure E.2: Mother-diagrams that contain the leading order (that contains the propagation of a mediating atom) of the STM equation. We propose a counting scheme and state the resulting symmetry factor below the diagram.

that are generated by the perturbative expansion of the Green's function. Then we figure out which ones will be allowed to third order in the fugacity, and also sum up the effective vacuum two-particle scattering series. Then we determine the symmetry-factors of the appearing diagrams.

The diagrams that are generated by the term in the STM equation that contains the two-body vertices are shown in fig. E.2, together with a proposed counting scheme and the resulting prefactors. For the general logic behind the counting, see the two-body sector.

Similarly, the diagrams that are generated by the leading order term (that contains the three-body vertex) in the STM equation are shown in figure E.3. Note that diagram E.2(b) and E.3(b) do *not* have the same multiplicity. In the virial expansion however, they do have the same prefactor. Diagrammatically, the reason is that we have two choices which atom line of the innermost loop in E.2(b) we want to slash.
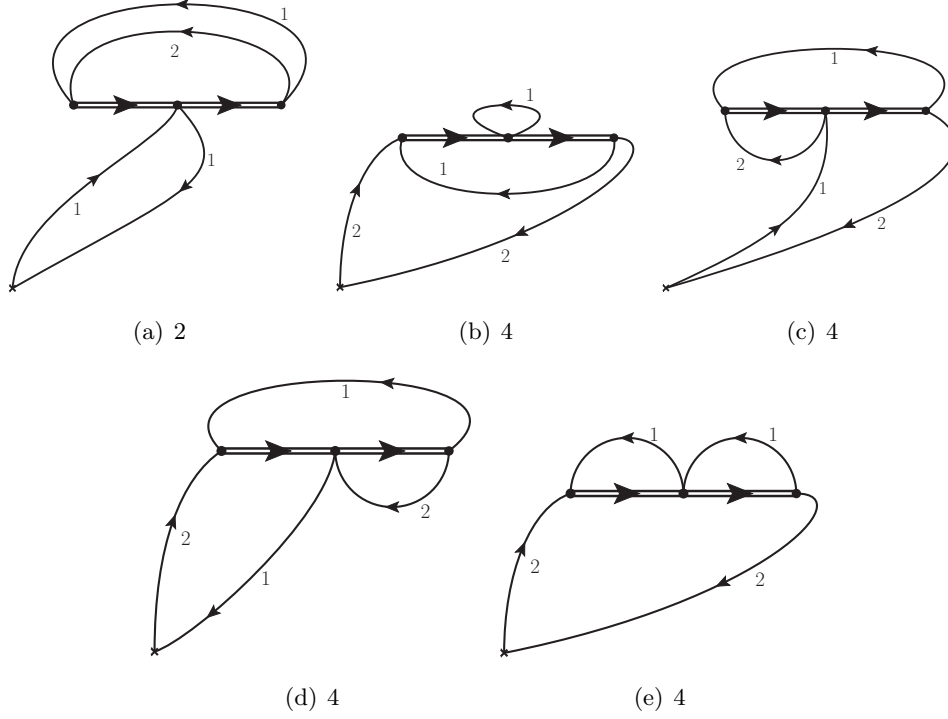
Figure E.3: Mother-diagrams that contain the leading order (that contains $g_3$) of the STM equation. We propose a counting scheme and state the resulting symmetry factor below the diagram.

In formulas, it comes from the fact that the expansion of the propagators in the inner loop reads

$$G(t_3, \mathbf{k})G(t_3, -\mathbf{k}) = G^{(0)}(t_3, \mathbf{k})G^{(0)}(t_3, -\mathbf{k}) + 2zG^{(0)}(t_3, \mathbf{k})G^{(1)}(t_3, -\mathbf{k}) + \dots \quad \text{(E.2)}$$

The first term generates a diagram that is contained in the vacuum dimer propagator and therefore does not contribute again.

We have now determined all the relative factors. To fix the global prefactor, i.e. prove that is indeed the $T_3$ defined by (3.50) that enters our diagrams, we now look at the sum of the contributions to the Green's function generated by diagrams E.2(a) and E.3(a). We now also expand the propagators in terms of the fugacity, i.e. we slash the lines like in figure 3.8(a). Further, we use the same time differences

$t_1, .., t_4$ (and the associated set $A$) as in section 3.3.1. We have:

$E.2(a) + E.3(a)$

$$= -z^3 \int_A \prod_i dt_i \int_{\mathbf{k},\mathbf{p}} G^{(0)}(t_1 + t_2 + t_3, \mathbf{q}) G^{(1)}(-t_1 - t_2, \mathbf{q}) \left(\frac{g_2^2}{4}\right)^2$$

$$e^{2\mu t_2} G_{dd}(t_2, \mathbf{k} + \mathbf{p}) e^{2\mu t_4} G_{dd}(t_4, \mathbf{k} + \mathbf{p}) G^{(1)}(-t_2 - t_3 - t_4, \mathbf{k})$$

$$G^{(1)}(-t_2 - t_3 - t_4, \mathbf{p}) \left[ -\frac{8}{16} G^{(0)}(t_3, \mathbf{p} + \mathbf{k} - \mathbf{q}) - \frac{2g_3}{36g_2^2} \delta(t_3 - 0^+) \right]$$

$$\overset{(3.48)}{=} -\frac{z^3}{2} \int_A \prod_i dt_i \int_{\mathbf{k},\mathbf{p}} e^{-t_2 \varepsilon_{\mathbf{q}}} T_2(t_2, \mathbf{k} + \mathbf{p}) e^{-t_4 \varepsilon_{\mathbf{q}}} T_2(t_4, \mathbf{k} + \mathbf{p}) e^{-t_1(\varepsilon_{\mathbf{q}} + \varepsilon_{\mathbf{k}} + \varepsilon_{\mathbf{p}})}$$

$$e^{-(\beta - t_1 - t_2 - t_3 - t_4)(\varepsilon_{\mathbf{q}} + \varepsilon_{\mathbf{k}} + \varepsilon_{\mathbf{p}})} \left[ e^{-t_3(\varepsilon_{\mathbf{k}+\mathbf{p}-\mathbf{q}} + 2\varepsilon_{\mathbf{q}})} - \frac{g_3}{9g_2^2} \delta(t_3 - 0^+) \right] \quad \text{(E.3)}$$

The $\delta(t_3 - 0^+)$ makes sure that the vertex of the three-body interaction is indeed ordered like $\bar{\psi}\bar{d}d\psi$. The numerators of the fractions are the symmetry factors of the diagrams. We also grouped the interaction vertices of the two-body interaction in such a way that makes it easy to identify the definition (3.48) of the $T_2$-matrix. We used this equation in the second equality, canceled all the exponentials that contain a $\mu$ against each other, and and multiplied by convenient factors of one to bring the integral into a form that now allows to apply the generalized convolution theorem (C.5) for the Laplace transform:

$$E.2(a) + E.3(a) = \frac{z^3}{2} \int_{BW} \frac{ds}{2\pi i} e^{-\beta s} \int_{\mathbf{k},\mathbf{p}} \frac{T_2^2(s - \varepsilon_{\mathbf{q}}, \mathbf{k} + \mathbf{p})}{(s - \varepsilon_{\mathbf{q}} - \varepsilon_{\mathbf{k}} - \varepsilon_{\mathbf{p}})^2}$$

$$\underbrace{\left[ \frac{1}{s - \varepsilon_{\mathbf{k}+\mathbf{p}+\mathbf{q}-\mathbf{q}-\mathbf{q}} - \varepsilon_{\mathbf{q}} - \varepsilon_{\mathbf{q}}} + \frac{g_3}{9g_2^2} \right]}_{\hat{=} T_3(s, \varepsilon_{\mathbf{q}}, \varepsilon_{\mathbf{q}}, \mathbf{k}+\mathbf{p}+\mathbf{q}, \mathbf{q}, \mathbf{q})}, \quad \text{(E.4)}$$

The term in the square brackets indeed is the inhomogeneity of the STM equation (3.50). Since diagrams E.2(a) and E.3(a) have a relative multiplicity of $1/2$ versus the other diagrams (after expanding in terms of the fugacity, remember the two choices for the slash in E.2(b)!), the other diagrams just have a simple prefactor of one. The expression (E.4) is compatible with the one we are using for diagram 3.8(a) in eq. (3.78). This concludes our calculation on how the three-body $T$-matrix enters the diagrams, as well as the symmetry factors of the diagrams.

## E.2  Fermions

We will directly start with the diagrams for the two-particle sector, since the one-particle sector trivially can not yield sign switches. In the following, we will make clear that when we draw diagrams very carefully, we can read off a sign switch from the number of crossings of the lines in the diagram. To understand this, recall that [26] when we use Wick's theorem on the correlator of four fermionic fields, we get a sign whenever the contraction lines cross (because an even or odd number of anti-commutations are needed to disentangle the fields). Hence, an even number of crossings corresponds to no sign switch, and an odd number of crossings yields a minus sign:

$$\langle T_\tau \psi(1)\psi(2)\overline{\psi}(3)\overline{\psi}(4)\rangle_0 = \langle T_\tau \psi(1)\psi(2)\overline{\psi}(3)\overline{\psi}(4)\rangle_0 + \langle T_\tau \psi(1)\psi(2)\overline{\psi}(3)\overline{\psi}(4)\rangle_0$$

$$= \langle T_\tau \psi(1)\overline{\psi}(4)\rangle_0 \langle T_\tau \psi(2)\overline{\psi}(3)\rangle_0 - \langle T_\tau \psi(1)\overline{\psi}(3)\rangle_0 \langle T_\tau \psi(2)\overline{\psi}(4)\rangle_0$$

$$, \tag{E.5}$$

where $i = (\tau_i, \mathbf{x}_i, \sigma_i)$ carries all information about the quantum numbers. Note that due to the expansion of our virial propagators in terms of the $G^{(n)}$, cf. eq. (3.43), which alternate in sign with the order of the expansion (even orders carry a $-$, odd orders carry a $+$), there are additional signs switches with respect to the sign of the mother diagrams. Having already invested the work for the bosonic case, we will actually be able to just give the signs with respect to the bosonic expressions without ever doing a real calculation. If you prefer to directly derive the results for the fermionic case, consult the bosonic section of this appendix, and use

$$T_2 = g_2^2 G_{dd} \tag{E.6}$$

for the $T_2$ matrix in terms of the fermionic dimer (vacuum) propagator.

### E.2.1  Two-particle diagrams

To determine the sign of the mother diagram E.1 for the fermionic case, where the external line is now an ↑-fermion and the loop consists of a ↓-fermion, it is convenient to use the $\mathcal{S}$-matrix expansion (3.31) of the Green's function. The diagram is related to the connected contraction of the correlator

$$\langle T_\tau \underbrace{\overline{\psi}_\uparrow \overline{\psi}_\downarrow d}_{t_1+t_2} \underbrace{\overline{d}\psi_\downarrow \psi_\uparrow}_{t_1} \underbrace{\overline{\psi}_\uparrow \psi_\uparrow}_{t_0=0} \rangle_0, \tag{E.7}$$

If we just use the effective Feynman-rule that $\langle d\bar{d}\rangle_0$ shall corresponds to an insertion of the vacuum dimer propagator, we actually get the diagram from the above correlator (otherwise just the first term in a series expansion of the vacuum dimer propagator). Here is the contraction that the mother diagram E.1 corresponds to:

$$E.1_{\text{Fermi}} \quad = \quad \langle T_\tau \bar{\psi}_\uparrow \bar{\psi}_\downarrow d \; \bar{d} \psi_\downarrow \psi_\uparrow \; \bar{\psi}_\uparrow \psi_\uparrow \rangle_0 \tag{E.8}$$

Since the dimer counts as a bosonic field (its equation of motion is $d = \psi_\downarrow \psi_\uparrow$, also see sec. 3.1.2), commuting it through the correlator will not yield a sign and we draw the contraction above. We have zero crossings of the contraction lines, meaning that the sign of this contraction is $(-1)^0 = 1$.

A back-running fermionic line contributes a Green's function $G$ (instead of $-G$ in the bosonic case, or the forward-running fermionic case), so the diagram can symbolically be written as

$$-G(-G_{dd})GG = GG_{dd}GG, \tag{E.9}$$

while the bosonic contribution to the Green's function (which carries an additional external minus sign from $\mathcal{G} \sim -\langle \bar{\psi}\psi \rangle$) is symbolically given by

$$-GG_{dd}GG. \tag{E.10}$$

We now want to fix the sign of the fermionic diagram 3.7(a). Slashing two times results in two additional minus signs with respect to the bosonic version of the diagram, because the slashed propagators alternate in sign in fermionic case. Thus, in summary[2] we have that

$$3.7(a)_{\text{Fermi}} = -3.7(a)_{\text{Bose}}, \tag{E.11}$$

where the diagram numbers always correspond to the results for the Green's function. Note that the above equation that the expressions for the momentum distribution and density are *equal*. Now, since diagrams 3.7(b)-3.7(d) are just slashed one more time, we get an additional sign for them and get

$$3.7(b)_{\text{Fermi}} = 3.7(b)_{\text{Bose}} \tag{E.12}$$

$$3.7(c)_{\text{Fermi}} = 3.7(c)_{\text{Bose}} \tag{E.13}$$

$$3.7(d)_{\text{Fermi}} = 3.7(d)_{\text{Bose}} \tag{E.14}$$

---

[2]Note that this does not correspond to the sign Leyronas gives to the diagram in the article [9]. Our diagrams 3.7(b)-3.7(d) agree with his results however. Furthermore, I can only reproduce the standard Beth-Uhlenbeck result for the second virial coefficient with the sign given here.

### E.2.2 Three-particle diagrams

We will first take a look at the contractions again, and then, in the same spirit as in the two-particle sector, fix a global sign by comparison to the bosonic contribution to the Green's function. To express the three-body diagrams in terms of contractions, we write the diagrammatic three-body $T$-matrix insertion as the effective vertex

$$\bar{\psi}_\sigma \bar{d}(t)\left[t_{3,\sigma}(t,...)\right]d\psi_\sigma(0), \tag{E.15}$$

where $t_{3,\sigma}(t,...)$ is a function that solves the STM equation, and only (imaginary) time arguments are shown. Since all the three-body diagrams have three slashes, the only variation in sign will come from the signs of the effective contractions. This fixes the relative signs between the diagrams. Afterwards, we will determine the sign of diagram 3.11(a), which then fixes the global sign and allows to give the results in terms of the bosonic ones (as always in this section: replaced with the fermionic $T$-matrices).

Diagrams 3.11(a)-3.11(f) corresponds to different effective contractions of the correlator

$$\langle \underbrace{\bar{\psi}_\uparrow \bar{\psi}_\downarrow d}_{t_1+t_2+t_3+t_4} \underbrace{\bar{\psi}_\sigma \bar{d}}_{t_1+t_2+t_3} \underbrace{d\psi_\sigma}_{t_1+t_2} \underbrace{\bar{d}\psi_\downarrow \psi_\uparrow}_{t_1} \underbrace{\bar{\psi}_\uparrow \psi_\uparrow}_{t_0=0} \rangle_0. \tag{E.16}$$

Once again omitting all the details, we have:

$$3.11(a) \quad \sim \langle T_\tau \bar{\psi}_\uparrow \bar{\psi}_\downarrow d \;\; \bar{\psi}_\uparrow \bar{d} d\psi_\uparrow \;\; d\psi_\downarrow \psi_\uparrow \;\; \bar{\psi}_\uparrow \psi_\uparrow \rangle_0 \qquad \text{sign: } (-1)^4 \quad \text{(E.17)}$$

$$3.11(b) \quad \sim \langle T_\tau \bar{\psi}_\uparrow \bar{\psi}_\downarrow d \;\; \bar{\psi}_\uparrow \bar{d} d\psi_\uparrow \;\; d\psi_\downarrow \psi_\uparrow \;\; \bar{\psi}_\uparrow \psi_\uparrow \rangle_0 \qquad \text{sign: } (-1)^3 \quad \text{(E.18)}$$

$$3.11(c) \quad \sim \langle T_\tau \bar{\psi}_\uparrow \bar{\psi}_\downarrow d \;\; \bar{\psi}_\uparrow \bar{d} d\psi_\uparrow \;\; d\psi_\downarrow \psi_\uparrow \;\; \bar{\psi}_\uparrow \psi_\uparrow \rangle_0 \qquad \text{sign: } (-1)^3 \quad \text{(E.19)}$$

$$3.11(d) \quad \sim \langle T_\tau \bar{\psi}_\uparrow \bar{\psi}_\downarrow d \;\; \bar{\psi}_\uparrow \bar{d} d\psi_\uparrow \;\; d\psi_\downarrow \psi_\uparrow \;\; \bar{\psi}_\uparrow \psi_\uparrow \rangle_0 \qquad \text{sign: } (-1)^0 \quad \text{(E.20)}$$

$$3.11(e) \quad \sim \langle T_\tau \bar{\psi}_\uparrow \bar{\psi}_\downarrow d \;\; \bar{\psi}_\downarrow \bar{d} d\psi_\downarrow \;\; d\psi_\downarrow \psi_\uparrow \;\; \bar{\psi}_\uparrow \psi_\uparrow \rangle_0 \qquad \text{sign: } (-1)^0 \quad \text{(E.21)}$$

$$3.11(e) \quad \sim \langle T_\tau \bar{\psi}_\uparrow \bar{\psi}_\downarrow d \;\; \bar{\psi}_\downarrow \bar{d} d\psi_\downarrow \;\; d\psi_\downarrow \psi_\uparrow \;\; \bar{\psi}_\uparrow \psi_\uparrow \rangle_0 \qquad \text{sign: } (-1)^1 \quad \text{(E.22)}$$

This proves the claim that I was making earlier: We can effectively see the the sign switches by looking at the topology of a diagram. When two fermionic lines cross,

this means a relative minus sign. To determine the global sign of diagram 3.11(a), we write it symbolically (two-body vertices again missing, but since there are two of them, the do not contribute a sign) as

$$3.11(a) \quad = \quad (-G)(-G_{dd})T_3(-G_{dd})GGG, \tag{E.23}$$

while the bosonic version (see the bosonic section E.1.2 of this appendix, but ignore the symmetry factor 1/2) reads

$$3.8(a) \quad = \quad -GG_{dd}T_3G_{dd}GGG. \tag{E.24}$$

Since the expansion of the three back-running propagators yields three sign changes with respect to the bosonic version, we have that $3.11(a) = -3.8(a)$ (with symmetry factors ignored). Note that we are again comparing the diagrams for the Green's functions, which means that the contributions to the density are of equal sign. In summary, by either comparing topologies or writing down the diagrams in explicit form, we have:

$$3.11(a) \quad = \quad -3.8(a) \tag{E.25}$$
$$3.11(b) \quad = \quad 3.8(c) \tag{E.26}$$
$$3.11(c) \quad = \quad 3.8(d) \tag{E.27}$$
$$3.11(d) \quad = \quad -3.8(b) \tag{E.28}$$
$$3.11(e) \quad = \quad -3.8(b) \tag{E.29}$$
$$3.11(f) \quad = \quad 3.8(e) \tag{E.30}$$

with the usual replacement of the meaning of the $T$-matrices. Note that similar arguments as the ones discussed here lead to the different sign of the kernel in the fermionic STM equation.

# Appendix F

# Trap averaging procedure

This appendix outlines how we have mapped our momentum distributions for the homogeneous system to the case of an harmonic confinement. We will assume that the density distribution of the cloud is given by a Thomas-Fermi profile, and that equilibrium is only achieved locally, which results in a position independent fugacity [102].

## F.1  Useful definitions

We define a wavevector $k_F$ in the same way as for a single component Fermi gas:

$$k_F = (6\pi^2 n)^{1/3}. \tag{F.1}$$

The corresponding temperature is

$$k_B T_F = \frac{\hbar^2 k_F^2}{2m} = \frac{\hbar^2}{2m}(6\pi^2 n)^{2/3}. \tag{F.2}$$

The degeneracy parameter of the gas now be written as:

$$\lambda_T^3 n = \frac{4}{3\sqrt{\pi}}\left(\frac{T_F}{T}\right)^{3/2}, \tag{F.3}$$

where $\lambda_T = \sqrt{2\pi\hbar^2/mk_B T}$ is the thermal wavelength. In particular, we have:

$$\lambda_T k_F = 2\pi^{1/2}\sqrt{\frac{T_F}{T}}. \tag{F.4}$$

### F.1.1  Thomas-Fermi profile

The density of the cloud is given by the Thomas-Fermi profile [102]:

$$n(r) = n(0)\left(1 - \frac{r^2}{R^2}\right), \tag{F.5}$$

where

$$n(0) = \frac{\mu_{\text{TF}}}{g} = \frac{1}{8\pi} \frac{1}{a_{\text{ho}}^2 a} \left( \frac{15Na}{a_{\text{ho}}} \right)^{2/5} = \frac{15N}{8\pi R^3}, \tag{F.6}$$

where $N$ is the total particle number, and, furthermore:

$$R = a_{\text{ho}} \left( \frac{15Na}{a_{\text{ho}}} \right)^{1/5}. \tag{F.7}$$

Here, $a_{\text{ho}} = \sqrt{\hbar/m\omega}$ is the harmonic oscillator length of the confining potential and $a$ is the initial scattering length of the gas [102]. The average density of the trap is given by:

$$\langle n \rangle = \frac{3N}{4\pi R^3} \tag{F.8}$$

The density $n(0)$ at the trap center can be related to $k_F$ as

$$n(0) = \frac{5}{2}\langle n \rangle = \frac{5}{12\pi^2} k_F^3. \tag{F.9}$$

We assume that the density profile after the ramp still is of the Thomas-Fermi form. In particular, note that

$$\frac{\kappa_*}{k_0} = \left( \frac{2}{5} \right)^{1/3} \frac{\kappa_*}{k_F}. \tag{F.10}$$

Here, we have defined the Fermi wave vector given by the density in the center of trap: $k_0 = k_F(n(0))$. We will neglect possible particle losses, but keep in mind that $\langle n \rangle$ only measures the initial total density *before* the ramp to unitarity [94].

Assuming only local equilibrium in the trap [102], one has:

$$k_B T(r) \sim \frac{\hbar^2 k_F^2}{m} \sim \frac{\hbar^2 n(r)^{2/3}}{m}. \tag{F.11}$$

This implies that the following quantity is constant at each point in the trap:

$$\lambda_T^3(r) n(r) = b_1 z + 2b_2 z^2 + 3b_3 z^3 = D = \text{const.} \tag{F.12}$$

Thus, under this assumption the fugacity $z$ is constant and independent of the position in the trap. The inclusion of a local dimensionless three-body parameter distorts this picture: the fugacity certainly can depend on the position in the trap, in particular due to the variation of the local density with respect to this dimensionless three-body parameter. In the following, we neglect these effects for simplicity and set $\kappa_*/k_F$ equal to its value at the trap center, at all positions in the trap.

## F.2  Local density approximation

Our numerical results are given as a function of the dimensionless momentum $q\lambda_T$ and the dimensionless three-body parameter $\kappa_*\lambda_T$. In the local density approximation, the momentum distribution is obtained by integrating the homogeneous solution over the cloud profile with a spatially varying temperature:

$$n_T(q) = A \int d^3u\, n(q, \kappa_*, T(u)), \tag{F.13}$$

where we define $u = r/R$ and $n(k)$ is the dimensionless momentum distribution which has the norm

$$\lambda_T^3 \int \frac{d^3q}{(2\pi)^3} n(q) = D. \tag{F.14}$$

The constant $A$ is determined from the normalization condition used in the experiment:

$$
\begin{aligned}
\frac{1}{k_F^3} \int \frac{d^3q}{(2\pi)^3} n_T(q, \kappa_*) &= \frac{A}{k_F^3} \int \frac{d^3q}{(2\pi)^3} \int d^3u\, n(q, \kappa_*, T(u)) \\
&= \frac{A}{k_F^3} \int d^3u\, n(u, \kappa_*, T(u)) \\
&= \frac{4\pi A n(0)}{k_F^3} \int_0^1 du\, u^2 \left(1 - u^2\right) \\
&= \frac{2A}{9\pi} = 1.
\end{aligned}
\tag{F.15}
$$

Hence, we have:

$$A = \frac{9\pi}{2} \tag{F.16}$$

We know the total density of particles in the trap in the experiment [94], and we know $a_-$ from ref. [90], hence we can infer $\kappa_*/k_F$ (or $\kappa_*/k_0$). We specify a value of $\kappa_*\lambda_T$ (implicitly, we thus specify $T/T_F$). Since at the trap center, $n(0) = \frac{5}{2}\langle n \rangle$, the local dimensionless temperatures and $\kappa_*$ are:

$$\frac{T}{T_{r=0}} = \left(\frac{2}{5}\right)^{2/3} \frac{T}{T_F} \tag{F.17}$$

$$\kappa_*\lambda_0 = \left(\frac{2}{5}\right)^{1/3} \kappa_*\lambda_{T_F} = \left(\frac{2}{5}\right)^{1/3} k_n\lambda_{T_F} \frac{\kappa}{k_F} = 2\pi^{1/2} \left(\frac{2}{5}\right)^{1/3} \sqrt{\frac{T_F}{T}} \frac{\kappa}{k_F} \tag{F.18}$$

$$q\lambda_0 = 2\pi^{1/2} \left(\frac{2}{5}\right)^{1/3} \sqrt{\frac{T_F}{T}} \frac{q}{k_F}. \tag{F.19}$$

If we assume that $\lambda_T^3 n = D = \text{const}$, the temperature at a distance $u$ from the trap center is

$$T(u) = T_0(1 - u^2)^{2/3} \tag{F.20}$$

$$\kappa_* \lambda_{T(u)} = \kappa_* \lambda_0 (1 - u^2)^{-1/3}. \tag{F.21}$$

The local momentum distribution is thus

$$n\big(q, \kappa_*, T(u)\big) = n\big(q\lambda_0(1 - u^2)^{-1/3}, \kappa_* \lambda_0 (1 - u^2)^{-1/3}\big). \tag{F.22}$$

For simplicity, we neglect the position-dependence of $\kappa_* \lambda_T$ and set $\kappa_* \lambda_{T(u)} = \kappa_* \lambda_0$. The trap-averaged momentum distribution is then given by the integral

$$n_T(q/k_F, \kappa_*/k_F) \sim \int_0^1 du\, u^2\, n\left(\frac{q\lambda_0}{(1 - u^2)^{1/3}}, \kappa_* \lambda_0\right). \tag{F.23}$$

Normalizing this to one yields the results for the momentum distribution which we can compare to experiment. Unless reducing the experimental $\kappa_*/k_F$ by 22.7, we never find good agreement for our fifty different momentum distributions with temperature guesses in the range $\kappa_* \lambda_{T_0} = 0.125$ and $\kappa_* \lambda_{T_0} = 44.8$.

# Appendix G

# Auxiliary calculations for the OPEs of the Coulomb problem

In the part G.1 of this appendix, we discuss auxiliary integrals that are needed during the matching in secs. 4.4 and 4.5. In part G.2.1, we carefully derive the series expansion of the scattering amplitude $i\mathcal{A}$ around $\xi = \infty$. In the last part G.2.2, we show that, in two dimensions, the quartic derivative operator $D_4^\sigma$ is indeed renormalized by subtraction of a term containing the contact operator.

## G.1 Static Structure Factor

During the matching for the OPE of the density-density correlator, the short-distance expansion of the auxiliary integral (4.35) is needed. In particular, it also defines the matrix elements of the Contact operator via equation (4.39), and is thus also of relevance for the OPE of the one-particle density matrix. The auxiliary integral we want to solve is

$$
\mathcal{Z}_d(\mathbf{r}, k_0) = \int_{\mathbf{q}} e^{i\mathbf{q}\cdot\mathbf{r}} \frac{i}{\frac{k_0^2}{m} - \frac{\mathbf{q}^2}{m} + i\epsilon} i\mathcal{A}(k_0, \mathbf{q}, \mathbf{0})
$$

$$
= -\frac{4\pi}{a_0} \int_0^1 dx\, x^{i\xi} \frac{d}{dx}
\begin{cases}
d = 2 : & \dfrac{x^{\frac{1}{2}}}{1+x} \displaystyle\int_{\mathbf{q}} \dfrac{e^{i\mathbf{q}\cdot\mathbf{r}}}{\sqrt{q^2 - \left(\frac{1-x}{1+x}\right)^2 k_0^2}} \dfrac{1}{q^2 - k_0^2} \\[4mm]
d = 3 : & \dfrac{4x}{(1+x)^2} \displaystyle\int_{\mathbf{q}} \dfrac{e^{i\mathbf{q}\cdot\mathbf{r}}}{q^2 - \left(\frac{1-x}{1+x}\right)^2 k_0^2} \dfrac{1}{q^2 - k_0^2}
\end{cases} .
$$

$$\tag{G.1}$$

Note that the above expression should be read as $k_0^2 \to k_0^2 + i\epsilon$ ($\epsilon > 0$) whenever a $k_0$ appears, so that poles and cuts lie on a well defined side of the real $q$-axis. In

order to solve the integrations above, let us treat the two- and three-dimensional case separately. In the following, we will use the shorthands $a^2 = k_0^2[(1-x)/(1+x)]^2 + i\epsilon$, $b^2 = k_0^2 + i\epsilon$. The three-dimensional case is the more straightforward one:

$$
\begin{aligned}
I_3 &= \int \frac{d^3q}{(2\pi)^3} \frac{e^{i\mathbf{q}\cdot\mathbf{r}}}{q^2 - a^2} \frac{1}{q^2 - b^2} \\
&= \frac{1}{ir(2\pi)^2} \int_{-\infty}^{\infty} dq \, \frac{qe^{iqr}}{q^2 - a^2} \frac{1}{q^2 - b^2} \\
&= \frac{1}{2\pi r} \sum_{z_0 = a,b} \text{Res} \left[ \frac{ze^{izr}}{z^2 - a^2} \frac{1}{z^2 - b^2} \right] \Bigg|_{z=z_0} \\
&= \frac{1}{4\pi r} \frac{1}{b^2 - a^2} \left( e^{ibr} - e^{iar} \right) \\
&= \frac{i}{4\pi} \frac{1}{a + b} - \frac{r}{8\pi} + \mathcal{O}(r^2)
\end{aligned}
\tag{G.2}
$$

In the second line, we extended the lower bound of the integral to $-\infty$ and traded this for the $\sim e^{-iqr}$ term that came from the angular integration. For the third line, we realized that we can view the integral as part of a contour that is closed in the *upper* complex plane. Because of the $i\epsilon$ prescription, only two of the poles lie in the upper complex plane, namely $z = a$ and $z = b$. Since the arc at infinity does not contribute (for this we had to close the contour in the upper complex $q$-plane!), the integral is equal to the sum of the residues at the enclosed poles. In the last line, we expanded the result to order $r$, since this is all we need to determine the leading order Wilson coefficient of the contact operator.

Using the same shorthands as before, the two-dimensional integral we need to solve is given by:

$$
\begin{aligned}
I_2 &= \int \frac{d^2q}{(2\pi)^2} \frac{e^{i\mathbf{q}\cdot\mathbf{r}}}{\sqrt{q^2 - a^2}} \frac{1}{q^2 - b^2} \\
&= \int \frac{dq}{2\pi} \frac{q}{\sqrt{q^2 - a^2}} \frac{J_0(qr)}{q^2 - b^2} \\
&= \int \frac{dq}{4\pi} \int_0^1 dy \frac{qJ_0(qr)y^{-1/2}}{(q^2 - ya^2 - (1-y)b^2)^{3/2}}
\end{aligned}
\tag{G.3}
$$

In the second line, we performed the angle integration. In the third line, we introduced a Feynman parameter. The anti-derivative of the integrand (with respect to $y$) is given by $2\sqrt{y}/[(q^2 - b^2)\sqrt{q^2 - ya^2 - (1-y)b^2}]$, and thus we had to include an additional factor $1/2$ in the third line. The $q$-integral is tabulated in ref. [149], in the section on Hankel transforms of order zero:

$$
\int_0^\infty dx \frac{xJ_0(yx)}{(x^2 + c^2)^{3/2}} = \frac{e^{-cy}}{c}
\tag{G.4}
$$

The small subtlety here is that we are calculating a complex extension of the tabulated integral. We have $c^2 = -ya^2 - (1-y)b^2$. The $i\epsilon$ prescription determines the phase of $c$: $c = -i\sqrt{ya^2 + (1-y)b^2}$. Thus, we have for $I_2$:

$$
\begin{aligned}
I_2 &= \frac{i}{4\pi} \int_0^1 dy \frac{y^{-1/2} e^{ir\sqrt{ya^2 + (1-y)b^2}}}{\sqrt{ya^2 + (1-y)b^2}} \\
&= \frac{i}{4\pi b} \int_0^1 dy\, y^{-1/2} \sum_{n=0}^\infty \frac{(ibr)^n}{n!} \left[ 1 - y\left( 1 - \frac{a^2}{b^2} \right) \right]^{\frac{n-1}{2}} \\
&= \frac{i}{2\pi b} \sum_{n=0}^\infty \frac{(ibr)^n}{n!} {}_2F_1\left( \frac{1-n}{2}, \frac{1}{2}, \frac{3}{2}; 1 - \frac{a^2}{b^2} \right) \\
&= \frac{i}{2\pi} \frac{\arccos \frac{a}{b}}{\sqrt{b^2 - a^2}} - \frac{r}{2\pi} + \mathcal{O}(r^2)
\end{aligned}
\tag{G.5}
$$

In the second line, the integral representation [113]

$$
\frac{\Gamma(\beta)\Gamma(\gamma - \beta)}{\Gamma(\gamma)} {}_2F_1(\alpha, \beta, \gamma; z) = \int_0^1 dy\, y^{\beta-1}(1-y)^{\gamma-\beta-1}(1-zy)^{-\alpha} \tag{G.6}
$$

of the hypergeometric function ${}_2F_1(\alpha, \beta, \gamma; z)$ was used. The integral representation is valid for $\Re\gamma > \Re\beta > 0$ and $\arg(1-z) < \pi$, which in our case translates to $|z| \leq 1$. Indeed, from our definitions of $a^2 = k_0^2[(1-x)/(1+x)]^2 + i\epsilon$, $b^2 = k_0^2 + i\epsilon$, we see that for $x \in [0,1]$ the argument $1 - a^2/b^2$ of the hypergeometric function fulfills this restriction. In the last line, the result was expanded to order $r$, which is all we need to determine the Wilson coefficient of the contact to leading order.

## G.2 Momentum Distribution

### G.2.1 Expansions of the matrix elements to leading orders in the off-shell energy

The matching of the momentum distribution greatly simplifies when taking the the leading orders of the matrix elements (in states with zero vanishing external momenta) in a series around $k_0 = 0$ ($\xi = \infty$). For this, we in particular need the expansion of the amplitude $i\mathcal{A}(k_0, \mathbf{q}, \mathbf{0}$ (defined in eqs. (4.27) and (4.21) for the 2D

and 3D case, respectively):

$$
i\mathcal{A}(k_0, \mathbf{q}, \mathbf{0}) = \begin{cases} 2\pi i e^2 \left[ -\dfrac{1}{q} + 2i\xi \displaystyle\int_0^1 dx \dfrac{x^{i\xi - 1/2}}{\sqrt{q^2(1+x)^2 - k_0^2(1-x)^2}} \right] & \text{(2D)} \\[4mm] 4\pi i e^2 \left[ -\dfrac{1}{q^2} + 4i\xi \displaystyle\int_0^1 dx \dfrac{x^{i\xi}}{q^2(1+x)^2 - k_0^2(1-x)^2} \right] & \text{(3D)} \end{cases}
$$

$$
= \begin{cases} 2\pi i e^2 \left[ -\dfrac{1}{q} + 2i \displaystyle\int_0^1 dy \dfrac{y^{-i-1+\frac{1}{2\xi}}}{\sqrt{q^2\left(1+y^{\frac{1}{\xi}}\right)^2 - (\frac{1}{2a_0\xi})^2\left(1-y^{\frac{1}{\xi}}\right)^2}} \right] & \text{(2D)} \\[6mm] 4\pi i e^2 \left[ -\dfrac{1}{q^2} + 4i \displaystyle\int_0^1 dy \dfrac{y^{i-1+\frac{1}{\xi}}}{q^2\left(1+y^{\frac{1}{\xi}}\right)^2 - (\frac{1}{2a_0\xi})^2\left(1-y^{\frac{1}{\xi}}\right)^2} \right] & \text{(3D)} \end{cases}
$$

$$\tag{G.7}$$

In the first line, partial integration was used to rewrite the amplitude in an advantageous form for what follows. In the second line, the substitution $x = y^{1/\xi} \Rightarrow dx = dy\, y^{-1+1\xi}/\xi$ is performed. We also replaced $k_0 = 1/2a_0\xi$, which is just the definition of $\xi$. The last form now has a straightforward series expansion around $\xi = \infty$:

$$
i\mathcal{A}(k_0, \mathbf{q}, \mathbf{0}) = \begin{cases} 2\pi i e^2 \left[ -\dfrac{1}{q} + 2i \displaystyle\int_0^1 dy\, y^{-1+i+\epsilon} \left( \dfrac{1}{2q} - \dfrac{\log^2 y}{16 q \xi^2} + \mathcal{O}\left(\dfrac{1}{\xi^4}\right) \right) \right] & \text{(2D)} \\[4mm] 4\pi i e^2 \left[ -\dfrac{1}{q^2} + 4i \displaystyle\int_0^1 dy\, y^{-1+i+\epsilon} \left( \dfrac{1}{4q^2} - \dfrac{\log^2 y}{16\xi^2 q^2} + \mathcal{O}\left(\dfrac{1}{\xi^4}\right) \right) \right] & \text{(3D)} \end{cases}
$$

$$
= \begin{cases} \dfrac{2\pi i e^2}{4q\xi^2} + \mathcal{O}\left(\dfrac{1}{\xi^4}\right) & \text{(2D)} \\[4mm] \dfrac{4\pi i e^2}{2q^2\xi^2} + \mathcal{O}\left(\dfrac{1}{\xi^4}\right) & \text{(3D)} \end{cases}
$$

$$\tag{G.8}$$

In order to make the integrals well-defined, we need an $\epsilon > 0$. I want to stress that this $\epsilon > 0$ prescription is *not* ambiguous. It is indeed a subtle leftover from the $i\epsilon$ prescription that was used in the Lippmann-Schwinger equation (4.15). This $i\epsilon$ determined the sign of the $k_0$ term, and if we would have been completely careful, we would need to write $me^2/2\sqrt{-k_0^2 - i\epsilon} \approx i\xi + \epsilon$ for the exponent in the one parameter integral representations (4.27) and (4.21) of the scattering amplitudes.

## G.2.2 Renormalization of the operator $D_4^\sigma(\mathbf{r}, \mathbf{R})$

In the following, we want to show that (4.72) indeed renormalizes the operator $D_4^\sigma(\mathbf{r}, \mathbf{R})$ to all orders, and – in particular – for any external state. For this, consider

diagram 4.5(d) in two dimensions, now with arbitrary values $k_0^2/m$ of the external energy:

$$
\begin{aligned}
4.5(d) &= \int_{\mathbf{q}} \frac{(i\mathbf{q}\cdot\mathbf{r})^4}{4!} \left( \frac{i}{\frac{k_0^2}{m} - \frac{q^2}{m} + i\epsilon} \right)^2 (i\mathcal{A}(k_0, \mathbf{q}, \mathbf{0}))^2 \\
&= \frac{1}{4!} \left( \frac{4\pi}{a_0} \right)^2 \frac{3\pi r^4}{4} \int_0^1 dx\, x^{i\xi} \frac{d}{dx} \frac{x^{\frac{1}{2}}}{1+x} \int_0^1 dx'\, \frac{d}{dx'} \frac{x'^{\frac{1}{2}}}{1+x'} \\
&\quad \underbrace{\int_0^\Lambda dq \frac{q^5}{(q^2 - k_0^2 - i\epsilon)^2} \frac{1}{\sqrt{q^2 - \left(\frac{1-x}{1+x}\right)^2 k_0^2}} \frac{1}{\sqrt{q^2 - \left(\frac{1-x'}{1+x'}\right)^2 k_0^2}}}_{\equiv I(0,\Lambda)}, \quad \text{(G.9)}
\end{aligned}
$$

where we have evaluated the angular integration over $\cos^4\phi$, which gave $3\pi/4$. We also have defined an integral $I(x, y)$, where $x$ denotes the lower bound of the integral and $y$ the upper bound. Now, from the form the integrand, we see that there exists a momentum scale $\Lambda'$ (set by $k_0$), after which we can savely replace the integrand by its leading order series expansion $1/q$. We split up the integral $I(0, \Lambda)$ as

$$
\begin{aligned}
I(0, \Lambda) &= I(0, \Lambda') + I(\Lambda', \Lambda) \\
&= I(0, \Lambda') + \int_{\Lambda'}^\Lambda dq \frac{1}{q} + \mathcal{O}(\Lambda^{-1}, \Lambda'^{-1}) \\
&= \text{finite} + \log\Lambda + \mathcal{O}(\Lambda^{-1}) \quad\quad\quad\quad\quad \text{(G.10)}
\end{aligned}
$$

Plugging this into (G.9) yields

$$
\begin{aligned}
4.5(d) &= \text{finite} + \frac{\log\Lambda}{4!} \left( \frac{4\pi}{a_0} \right)^2 \frac{3\pi r^4}{4} \int_0^1 dx\, x^{i\xi} \frac{d}{dx} \frac{x^{\frac{1}{2}}}{1+x} \int_0^1 dx'\, \frac{d}{dx'} \frac{x'^{\frac{1}{2}}}{1+x'} \\
&= \text{finite} + \frac{\pi r^4 \log\Lambda}{8a_0^2} \int_0^1 dx\, x^{i\xi} \frac{d}{dx} \frac{x^{\frac{1}{2}}}{1+x} \int_0^1 dx'\, \frac{d}{dx'} \frac{x'^{\frac{1}{2}}}{1+x'} \quad\quad \text{(G.11)}
\end{aligned}
$$

The matrix element of the subtracted term in eq. (4.72) is given by the sum of the four diagrams 4.3(a)-4.3(d), the result of which is given in eq. (4.40). Plugging everything in, we get:

$$
-\left( \frac{2\pi}{a_0} \right)^2 \frac{|\mathbf{r}|^4}{128\pi} \log\Lambda \sum_{\text{diags. 4.3}} = -\frac{\pi r^4 \log\Lambda}{8\pi a_0^2} \left[ \int_0^1 dx\, x^{i\xi} \frac{d}{dx} \frac{x^{\frac{1}{2}}}{1+x} \right]^2 \quad \text{(G.12)}
$$

which indeed exactly cancels the divergent part of $D_4^q(\mathbf{r}, \mathbf{R})$! Note that finite external momenta $\pm\mathbf{p}$ complicate the above calculation, however the basic argumentation stays the same. Of course, in this case the momentum scale $\Lambda'$, after which we assume it to be safe to use a series expansion for the integrand, will be set by the maximum of $k_0$ and $|\mathbf{p}|$.

# Appendix H

# List of publications

In the following, the electronic preprints (from arXiv.org) of the articles that were published in the context of this thesis are re-printed. The articles, listed in chronological order, are:

- Christian Langmack, Marcus Barth, Wilhelm Zwerger and Eric Braaten
  *Clock shift in a strongly interacting two-dimensional Fermi gas*
  Phys. Rev. Lett. **108**, 060402 (2012)

- Johannes Hofmann, Marcus Barth and Wilhelm Zwerger
  *Short-distance properties of Coulomb systems*
  Phys. Rev. B **87**, 235125 (2013)

- Marcus Barth and Johannes Hofmann
  *Pairing effects in the nondegenerate limit of the two-dimensional Fermi gas*
  Phys. Rev. A **89**, 013614 (2014)

- Marcus Barth and Johannes Hofmann
  *Efimov correlations in strongly interacting Bose gases*
  arXiv:1506.06751 (2015)

# Clock shift in a strongly interacting two-dimensional Fermi gas

Christian Langmack[1], Marcus Barth[2], Wilhelm Zwerger[2], and Eric Braaten[1]

[1]*Department of Physics, The Ohio State University, Columbus, OH 43210, USA*
[2]*Technische Universität München, Physik Department,  James-Franck-Strasse, 85748 Garching, Germany*

(Dated: September 3, 2012)

We derive universal relations for the radio-frequency (rf) spectroscopy of a two-dimensional Fermi gas consisting of two spin states interacting through an S-wave scattering length. The rf transition rate has a high-frequency tail that is proportional to the contact and displays logarithmic scaling violations, decreasing asymptotically like $1/(\omega^2 \ln^2 \omega)$. Its coefficient is proportional to $\ln^2(a'_{2D}/a_{2D})$, where $a_{2D}$ and $a'_{2D}$ are the 2-dimensional scattering lengths associated with initial-state and final-state interactions. The clock shift is proportional to the contact and to $\ln(a'_{2D}/a_{2D})$. If $|\ln(a'_{2D}/a_{2D})| \gg 1$, the clock shift arises as a cancellation between much larger contributions proportional to $\ln^2(a'_{2D}/a_{2D})$ from bound-bound and bound-free rf transitions.

PACS numbers: 03.75.Ss, 05.30.Fk, 67.85.-d.

Spectroscopy of the internal levels of atoms is a central subject of atomic physics. The associated transition frequencies of a single atom are known with the precision of atomic clocks. In fact, atomic clocks use a hyperfine transition in cesium to keep our standard of time. In a gas, the atoms experience energy shifts due to interactions with the surrounding atoms, resulting in transition frequencies that differ from those of free atoms. Such density-dependent interaction shifts are a major source of systematic errors in atomic clocks, and are thus called *clock shifts*. Precision spectroscopy aims to avoid these shifts as far as possible, e.g. by working at extremely low densities or by using a purely spin-polarized gas of fermions in the ultracold limit where the remaining S-wave collisions are forbidden by the Pauli principle [1]. Alternatively, the atoms may be stored in an optical lattice, where both the center-of-mass motion and the interactions are completely quenched [2].

In investigations of many-body physics using ultracold gases, the clock shift is, however, a signal of interest rather than a nuisance. It can be especially interesting when the atoms are strongly interacting, i.e. their scattering length is large compared to both the range of interactions and the average interparticle distance. The interaction energy [1, 3] and the pairing gap [4] have been measured for strongly-interacting fermionic atoms near a Feshbach resonance. The generic setup for these experiments involves a gas containing atoms in just two hyperfine states $|1\rangle$ and $|2\rangle$. A radio-frequency (rf) pulse, tuned to the hyperfine splitting between $|2\rangle$ and a third, unoccupied state $|3\rangle$ will then transfer atoms from $|2\rangle$ into $|3\rangle$. If, for example, states $|1\rangle$ and $|2\rangle$ form a molecular bound state, the rf pulse has to be detuned compared to the bare hyperfine splitting by a frequency $\omega$ associated with the binding energy of the molecule. At the two-body level, effects like these can be analyzed in a straightforward manner, even in the presence of strong final-state interactions between $|1\rangle$ and $|3\rangle$ [5]. In a genuine many-body situation, however, analytic methods for calculating the

rf transition rate $\Gamma(\omega)$ are not available. Exact relations for $\Gamma(\omega)$ that hold independent of density and interaction strength are therefore of considerable interest.

For strongly interacting fermions with two spin states in three dimensions (3D), a number of exact relations that connect thermodynamic variables to large-momentum and high-frequency tails of correlation functions have been derived by Tan [6, 7]. These relations all involve the contact $C$, which basically measures the probability for pairs of fermions in states $|1\rangle$ and $|2\rangle$ to be very close together. More precisely, the contact may be defined by the universal power-law tail

$$n_\sigma(k) \longrightarrow C/k^4, \qquad \sigma = 1, 2 \qquad (1)$$

of the momentum distribution of either spin state at large momentum $k$. The Tan relations are universal in the sense that they apply to *any* state of the system, e.g. few-body or many-body, homogeneous or in a trapping potential, Fermi-liquid or superfluid state, provided only that the length scales associated with the temperature and number densities are large compared to the range of interactions. The origin of this universality is that the Tan relations are a consequence of operator identities, some of which follow from the operator product expansion of quantum field theory [8]. There are also universal relations governing rf spectroscopy. Specifically, the average clock shift, i.e. the first moment of $\Gamma(\omega)$, is proportional to the contact $C$ [9] or, equivalently, to a derivative of the total energy with respect to the scattering length [10]. Moreover, the rf transition rate $\Gamma(\omega)$ has a high-frequency tail that is proportional to $C$ and decreases like $1/\omega^n$, where the exponent $n$ is either $\frac{5}{2}$ or $\frac{3}{2}$ depending on the strength of the final-state interactions between $|1\rangle$ and $|3\rangle$ [11–13]. Some of the universal relations have been verified experimentally, e.g. by comparing the values of $C$ obtained from the tail of the momentum distribution in Eq. (1) and from the rf transition rate at large $\omega$ [14].

In our present work, we derive universal relations for

rf spectroscopy in *two*-dimensional Fermi gases. These systems have been investigated in several recent experiments [15–17]. Beyond the motivation provided by these experiments, universal relations that constrain the rf transition rate in two dimensions (2D) are of interest also for other reasons. First, rf spectroscopy measurements can be performed within a rather short time scale. It thus allows access to not only equilibrium but also excited states of the many-body system, e.g. the polaron on the repulsive branch of a Feshbach resonance [18] or Bose gases in the regime of strong repulsion. A second reason is that a 2D gas with zero-range interactions provides an example of a non-relativistic many-body system that is scale invariant at the classical but not at the quantum level. This breaking of the scale invariance by quantum effects is an elementary example of an anomaly [19]. It implies that the coupling constant $g$ (which will be defined explicitly below) is in fact a running coupling constant $g(\mu) = -2\pi/\ln(a_{2D}\mu)$ that changes logarithmically with the momentum scale $\mu$, reminiscent of the coupling constant of Quantum Chromodynamics. The associated intrinsic length $a_{2D}$ sets the scale for the two-body scattering amplitude which, at low energies, has the characteristic form [20, 21]

$$f(q) = \frac{4\pi}{\ln(1/q^2 a_{2D}^2) + i\pi}. \qquad (2)$$

For any positive value of $a_{2D}$, this amplitude has a pole at $q = i/a_{2D}$, which signifies the presence of a diatomic molecule with binding energy $E_d = \hbar^2/ma_{2D}^2$ that we will call the (12)-dimer.

In experiments with ultracold atoms, the 2D gas arises from a 3D system by adding a strong transverse confining potential that restricts the atoms to the ground state in the third dimension. For harmonic trapping with angular frequency $\omega_z$, the relation between $a_{2D}$ and the experimentally tunable 3D scattering length $a$ is given by $\ell/a = f_1(\ell^2/a_{2D}^2)$, where $\ell^2 = \hbar/m\omega_z$ and the function $f_1(x)$ is given in section V.A of Ref. [21].

A system consisting of fermions with the two spin states $|1\rangle$ and $|2\rangle$ can be described by a quantum field theory with the interaction Hamiltonian

$$H_{\text{int}} = (g/m)\int d^2R\,\psi_1^\dagger\psi_2^\dagger\psi_2\psi_1(\boldsymbol{R}). \qquad (3)$$

Here $g$ is the bare coupling constant, which can be identified with the running coupling constant at the momentum scale of the ultraviolet cutoff. Within this framework, universal relations for both equilibrium properties and rf spectra can be derived using the operator product expansion (OPE) [8]. In particular, the tail of the momentum distribution in Eq. (1) follows from the OPE for $\psi_\sigma^\dagger(\boldsymbol{R} + \frac{1}{2}\boldsymbol{r})\psi_\sigma(\boldsymbol{R} - \frac{1}{2}\boldsymbol{r})$. The leading contribution that is non-analytic as $\boldsymbol{r} \to 0$ comes from the operator $\psi_1^\dagger\psi_2^\dagger\psi_2\psi_1(\boldsymbol{R})$, whose coefficient exhibits a logarithmic singularity in 2D of the form $|\boldsymbol{r}|^2 \log|\boldsymbol{r}|$. As a result,

$n_\sigma(k)$ behaves asymptotically like $C/k^4$ with no logarithmic corrections, as in 3D and also in 1D [22]. The contact $C = \int d^2R\,\mathcal{C}(\boldsymbol{R})$ is an integral of the contact density

$$\mathcal{C}(\boldsymbol{R}) = g^2\langle\psi_1^\dagger\psi_2^\dagger\psi_2\psi_1(\boldsymbol{R})\rangle, \qquad (4)$$

which is the expectation value of a local operator that annihilates and recreates a pair of fermions. The structure of these results is identical to the 3D case and, indeed, many of Tan's universal relations may be generalized to 2D [23]. Universal relations for current correlators, structure factors, and hydrodynamic correlators in 2D have also been derived using the OPE [24].

We now consider the rf spectroscopy of the 2D system consisting of fermions in states $|1\rangle$ and $|2\rangle$. Beyond the interaction described by $a_{2D}$, we also include final-state interactions between $|1\rangle$ and $|3\rangle$ with 2D scattering length $a_{2D}'$. We will refer to the diatomic molecule consisting of $|1\rangle$ and $|3\rangle$, which has binding energy $E_d' = \hbar^2/ma_{2D}'^2$, as the (13)-dimer. The transfer rate $\Gamma(\omega)$ between $|2\rangle$ and $|3\rangle$ can be expressed in terms of the imaginary part of a time-ordered correlation function:

$$\Gamma(\omega) = \Omega^2 \int d^2R \,\text{Im}\left(i\,\langle\mathcal{O}_{\text{rf}}(\omega + i\epsilon, \boldsymbol{R})\rangle\right), \qquad (5)$$

where $\Omega$ is the Rabi frequency of the rf transition and $\mathcal{O}_{\text{rf}}(\omega, \boldsymbol{R})$ is an operator that depends on a complex variable $\omega$:

$$\mathcal{O}_{\text{rf}}(\omega, \boldsymbol{R}) = \int dt\, e^{i\omega t}\int d^2r$$
$$\times \mathcal{T}\psi_2^\dagger\psi_3\left(\boldsymbol{R} + \tfrac{1}{2}\boldsymbol{r}, t\right)\psi_3^\dagger\psi_2\left(\boldsymbol{R} - \tfrac{1}{2}\boldsymbol{r}, 0\right). \qquad (6)$$

(The time-ordering symbol $\mathcal{T}$ acts on all operators to the right.) The bilocal operator can be expanded in terms of local operators by using the OPE:

$$\mathcal{O}_{\text{rf}}(\omega, \boldsymbol{R}) = \sum_n C_n(\omega)\mathcal{O}_n(\boldsymbol{R}). \qquad (7)$$

Local operators can be assigned scaling dimensions. The quantum fields $\psi_\sigma$ have dimension 1. The gradient $\nabla$ and the time derivative $\partial/\partial t$ increase the dimension by 1 and 2, respectively. At large frequency $\omega$, higher dimension operators in the OPE have Wilson coefficients $C_n(\omega)$ that decrease with higher powers of $\omega$. The Wilson coefficients $C_n(\omega)$ in Eq. (7) can be calculated by matching Green functions of the bilocal rf operator on the left side of the OPE with Green functions of the local operators on the right side. For operators of dimensions 2 and 4, it is sufficient to match the Green functions in the 1-atom and 2-atom sectors. Our final result for the expectation value of $\mathcal{O}_{\text{rf}}(\omega, \boldsymbol{R})$ at large complex $\omega$, including all operators with dimensions up to 4, is

$$\langle\mathcal{O}_{\text{rf}}(\omega, \boldsymbol{R})\rangle \longrightarrow \frac{i}{\omega}n_2(\boldsymbol{R}) + \frac{i\,\nabla^2 n_2(\boldsymbol{R}) + 4m\nabla \cdot \boldsymbol{J}_2(\boldsymbol{R})}{8m\omega^2}$$
$$+ \frac{i\ln(a_{2D}'/a_{2D})\ln(a_{2D}\sqrt{-m\overline\omega})}{2\pi m\omega^2\ln(a_{2D}'\sqrt{-m\overline\omega})}\mathcal{C}(\boldsymbol{R}), \qquad (8)$$

where $n_2$ and $\boldsymbol{J}_2$ are the number density and current density for $|2\rangle$. If the system is in a steady state, $\nabla \cdot \boldsymbol{J}_2$ vanishes because of current conservation. The integral of $\nabla^2 n_2$ vanishes by the divergence theorem. The terms shown explicitly in Eq. (8) are not affected by final-state interactions between $|2\rangle$ and $|3\rangle$, which first enter into the coefficients of dimension-6 operators.

We can derive various universal relations from the OPE in Eq. (8). The tail of the rf transition rate at large positive frequencies $\omega$ can be obtained by extrapolating Eq. (8) to the real axis, taking the imaginary part, and then inserting it into Eq. (5):

$$\Gamma(\omega) \longrightarrow \frac{\ln^2(E_d'/E_d)\Omega^2 C}{4m\omega^2 \left[\ln^2(\omega/E_d') + \pi^2\right]}. \qquad (9)$$

Higher dimension operators in the OPE give contributions to the high-frequency tail that decrease faster than $\omega^{-3}$. These contributions are suppressed by a positive power of an energy scale of the many-body system divided by $\omega$. The relevant energy scales of the many-body system include $E_d$, the thermal energy $k_B T$, and the two Fermi energies $4\pi^2 n_1/m$ and $4\pi^2 n_2/m$. The factor $\ln^2(E_d'/E_d)$ in Eq. (9) can be interpreted as $16\pi^2/g^2(1/a_{2D}')$, where $g(1/a_{2D}')$ is the running coupling constant at the momentum scale $1/a_{2D}'$. If $a_{2D}' = a_{2D}$, the high-frequency tail in Eq. (9) vanishes identically. In this case, $\Gamma(\omega)$ just consists of an unshifted peak $\pi\Omega^2 N_2\delta(\omega)$, because the rf pulse merely rotates $|2\rangle$ and $|3\rangle$ in spin space [10]. The nontrivial dependence on $\omega$ in Eq. (9) is a consequence of the anomalous scale invariance. If $|\ln(\omega/E_d')| \ll \pi$, the high-frequency tail in Eq. (9) has the simple scaling behavior $\Gamma(\omega) \sim 1/\omega^2$. However at much larger or much smaller frequencies, there are logarithmic scaling violations and the asymptotic behavior is $\Gamma(\omega) \sim (\omega^2 \ln^2 \omega)^{-1}$. Simple scaling behavior also arises in the limit of negligible final-state interactions in which $\ln(E_d'/\omega) \to \infty$. In this limit, the high-frequency tail in Eq. (9) reduces to $\Omega^2 C/4m\omega^2$. This relation has been used in recent experiments with $^{40}$K atoms to extract the contact density in the normal state of the 2D Fermi gas [25]. The contact density and its dependence on $a_{2D}$ is close to that obtained from variational Monte Carlo calculations at $T = 0$ [26].

Sum rules can be derived by expressing weighted integrals of $\Gamma(\omega)$ as contour integrals in the complex-$\omega$ plane:

$$\int_{-\infty}^{+\infty} d\omega f(\omega)\Gamma(\omega) = \frac{\Omega^2}{2} \int d^2R \oint d\omega f(\omega)\langle\mathcal{O}_{\mathrm{rf}}(\omega, \boldsymbol{R})\rangle, \quad (10)$$

where the $\omega$ contour runs from $+\infty$ to $-\infty$ just below the real axis and then from $-\infty$ to $+\infty$ just above the axis. If the contour is deformed into a circle of infinite radius, the OPE in Eq. (8) will be exact everywhere on the contour. Choosing $f(\omega) = 1$ and $f(\omega) = \omega$, we obtain
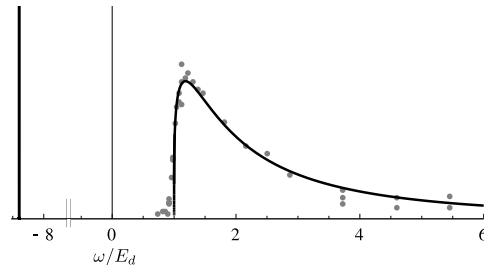


FIG. 1. Rf transition rate for the (12)-dimer as a function of $\omega/E_d$ for the case $E_d' = 9.4 E_d$. There is a delta function at $\omega = -(E_d' - E_d)$ from the bound-bound transition. The threshold for bound-free transitions is at $\omega = E_d$. The grey dots in the bound-free region are data from Zwierlein and collaborators [27], normalized by a least-squares fit to the theory curve.

$$\int_{-\infty}^{+\infty} d\omega\, \Gamma(\omega) = \pi\Omega^2 N_2, \qquad (11a)$$

$$\int_{-\infty}^{+\infty} d\omega\, \omega\Gamma(\omega) = \frac{\ln(a_{2D}'/a_{2D})\Omega^2 C}{2m}. \qquad (11b)$$

These sum rules are exact: they receive no contributions from higher dimension operators in the OPE. The first sum rule guarantees that interactions do not change the integrated rf signal. The second sum rule determines the clock shift $\langle\omega\rangle$, which is defined as the ratio of the integrals in Eqs. (11):

$$\langle\omega\rangle = -\frac{\ln(E_d'/E_d)\, C}{4\pi m N_2}. \qquad (12)$$

Note that both the clock shift and the tail of the rf transition rate in Eq. (9) are unaffected by final-state interactions between $|2\rangle$ and $|3\rangle$.

The universal relations in Eqs. (9) and (11) can be illustrated by considering rf spectroscopy on the two-body system consisting of a single (12)-dimer with binding energy $E_d$. The rf transition rate is

$$\Gamma(\omega) = \frac{\pi\Omega^2 E_d' E_d \ln^2(E_d'/E_d)}{(E_d' - E_d)^2} \, \delta(\omega - E_d + E_d')$$
$$+ \frac{\pi\Omega^2 E_d \ln^2(E_d'/E_d)}{\omega^2[\ln^2((\omega - E_d)/E_d') + \pi^2]} \, \theta(\omega - E_d). \quad (13)$$

By evaluating the integrals in Eqs. (11), we verify that the sum rules are satisfied exactly with $N_2 = 1$ and $C = 4\pi m E_d$, the contact for the (12)-dimer obtained from the adiabatic universal relation $dE_d/da_{2D} = -C/(2\pi m a_{2D})$ [23]. The universal relation for the tail in Eq. (9) holds for $|\omega| \gg E_d$. The clock shift for the (12)-dimer has a negative contribution proportional to $\ln^2(E_d'/E_d)$ from bound-bound transitions. If $|\ln(E_d'/E_d)| \gg 1$, there is

a large canceling contribution from bound-free transitions, such that the total clock shift agrees with Eq. (12). Near the threshold, the bound-free transition rate has the behavior $1/\ln^2((\omega - E_d)/E'_d)$. This follows from the inverse-logarithmic behavior of the two-body scattering amplitude for $|1\rangle$ and $|3\rangle$ analogous to Eq. (2). Recent experiments using $^6$Li atoms in 2D [17] are in good agreement with the bound-free transition rate in Eq. (13) for a single (12)-dimer in the presence of final-state interactions. The data in Fig. 1 [27] were measured near the 3D Feshbach resonance for $|1\rangle$ and $|2\rangle$ at a magnetic field of 690.7 G and a lattice depth to recoil energy ratio of 18.6(7), and they extend out to higher $\omega$ than in Ref. [17]. The ratio $E'_d/E_d$ is around 9.4 and $E_d$ is about a factor 6 larger than the Fermi energy [27]. This places the system in the BEC limit of the many-body problem where the two-body result in Eq. (13) applies.

We now consider the many-body system in the limit in which $E'_d$ is much greater than $E_d$ and the other relevant energy scales. The bound-bound and free-bound region is then well separated from the free-free and free-bound region of the rf spectrum. There could be additional structure in the region of $\omega$ between $-(E'_d - E_d)$ and $0$ associated with clusters of three or more atoms. However, if this region is featureless, it is useful to define a clock shift for the rf transition rate restricted to a range of frequencies $-\omega_0 < \omega < \omega_0$ that excludes the bound-bound peak. We choose $\omega_0$ and $E'_d - \omega_0$ to be much greater than the energy scales of the system. This clock shift is given by a ratio of integrals analogous to those in Eq. (11). They can be expressed as contour integrals analogous to those in Eq.(10), except that the contour runs from $+\omega_0$ to $-\omega_0$ just below the real axis and then back to $+\omega_0$ just above the axis. If the contour is deformed into a circle of radius $\omega_0$, we can apply the OPE in Eq. (8) and obtain the sum rules

$$\int_{-\omega_0}^{+\omega_0} d\omega \, \Gamma(\omega) = \pi \Omega^2 N_2 - [\text{Im Ei}(-L_0 + i\pi)]$$
$$\times \left( \ln \frac{a'_{2D}}{a_{2D}} \right) \frac{\Omega^2 C}{\pi m E'_d} + \ldots, \quad (14a)$$

$$\int_{-\omega_0}^{+\omega_0} d\omega \, \omega\Gamma(\omega) = \left( \ln \frac{a'_{2D}}{a_{2D}} - \frac{2}{\pi} \ln^2 \frac{a'_{2D}}{a_{2D}} \arctan \frac{\pi}{L_0} \right) \frac{\Omega^2 C}{2m}$$
$$+ \ldots, \quad (14b)$$

where $\text{Ei}(x)$ is the exponential integral function and $L_0 = \ln(\omega_0/E'_d)$. One advantage of finite-frequency sum rules such as those in Eqs. (14) is that they can be evaluated using measured rf spectra without extrapolations to larger frequencies. As indicated by "$+\ldots$" in Eqs. (14), these sum rules are not exact. They receive contributions from higher dimensional operators in the OPE that are suppressed by powers of an energy scale of the system divided by $\omega_0$ or $E'_d$. For example, the higher dimension contribution in Eq. (14a) is suppressed by a factor of $C/mE'_d N_2$. The corrections that are suppressed

by inverse powers of $\omega_0$ can be minimized by choosing $\omega_0$ as large as possible while still avoiding contributions from the bound-bound peak. Neglecting the contributions from higher dimension operators, the clock shift obtained from Eqs. (14) reduces to

$$\langle \omega \rangle = \left( \frac{1}{\pi} \ln^2 \frac{E'_d}{E_d} \arctan \frac{\pi}{|L_0|} - \ln \frac{E'_d}{E_d} \right) \frac{C}{4\pi m N_2} . \quad (15)$$

If $|\ln(E'_d/E_d)| \gg 1$, this clock shift is much larger than that in Eq. (12). The clock shift in Eq. (15), which excludes the contribution from bound-bound transitions, is the one that is more relevant to the limit of weak final-state interactions. The factor $\ln^2(E'_d/E_d)$ diverges in the limit $a'_{2D} \to 0$, indicating that the clock shift in this case is quadratically logarithmically sensitive to the range of interactions.

In summary, we have presented universal relations for the rf spectroscopy of strongly interacting fermions in a 2D Fermi gas. They are of direct relevance to current experiments with ultracold atoms, providing rigorous connections between rf spectrocopy, thermodynamics, and various correlation functions. They reveal aspects of these many-body systems that are directly related to the breaking of scale invariance in 2D and will hopefully provide inspiration for further investigations of these unusual systems.

[1] S. Gupta et al., Science **300**, 1723 (2003).
[2] M. Swallows et al., Science **331**, 1043 (2011).
[3] C. A. Regal and D. S. Jin, Phys. Rev. Lett. **90**, 230404 (2003).
[4] C. Chin et al., Science **305**, 1128 (2004).
[5] C. Chin and P. S. Julienne, Phys. Rev. A **71**, 012713 (2005).
[6] S. Tan, Ann. Phys. (N.Y.) **323**, 2952 (2008); **323**, 2971 (2008); **323**, 2987 (2008).
[7] E. Braaten, in *The BCS-BEC Crossover and the Unitary Fermi Gas*, edited by W. Zwerger (Springer-Verlag, 2012).
[8] E. Braaten and L. Platter, Phys. Rev. Lett. **100**, 205301 (2008).
[9] M. Punk and W. Zwerger, Phys. Rev. Lett. **99**, 170404 (2007).
[10] G. Baym, C.J. Pethick, Z. Yu, and M.W. Zwierlein, Phys. Rev. Lett. **99**, 190407 (2007).
[11] R. Haussmann, M. Punk, and W. Zwerger, Phys. Rev. A **80**, 063612 (2009).
[12] W. Schneider and M. Randeria, Phys. Rev. A **81**, 021601 (2010).
[13] E. Braaten, D. Kang, and L. Platter, Phys. Rev. Lett. **104**, 223004 (2010).

5

[14] J.T. Stewart, J.P. Gaebler, T.E. Drake, and D.S. Jin, Phys. Rev. Lett. **104**, 235301 (2010).

[15] B. Fröhlich et al., Phys. Rev. Lett. **106**, 105301 (2011).

[16] M. Feld et al., Nature (London) **480**, 75 (2011).

[17] A. Sommer et al., Phys Rev. Lett. **108**, 045302 (2012).

[18] R. Schmidt, T. Enss, V. Pietilä, and E. Demler, Phys. Rev. A **85**, 021602(R) (2012).

[19] B. Holstein, Am. J. Phys. **61**, 142 (1993).

[20] D.S. Petrov and G.V. Shlyapnikov, Phys. Rev. A **64** 012706 (2001).

[21] I. Bloch, J. Dalibard, and W. Zwerger, Rev. Mod. Phys. **80**, 885 (2008).

[22] M. Barth and W. Zwerger, Ann. Phys. **326**, 2544 (2011).

[23] F. Werner and Y. Castin, arXiv:1001.0774.

[24] J. Hofmann, Phys. Rev. A. **84**, 043603 (2011).

[25] B. Fröhlich, Ph.D. thesis, University of Cambridge, July 2011.

[26] G. Bertaina and S. Giorgini, Phys. Rev. Lett. **106**, 110403 (2011).

[27] A. Sommer and M. Zwierlein, private communication.

# Short-distance properties of Coulomb systems

Johannes Hofmann,[1, *] Marcus Barth,[2, †] and Wilhelm Zwerger[2]

[1]*Department of Applied Mathematics and Theoretical Physics, University of Cambridge,*
*Centre for Mathematical Sciences, Cambridge CB3 0WA, United Kingdom*
[2]*Technische Universität München, Physik Department, James-Franck-Strasse, 85748 Garching, Germany*
(Dated: July 12, 2013)

We use the operator product expansion to derive exact results for the momentum distribution and the static structure factor at high momentum for a jellium model of electrons in both two and three dimensions. It is shown that independent of the precise state of the Coulomb system and for arbitrary temperatures, the asymptotic behavior is a power law in the momentum, whose strength is determined by the contact value of the pair distribution function $g(0)$. The power-law tails are quantum effects which vanish in the classical limit $\hbar \to 0$. A leading order virial expansion shows that the classical and the high-temperature limit do not agree.

PACS numbers: 71.10.Ca, 05.30.Fk, 31.15.-p

## I. INTRODUCTION

The basic constituents of ordinary matter are electrons and nuclei combined in such a way that there is no net overall charge. Within a non-relativistic approximation and treating the nuclei as point particles, the interaction is fully described by an instantaneous Coulomb potential $\sim e^2/r$ at arbitrary distances. In spite of the long-range nature of this interaction and the divergent attractive force between electrons and nuclei at short distances, one expects an overall neutral Coulomb system to be stable in the sense that the ground state energy (or free energy at finite temperature) is finite and scales *linearly* with the total number $N$ of particles. It is one of the major accomplishments of theoretical physics to show that - beyond the exactly solvable case of the hydrogen atom - these expectations can indeed be proven rigorously. The proof crucially relies on the fact that electrons are fermions and are thus constrained by the Pauli principle[1]. Since neither the size and mass nor the statistics of the nuclei play a role in this context, a simple approximation which captures much of the basic physics of Coulomb systems is the well-known jellium model, where the nuclei are treated as a homogeneous background that precisely cancel the negative charge of the Coulomb gas of electrons[2]. At zero temperature, this model is fully specified by the standard dimensionless interaction strength $r_s = r_0/a_0$. Here $a_0 = \hbar^2/me^2$ is the Bohr radius while $r_0$ is the average spacing between electrons, connected with the electron density $n$ via $r_0 = (3/4\pi n)^{1/3}$ in 3D and $r_0 = (1/\pi n)^{1/2}$ in 2D, respectively. Despite the fact that the periodic arrangement of the nuclei is ignored, the jellium model provides a reasonable starting point to describe elementary properties of metals like their cohesion energy or compressibility[2–4]. Unfortunately, however, beyond the fundamental issue of stability and extensivity, there are hardly any exact results even for this highly simplified model. It is only in the high-density limit $r_s \ll 1$ where a perturbative expansion around the non-interacting Fermi gas is possible. A simple argument for this is provided by writing the jellium Hamiltonian

$$H = -\frac{1}{r_s^2}\sum_i \nabla_i^2 + \frac{1}{r_s}\sum_{i<j}\frac{2}{|\mathbf{r}_i - \mathbf{r}_j|} + H_{\rm b} \qquad (1)$$

in dimensionless form, with Ry$= e^2/2a_0$ as the unit of energy and particle coordinates $\mathbf{r}_i$ measured in units of $r_0$ (both the energy $H_{\rm b}$ of the background as well as the interaction energy between electrons and the background are constants and thus need not be written explicitly). Clearly, as $r_s \to 0$, the kinetic energy dominates and the Coulomb interaction can be treated within perturbation theory. The expected ground state is a Fermi liquid, with a finite jump $0 < Z < 1$ of the momentum distribution at a spherical Fermi surface $|\mathbf{k}| = k_F$[5]. While typical values of $r_s \approx 1-5$ in metals[7] are outside the range of perturbation theory, at least the qualitative features of electrons in metals are captured correctly in this picture. For very large values of $r_s$, the uniform electron liquid is expected to eventually form a Wigner crystal, which minimizes the interaction energy in (1). In addition, non-trivial phases such as anisotropic quantum liquid crystals are likely to appear at intermediate values of $r_s$. Indeed, in two dimensions a direct transition from a uniform electron liquid to a Wigner crystal as a function of $r_s$ can be ruled out by a quite general thermodynamic argument[8]. Moreover, even in the Wigner crystal, the electron spin gives rise to strong quantum fluctuations due to ring exchange processes, leading to a complex magnetic structure, see e.g. Refs.[9–11].

In view of the still poorly understood phase diagram of even the simplest model for a many-body system with Coulomb interactions, it is of considerable interest to derive exact relations that hold independent of the interaction strength and the particular state in question. Our aim in the present work is to show that such relations follow directly from the operator product expansion (OPE) of quantum field theory. They constrain the short-distance physics of Coulomb systems in a manner which is analogous to the so-called Tan relations[12–14] for fermions with interactions that have effectively zero

range. Physically, these relations rely on the fact that at sufficiently short distances only the two-body interaction is relevant. At the level of the many-body ground state wave function for Coulomb systems, this observation goes back to Kimball[15–17]. Beyond providing a concise derivation of these relations, a novel and quite non-trivial aspect of our present derivation via the OPE is the fact that the relations will be shown to be valid at the level of *operators*. As a result, they apply to *any* state of the system, e.g., to a Fermi liquid or a Wigner crystal, at zero or at finite temperature and also in a few-body situation. The only change is the value of the 'contact' $g(0)$, a dimensionless measure of the probability that two electrons with opposite spin are found at a coincident point in space.

In order to illustrate the universal features in the short-distance behavior of Coulomb systems, it is instructive to consider the hydrogen atom as a simple and exactly solvable system. In fact, the basic relations that will subsequently be proven for the many-body case show up already in this elementary textbook problem[18]. The wave function for relative motion in the hydrogen atom has the well-known form[19]

$$\psi_{nlm}(\mathbf{r}) = \left(\frac{2}{a_0 n}\right)^{3/2} \sqrt{\frac{(n-l-1)!}{2n(n+l)!}} Y_{lm}(\theta, \varphi)$$
$$\times \left(\frac{2r}{a_0 n}\right)^l e^{-\frac{r}{a_0 n}} L_{n-l-1}^{2l+1}\left(\frac{2r}{a_0 n}\right), \quad (2)$$

where $Y_{lm}(\theta, \varphi)$ and $L_{n-l-1}^{2l+1}(x)$ are spherical harmonics and generalized Laguerre polynomials, respectively (we assume the proton to be infinitely heavy, so the reduced mass is equal to the electron mass $m$). Its Fourier transform $\Upsilon_{nlm}(\mathbf{q})$ has been calculated by Podolsky and Pauling[20]. It is given by

$$\Upsilon_{nlm}(\mathbf{q}) = 2^{2l+4}\pi(a_0 n)^{3/2}(-i)^l l! \sqrt{\frac{n(n-l-1)!}{(n+l)!}} Y_{lm}(\vartheta, \phi)$$
$$\times \frac{\zeta^l}{(\zeta^2+1)^{l+2}} C_{n-l-1}^{l+1}\left(\frac{\zeta^2-1}{\zeta^2+1}\right), \quad (3)$$

where $\zeta = q a_0 n$, and $C_{n-l-1}^{l+1}(x)$ denotes a Gegenbauer polynomial. The momentum distribution of the electron is the absolute square of the momentum space wave function. Using Eq. (3), $|\Upsilon_{nlm}(\mathbf{q})|^2$ turns out to decrease asymptotically as $1/q^{8+2l}$ for large momentum $\zeta = q a_0 n \gg 1$. The leading order term

$$|\Upsilon_{n00}(\mathbf{q})|^2 = \left(\frac{8\pi}{a_0}\right)^2 \frac{|\psi_{n00}(0)|^2}{q^8} + \mathcal{O}(1/q^{10}) \quad (4)$$

in the momentum distribution therefore only involves the contribution from $s$-states. They are the only ones with a finite probability density $|\psi_{n00}(0)|^2 = 1/\pi(a_0 n)^3$ for the electron and proton to be found at a coincident point in space.

Remarkably, the same 'contact' density also appears in the high-momentum tail of the atomic form factor $\rho_{nlm}(\mathbf{q})$, which is the Fourier transform of the electronic density distribution. Its leading contribution at large $q$

$$\rho_{n00}(\mathbf{q}) = \int d^3r \, e^{-i\mathbf{q}\cdot\mathbf{r}}|\psi_{n00}(\mathbf{r})|^2$$
$$= \frac{16\pi}{a_0}\frac{|\psi_{n00}(0)|^2}{q^4} + \mathcal{O}(1/q^5) \quad (5)$$

comes again from $s$-states, while higher angular momenta are associated with faster decaying power laws. As for the momentum distribution, the coefficient of the high-momentum tail contains the contact density $|\psi_{n00}(0)|^2$. Moreover, both the momentum distribution and the form factor depend only on the magnitude $q = |\mathbf{q}|$ of the wave vector, i.e., they have spherically symmetric tails since only $s$-states contribute. As will be shown in the following, the power laws found in the hydrogen atom and the fact that the physics at short distances is rotation invariant also show up in the many-body context, even for inhomogeneous or anisotropic phases. More precisely, the momentum distribution is replaced by the Fourier transform of the one-particle density matrix, while the atomic form factor becomes the static structure factor $S(\mathbf{q})$ of the many-body system.

The article is structured as follows: in Sec. II, we introduce the jellium model, the one- and two-particle density matrix as well as some basics of the operator product expansion. In Sec. III, the OPE is used to derive the exact short-distance behavior of general many-body wave functions. Moreover, it is shown that this implies power-law tails in both the momentum distribution and the static structure factor which depend on the particular state in question only through the value of the contact $g(0)$. A direct computation of the short-distance OPE of the density-density correlator and the one-particle density matrix is presented in Sec. IV. Finally, an explicit calculation of the contact in both the classical and the high-temperature limit is given in Sec. V. It is shown that for a Coulomb system these limits give opposite results and thus are not equivalent. The article is concluded by a summary and outlook, Sec. VI. The Feynman rules of the diagrammatic calculation and some details of the evaluation of some few-particle matrix elements are discussed in Apps. A and B.

## II. JELLIUM AND OPE

In second-quantized form, the Hamiltonian of the jellium model is given by

$$H = H_{\mathrm{b}} + \int d^d x \, \psi_\sigma^\dagger \frac{-\hbar^2\nabla^2}{2m}\psi_\sigma(\mathbf{x})$$
$$+ \frac{1}{2}\int d^d x \int d^d x' \, \psi_\sigma^\dagger(\mathbf{x})\psi_{\sigma'}^\dagger(\mathbf{x})\frac{e^2}{|\mathbf{x}-\mathbf{x}'|}\psi_{\sigma'}(\mathbf{x}')\psi_\sigma(\mathbf{x}),$$
$$(6)$$

where a summation over spin indices $\sigma = \uparrow, \downarrow$ is implied. Since the Hamiltonian involves only one- and two-body interactions, the expectation value of the energy in a state described by an arbitrary $N$-body density matrix only involves the reduced one- and two-particle density matrices $\gamma^{(1)}$ and $\gamma^{(2)1}$. In a spin-resolved form and in a position space representation, the former can be expressed as

$$\gamma_\sigma^{(1)}(\mathbf{x}, \mathbf{x}') = \langle \psi_\sigma^\dagger(\mathbf{x}) \psi_\sigma(\mathbf{x}') \rangle. \tag{7}$$

Its Fourier transform with respect to $\mathbf{x} - \mathbf{x}'$ then gives the momentum distribution (see Eq. (30) below). Regarding the two-particle density matrix $\gamma^{(2)}(1, 1'; 2, 2')$, one only needs the diagonal elements $1 = 1'$, $2 = 2'$, which define a dimensionless, spin-resolved pair distribution function

$$n_\sigma(\mathbf{x}) \, n_{\sigma'}(\mathbf{x}') \, g_{\sigma,\sigma'}(\mathbf{x}, \mathbf{x}') = \left\langle \psi_\sigma^\dagger(\mathbf{x}) \psi_{\sigma'}^\dagger(\mathbf{x}') \psi_{\sigma'}(\mathbf{x}') \psi_\sigma(\mathbf{x}) \right\rangle. \tag{8}$$

The pair distribution function is a measure of the probability to find an electron with spin projection $\sigma'$ at position $\mathbf{x}'$ given an electron with spin projection $\sigma$ is at $\mathbf{x}$. For a completely uncorrelated system one has $g(\mathbf{x}, \mathbf{x}') \equiv 1$. Note that there is no assumption here about translation invariance, which is certainly broken in the Wigner crystal. The total pair distribution function

$$g(\mathbf{x}, \mathbf{x}') = \sum_{\sigma, \sigma'} \frac{n_\sigma(\mathbf{x}) n_{\sigma'}(\mathbf{x}') g_{\sigma\sigma'}(\mathbf{x}, \mathbf{x}')}{n(\mathbf{x}) n(\mathbf{x}')} \tag{9}$$

of a spin one half Fermi gas is a weighted sum of contributions $g_{\sigma,\sigma'}$. They all approach unity as $\mathbf{x} - \mathbf{x}' \to \infty$ and so does $g(\mathbf{x}, \mathbf{x}')$. For small separations $\mathbf{x} - \mathbf{x}' \to 0$, in turn, the pair distribution function for equal spins vanishes quadratically because of the Pauli principle. Taking into account the possibility of a non-vanishing spin polarization $\zeta = (n_\uparrow - n_\downarrow)/n$, one finds

$$g(0) = \frac{1}{2} \left(1 - \zeta^2\right) g_{\uparrow\downarrow}(0) \tag{10}$$

for the total pair distribution function at vanishing separation in the translationally invariant case. Note that in a situation where the electronic state is not translation invariant, the local value $g(0) = g(\mathbf{R}, 0)$ of the pair distribution function depends also on the 'center-of-mass' coordinate $\mathbf{R} = (\mathbf{x} + \mathbf{x}')/2$, a dependence which is suppressed in the following.

Both the one-particle density matrix and the pair distribution function can be expressed as expectation values of operators at different points in space. The operator product expansion - specified here to the relevant case of equal times - provides an expansion of an operator product $\mathcal{O}_a \mathcal{O}_b$ at nearby points in space in terms of local operators:

$$\mathcal{O}_a\left(\mathbf{R} - \frac{\mathbf{r}}{2}\right) \mathcal{O}_b\left(\mathbf{R} + \frac{\mathbf{r}}{2}\right) = \sum_n W_n(\mathbf{r}) \mathcal{O}_n(\mathbf{R}). \tag{11}$$

It is important to emphasize that Eq. (11) is an operator relation, i.e., it is valid for expectation values

between *any* state. The state-independent coefficients $W_n(\mathbf{r})$ are ordinary c-numbers and are called the Wilson coefficients. They depend both on $n$ and the specific operators $\mathcal{O}_a$ and $\mathcal{O}_b$ which appear on the left-hand side of Eq. (11). The scaling dimension $\Delta_n$ of a local operator $\mathcal{O}_n$ that contains $N_\mathcal{O}$ fermion creation and annihilation operators is defined by the property that the correlation between $\mathcal{O}_n$ and its hermitian conjugate at points separated by a small distance $r$ and time $t$ asymptotically scales as $t^{-\Delta_n} \exp\left[-iN_\mathcal{O} mr^2/2t\right]$. For example, the operator $\psi_\sigma^\dagger$ has scaling dimension $\Delta = d/2$. The values of $\Delta_n$ determine the dependence of the Wilson coefficients at small separation $\mathbf{r}$ via

$$W_n(\mathbf{r}) = r^{\Delta_n - \Delta_a - \Delta_b} f(r/a_0, \hat{\mathbf{e}}_\mathbf{r}), \tag{12}$$

where $f$ is a function of the dimensionless ratio $r/a_0$ and the unit vector $\hat{\mathbf{e}}_\mathbf{r}$, which reflects a possible angular dependence. The operators $\mathcal{O}_n$ with the lowest scaling dimension therefore govern the behavior of an operator product at small separation. In particular, Wilson coefficients which are non-analytic in $r$ give rise to power law tails of the associated correlator $\mathcal{O}_a \mathcal{O}_b$ at large momentum.

Regarding the question whether the OPE (11) is a convergent rather than an asymptotic expansion, precise statements have only been given in the context of relativistic[21] and, in particular, conformal field theories. In the latter case the OPE can be shown to have infinite radius of convergence[22,23]. For non-relativistic quantum field theories, like in our present problem, mathematically precise results on the convergence of the OPE are unfortunately not available. The OPE for the specific case of Coulomb systems may however be justified a posteriori by the fact that our main results like the short distance behavior of the many body wave function (20) and the cusp condition (24) agree with results derived in a mathematically precise manner via different methods[24].

In practice, the Wilson coefficients may be determined by performing few-particle calculations. Indeed, since they are state-independent, it is sufficient to calculate the matrix element of Eq. (11) between simple (few-particle) states for which $\langle \mathcal{O}_n \rangle \neq 0$. The coefficients $W_n(\mathbf{r})$ then follow by matching both sides of Eq. (11). As will be shown below, an operator of particular interest in the present context is the two-particle operator

$$\mathcal{O}_c(\mathbf{R}) = \psi_\uparrow^\dagger \psi_\downarrow^\dagger \psi_\downarrow \psi_\uparrow(\mathbf{R}). \tag{13}$$

In analogy to the notion used for fermions with short range interactions, we shall refer to this as the contact operator. It has a finite expectation value in the presence of Coulomb interactions and thus the scaling dimension $\Delta_c = 2d$ of the contact operator is the one inferred from simple dimensional analysis. This is quite different from the case where the interactions have zero range and $\mathcal{O}_c$ acquires an anomalous dimension two[25]. The contact is a central quantity which determines the leading short-distance singularities of Coulomb systems and, in particular, the magnitude of the high-momentum tails of both

the momentum distribution and the structure factor. In a translation invariant situation, the contact is equal to $n^2$ times the local value of the pair distribution function $g(0)$. Before proceeding to derive these results from the OPE in explicit form, we note that our derivation remains unchanged if the sign of the interaction is reversed. All the results of this article can thus be extended to the case of an attractive Coulomb interaction by simply changing $e^2 \to -e^2$.

## III.   OPE FOR THE MANY-BODY WAVEFUNCTION

The crucial physical insight, already implicit in the work of Kimball[15–17], relies on the intuition that the many-body wavefunction factorizes into a two-body contribution and a remainder whenever two particle coordinates come closer than the average interparticle distance. In this limit, the two particles only feel their mutual Coulomb repulsion at short distance, with negligible corrections from the medium. This type of argument has in fact been used by various authors[26,27] in the derivation of the Tan relations for Fermi gases with short range interactions. In order to prove the validity of this intuitive picture, we use the operator product expansion for the special case of the operator

$$\mathcal{O}_a(\mathbf{x})\mathcal{O}_b(\mathbf{y}) = \psi_\uparrow(\mathbf{x})\psi_\downarrow(\mathbf{y}). \tag{14}$$

Inserting the general form (11) of the OPE, the $N$-particle wavefunction $\Psi$ corresponding to an arbitrary $N$-particle state $|\Psi_N\rangle$ can be expanded as a formal power series

$$\Psi(-\frac{\mathbf{r}}{2}, \uparrow; \frac{\mathbf{r}}{2}, \downarrow; \mathbf{r}_3, \sigma_3; \dots)$$

$$= \frac{1}{\sqrt{N_\uparrow! N_\downarrow!}} \langle 0|\psi_\uparrow(-\frac{\mathbf{r}}{2})\psi_\downarrow(\frac{\mathbf{r}}{2}) \prod_{l=3}^{N} \psi_{\sigma_l}(\mathbf{r}_l)|\Psi_N\rangle$$

$$= \sum_n W_n(\mathbf{r}) \frac{1}{\sqrt{N_\uparrow! N_\downarrow!}} \langle 0|\mathcal{O}_n(\mathbf{0}) \prod_{l=3}^{N} \psi_{\sigma_l}(\mathbf{r}_l)|\Psi_N\rangle, \tag{15}$$

where $W_n(\mathbf{r})$ are the Wilson coefficients in an OPE of the operator $\psi_\uparrow(\mathbf{x})\psi_\downarrow(\mathbf{y})$, which can be written as the sum of a spin singlet operator

$$\psi(\mathbf{x})\psi(\mathbf{y}) = \frac{1}{2}(\psi_\uparrow(\mathbf{x})\psi_\downarrow(\mathbf{y}) - \psi_\downarrow(\mathbf{x})\psi_\uparrow(\mathbf{y})) \tag{16}$$

and a triplet operator which is symmetric in the spin indices. The leading order term in the OPE is associated with the operator $\psi\psi(0)$, whereas a similar contribution of the triplet operator vanishes since the fermion fields anticommute. Both singlet and triplet operators contribute in higher orders involving additional derivatives. The Wilson coefficient of the leading order can be obtained by taking the expectation value of Eq. (16) between the vacuum and a two-particle state with (on-shell)
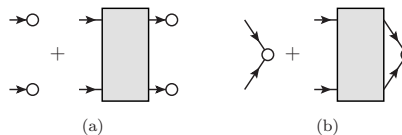


FIG. 1. (a) Contribution to the two-particle matrix element of the operator $\psi(-\frac{\mathbf{r}}{2})\psi(\frac{\mathbf{r}}{2})$, denoted by the white circles. (b) Same for the operator $\psi\psi(0)$. The T-matrix is denoted by a gray rectangle.

energy $p^2/m$. The corresponding diagrams are sketched in Fig. 1. (A brief summary of the Feynman rules in momentum space for the jellium Hamiltonian (6) is given in App. A.) We can express this matrix element as a one-body scattering wave function

$$\langle 0|\psi(-\frac{\mathbf{r}}{2})\psi(\frac{\mathbf{r}}{2})|\mathbf{p}, \uparrow; -\mathbf{p}, \downarrow\rangle$$

$$= \langle \mathbf{r}|1 + G_0 T|\mathbf{p}, \uparrow; -\mathbf{p}, \downarrow\rangle = \psi_p(\mathbf{r}), \tag{17}$$

using the bare retarded two-particle propagator $G_0$ and the T-matrix $T$. In the second line, we have used the Lippmann-Schwinger equation for the scattering wavefunction $\psi_p(\mathbf{r})$ with energy $p^2/m$. Similarly, the matrix element of the operator $\psi\psi(0)$ is $\psi_p(0)$[28]. We determine its Wilson coefficient by matching this matrix element to leading order in the energy $p^2/m$ of the external state. As a result, it turns out that $W_{\psi\psi}(\mathbf{r})$ solves the two-particle $s$-wave Schrödinger equation at zero energy

$$\left[-\nabla^2 + \frac{1}{a_0 r}\right] W_{\psi\psi}(\mathbf{r}) = 0 \tag{18}$$

with boundary condition $W_{\psi\psi}(0) = 1$. The solution of Eq. (18) up to linear order in $r$ is

$$W_{\psi\psi}(\mathbf{r}) = \begin{cases} 1 + \dfrac{r}{2a_0} + \dots & (3\mathrm{D}) \\ 1 + \dfrac{r}{a_0} + \dots & (2\mathrm{D}) \end{cases}. \tag{19}$$

The OPE therefore provides a concise derivation of the intuitive short-distance factorization

$$\lim_{r\to 0} \Psi(-\frac{\mathbf{r}}{2}, \uparrow; \frac{\mathbf{r}}{2}, \downarrow; \dots) = W_{\psi\psi}(\mathbf{r}) \Psi(\mathbf{0}, \uparrow; \mathbf{0}, \downarrow; \dots) \tag{20}$$

of the many-particle wavefunction (15) if two particles of opposite spin are close to each other. This factorization was previously considered by Lepage for two-particle systems in the context of effective field theories[31]. Recently, this was used to derive high-momentum tails for the unitary Fermi gas and the Coulomb gas[32].

Focusing on pure states, e.g., the ground state of jellium, the result (20) together with the fact that the two-particle wave function $W_{\psi\psi}(\mathbf{r})$ is non-analytic at short distances implies power-law tails in the ground state momentum distribution and the static structure factor. Indeed, for a pure state, the dimensionless and intensive

momentum distribution is given by

$$n(\mathbf{q}) = \frac{N}{V} \int d^d R \int d^d r \prod_{l=2}^{N} d^d r_l \, e^{-i\mathbf{q}\cdot\mathbf{r}}$$
$$\times \Psi^*(\mathbf{R} - \frac{\mathbf{r}}{2}, \mathbf{r}_2, \ldots, \mathbf{r}_N) \, \Psi(\mathbf{R} + \frac{\mathbf{r}}{2}, \mathbf{r}_2, \ldots, \mathbf{r}_N). \quad (21)$$

Its asymptotic behavior for large momentum is determined by the integration regions in which both $\mathbf{R} + \mathbf{r}/2$ and $\mathbf{R} - \mathbf{r}/2$ approach one of the particle coordinates $\mathbf{r}_l$ for $l = 2, \ldots N$ *simultaneously*. By substituting the result (20) in Eq. (21), the resulting high-momentum tail of the momentum distribution turns out to be given by

$$n(\mathbf{q}) = \begin{cases} \left(\dfrac{4\pi}{a_0}\right)^2 \dfrac{n^2 g(0)}{q^8} + \ldots & \text{(3D)} \\[2mm] \left(\dfrac{2\pi}{a_0}\right)^2 \dfrac{n^2 g(0)}{q^6} + \ldots & \text{(2D)} \end{cases}, \quad (22)$$

in accordance with the results in Refs.[15–17,32].

The pair distribution function in first-quantized form reads (specifying to the translation invariant case)

$$n^2 g(\mathbf{r}) = N(N-1) \int \prod_{l=3}^{N} d^d r_l |\Psi(\mathbf{0}, \mathbf{r}, \mathbf{r}_3, \ldots, \mathbf{r}_N)|^2. \quad (23)$$

Inserting Eq. (20) in the definition of the pair correlation function, Eq. (23), we obtain

$$g(r) = \begin{cases} \left(1 + \dfrac{r}{a_0}\right) g(0) + \ldots & \text{(3D)} \\[2mm] \left(1 + \dfrac{2r}{a_0}\right) g(0) + \ldots & \text{(2D)} \end{cases}. \quad (24)$$

The pair distribution function at short distance therefore exhibits a dip, rising linearly with slope $g(0)/a_0$. For an *attractive* Coulomb force, where $a_0 \to -a_0$, the dip is replaced by a cusp. The result (24) agrees with the one obtained previously by Kimball[15–17]. Following Rajagopal *et al.*[33], we call this the cusp condition. It is interesting to note that a result which is completely analogous to that in Eq. (24) holds for Fermi systems with zero range interactions in one dimension, with the 1D scattering length $a_1$ replacing the Bohr radius[34]. Moreover, it is important to mention that various approximate schemes which have been developed to treat the jellium problem at least in its Fermi liquid phase in fact violate the cusp condition (24). This is true in particular for the standard RPA approximation, which is exact in the long wavelength limit but violates the cusp condition, see e.g. Ref.[39]. It is obeyed within extensions of the RPA which include local field corrections like the one developed by Singwi, Tosi, Land and Sjölander[40], at the expense, however, of violating the compressibility sum rule $S(\mathbf{q}) \sim q^2$ at long wavelengths $\mathbf{q} \to 0$[4,41].

The short-distance nonanalyticity in the pair distribution function leads to an asymptotic power law in the static structure factor

$$S(\mathbf{q}) = 1 + n \int d^d r \, e^{-i\mathbf{q}\cdot\mathbf{r}} \, (g(r) - 1). \quad (25)$$

Substituting Eq. (24), the static structure factor behaves like

$$S(\mathbf{q}) - 1 = \begin{cases} -\dfrac{8\pi}{a_0} \dfrac{n g(0)}{q^4} & \text{(3D)} \\[2mm] -\dfrac{4\pi}{a_0} \dfrac{n g(0)}{q^3} & \text{(2D)} \end{cases}, \quad (26)$$

at large momentum, where we have used that the Fourier transform of $r$ in three and two dimensions is $-8\pi/q^4$ and $-2\pi/q^3$, respectively, in the sense of distributions. The results in Eq. (26) are again in accordance with those obtained in Refs.[15–17,32].

The tails (22) and (26) in both the momentum distribution and the static structure factor are present for any state of the Coulomb system, a property that will be derived in detail in the following section. Here, we focus on the particular case of zero temperature and moderate values of $r_s$, where the jellium ground state is a uniform Fermi liquid. The characteristic momentum scale beyond which the asymptotic behavior applies is then set by the Fermi wave vector $k_F$, which is related to the average interparticle distance $r_0$ via $k_F = 1/(\alpha r_0)$, with $\alpha = (4/9\pi)^{1/3} \simeq 0.521$ in 3D and $\alpha = 1/\sqrt{2} \simeq 0.707$ in 2D. Introducing a dimensionless strength $s$ of the tail in the momentum distribution via $n_\sigma(\mathbf{q}) \to s \, (k_F/q)^{2d+2}$ one obtains[35]

$$s(r_s) = \begin{cases} \dfrac{9}{2}\alpha^8 \, g(0) r_s^2 & \text{(3D)} \\[2mm] 2\alpha^6 \, g(0) r_s^2 & \text{(2D)} \end{cases}. \quad (27)$$

The dimensionless strength $s$ is a continuous function of $r_s$, vanishing in both limits $r_s \to 0$ and $r_s \to \infty$. Indeed, the power-law tail in the momentum distribution is present even in the Wigner crystal, as long as the spin-polarization $\zeta$ remains less than one (recall Eq. (10)). The contact in this limit is expected to vanish in an exponential manner with $r_s$. In the opposite limit of high density, the fact that $g(0) = 1/2 + \mathcal{O}(r_s)$[36] yields $s \sim r_s^2$. The function $s(r_s)$, therefore, must have a maximum, whose value appears to be much smaller than one. Indeed, according to recent quantum Monte Carlo calculations of the momentum distribution in the Fermi liquid phase of the jellium model in 2D[37] and 3D[38], the resulting dimensionless strengths $s(10) \simeq 0.006$ (2D) or $\simeq 0.009$ (3D) of the power law tail are surprisingly small even at $r_s = 10$. In particular, they are almost two orders of magnitude smaller than the corresponding value $s(\infty) = 32 \ln 2/(3\pi^2) \simeq 0.749$ of a Fermi gas with infinite short range repulsion in 1D[34].

In contrast to zero range interactions, where the value of the contact determines the complete thermodynamics

by a simple coupling constant integration[12], the ground state energy of the jellium model requires knowledge of the pair distribution function at *all* distances. Interpolation schemes for the static structure factor and thus the complete pair distribution function $g(r)$ which properly account for both the long- and short-distance behavior of the homogeneous, unpolarized electron gas have been proposed by Gori-Giorgi, Sacchetti and Bachelet[42] and may be used to develop improved versions of the exchange and correlation energy functionals in density functional theory[43,44].

## IV.   DIRECT OPE OF THE CORRELATORS

In the following, we will show how the OPE can be used to perform an expansion of the one-particle density matrix and the pair distribution function (7) and (8) at the operator level. Apart from providing an alternative derivation of the high-momentum tails which avoids discussing the many-particle wavefunction, this method makes evident a point stressed already in our introduction: the short-distance properties derived here are valid completely independent of the state of the system. In particular, they hold in arbitrary few- or many-body states or in equilibrium at any temperature.

We start by considering the static structure factor, which - for $\mathbf{q} \neq 0$ - is just the Fourier transform

$$S(\mathbf{q}) = \frac{1}{N} \int d^d R \int d^d r \, e^{-i\mathbf{q}\cdot\mathbf{r}} \langle n\left(\mathbf{R} - \frac{\mathbf{r}}{2}\right) n\left(\mathbf{R} + \frac{\mathbf{r}}{2}\right)\rangle \tag{28}$$

of the density correlator. Equations (8) and (28) imply that its asymptotic behavior for large momentum $q$ is dominated by the short distance behavior of the pair distribution function. The pair distribution function is connected to the $\uparrow\downarrow$ density correlator $\psi_\uparrow^\dagger \psi_\uparrow \left(-\frac{\mathbf{r}}{2}\right) \psi_\downarrow^\dagger \psi_\downarrow \left(\frac{\mathbf{r}}{2}\right)$

via definition (8). As shown in detail in App. B, the short-distance OPE of this correlator to linear order in $r$ is

$$\psi_\uparrow^\dagger \psi_\uparrow \left(-\frac{\mathbf{r}}{2}\right) \psi_\downarrow^\dagger \psi_\downarrow \left(\frac{\mathbf{r}}{2}\right)$$
$$= \begin{cases} \left(1 + \dfrac{r}{a_0}\right) \psi_\downarrow^\dagger \psi_\uparrow^\dagger \psi_\uparrow \psi_\downarrow(0) + \dots & \text{(3D)} \\ \left(1 + \dfrac{2r}{a_0}\right) \psi_\downarrow^\dagger \psi_\uparrow^\dagger \psi_\uparrow \psi_\downarrow(0) + \dots & \text{(2D)} \end{cases}, \tag{29}$$

where we have omitted the analytic term of order $\mathbf{r}$ since it does not contribute to the high-momentum asymptotics. At this order, additional four-fermion operators involving only one particle species do not contribute because of the anticommutation relations obeyed by the fermion fields. The OPE (29), together with the definitions of the pair correlation function (8) and the static structure factor (28), reproduces the high-momentum behavior (26). In particular, when taking the expectation value of (29), the contact operator $\psi_\downarrow^\dagger \psi_\uparrow^\dagger \psi_\uparrow \psi_\downarrow(0)$ produces the pair correlation function at zero separation.

The momentum distribution $n_\sigma(\mathbf{q})$ describes the probability to find a particle of spin $\sigma$ with momentum $\mathbf{q}$. In second quantization, it is defined as the Fourier transform of the one-particle density matrix:

$$n_\sigma(\mathbf{q}) = \frac{1}{V} \int d^d x \int d^d y \, e^{-i\mathbf{q}\cdot(\mathbf{y}-\mathbf{x})} \langle \gamma_\sigma^{(1)}(\mathbf{x},\mathbf{y})\rangle$$
$$= \frac{1}{V} \int d^d R \int d^d r \, e^{-i\mathbf{q}\cdot\mathbf{r}} \langle \psi_\sigma^\dagger\left(\mathbf{R} - \frac{\mathbf{r}}{2}\right) \psi_\sigma\left(\mathbf{R} + \frac{\mathbf{r}}{2}\right)\rangle. \tag{30}$$

The non-analytic Wilson coefficients in a short-distance expansion of the one-particle density matrix therefore determine the high momentum tail of $n_\sigma(\mathbf{q})$. A quite elaborate calculation, which is discussed in detail in App. B, shows that the OPE of the one-particle density matrix is given by

$$\psi_\sigma^\dagger\left(-\frac{\mathbf{r}}{2}\right)\psi_\sigma\left(\frac{\mathbf{r}}{2}\right) = \begin{cases} \left[e^{-\frac{\mathbf{r}}{2}\cdot\nabla}\psi_\sigma^\dagger(0)\right]\left[e^{\frac{\mathbf{r}}{2}\cdot\nabla}\psi_\sigma(0)\right] - \dfrac{r^5}{2880\pi}\left(\dfrac{4\pi}{a_0}\right)^2 \psi_\downarrow^\dagger\psi_\uparrow^\dagger\psi_\uparrow\psi_\downarrow(0) + \dots & \text{(3D)} \\ \left[e^{-\frac{\mathbf{r}}{2}\cdot\nabla}\psi_\sigma^\dagger(0)\right]\left[e^{\frac{\mathbf{r}}{2}\cdot\nabla}\psi_\sigma(0)\right] - \dfrac{r^4\log r}{128\pi}\left(\dfrac{2\pi}{a_0}\right)^2 \psi_\downarrow^\dagger\psi_\uparrow^\dagger\psi_\uparrow\psi_\downarrow(0) + \dots & \text{(2D)} \end{cases}. \tag{31}$$

The first Wilson coefficients of the bilinear operators are the coefficients in a Taylor expansion of the operators on the left-hand side. The contact operator $\mathcal{O}_c$ defined in Eq. (13) is the leading order term associated with a non-analytic Wilson coefficient of order $\mathcal{O}(r^5)$ and $\mathcal{O}(r^4 \log r)$ in 3D and 2D, respectively. Substituting Eq. (31) in (30),

we obtain

$$n_\sigma(\mathbf{q}) = \begin{cases} \left(\dfrac{4\pi}{a_0}\right)^2 \dfrac{n_\uparrow n_\downarrow g_{\uparrow\downarrow}(0)}{q^8} + \dots & \text{(3D)} \\ \left(\dfrac{2\pi}{a_0}\right)^2 \dfrac{n_\uparrow n_\downarrow g_{\uparrow\downarrow}(0)}{q^6} + \dots & \text{(2D)} \end{cases} \tag{32}$$

for an arbitrary state with a possible non-vanishing spin

polarization $\zeta$. Summing over $\sigma = \uparrow, \downarrow$, we recover the previous result for the momentum distribution at large momentum in the spin-balanced Coulomb gas, Eq. (22). The fact that the non-analytic terms in Eq. (31) appear at the level of operators shows that the tails in the momentum distribution are also present in phases where translation invariance is broken, in a few-body situation, or at arbitrary temperatures. In a Wigner crystal, for instance, the product $n_\uparrow n_\downarrow g_{\uparrow\downarrow}(0)$ has to be replaced by

$$\frac{1}{V} \int d^d R \, \langle \psi_\downarrow^\dagger \psi_\uparrow^\dagger \psi_\uparrow \psi_\downarrow (\mathbf{R}) \rangle, \tag{33}$$

which is again an intensive quantity in the thermodynamic limit $N, V \to \infty$ at fixed average densities $n_\uparrow, n_\downarrow$. In a few-body situation, in turn, these densities vanish but there is still a finite expectation value of the contact operator. For the hydrogen atom for instance, one finds

$$\int d^3 R \, \langle \psi_\downarrow^\dagger \psi_\uparrow^\dagger \psi_\uparrow \psi_\downarrow (\mathbf{R}) \rangle = |\psi_{n00}(0)|^2, \tag{34}$$

in agreement with the result derived in the introduction.

## V. HIGH-TEMPERATURE VERSUS CLASSICAL LIMIT

Beyond the derivation of exact relations which constrain the short-distance properties of Coulomb systems in quite general terms and which - as has been shown in the preceding sections - all involve the contact $\langle \mathcal{O}_c(\mathbf{R}) \rangle$, quantitative results for specific phases of jellium or non-trivial few-body Coulomb systems require to calculate the value of the contact as a function of both the interaction strength $r_s$ and temperature $T$. Since relevant values of $r_s$ are beyond the regime where perturbation theory can be applied, this can only be achieved numerically, for instance via quantum Monte Carlo calculations, see e.g. Refs.[37,38] for some recent results. In the following, we calculate the value of the contact in the classical and the high-temperature limit. Surprisingly, it turns out that for Coulomb interactions these two limits are not equivalent. In fact, they turn out to be completely opposite.

Consider the Coulomb gas in the regime

$$k_B T \gg \frac{\hbar^2 n^{2/d}}{m}, \tag{35}$$

where the thermal energy is much larger than the degeneracy energy. This is the standard limit of a non-degenerate gas, in which the average interparticle spacing $n^{-1/d}$ is much larger than the thermal wavelength $\lambda_T = \hbar (2\pi/m k_B T)^{1/2}$:

$$n^{1/d} \lambda_T \ll 1. \tag{36}$$

In this limit, thermodynamic properties can be calculated by expanding in powers of the fugacity $z = \exp(\beta\mu) =$

$n\lambda_T^d/2 \ll 1$[45]. The non-degeneracy condition (36) does not involve the strength $e^2$ of the interaction and is satisfied both in the infinite temperature and in the classical limit. Now, for systems with Coulomb interactions, there is a second and purely classical, so-called Bjerrum length $\ell_B = e^2/(k_B T)$, which - keeping $\hbar$ finite - eventually becomes shorter than the thermal length at sufficiently high temperatures. As a result – already noted in Ref.[46] – the order in which the limits $T \to \infty$ or $\hbar \to 0$ is taken matters. Taking $T \to \infty$ *before* $\hbar \to 0$ results in the following hierarchy of length scales:

$$n^{-1/d} \gg a_0 \gg \lambda_T \gg \ell_B. \tag{37}$$

In turn, taking the classical limit $\hbar \to 0$ before $T \to \infty$, we find:

$$n^{-1/d} \gg \ell_B \gg \lambda_T \gg a_0. \tag{38}$$

As will be shown below, these two limits give quite different results for the value of the contact. Since the gas is non-degenerate in both cases, the contact value of the pair distribution function can be calculated to leading order in the virial expansion, which just involves an integration

$$n^2 g(0) = z^2 \frac{2^{d/2}}{\lambda_T^d} \int \frac{d^d p}{(2\pi\hbar)^d} \, e^{-\beta p^2/m} |\psi_p(0)|^2, \tag{39}$$

of the square of the relative Coulomb wavefunction $|\psi_p(0)|^2$ at the origin with the classical Boltzmann distribution for the relative momentum $p$. Here, $z = e^{\beta\mu}$ is the fugacity while $|\psi_p(0)|^2$ is given by[19]

$$|\psi_p(0)|^2 = \begin{cases} \dfrac{2\pi\xi}{e^{2\pi\xi} - 1} & \text{(3D)} \\[2mm] \dfrac{2}{e^{2\pi\xi} + 1} & \text{(2D)} \end{cases}, \tag{40}$$

with $\xi = me^2/2\hbar p$. In the infinite temperature limit, the integration gives

$$g(0) = \begin{cases} \dfrac{1}{2}\left(1 - \sqrt{2}\pi \dfrac{\ell_B}{\lambda_T} + \dots\right) & \text{(3D)} \\[3mm] \dfrac{1}{2}\left(1 - \dfrac{\pi^2}{\sqrt{2}} \dfrac{\ell_B}{\lambda_T} + \dots\right) & \text{(2D)} \end{cases}. \tag{41}$$

The leading order term is the expected result for a classical ideal gas. The corrections involve the ratio $\ell_B/\lambda_T$ and thus vanish for large temperatures like $\sim 1/\sqrt{T}$. Note that, although $g(0)$ is of order one in this limit, the high-momentum tails in this limit are present only for very large $q \gg \lambda_T^{-1}$.

More relevant for low temperature, non-degenerate plasmas is the classical limit $\hbar \to 0$ for which Ry $\gg k_B T$. This limit is reached, for example, for Coulomb gases of charged dust particles in astrophysics[47]. In this limit the integration in (39) gives rise to a contact which vanishes

exponentially like

$$g(0) = \begin{cases} \dfrac{4\pi^2 2^{1/3}}{3^{1/2}} \left(\dfrac{\ell_B}{\lambda_T}\right)^{4/3} e^{-\frac{3\pi}{2^{1/3}}\left(\frac{\ell_B}{\lambda_T}\right)^{2/3}} + \dots & \text{(3D)} \\[2ex] \dfrac{2\pi 2^{1/3}}{3^{1/2}} \left(\dfrac{\ell_B}{\lambda_T}\right)^{1/3} e^{-\frac{3\pi}{2^{1/3}}\left(\frac{\ell_B}{\lambda_T}\right)^{2/3}} + \dots & \text{(2D)} \end{cases}.$$

$$(42)$$

Equations (41) and (42) are the main results of this section. The Wilson coefficients of the momentum distribution and the static structure factor diverge as $1/a_0^2 \sim 1/\hbar^4$ and $1/a_0 \sim 1/\hbar^2$ as $\hbar \to 0$. The high momentum tails are expected to occur for $q \gg \lambda_T^{-1}$. Thus, their characteristic momentum scale is pushed to infinity as $\hbar \to 0$. The total weight of the tails, containing both the Wilson coefficients and $g(0)$, is exponentially suppressed and guarantees a well defined kinetic energy in this limit. We point out that different high-momentum tails are present in the classical system. Indeed, the structure factor of the classical electron gas decreases as $1/q^2$ at intermediate momentum $\kappa < q < 1/l_B$, where $\kappa = \sqrt{nl_B}$ is the inverse Debye-Hückel length[48].

### A. Diagrammatic derivation

In the infinite temperature limit, the virial expansion of the contact $g(0)$ in Eq. (41) can also be obtained using a diagrammatic formalism. This method was originally introduced by Vedenov and Larkin to derive the equation of state of an electron gas[49], and was recently used by various groups to determine the virial expansion of a Fermi gas with short-range interactions[50-53].

The perturbation series of an arbitrary correlator involves all Feynman diagrams that connect to the operator insertions. In the absence of a small parameter, this gives rise to a very large number of diagrams. The key point of the method is that in the infinite temperature limit, this number is drastically reduced by exploiting the causal structure of the propagators, which are defined as

$$G(\tau, \mathbf{k}) = \begin{cases} -(1 - n_\mathbf{k})e^{-(\varepsilon_\mathbf{k} - \mu)\tau} & \tau > 0 \\ n_\mathbf{k} e^{-(\varepsilon_\mathbf{k} - \mu)\tau} & \tau < 0 \end{cases}, \quad (43)$$

where $n_\mathbf{k} = 1/(e^{\beta(\varepsilon_\mathbf{k} - \mu)} + 1)$ is the Fermi-Dirac distribution. In imaginary time, they carry the whole dependence on the fugacity and, thus, an expansion of a diagram in the fugacity corresponds to an expansion of the propagators:

$$G(\tau, \mathbf{k}) = G^{(0)}(\tau, \mathbf{k}) + G^{(1)}(\tau, \mathbf{k}) + \mathcal{O}(z^2), \quad (44)$$

with

$$G^{(0)}(\tau, \mathbf{k}) = -\Theta(\tau)\, e^{\mu\tau} e^{-\varepsilon_\mathbf{k}\tau} \quad \text{and} \quad (45)$$

$$G^{(1)}(\tau, \mathbf{k}) = z\, e^{\mu\tau} e^{-\varepsilon_\mathbf{k}(\beta+\tau)}. \quad (46)$$
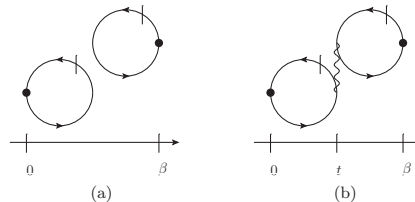


FIG. 2. (a) $\mathcal{O}(e^0)$ and (b) $\mathcal{O}(e^2)$ contribution to $g(0)$. Imaginary time runs from the left to the right. Black dots denote the density operator, the wavy line the instantaneous Coulomb interaction, and (slashed) lines the particle propagator as explained in the text.

$\Theta$ is the Heaviside step function. The coefficients $G^{(i)}$ with $i = 1, 2, \dots$ can be treated as separate diagrammatic elements, e.g. by denoting them by a line that is slashed $i$ times. The order of a diagram in $z$ is then set by the sum $\sum_i iN_i$, where $N_i$ is the number of propagators of type $i$. It is important to note that the leading order term (45) is purely retarded, and while the calculation of a general order may be unwieldy, only a very limited number of diagrams contribute to the virial expansion of a correlator to leading order in $z$.

Figure 2 shows the two leading order contribution in $e^2$ to the pair correlation function

$$g_{\uparrow\downarrow}(0) = \frac{1}{n_\uparrow n_\downarrow} \langle T_\tau n_\uparrow(\beta) n_\downarrow(0)\rangle, \quad (47)$$

where we define the density operator in the usual sense $n_\sigma = -\lim_{\tau\to 0-} T_\tau \psi_\sigma(\tau)\psi_\sigma^\dagger(0)$ to avoid an ordering ambiguity[3]. Figure 2(a) corresponds to the noninteracting result

$$g_{\uparrow\downarrow}^a(0) = 1, \quad (48)$$

where we use the relation $n_\sigma = z_\sigma \lambda_T^{-d}$. The $\mathcal{O}(e^2)$ contribution in Fig. 2(b) reads

$$g_{\uparrow\downarrow}^b(0) = \begin{cases} -\sqrt{2}\pi \dfrac{\ell_B}{\lambda_T} & \text{(3D)} \\[2ex] -\dfrac{\pi^2}{\sqrt{2}} \dfrac{\ell_B}{\lambda_T} & \text{(2D)} \end{cases}, \quad (49)$$

which coincides with our previous result (41). Note that higher order contributions to $g(0)$ contain infrared divergences. They can be removed by summing the divergent parts of an infinite number of ring diagrams[49], which gives rise to Debye-Hückel corrections that are of higher order in the density.

### VI. SUMMARY AND CONCLUSIONS

In summary, we used a short-distance operator product expansion to derive the high-momentum tail of the

structure factor and the momentum distribution of the Coulomb gas. Since these results are based on operator identities, they hold for pure states as well as for mixtures, and, in particular, for different phases, such as a Fermi liquid or a Wigner crystal. The key idea behind the derivation of our exact results is the separation of short and long distance scales. The functional dependence on the high-energy scales can be calculated exactly while the low-energy contribution factorizes. This multiplicative constant is the contact value of the pair distribution function, consistent with the intuitive expectation that the short-distance physics is determined by the probability to find two particles at the same point. These results are in close analogy to the Tan relations for zero range interactions[12], in which an analogous contact enters the coefficients of the high-momentum tails.

Furthermore, we calculated the contact in explicit form for non-degenerate Coulomb gases, using a virial expansion. It turns out that there are two possible limits which yield quite different results: in the high-temperature limit, the contact approaches the ideal Fermi gas value with power-law corrections in the temperature. By contrast, in the classical limit, the contact vanishes exponentially as $\hbar \to 0$, a behavior which is crucial to ensure a well-defined transition to the classical regime in which the Coulomb repulsion between the particles prevents them from being at coincident points.

The universal relations obtained in the present article are by far not exhaustive. Indeed, many more relations could be derived within the framework introduced here. A short-time OPE analogous to Refs.[54–56] would give results for dynamical correlators, such as, for example, the current response function or the dynamic structure factor, which display short-range correlations that are not captured in a random phase approximation[57]. A similar analysis can be carried out for the spectral function, which possesses a high-frequency tail as derived in[58,59]. Beyond applying the OPE to the Coulomb gas, it should be straightforward to generalize the results in this article to other many-fermion systems with long-range interactions, such as quantum gases of dipolar particles, which have recently been studied experimentally[60–62].

## Appendix A: Feynman Rules

This appendix summarizes the Feynman rules of the Hamiltonian (6) in momentum space. An energy $\omega$ and a momentum $\mathbf{q}$ are assigned to each internal and external line. The bare propagator is denoted by a continuous line and contributes a factor $G_0(\omega, \mathbf{q}) = i/(\omega - q^2/2m + i0)$. We represent the interaction between two fermions by a wavy line. It contributes a factor $4\pi i e^2/q^2$ in 3D and $2\pi i e^2/q$ in 2D, where q is the difference between the center of mass momenta of the ingoing and outgoing fermions. Finally, each undetermined momentum and energy is integrated with measure $\int d^d q/(2\pi)^d \int d\omega/2\pi$.

The T-matrix insertion $iT(\mathbf{p}, \mathbf{p}', k)$ is denoted by a gray rectangle, where $\mathbf{p}$ and $\mathbf{p}'$ are the center of mass momentum of the ingoing and outgoing atoms, respectively. We denote the center of mass energy of the ingoing atoms by $E = k^2/m$. Note that this energy is not necessarily on-shell, i.e. we do not impose the condition $k^2 = p^2 = p'^2$. The T-matrix solves the Bethe-Salpeter equation, depicted diagrammatically in Fig. 3(a), and reads[29,30,63,64]

$$iT(\mathbf{p}, \mathbf{p}', k)$$
$$= \begin{cases} -16 i \pi e^2 k^2 \int_0^1 dx \, x^{i\xi} \dfrac{d}{dx} \dfrac{x}{H(\mathbf{p}, \mathbf{p}', k)} & \text{(3D)} \\ -4 i \pi e^2 k \int_0^1 dx \, x^{i\xi} \dfrac{d}{dx} \dfrac{x^{1/2}}{H^{1/2}(\mathbf{p}, \mathbf{p}', k)} & \text{(2D)} \end{cases}, \text{ (A1)}$$

where $H(\mathbf{p}, \mathbf{p}', k) = 4k^2(\mathbf{p} - \mathbf{p}')^2 x - (k^2 - p^2)(k^2 - p'^2)(1 - x)^2$ and $\xi = me^2/2k$ is called the Sommerfeld parameter.

## Appendix B: Operator Product Expansion

In this appendix, we collect the matrix elements and momentum integrals needed to perform the OPE for the Coulomb gas. For simplicity, we set $\hbar = 1$ in the following. Since the operator product expansion is state-independent, it is sufficient to evaluate the matrix elements of the operator products (7) and (8) and the local operators between selected few-particle states. The Wilson coefficients are determined by matching the terms in an expansion of these expectation values in the external parameters of the state. The Wilson coefficients of the bilinear operators, i.e., operators that contain one field operator and its hermitian conjugate, are the coefficients in a Taylor expansion of the operator product, which can be obtained by matching the matrix elements between a one-particle state. To compute the contact's Wilson coefficient, we choose a two-particle state with zero relative momentum and (off-shell) energy $k^2/m$, which we denote by $\langle k|\mathcal{O}|k \rangle$. These matrix elements are the sum of four diagrams with either scattering or no scattering in the initial and final states. Some of them are depicted in Fig. 3.
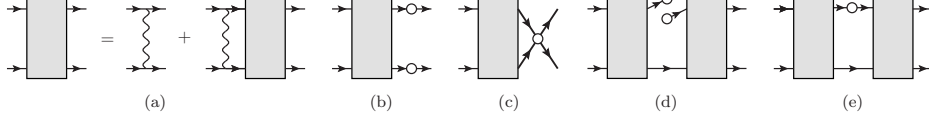
FIG. 3. (a) Bethe-Salpeter equation for the T-matrix, which is indicated by a gray rectangle. (b-e) Contribution to the two-particle matrix elements of (b) the density-density correlator $n_\uparrow(-\frac{\mathbf{r}}{2})n_\downarrow(\frac{\mathbf{r}}{2})$, (c) the contact of the pair distribution function $g(0)$, (d) the one-particle density matrix $\psi_\sigma^\dagger(-\frac{\mathbf{r}}{2})\psi_\sigma(\frac{\mathbf{r}}{2})$, and (e) bilinear operators, respectively.

####### a. Structure factor

As explained in Sec. IV, the short-distance behavior of the pair correlation function is inferred from an OPE of the $\uparrow\downarrow$ density correlator $n_\uparrow(-\frac{\mathbf{r}}{2})n_\downarrow(\frac{\mathbf{r}}{2})$. The matrix element of this operator between a two-particle state can be expressed in terms of diagram 3(b). The complete matrix element is the sum of four diagrams with either scattering or no scattering in the initial and final states:

$$\langle k|n_\uparrow(-\frac{\mathbf{r}}{2})n_\downarrow(\frac{\mathbf{r}}{2})|k\rangle = \left[1 + \int \frac{d\omega}{2\pi}\int \frac{d^dq}{(2\pi)^d}e^{i\mathbf{q}\cdot\mathbf{r}}iT(\mathbf{0},\mathbf{q},k)G_0(\omega,\mathbf{q})G_0(E-\omega,-\mathbf{q})\right]^2$$

$$= \begin{cases} \left(1+\frac{r}{a_0}\right)\left[4\int_0^1 dx\, x^{i\xi}\frac{d}{dx}\frac{x}{(1+x)^2}\right]^2 + \mathcal{O}(r^2) & \text{(3D)} \\ \left(1+\frac{2r}{a_0}\right)\left[2\int_0^1 dx\, x^{i\xi}\frac{d}{dx}\frac{x^{1/2}}{1+x}\right]^2 + \mathcal{O}(r^2) & \text{(2D)}, \end{cases} \tag{B1}$$

where we used the integrals

$$\int \frac{d^3q}{(2\pi)^3}\frac{e^{i\mathbf{q}\cdot\mathbf{r}}}{(q^2-a^2)(q^2-b^2)} = \frac{i}{4\pi}\frac{1}{a+b} - \frac{r}{8\pi} + \mathcal{O}(r^2) \tag{B2}$$

and

$$\int \frac{d^2q}{(2\pi)^2}\frac{e^{i\mathbf{q}\cdot\mathbf{r}}}{(q^2-a^2)^{1/2}(q^2-b^2)} = \frac{i}{2\pi}\frac{\arccos\frac{a}{b}}{\sqrt{b^2-a^2}} - \frac{r}{2\pi} + \mathcal{O}(r^2). \tag{B3}$$

The factor in square brackets in Eq. (B1) depends on the details of the states and must not contribute to the Wilson coefficients. It is matched by the expectation value of the contact $\psi_\downarrow^\dagger\psi_\uparrow^\dagger\psi_\uparrow\psi_\downarrow(0)$. Consider the diagram in Fig. 3(c):

$$\int \frac{d^dq}{(2\pi)^d}\int \frac{d\omega}{2\pi}(iT(\mathbf{0},\mathbf{q},k))G_0(\omega,\mathbf{q})G_0(E-\omega,-\mathbf{q}) = \begin{cases} -4i\xi\int_0^1 dx\frac{x^{i\xi}}{(1+x)^2} & \text{(3D)} \\ -2i\xi\int_0^1 dx\frac{x^{i\xi-1/2}}{1+x} & \text{(2D)} \end{cases}. \tag{B4}$$

The full matrix element of $\psi_\downarrow^\dagger\psi_\uparrow^\dagger\psi_\uparrow\psi_\downarrow(0)$ contains three additional diagrams:

$$\langle k|\psi_\downarrow^\dagger\psi_\uparrow^\dagger\psi_\uparrow\psi_\downarrow(0)|k\rangle = \begin{cases} \left[4\int_0^1 dx\, x^{i\xi}\frac{d}{dx}\frac{x}{(1+x)^2}\right]^2 \approx \frac{1}{4\xi^4} & \text{(3D)} \\ \left[2\int_0^1 dx\, x^{i\xi}\frac{d}{dx}\frac{x^{1/2}}{1+x}\right]^2 \approx \frac{1}{16\xi^4} & \text{(2D)} \end{cases}, \tag{B5}$$

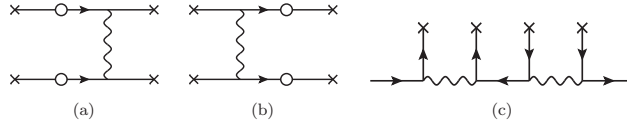where we have expanded the result to leading order in $k$.

FIG. 4. Leading-order contributions to the structure factor (a,b) and momentum distribution (c).

### b.  *Momentum distribution*

To obtain the asymptotic form of the momentum distribution (30), one performs an OPE of the nonlocal operator $\psi_\sigma^\dagger(-\frac{\mathbf{r}}{2})\psi_\sigma(\frac{\mathbf{r}}{2})$, whose expectation value gives the one-particle density matrix $\gamma(\frac{\mathbf{r}}{2}, -\frac{\mathbf{r}}{2})$, cf. Eq. (7). Since insertions of this operator on external legs are matched by bilinear operators, the only relevant diagram that contributes to the Wilson coefficient of the contact operator involves scattering in both initial and final state as shown in Fig. 3(d). As we are only interested in the leading order non-analyticity of the Wilson coefficient of the zero distance pair correlator, we expand the T-matrix, as well as our diagram, as a power series in $k$ around $k = 0$. This procedure introduces infrared divergences, which we regulate by introducing an infrared cutoff $\mu$. The expansion of the T-matrix with respect to $k \sim 1/\xi$ is given by

$$iT(\mathbf{0}, \mathbf{q}, k) = \begin{cases} i\dfrac{2\pi e^2}{\xi^2 q^2} = \lim_{\mu \to 0} i\dfrac{2\pi e^2}{\xi^2(q^2 + \mu^2)} & \text{(3D)} \\[3mm] i\dfrac{\pi e^2}{2\xi^2 q} = \lim_{\mu \to 0} i\dfrac{\pi e^2}{\xi^2\sqrt{q^2 + \mu^2}} & \text{(2D)}. \end{cases} \tag{B6}$$

In addition, we expand our propagators as $1/(q^2 - k^2) = 1/(q^2 + \mu^2) + \mathcal{O}(k^2)$. In the limit $k \to 0$, diagram 3(d) is given by

$$\int \frac{d^d q}{(2\pi)^d} \int \frac{d\omega}{2\pi} e^{i\mathbf{q}\cdot\mathbf{r}}(iT(\mathbf{0}, \mathbf{q}, k \to 0))^2 G_0(\omega, \mathbf{q})^2 G_0(E - \omega, -\mathbf{q})$$

$$= \begin{cases} \dfrac{\pi}{48 a_0^2 \xi^4}\left[\dfrac{3}{\mu^5} - \dfrac{r^2}{2\mu^3} + \dfrac{r^4}{8\mu} - \dfrac{r^5}{15}\right] + \mathcal{O}(r^6) & \text{(3D)} \\[4mm] \dfrac{\pi}{16 a_0^2 \xi^4}\left[\dfrac{1}{2\mu^4} - \dfrac{r^2}{8\mu^2} + \dfrac{r^4}{32}\left(\dfrac{3}{4} - \log\dfrac{e^{\gamma_E}\mu r}{2}\right)\right] + \mathcal{O}(r^5) & \text{(2D)}. \end{cases} \tag{B7}$$

The matrix elements of the one-particle operators (Fig. 3(e)) match the analytic terms in this expansion. The remainder is of order $\mathcal{O}(r^5)$ and $\mathcal{O}(r^4 \log r)$ and is matched by the contact operator:

$$W_{\mathcal{O}_c}(r) = \begin{cases} -\left(\dfrac{4\pi}{a_0}\right)^2 \dfrac{r^5}{2880\pi} + \mathcal{O}(r^6) & \text{(3D)} \\[4mm] -\left(\dfrac{2\pi}{a_0}\right)^2 \dfrac{r^4}{128\pi}\left(-\dfrac{3}{2} + \log\dfrac{e^{\gamma_E}r}{2}\right) + \mathcal{O}(r^5) & \text{(2D)} \end{cases}. \tag{B8}$$

### c.  *Green's function OPE*

In addition to the derivation outlined in the previous section, the high-momentum tail of the structure factor can also be obtained from a short-time and -distance OPE of the time-ordered density Green's function

$$iG_n(\omega, \mathbf{q}) = \int dt \int d^d x \, e^{i\omega t - i\mathbf{q}\cdot\mathbf{x}} \langle Tn(t, \mathbf{x})n(0, \mathbf{0})\rangle. \tag{B9}$$

For $\mathbf{q} \neq 0$, it is related to the structure factor by

$$S(\mathbf{q}) - 1 = \frac{1}{n}\lim_{t \to 0-}\int \frac{d\omega}{2\pi} e^{-i\omega t} iG_n(\omega, \mathbf{q}). \tag{B10}$$

The integral is evaluated by closing the contour in a large semicircle in the lower half of the complex $\omega$-plane. Only Wilson coefficients with poles in both half-planes contribute to the high-momentum tail. In the limit of negligible external scales, diagrams have vanishing residue if they can be traversed from one operator insertion to the

other by following the fermion lines. The Wilson coefficient of the operator $\mathcal{O}_c$ are read off directly from the diagrams in Figs. 4(a) and 4(b):

$$W_{\mathcal{O}_c}(\omega, \mathbf{q})$$
$$= \begin{cases} \dfrac{8\pi e^2}{q^2} \dfrac{1}{(\omega - \varepsilon_{\mathbf{q}} + i0)(-\omega - \varepsilon_{\mathbf{q}} + i0)} & \text{(3D)} \\[2ex] \dfrac{4\pi e^2}{q^2} \dfrac{1}{(\omega - \varepsilon_{\mathbf{q}} + i0)(-\omega - \varepsilon_{\mathbf{q}} + i0)} & \text{(2D)} \end{cases}, \quad \text{(B11)}$$

where $\varepsilon_{\mathbf{q}} = q^2/2m$, and the external lines couple to the contact $g_{\uparrow\downarrow}(0)$. Performing the contour integration reproduces the result (26).

We can apply a similar argument to determine the high-momentum tail of the momentum distribution, which is related to the single-particle Green's function $iG_{\sigma}(t, \mathbf{x}) = \langle T\psi_{\sigma}(t, \mathbf{x})\psi_{\sigma}^{\dagger}(0, \mathbf{0})\rangle$ by[3]

$$n_{\sigma}(\mathbf{q}) = -\lim_{t \to 0-} \int \frac{d\omega}{2\pi} e^{-i\omega t} iG_{\sigma}(\mathbf{q}, \omega). \quad \text{(B12)}$$

This relation was used to derive the momentum distribution of a Fermi gas with short-range interactions[54]. The first nonzero contribution is given by the contact operator, which has the Wilson coefficient (cf. Fig. 4(c))

$$W_{\mathcal{O}_c}(\omega, \mathbf{q})$$
$$= \begin{cases} \left(\dfrac{4\pi e^2}{q^2}\right)^2 \dfrac{-1}{(\omega - \varepsilon_{\mathbf{q}} + i0)^2(-\omega - \varepsilon_{\mathbf{q}} + i0)} & \text{(3D)} \\[2ex] \left(\dfrac{2\pi e^2}{q}\right)^2 \dfrac{-1}{(\omega - \varepsilon_{\mathbf{q}} + i0)^2(-\omega - \varepsilon_{\mathbf{q}} + i0)} & \text{(2D)} \end{cases}.$$
$$\text{(B13)}$$

Calculating the residue in Eq. (B12) yields the previous result (32).

* j.b.hofmann@damtp.cam.ac.uk
† marcus.barth@ph.tum.de
1 E. H. Lieb and R. Seiringer, *Stability of Matter in Quantum Mechanics* (Cambridge University Press, Cambridge, 2010).
2 D. Pines and P. Nozières, *The Theory of Quantum Liquids, Vol. I Normal Fermi Liquids* (W. A. Benjamin, Inc., New York, 1966).
3 A. L. Fetter and J. D. Walecka, *Quantum Theory of Many-Particle Systems* (Dover Publications, Mineola, 2003).
4 G. F. Giuliani and G. Vignale, *Quantum Theory of the Electron Liquid*, (Cambridge University Press, Cambridge, 2005).
5 This neglects the possibility of a pairing instability in a purely repulsive gas of fermions via the Kohn-Luttinger effect[6].
6 W. Kohn and J. M. Luttinger, Phys. Rev. Lett. **15**, 524 (1965).
7 N. W. Ashcroft and N. D. Mermin, *Solid State Physics* (Brooks/Cole, Belmont, 1976).
8 R. Jamei, S. Kivelson and B. Spivak, Phys. Rev. Lett. **94**, 056805 (2005).
9 S. Chakravarty, S. Kivelson, C. Nayak and K. Voelker, Phil. Mag. B **79**, 859 (1999).
10 B. Bernu, L. Cândido and D. M. Ceperley, Phys. Rev. Lett. **86**, 870 (2001).
11 M. Katano and D. S. Hirashima, Phys. Rev. B **62**, 2573 (2000).
12 S. Tan, Annals of Physics **323**, 2952 (2008); *ibid.* **323**, 2971 (2008); *ibid.* **323**, 2987 (2008).
13 E. Braaten in *The BCS-BEC Crossover and the Unitary Fermi Gas*, edited by W. Zwerger (Springer-Verlag, Berlin, 2012).
14 Y. Castin and F. Werner in *The BCS-BEC Crossover and the Unitary Fermi Gas*, edited by W. Zwerger (Springer-Verlag, Berlin, 2012).
15 J. C. Kimball, Phys. Rev. A **7**, 1648 (1973).
16 J. C. Kimball, J. Phys. A: Math. Gen. **8**, 1513 (1975).

17 A. K. Rajagopal and J.C. Kimball, Phys. Rev. B **15**, 2819 (1977).
18 More precisely, the exact relations from Secs. III and IV are recovered for the hydrogen atom if we replace $1/a_0 \to -2/a_0$ in Eqs. (22) and (26). This replacement takes into account the change of the reduced mass from $m$ to $m/2$ as well as the change of the sign of the interaction.
19 K. Gottfried, *Quantum Mechanics, Volume I: Fundamentals* (W. A. Benjamin, Inc., New York, 1966).
20 B. Podolsky and L. Pauling, Phys. Rev. **34**, 109 (1929).
21 K. G. Wilson and W. Zimmermann, Commun. Math. Phys. **24**, 87 (1972).
22 G. Mack, Commun. Math. Phys. **53**, 155 (1977).
23 D. Pappadopulo, S. Rychkov, J. Espin and R. Rattazzi, Phys. Rev. D **86**, 105043 (2012).
24 M. Hoffmann-Ostenhof, T. Hoffmann-Ostenhof and H. Stremnitzer, Phys. Rev. Lett. **68**, 3857 (1992).
25 E. Braaten and L. Platter, Phys. Rev. Lett. **100**, 205301 (2008).
26 S. Zhang and A. J. Leggett, Phys. Rev. A **79**, 023601 (2009).
27 F. Werner and Y. Castin, Phys. Rev. A **86**, 013626 (2012).
28 Since the Coulomb potential is long-ranged, the matrix elements reproduce the quantum mechanical result only up to a divergent but $r$-independent phase factor, cf. Refs.[29,30]. This does not affect the argument in Sec. III.
29 J. Schwinger, J. of Math. Phys. **5**, 1606 (1964).
30 B. R. Holstein, Am. J. Phys. **63**, 710 (1994).
31 G. P. Lepage, arXiv:9706029.
32 S. K. Bogner and D. Roscher, Phys. Rev. C **86**, 064304 (2012).
33 A. K. Rajagopal, J. C. Kimball, and M. Banerjee, Phys. Rev. B **18**, 2339 (1978).
34 M. Barth and W. Zwerger, Annals of Physics **326**, 2544 (2011).
35 P. Gori-Giorgi and P. Ziesche, Phys. Rev. B **66**, 235116 (2002).
36 J. C. Kimball, Phys. Rev. B 14, 2371 (1976).

[37] N. D. Drummond and R. J. Needs, Phys. Rev. B **79**, 085414 (2009).

[38] M. Holzmann, B. Bernu, C. Pierleoni, J. McMinis, D. M. Ceperley, V. Olevano, and L. DelleSite, Phys. Rev. Lett. **107**, 110402 (2011).

[39] G. Niklasson, Phys. Rev. B **10**, 3052 (1974).

[40] K. S. Singwi, M. P. Tosi, R. H. Land and A. Sjölander, Phys. Rev. **176**, 589 (1968).

[41] K. S. Singwi and M. P. Tosi, in Solid State Physics **36**, 177 (1981).

[42] P. Gori-Giorgi, F. Sacchetti and G. B. Bachelet, Phys. Rev. B **61**, 7353 (2000).

[43] C. Attaccalite, S. Moroni, P. Gori-Giorgi and G. B. Bachelet, Phys. Rev. Lett. **88**, 256601 (2002).

[44] P. Gori-Giorgi and A. Savin, Phys. Rev. A **73**, 032506 (2006).

[45] Note that due to the long-range nature of the Coulomb interaction the corrections to this leading order result are non-analytic in the density. For the calculation of the contact at high temperatures or in the classical limit $\hbar \to 0$, however, these corrections are irrelevant.

[46] H. K. Schweng, H. M. Böhm, A. Schinner, and W. Macke, Phys. Rev. B **44**, 13291 (1991).

[47] A. V. Ivlev, H. Löwen, G. E. Morfill, C. P. Royall, *Complex plasmas and colloidal dispersions: particle-resolved studies of classical liquids and solids* World Scientific, (2012).

[48] K.-F. Berggren, Phys. Rev. A **1**, 1783 (1969).

[49] A. A. Vedenov and A. I. Larkin, Zh. Eksp. Teor. Fiz. **36**, 1133 (1959) [Sov. Phys. JETP, **36**, 806 (1959)].

[50] P. F. Bedaque and G. Rupak, Phys. Rev. B **67**, 174513 (2003).

[51] G. Rupak, Phys. Rev. Lett. **98**, 090403 (2007).

[52] D. B. Kaplan and S. Sun, Phys. Rev. Lett. **107**, 030601 (2011).

[53] X. Leyronas, Phys. Rev. A **84**, 053633 (2011).

[54] D. T. Son and E. G. Thompson, Phys. Rev. A **81**, 063634 (2010).

[55] J. Hofmann, Phys. Rev. A **84**, 043603 (2011).

[56] Y. Nishida, Phys Rev. A **85**, 053643 (2012).

[57] C. Sternemann *et al.*, Phys. Rev. Lett. **95**, 157401 (2005).

[58] A. J. Glick and W. F. Long, Phys. Rev. B **4**, 3455 (1971).

[59] Y. Pavlyukh, A. Rubio and J. Berakdar, arXiv:1212.3486.

[60] A. Griesmaier, J. Werner, S. Hensler, J. Stuhler, and T. Pfau, Phys. Rev. Lett. **94**, 160401 (2005).

[61] K. Aikawa *et al.*, Phys. Rev. Lett. **108**, 210401 (2012).

[62] M. Lu, N. Q. Burdick, and B. L. Lev, Phys. Rev. Lett. **108**, 215301 (2012).

[63] W. Dittrich, Am. J. Phys. **67**, 768 (1999).

[64] J. C. Y. Chen and A. C. Chen, Advances in Atomic and Molecular Physics **8**, 71 (1972).

# Pairing effects in the nondegenerate limit of the two-dimensional Fermi gas

Marcus Barth[1, *] and Johannes Hofmann[2, †]

[1]*Physik Department, Technische Universität München, James-Franck-Strasse, 85748 Garching, Germany*
[2]*Condensed Matter Theory Center, Department of Physics,*
*University of Maryland, College Park, Maryland 20742-4111 USA*
(Dated: January 23, 2014)

The spectral function of a spin-balanced two-dimensional Fermi gas with short-range interactions is calculated by means of a quantum cluster expansion. Good qualitative agreement is found with a recent experiment by Feld *et al.* [Nature (London) **480**, 75 (2011)]. The effects of pairing are clearly visible in the density of states, which displays a suppression of spectral weight due to the formation of a two-body bound state. In addition, the momentum distribution and the radio-frequency spectrum are derived, which are in excellent agreement with exact universal results. It is demonstrated that in the limit of high temperature, the quasiparticle excitations are well defined, allowing for a kinetic description of the gas.

## I. INTRODUCTION

Feshbach resonances in ultracold atoms provide us with the possibility of tuning the strength of the interparticle interaction at will, allowing us to probe vastly different types of physics. For a Fermi gas at low temperature, this ranges from a BCS-type superfluid at small attractive interaction to a Bose-Einstein condensate (BEC) of tightly bound dimers as the interaction strength is increased. This BEC-BCS crossover has been the subject of intense research over the past decade [1]. An interesting question is whether pairing affects the properties of a Fermi gas above the superfluid transition temperature as well. In contrast to standard BCS theory, which predicts pairing and condensation to appear simultaneously, it has been conjectured that pairing occurs at a temperature larger than the superfluid transition temperature, and that the remnant of a pairing gap remains in the normal phase. This regime is known as the pseudogap phase. It is expected that in the pseudogap phase, the single-particle excitation spectrum assumes a BCS-type dispersion relation $\omega(\mathbf{q}) = \sqrt{(\varepsilon_{\mathbf{q}} - \mu)^2 + \Delta^2}$, where $\varepsilon_{\mathbf{q}} = q^2/2m$, $\mu$ is the chemical potential, and $\Delta$ is a superfluid order parameter, which predicts a "back-bending" of the dispersion relation around the Fermi momentum. For a three-dimensional unitary Fermi gas, the single-particle excitation spectrum has been probed using momentum-resolved radio-frequency spectroscopy [2], and evidence of pseudogap behavior has been reported [3]. Various theoretical works indicate the existence of a pseudogap [4, 5], while some others do no observe this [6]. Generally, fluctuations are more relevant in two-dimensional (2D) systems, suggesting that pseudogap effects are more pronounced in 2D. Indeed, Feld *et al.* recently reported the observation of a pairing pseudogap in a two-dimensional Fermi gas [7].

* marcus.barth@ph.tum.de
† hofmann@umd.edu

Experimentally, quasi two-dimensional Fermi gases are created by trapping the system in a strongly oblate trapping geometry. For a harmonic trapping potential, the strength of the confinement is set by the ratio of the harmonic oscillator length in the confining direction, $l_z = \sqrt{1/m\omega_z}$, and the 2D scattering length $a_2$, which is related to the 3D scattering length via the transcendental equation $l_z/a_3 = f_1(l_z^2/a_2^2)$. The function $f_1$ is for example given in Sec. V of Ref. [8]. In this paper, we set $\hbar = k_B = 1$. In the limit of strong confinement in which $l_z$ is much smaller compared to $a_2$, the perpendicular degree of freedom decouples from the dynamics, rendering the system effectively two-dimensional. Note that in contrast to the 3D case, $a_2$ is always positive and there exists a two-body bound state with binding energy $E_b = 1/ma_2^2$ for all scattering lengths. In recent years, it has become possible to prepare and probe Fermi gases in the strictly two-dimensional regime [9, 10], and we restrict our attention to this purely 2D case.

Momentum-resolved rf spectroscopy induces a transition from an initial occupied spin state to an unoccupied state of same momentum, followed by a time-of-flight measurement to extract the momentum distribution of the out-coupled atoms. This transition rate is directly related to the spectral function, which encodes the single-particle excitation spectrum. While the spectral function is fundamental to the description of many-body systems, it is usually a very challenging and complex task to calculate this quantity theoretically. Quite generally, the analysis of strongly interacting Fermi gases is complicated by the lack of a small parameter which could be used in a perturbative expansion, and in many cases, one has to resort to complex numerical calculations to obtain quantitatively reliable results. The experiment [7] has thus far been analyzed using different resummation schemes for the spectral function [11–13]. In this paper, we apply a quantum cluster expansion to the spectral function, which provides a systematic expansion about the nondegenerate or high-temperature limit. This virial expansion has already been successfully applied to ex-

tract thermodynamic properties of the two-dimensional gas in a trap [14] as well as the spectral function in the three-dimensional gas [15]. We find that even the leading order provides a qualitative description of the measured data [7]. We discuss the properties of the spectral function in detail, focusing in particular on the density of states and the implications of an incoherent spectral weight found at negative frequencies.

This paper is structured as follows: In Sec. II, we start by discussing the phenomenology of the spectral function and its characteristic behavior throughout the BCS-BEC crossover. Section III introduces the virial expansion. It is established that the virial expansion should be quantitatively reliable up to temperatures as low as the Fermi temperature, and we outline how the spectral function is calculated within the virial expansion. Section IV presents the results of this calculation. While the onset of a gap is clearly visible in the density of states, we argue that the observed backbending of the lower branch is not a feature of the spectral function, but a consequence of the asymmetric structure of the bound state branch and the thermal occupation of states. The density of states is presented in Sec. IV A. Section IV B extracts the momentum distsribution and the rf transition rate from the spectral functions. Our results reproduce known universal results valid in the high-momentum and high-frequency limits, respectively, which are linked to the incoherent weight of the spectral function at large and negative frequency. Furthermore, in Sec. IV C, we compute the quasiparticle properties. The paper is concluded by a summary in Sec. V.

## II.  THE SPECTRAL FUNCTION

We begin by discussing the properties of the spectral function, which contains information about the single-particle spectrum. The spectral function is defined as the imaginary part of the retarded single-particle Green's function:

$$A(\omega, \mathbf{q}) = -2 \operatorname{Im} G(\omega, \mathbf{q}). \tag{1}$$

It describes the probability density of creating either a particle or a hole excitation with momentum $\mathbf{q}$ and energy $\omega$. For a noninteracting gas with dispersion $\omega(\mathbf{q})$, the spectral function is a $\delta$-function centered at $\omega(\mathbf{q})$. In the presence of interactions, the peak acquires a finite width, which is proportional to the inverse lifetime of the excitation. As an example, consider the Fermi gas at low temperature and large scattering length, i.e., in the BCS regime. The spectral function takes the form

$$A(\omega, \mathbf{q}) = 2\pi v_{\mathbf{q}}^2 \delta(\omega + \sqrt{(\varepsilon_{\mathbf{q}} - \mu)^2 + \Delta^2})$$
$$+ 2\pi u_{\mathbf{q}}^2 \delta(\omega - \sqrt{(\varepsilon_{\mathbf{q}} - \mu)^2 + \Delta^2}). \tag{2}$$

Here, $v_{\mathbf{q}}$ and $u_{\mathbf{q}}$ are the Bogoliubov parameters, and the chemical potential is positive $\mu = k_F^2/2m > 0$, whereby
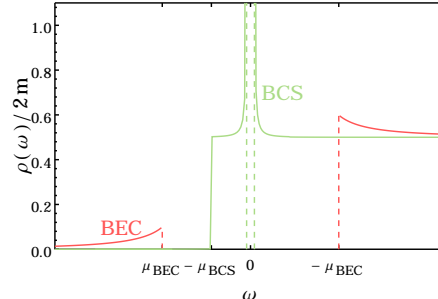


FIG. 1. (Color online) Sketch of the density of states at zero temperature in the BCS and the BEC limits.

the Fermi momentum $k_F$ is related to the density $n$ via $k_F = \sqrt{2\pi n}$. For any fixed momentum, it is not possible to create an excitation in the energy range between $\pm\Delta$: the single-particle spectrum is gapped. Note that the hole-part of the spectral function, which starts at $\omega = -\sqrt{\mu^2 + \Delta^2}$, bends back at $q = k_F$ towards negative frequency at large momentum. Interactions are expected to renormalize the scale at which the backbending occurs to some $k_0 \neq k_F$.

As the strength of the interaction is increased, there is a crossover from the BCS to the BEC regime, in which the quasiparticles are not Cooper pairs but two-particle bound states. In this limit, the spectral function is

$$A(\omega, \mathbf{q}) = 2\pi Z_{\mathbf{q}} \delta(\omega + \varepsilon_{\mathbf{q}} - \mu)$$
$$+ 2\pi(1 - Z_{\mathbf{q}}) \delta(\omega - \varepsilon_{\mathbf{q}} + \mu), \tag{3}$$

where the chemical potential is half the bound-state energy, $\mu = -E_b/2$, and the residue is $Z_{\mathbf{q}} = |\varphi(q)|^2 n$, with $|\varphi(q)|^2 = 4\pi a_2^2/(1 + q^2 a_2^2)^2$ being the square of the bound-state wave function in momentum space. Note that there is no backbending at finite momentum in the dispersion relation, but the spectral function still possesses a gap of size $E_b$ [16].

The pairing gap is also manifested in the density of states. The density of states counts the excitations with energy $\omega$, and is obtained by integrating the spectral function over momentum:

$$\rho(\omega) = \int \frac{d^2 q}{(2\pi)^2} A(\omega, \mathbf{q}). \tag{4}$$

In BCS theory below the superfluid transition temperature, this density of states exhibits a gap of width $2\Delta$ around the Fermi energy, while in the BEC limit the gap size is given by the binding energy $E_b$ of the two-body bound state. The density of states at zero temperature for both limits is sketched in Fig. 1. As the temperature increases beyond the critical temperature, mean-field theory predicts the gap to vanish.

Pairing is possible even above the critical temperature, which can affect the properties of the normal phase. In

the high-temperature limit, the quasiparticle excitations are well defined and the fermions are unpaired. Below a certain temperature $T^*$, most fermions are bound in pairs, giving rise to significant deviations from a simple quasiparticle picture. On the BCS side of the crossover, this regime is known as the pseudogap phase. The hallmark of the pseudogap phase is a depletion of spectral weight in the density of states around the Fermi surface at $\omega = \mu$. The pseudogap grows as the temperature is lowered and eventually forms a full gap below $T_c$. Often, a backbending of the dispersion relation akin to that in the BCS model is taken as a phenomenological sign of a pseudogap phase. This, however, has to be treated with caution, since the backbending at large momentum is a generic feature of an interacting Fermi gas, as pointed out by Schneider and Randeria [17]. On the BEC side, one also may find a depletion of spectral weight, which in this case is associated with the formation of a two-body bound state and occurs at $\omega = -\mu$. While the pseudogap is considered to be a many-body effect, the depletion on the BEC side can be understood already from a two-body calculation, as will also be shown in Sec. IV A.

In the BEC limit, the density of fermions $n_f$ and of fermions bound in dimers $n_d$ can be estimated using a thermodynamic argument assuming a noninteracting gas of fermions and dimers [18, 19]. It is given by the so-called Saha formula

$$\frac{n_f^2}{n_d} = \frac{mT}{4\pi}\, e^{-E_b/T}, \qquad (5)$$

where the total density of particles $n = 2n_f + 2n_d$ is kept fixed. We can define a temperature $T^*$ at which there is an equal number of dimers and unpaired fermions in the normal phase of the gas. This temperature is

$$\frac{T^*}{T_F} = \frac{E_b/E_F}{W(E_b/E_F)}, \qquad (6)$$

where $T_F = k_F^2/2m$ denotes the Fermi temperature and $W$ is the Lambert-$W$ function. Below this temperature, fermions are predominantly paired and we expect pronounced pairing effects on the properties of the gas.

Experimentally, the single-particle excitations of cold atomic gases have been measured using momentum-resolved radio-frequency spectroscopy, which is analogous to angle-resolved photoelectron spectroscopy in condensed matter physics [2, 3, 7]. The experiment detects the hole excitations, i.e., the rate of transition from occupied to unoccupied states. According to Fermi's golden rule, the transition rate is proportional to

$$A_-(\omega, \mathbf{q}) = 2\pi \sum_{n,m} e^{-\beta E_m}\, |\langle n|c_{\mathbf{q}}|m\rangle|^2\, \delta(\omega - E_n + E_m). \qquad (7)$$

This quantity is known as the *occupied spectral function*. Here, the annihilation operator $c_{\mathbf{q}}$ destroys a particle with momentum $\mathbf{q}$. The full spectral function also includes processes that probe the transition from an unoccupied state to an occupied state if one particle is added
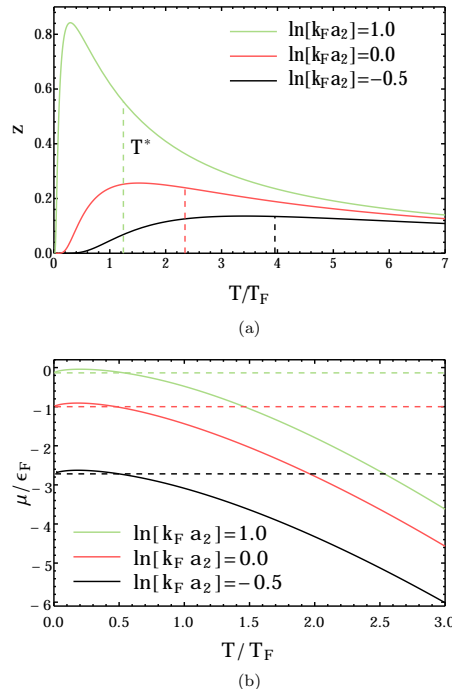


FIG. 2. (Color online) (a) Fugacity as a function of temperature for fixed density. The dashed lines indicate the Saha estimate for $T^*$, Eq. (6). (b) Chemical potential as a function of temperature. Dashed lines correspond to half the bound-state energy $-E_b/2E_F$.

to the system. The occupied spectral function is related to the full spectral function by a Fermi-Dirac distribution $f(\omega) = 1/(\exp \beta\omega + 1)$:

$$A_-(\omega, \mathbf{q}) = f(\omega) A(\omega, \mathbf{q}). \qquad (8)$$

In the following, we use a quantum cluster expansion to calculate the spectral function in the nondegenerate limit.

## III. THE VIRIAL EXPANSION

The virial expansion provides a systematic method for analyzing a Fermi gas at high temperature. The virial expansion is applied to a nondegenerate gas for which the thermal energy $E_T = T$ outweighs its kinetic energy $E_K = \pi n/m$: $E_T \gg E_K$. Equivalently, this corresponds to the limit in which the thermal deBroglie wavelength $\lambda_T = \sqrt{2\pi/mT}$ is small compared to the interparticle spacing $n^{-1/2}$: $\lambda_T \ll n^{-1/2}$. In this limit, the grand
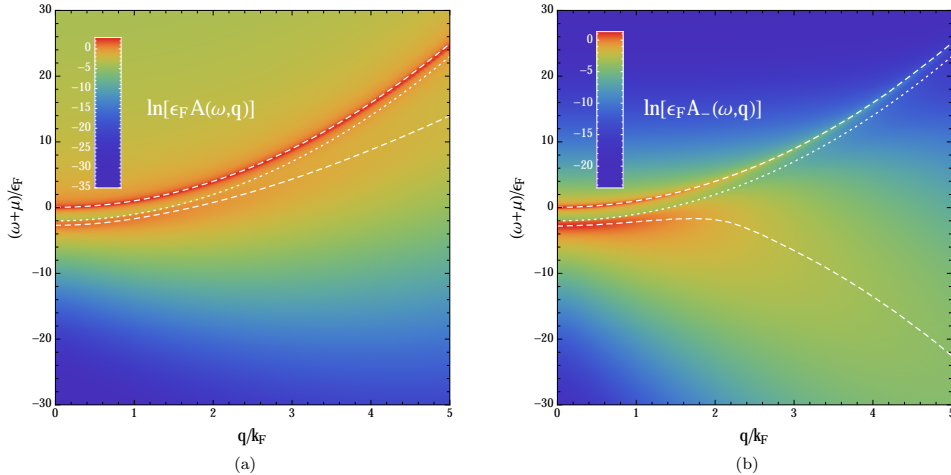
FIG. 3. (Color online) (a) Spectral function at $T = T_F$ and $\ln k_F a_2 = 0.0$. (b) Occupied spectral function for the same parameters. The white dashed lines in both figures mark the maxima of the quasiparticle and the lower branch. The white dotted line corresponds to the threshold dispersion $\omega_{\text{th}}(\mathbf{q}) + \mu = -E_b + \varepsilon_{\mathbf{q}}$.

canonical partition function

$$\mathcal{Z} = \text{tr} e^{-\beta(H-\mu N)} = \sum_{N=1}^{\infty} z^N \text{tr}_N e^{-\beta H} \qquad (9)$$

can be expanded in terms of the fugacity $z = e^{\beta\mu} \ll 1$. The traces $\text{tr}_N$ on the right-hand side of Eq. (9) are restricted to the $N$-particle Fock spaces. Thus, the coefficients of the expansion are determined by clusters that involve one-, two-, and three-body processes, and so on. In this sense, the virial expansion bridges the gap between known few-particle results and the behavior of a complicated many-body system. In particular, the expansion is valid even in a strongly interacting regime. The number density can be obtained directly from Eq. (9):

$$n = \frac{2}{\lambda_T^2} \left( b_1 z + 2 b_2 z^2 + \cdots \right), \qquad (10)$$

where $b_1$ and $b_2$ are known as the virial coefficients. The prefactor of 2 counts the two spin species.

For a noninteracting gas, a direct calculation of the virial coefficients gives $b_n^{(0)} = (-1)^{n-1}/n^2$. Interactions enter only in second and higher orders. The correction to the second order is given by the well-known Beth-Uhlenbeck term [20]

$$\Delta b_2 = b_2 - b_2^{(0)} = \frac{1}{\pi} \int_0^{\infty} dk \frac{\partial \delta(k)}{\partial k} e^{-\beta k^2/m} + e^{\beta E_b}, \qquad (11)$$

where the scattering phase shift is $\cot \delta(k) = (2/\pi) \ln a_2 k$. The interaction correction (11) consists of

a bound state contribution and a contribution due to scattering states. The attractive interaction between the particles increases the virial coefficients compared to the noninteracting case and thus tends to increase the density at a given chemical potential. In Fig. 2(a), we show the fugacity as a function of $T/T_F$ as determined from Eq. (10). The curves for different coupling strengths have a maximum and then tend to zero with decreasing temperature. For comparison, we also include the Saha estimate for $T^*$ as a dashed line in Fig. 2(a). The virial expansion appears to be valid even in a temperature range below $T^*$. This suggests that the leading-order term is sufficient to quantify pairing effects on the Fermi gas.

In Fig. 2(b), we show the chemical potential for the same coupling strengths as in Fig. 2(a). For all three of them, the chemical potential exceeds the dimer chemical potential $-E_b/2$ at roughly $T/T_F = 0.5$. Since the second-order calculation includes only two-body effects, it should be energetically cheaper for the particles to just form a dimer bound state. This inconsistency provides a clear lower bound $T/T_F = 0.5$ on the extrapolation of the second order results to low temperatures. We regard the virial expansion to be valid down to a temperature of $T_F$, consistent with the findings of other applications of the virial expansion to Fermi gases [14, 15]. We argue that the results of our virial expansion qualitatively describe the experiment of Ref. [7], which was carried out in a temperature range $T/T_F = 0.27$–$0.65$ for scattering lengths in the range between $\ln k_F a_2 = -2$ and 1. For these interaction strengths, the chemical potential is negative and there exists no Fermi surface [21]. The single-particle spectrum should be dominated by the

dimer pairing, which is precisely what is captured by the virial expansion.

The starting point of our calculation is the virial expansion of the self-energy, i.e., the one-particle irreducible contribution to the single-particle Green's function. It is related to the Green's function by a Dyson equation [22],

$$G(\omega, \mathbf{q}) = \frac{1}{\omega + \mu - \varepsilon_{\mathbf{q}} - \Sigma(\omega, \mathbf{q})}. \qquad (12)$$

To linear order in $z$, the self-energy is given by a Boltzmann-weighted integral of the $T$-matrix element (similar to the bosonic case [23]):

$$\Sigma^{(1)}(i\omega_n, \mathbf{q}) = z \int \frac{d^2k}{(2\pi)^2} e^{-\beta \varepsilon_{\mathbf{P}}} T_2(i\omega_n + \mu + \varepsilon_{\mathbf{k}}, \mathbf{k} + \mathbf{q}), \qquad (13)$$

where $\omega_n = (2n+1)\pi T$ are fermionic Matsubara frequencies. Equation (13) describes the self-energy correction due to scattering with a single thermally excited particle-hole pair. In the Appendix, we provide a short derivation of this result. To obtain the retarded self-energy, we analytically continue Eq. (13) to real frequencies $i\omega_n \rightarrow \omega + i0$, replacing the $T$-matrix element in Matsubara representation by its real frequency counterpart

$$T_2(\omega, \mathbf{q}) = -\frac{2\pi}{m} \frac{1}{\ln a_2 \sqrt{-m(\omega - \varepsilon_{\mathbf{q}}/2) - i0}}. \qquad (14)$$

The remaining momentum integration in Eq. (13) is performed numerically. We emphasize that the analytic continuation is performed analytically and the numerical calculation determines the self-energy at real frequency. The imaginary part of Eq. (13) is computed directly using `Mathematica`. The real part is then obtained by a numerical Kramers-Kronig transformation.

## IV. RESULTS FOR THE SPECTRAL FUNCTION

In this section, we present results for the spectral function calculated to leading order in the virial expansion. Figure 3(a) shows the spectral function for a balanced Fermi gas at $T = T_F$ and $\ln k_F a_2 = 0$. The spectral function exhibits a double-peak structure with two clearly distinguishable branches. The upper one, which we shall refer to as the quasiparticle branch, starts around zero frequency. The lower branch is associated with the existence of a bound state and starts at a threshold frequency $\omega_{\text{th}} + \mu = -E_b$. The weight of both branches is shifted upwards with increasing momentum and displays a quadratic momentum dependence. The bound-state branch is strongly asymmetric: it quickly reaches its maximum below $\omega_{\text{th}}$, but falls off slowly with decreasing frequency. This behavior is illustrated in Fig. 4, which shows the spectral function at fixed momentum $\mathbf{q} = 0$
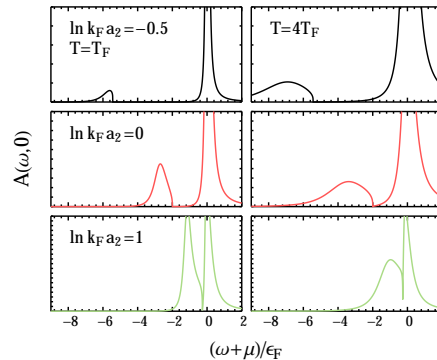


FIG. 4. (Color online) Spectral function $A(\omega, 0)$ at fixed momentum $q = 0$ and scattering lengths (rows) $\ln k_F a_2 = -0.5, 0$, and 1. The first column is at $T = T_F$, the second at $T = 4T_F$.

as a function of temperature and scattering length. We see that the bound-state branch and the quasiparticle branch begin to merge as the scattering length is increased. With increasing temperature, the quasiparticle peak gets sharper and the effects of pairing become less relevant, a statement that will be made more precise in the following sections.

The asymmetric line shape of the lower branch drastically changes the form of the *occupied* part of the spectral function, which is the one measured experimentally. It is shown in Fig. 3(b). The maximum of the lower branch increases quadratically at small momentum, but turns downwards at higher momentum. For small temperatures, the branch reaches its maximum at a momentum as low as the Fermi momentum. We emphasize that this is an effect of the thermal occupation of states and cannot be taken as a sign of a pseudogap. It is rather a generic feature of the occupied spectral function that is intrinsically linked to the enhanced short-range correlations in the system [17]. The spectral weight at large momentum is the origin of high-momentum and high-frequency tails in the momentum distribution and the rf transition, respectively, two quantities that can be readily obtained from the spectral function. We examine the aforementioned properties closely in Sec. IV B. We conclude by studying the properties of the quasiparticle branch in Sec. IV C: we determine the quasiparticle dispersion as well as its effective mass and lifetime and compare them with exact results.

### A. Density of states

Pairing effects are apparent in the density of states. Figure 5 shows the density of states for different scattering lengths and temperatures. At low temperature,
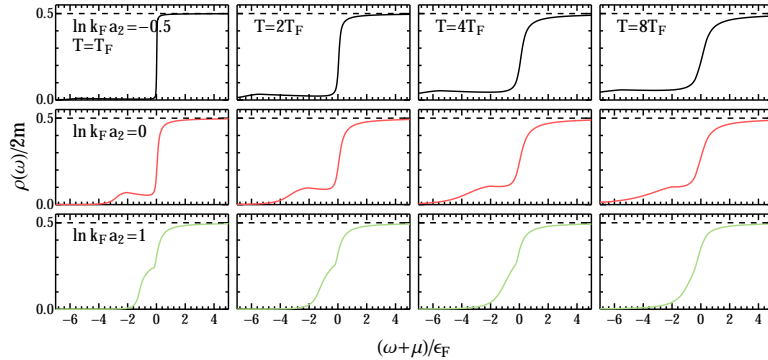
FIG. 5. (Color online) Densities of states at temperatures (columns) $T/T_F = 1, 2, 4$, and 8 for scattering lengths (rows) $\ln k_F a_2 = -0.5, 0$, and 1.0. The pairing gap is more pronounced as the scattering length decreases.

a depletion of spectral weight around $\omega = -\mu$ is clearly visible, indicating that this effect is associated with the formation of a molecular bound state. This effect increases as the scattering length is lowered towards the BEC side of the crossover. For positive frequency, the density of states is very close to that of a free Fermi gas, which in 2D is simply given by

$$\rho(\omega) = m\,\Theta(\omega + \mu). \qquad (15)$$

For comparison, we also show the temperature evolution of the density of states in Fig. 5. The dip in the spectral weight increases with decreasing temperature and resembles the density of states in the superfluid BEC regime shown in Fig. 1. The transition occurs at a temperature scale $T^*$ that is in good agreement with our estimate (6); see Fig. 2(a). The two-body calculation does not show, however, the typical depletion for a pseudogap around $\omega = \mu$.

## B. Negative-frequency weight and universal relations

We noted at the beginning of this section that the back-bending of the lower branch in the occupied spectral function is by itself not a sufficient sign of the pseudogap. It is rather a universal property of fermions with short-range interactions that exists independently of the phase or indeed temperature, and, in particular, it holds for any $N$-particle ensemble. At large momentum, the negative-energy weight gives the dominant contribution to the momentum distribution

$$n_\sigma(q) = \int \frac{d\omega}{2\pi}\, A_-(\omega, \mathbf{q}), \qquad (16)$$

resulting in a high-momentum tail $n_\sigma(q) \to \mathcal{C}/q^4$, where $\mathcal{C}$ is the so-called contact density [24], which is a measure

for the number of fermion pairs with opposite spins at short distances [25, 26]. The contact density is related to the derivative of the grand canonical potential through the adiabatic relation [25, 27]

$$\mathcal{C} = 2\pi m a_2 \frac{\partial \Omega/V}{\partial a_2}\bigg|_{T,\mu} = -2z^2 m^2 T^2 a_2 \frac{\partial b_2}{\partial a_2}\bigg|_T + O(z^3). \qquad (17)$$

To leading order in $z$, the contact density can be determined from the second virial coefficient $b_2$ given in Eq. (11). The universal high-momentum tail for the momentum distribution is indeed obeyed by the virial expansion: in Fig. 6(a), the asymptotic behavior of the momentum distribution for different coupling strengths is shown. The high-momentum tail is clearly visible and fits well with the contact determined from the adiabatic theorem (17). Quite generally, the scale at which the relation for the high-momentum tail holds is set by $q \gg \max(1/\lambda_T, 1/a_2, 1/k_F)$, which explains that the green curve for $\ln k_F a_2 = -0.5$ in Fig. 6(a) saturates much later than for the two larger values of $a_2$. In Fig. 6(b), we report the contact density to second order as obtained from the adiabatic relation (17). The dashed line denotes the bound state contribution

$$\mathcal{C}^{\text{bound}} = \frac{4\pi}{a_2^2}\, n_d, \qquad (18)$$

which dominates for most scattering lengths. The bound state contribution is a homogeneous function of the fermion density: $\mathcal{C}^{\text{bound}} \sim n^2$. Although small compared to the bound state part, the remaining interaction contribution violates this simple scaling behavior. This affects the oscillation frequency of collective modes at low temperature [28–30].

The spectral function also determines the total rf transition rate. Provided that the final state does not interact with the two other species and is initially not populated,
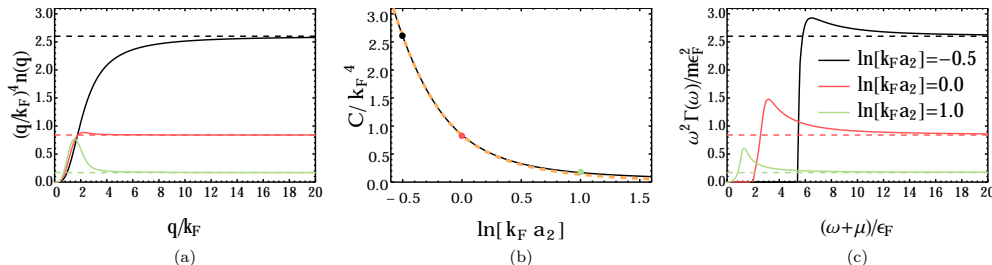
FIG. 6. (Color online) (a) Momentum distribution for $T = T_F$ and (top to bottom) $\ln k_F a_2 = -0.5$ (black), $\ln k_F a_2 = 0$ (red, gray) and $\ln k_F a_2 = 1$ (green, light gray) as obtained from the spectral function. To make the high-momentum tail visible, we multiplied the momentum distribution by $q^4$. Dashed lines are the values of the contact density as calculated from (17). (b) Contact density to leading order in the virial expansion at $T = T_F$. Points mark the values of the contact for the parameters used in figures (a) and (c). The dashed orange (gray) line is the contact for a gas of dimers. (c) rf spectra at the same parameter values. The spectra are multiplied by $\omega^2$ to extract the high-frequency tail. Dashed lines and parameters as in (a).

the transition rate is given by [6]

$$\Gamma(\omega) = \Omega^2 \int \frac{d^2 q}{(2\pi)^2} A_-(\varepsilon_{\mathbf{q}} - \omega - \mu, \mathbf{q}), \qquad (19)$$

which is just an integral over the occupied part of the spectral function evaluated at the free particle energies shifted by the transition frequency. In the following, we set the Rabi frequency $\Omega$ of the transition equal to 1, resulting in the normalization

$$\int \frac{d\omega}{2\pi} \Gamma(\omega) = \frac{n}{2}. \qquad (20)$$

At large frequency, the rf transition rate displays a universal tail [10, 31]

$$\Gamma(\omega) \to \frac{\mathcal{C}}{4m\omega^2}. \qquad (21)$$

It should be noted that final-state interactions introduce a logarithmic scaling violation $\sim 1/\omega^2 \ln^2 \omega$ [31]. From Eq. (19), we see that the high-frequency tail is a direct consequence of the incoherent negative weight at large momentum, just as for the momentum distribution. The asymptotic form is again very well reproduced by the virial expansion as can be seen from Fig. 6(c) which shows the asymptotic behavior of the transition rate at $T = T_F$. In Fig. 7, we report the corresponding rf spectra. The peak at $\omega = 0$ corresponds to transitions from the quasiparticle branch. The large incoherent weight starting at the binding energy $E_b$ corresponds to excitations that break up a dimer. For smaller binding energies (larger $\ln k_F a_2$), the bump of the dimer-free transition becomes sharper and begins to overlap with the free-free peak. This is to be expected, as for $E_b \to 0$, the spectrum needs to reproduce the one of free particles, which corresponds to a peak at $\omega = 0$. Due to thermal excitations, the peak has always a finite width.

It is indeed no coincidence that the universal relations are obeyed by the cluster expansion. As stressed at the beginning of this section, the exact relations hold for any contact interacting system of $N$ particles. A simple power counting in the fugacity shows that each order in the virial expansion will reproduce the asymptotic tail at the same order of the contact. The fact that our calculation reproduces the universal relations with high accuracy is not only a stringent test of our computation but also shows that the quantum cluster expansion captures the correct short-time and distance structure of the system.
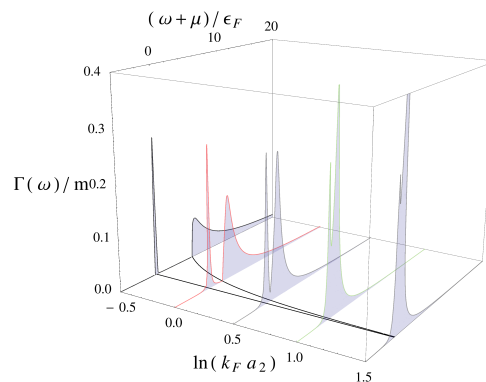


FIG. 7. (Color online) rf spectrum at $T = T_F$ for scattering lengths $\ln k_F a_2 = -0.5, 0.0, 0.5, 1.0,$ and 1.5. The peak at zero frequency is the transition from the quasiparticle branch. For energies larger than the bound-state energy (indicated by the black curve), there is an extended spectral weight due to bound-free transitions, which merges with the zero-frequency peak at large scattering length on the BCS side of the crossover.
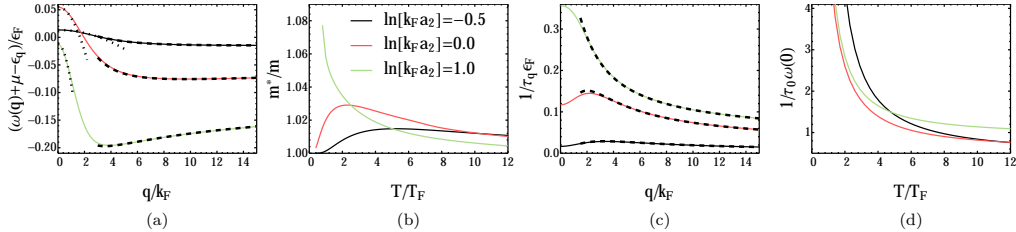
FIG. 8. (Color online) (a) Quasiparticle dispersion relation, (b) effective mass, and (c) inverse quasiparticle lifetime. The parameters are $T = T_F$ and $\ln k_F a_2 = -0.5$ (black), 0.0 (red, gray) and 1 (green, light gray). The dashed lines indicate the asymptotic forms (30) and (31). The dotted lines are the low-momentum limits of the dispersion relation with an effective mass (24). (d) Ratio of inverse quasiparticle lifetime and energy $1/\tau_0\omega(0)$ at zero momentum.

### C.   Quasiparticle branch

Let us now consider the quasiparticle branch. The spectral weight of this branch is centered around the quasiparticle energy $\omega(\mathbf{q})$, which is given by the pole in the Green's function [32]

$$\omega(\mathbf{q}) - \varepsilon_{\mathbf{q}} + \mu - \operatorname{Re}\Sigma(\omega(\mathbf{q}), \mathbf{q}) = 0. \qquad (22)$$

In Fig. 8(a), we plot the dispersion relation $\omega(\mathbf{q}) + \mu$ as a function of the momentum $q/k_F$ for $T = T_F$ and three different scattering lengths $\ln k_F a_2 = -0.5, 0$, and $1$. The dispersion relation starts at

$$\omega(\mathbf{0}) + \mu = \operatorname{Re}\Sigma(\omega, 0)|_{\omega=\omega(\mathbf{0})} \qquad (23)$$

and is quadratic at small momentum with an effective mass

$$\frac{m^*}{m} = \frac{1 - \dfrac{\partial \operatorname{Re}\Sigma}{\partial \omega}}{1 + \dfrac{\partial \operatorname{Re}\Sigma}{\partial \varepsilon_{\mathbf{q}}}}\Bigg|_{\omega=\omega(\mathbf{q}), q=0}. \qquad (24)$$

Figure 8(b) shows the effective mass as a function of temperature for various scattering lengths. Our calculation indicates a slightly enhanced effective mass $m^*/m = 1.05$. At high temperature, the effective mass approaches the mass of the free Fermi gas. A small effective mass is quite typical even for strongly interacting Fermi gases at low temperature [33]. In the zero-temperature limit, effective mass corrections in 2D are expected to get as large as $m^*/m \approx 1.5$ at $\ln k_F a_2 = 0$ for the so-called attractive polaron [34].

In the vicinity of $\omega(\mathbf{q})$, the spectral function assumes a Lorentzian shape:

$$A(\omega, \mathbf{q}) = \frac{2/\tau_{\mathbf{q}}}{(\omega - \varepsilon_{\mathbf{q}} + \mu - \operatorname{Re}\Sigma(\omega, \mathbf{q}))^2 + (1/\tau_{\mathbf{q}})^2}. \qquad (25)$$

The width of the Lorentzian, which is determined by the imaginary part of the self-energy, describes the rate at which a momentum state scatters into other momentum states [35]

$$\frac{1}{\tau_{\mathbf{q}}} = -\operatorname{Im}\Sigma(\omega(\mathbf{q}), \mathbf{q}). \qquad (26)$$

The inverse lifetime is plotted in Fig. 8(c) at $T = T_F$ for various scattering lengths. The quasiparticles are well defined if the inverse lifetime is much smaller compared to the excitation energy:

$$\frac{1}{\tau_{\mathbf{q}}} \ll \omega(\mathbf{q}). \qquad (27)$$

In Fig. 8(d), we plot the ratio $1/\tau_0\omega(\mathbf{0})$. It vanishes with the logarithm of temperature at high temperature. This shows that in the limit of high temperature, the low-energy excitations of the two-dimensional Fermi gas are indeed well-defined quasiparticles, allowing for a kinetic description of its non-equilibrium properties. This is consistent with an analogous result for the three-dimensional unitary Fermi gas [36].

As pointed out by Nishida [37] for the three-dimensional Fermi gas at a large scattering length, the self-energy at large momentum and frequency is universal, i.e., it is independent of the microscopic details of the system's state. The functional form can be calculated analytically by means of an operator product expansion [26, 37–39]. The magnitude of this high-momentum and high-frequency tail is set by the density:

$$\Sigma(\omega, \mathbf{q}) = W_n(\omega, \mathbf{q})n + \cdots, \qquad (28)$$

where $W_n(\omega, \mathbf{q})$ is the so-called Wilson coefficient of the density. It is given by the two-particle scattering amplitude:

$$W_n(\omega, \mathbf{q}) = T_2(\omega, \mathbf{q}). \qquad (29)$$

The relation (28) dictates the asymptotic form of the dispersion relation

$$\omega(\mathbf{q}) + \mu = \varepsilon_{\mathbf{q}} + \frac{2\pi n}{m} \frac{\ln \varepsilon_{\mathbf{q}}/2E_b}{\ln^2 \varepsilon_{\mathbf{q}}/2E_b + \pi^2} + O\left(\frac{1}{q\ln^2 q}\right) \qquad (30)$$

and the lifetime

$$\frac{1}{\tau_{\mathbf{q}}} = \frac{2\pi n}{m} \frac{\pi}{\ln^2 \varepsilon_{\mathbf{q}}/2E_b + \pi^2} + O\left(\frac{1}{q \ln^3 q}\right). \qquad (31)$$

This relation is obeyed by the virial expansion and indicated by dashed lines in Figs. 8(a) and 8(c). In particular, since in the high-momentum limit

$$\tau_{\mathbf{q}} \omega(\mathbf{q}) = \frac{1}{\pi} \ln \frac{\varepsilon_{\mathbf{q}}}{2E_b} \gg 1, \qquad (32)$$

excitations at large momentum are always well-defined quasiparticles. This result holds at all temperatures.

In addition, Eq. (28) implies that the spectral function decays with the inverse power of frequency at high $\omega \gg q^2/2m$:

$$A(\omega, \mathbf{q}) = \frac{2\pi n}{m} \frac{1}{\omega^2} \frac{2\pi}{\ln^2 \omega/E_b + \pi^2} + \mathcal{O}(1/\omega^3). \qquad (33)$$

To the best of our knowledge, this is a novel universal relation for fermions with short-range interactions in 2D. The next-to-leading order is proportional to the contact parameter. Calculating this contribution would require the inclusion of three-particle processes.

## V. CONCLUSION AND OUTLOOK

In conclusion, we have calculated the spectral function of a spin-balanced two-dimensional Fermi gas with short-range interactions to leading order in a virial expansion. This order takes into account two-particle effects and reproduces the salient features of the spectral function, which is dominated by a quasiparticle branch and a branch at lower energy that is associated with the two-particle bound state. Our results give a good qualitative description of recent experiments [7].

It turns out that the virial expansion can be applied to temperatures as low as the Fermi temperature $T_F$, a regime where pairing affects the single-particle spectrum and the density of states. While the onset of a pairing gap is visible in the density of states, it is interesting to note that the back-bending of the lower branch of the occupied spectral function with increasing momentum does not appear to be a sufficient sign of a pseudogap, for this is not seen in the full spectral function. It is an artifact of combining the finite width of the lower branch with the thermal occupation that weighs the measured spectra to lower frequencies.

The spectral function is related to various observable quantities, notably the momentum distribution and the rf transition rate, both of which were calculated in this paper, and excellent agreement with exact universal results was found. Furthermore, we analyzed the quasiparticle branch and determined the quasiparticle properties. Effective-mass corrections are found to be very small, while the lifetime of the quasiparticle branch approaches very large values as the temperature is increased.
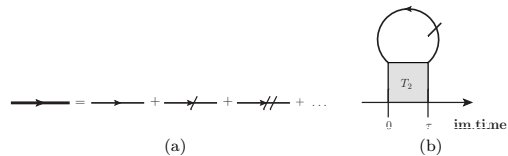
FIG. 9. (a) Diagrammatic representation of Eq. (A2). The bare propagator (thick line) is a series of expanded propagators $G_0^{(n)}$ (continuous thin lines). The number of slashes counts the expansion order $n$ in the fugacity. (b) Diagram for the self-energy expanded to first order in the fugacity $z$.

The present work could be straightforwardly extended in several ways, for example by including the effects of harmonic confinement in two- or quasi-two-dimensional geometries. It would also be interesting to extend the range of validity to even lower temperatures by performing the quantum cluster expansion to next-to-leading order, which takes into account three-particle processes.

*Note added:* Recently, we became aware of Ref. [40], where some of our results have been derived independently.

## Appendix A: Diagrammatic Formalism

In this appendix, we derive the leading-order contribution (13) to the virial expansion of the self-energy using a diagrammatic formalism. In Ref. [41], the relation (10) for the number density was taken as a starting point to calculate the virial coefficients of a three-dimensional contact-interacting Fermi gas up to third order using a diagrammatic approach. Some resummation schemes, such as the $T$-matrix approximation, seem to reproduce the results of the leadingorder virial expansion at high temperature [42]. It should be noted that the diagrammatic formalism is not restricted to contact interactions, but can also be applied to other systems such as the electron gas [43]. Here, we apply the same formalism to the two-dimensional Fermi gas. The starting point is the free-fermion propagator, which in imaginary time is given by

$$G_0(\tau, \mathbf{q}) = e^{-(\varepsilon_{\mathbf{q}} - \mu)\tau} \left( f(\varepsilon_{\mathbf{q}} - \mu) - \Theta(\tau) \right), \qquad (A1)$$

where $\Theta(\tau)$ denotes the Heaviside function. Expanding the Fermi distribution $f(\varepsilon_{\mathbf{q}} - \mu)$ with respect to the fu-

gacity $z$ in the above equation yields

$$G_0(\tau, \mathbf{q}) = e^{\mu\tau} \sum_{n \geq 0} G_0^{(n)}(\tau, \mathbf{q}) z^n, \qquad \text{(A2)}$$

where

$$G_0^{(n)}(\tau, \mathbf{q}) = \begin{cases} -\Theta(\tau) e^{-\varepsilon_{\mathbf{q}}\tau} & n = 0 \\ (-1)^{n-1} e^{-\varepsilon_{\mathbf{q}}\tau} e^{-n\beta\varepsilon_{\mathbf{q}}} & n \geq 1 \end{cases}. \qquad \text{(A3)}$$

Following Leyronas [41], we depict the $n$-th order term $G_0^{(n)}$ diagrammatically by a line that is slashed $n$ times [see Fig. 9(a)].

A given Feynman diagram with $G_0^{(n)}$ appearing $N_n$ times is of order $\sum_n n N_n$ in the fugacity. Since $G_0^{(0)}$ is a

retarded Green's function, it is not allowed to propagate backwards in imaginary time. The leading order in $z$ is thus given by the diagram with the least number of advanced propagators. The self-energy to first order in the fugacity can be inferred directly from Fig. 9(b), which is the only one-particle irreducible diagram containing only one backward-propagating propagator. It describes the interaction with a single particle-hole pair:

$$\Sigma^{(1)}(i\omega_n, \mathbf{q})$$
$$= z \int_0^\beta d\tau \int \frac{d^2k}{(2\pi)^2} e^{i\omega_n\tau} e^{\mu\tau} e^{-\varepsilon_{\mathbf{q}}(\beta-\tau)} T_2(\tau, \mathbf{k}+\mathbf{q}),$$
$$\text{(A4)}$$

which gives the result in Eq. (13). The $T$-matrix $T_2$ is the ladder series of all forward-propagating lines. It is of zeroth order in $z$ and equivalent to the vacuum $T$ matrix.

[1] *The BCS-BEC Crossover and the Unitary Fermi Gas*, edited by W. Zwerger (Springer-Verlag, Berlin, 2012).
[2] J. Stewart, J. Gaebler, and D. Jin, Nature (London) **454**, 744 (2008).
[3] J. P. Gaebler, J. T. Stewart, T. E. Drake, D. S. Jin, A. Perali, P. Pieri, and G. C. Strinati, Nat. Phys. **6**, 569 (2010).
[4] P. Magierski, G. Wlazłowski, A. Bulgac, and J. E. Drut, Phys. Rev. Lett. **103**, 210403 (2009).
[5] Q. Chen and K. Levin, Phys. Rev. Lett. **102**, 190402 (2009).
[6] R. Haussmann, M. Punk, and W. Zwerger, Phys. Rev. A **80**, 063612 (2009).
[7] M. Feld, B. Fröhlich, E. Vogt, M. Koschorreck, and M. Köhl, Nature (London) **480**, 75 (2011).
[8] I. Bloch, J. Dalibard, and W. Zwerger, Rev. Mod. Phys. **80**, 885 (2008).
[9] B. Fröhlich, M. Feld, E. Vogt, M. Koschorreck, W. Zwerger, and M. Köhl, Phys. Rev. Lett. **106**, 105301 (2011).
[10] A. T. Sommer, L. W. Cheuk, M. J. H. Ku, W. S. Bakr, and M. W. Zwierlein, Phys. Rev. Lett. **108**, 045302 (2012).
[11] S. N. Klimin, J. Tempere, and J. T. Devreese, New Journal of Physics **14**, 103044 (2012).
[12] V. Pietilä, D. Pekker, Y. Nishida, and E. Demler, Phys. Rev. A **85**, 023621 (2012).
[13] R. Watanabe, S. Tsuchiya, and Y. Ohashi, Phys. Rev. A **88**, 013637 (2013).
[14] X.-J. Liu, H. Hu, and P. D. Drummond, Phys. Rev. B **82**, 054524 (2010).
[15] H. Hu, X.-J. Liu, P. D. Drummond, and H. Dong, Phys. Rev. Lett. **104**, 240407 (2010).
[16] M. Randeria, J.-M. Duan, and L.-Y. Shieh, Phys. Rev. Lett. **62**, 981 (1989).
[17] W. Schneider and M. Randeria, Phys. Rev. A **81**, 021601 (2010).
[18] L. Landau and E. Lifshitz, *Course of Theoretical Physics, Statistical Physics, Part 1, Vol. 5* (Butterworth-Heinemann, Oxford, 2010).
[19] C. A. R. Sá de Melo, M. Randeria, and J. R. Engelbrecht, Phys. Rev. Lett. **71**, 3202 (1993).
[20] E. Beth and G. E. Uhlenbeck, Physica (Utrecht) **4**, 915 (1937).
[21] G. Bertaina and S. Giorgini, Phys. Rev. Lett. **106**, 110403 (2011).
[22] In this paper, we suppress spin indices because we are considering a balanced gas. Notice that our Green's functions are not summed over the two indices.
[23] Y. Nishida, Phys. Rev. B **88**, 224402 (2013).
[24] We have defined our momentum distribution with an intensive normalization $\int \frac{d^2q}{(2\pi)^2} n_\sigma(\mathbf{q}) = n/2$, thus the contact density, not the (extensive) contact, is the coefficient of the high-momentum tail.
[25] S. Tan, Ann. Phys. (N.Y.) **323**, 2971 (2008).
[26] E. Braaten, D. Kang, and L. Platter, Phys. Rev. A **78**, 053606 (2008).
[27] F. Werner and Y. Castin, Phys. Rev. A **86**, 013626 (2012).
[28] J. Hofmann, Phys. Rev. Lett. **108**, 185303 (2012).
[29] E. Taylor and M. Randeria, Phys. Rev. Lett. **109**, 135301 (2012).
[30] C. Chafin and T. Schaefer, Phys. Rev. A **88**, 043636 (2013).
[31] C. Langmack, M. Barth, W. Zwerger, and E. Braaten, Phys. Rev. Lett. **108**, 060402 (2012).
[32] L. Landau and E. Lifshitz, *Course of Theoretical Physics, Statistical Physics, Part 2, Vol. 9* (Butterworth-Heinemann, Oxford, 2010).
[33] R. Combescot, A. Recati, C. Lobo, and F. Chevy, Phys. Rev. Lett. **98**, 180402 (2007).
[34] R. Schmidt, T. Enss, V. Pietilä, and E. Demler, Phys. Rev. A **85**, 021602 (2012).
[35] G. F. Giuliani and G. G. Vignale, *Quantum Theory of the Electron Liquid* (Cambridge University Press, Cambridge, 2005).
[36] T. Enss, R. Haussmann, and W. Zwerger, Ann. Phys. (N.Y.) **326**, 770 (2011).
[37] Y. Nishida, Phys. Rev. A **85**, 053643 (2012).
[38] D. T. Son and E. G. Thompson, Phys. Rev. A **81**, 063634

11

(2010).

[39] J. Hofmann, Phys. Rev. A **84**, 043603 (2011).

[40] V. Ngampruetikorn, J. Levinsen,  and M. Parish, Phys. Rev. Lett. **111**, 265301 (2013).

[41] X. Leyronas, Phys. Rev. A **84**, 053633 (2011).

[42] R. Combescot, X. Leyronas,  and M. Y. Kagan, Phys. Rev. A **73**, 023618 (2006).

[43] J. Hofmann, M. Barth,  and W. Zwerger, Phys. Rev. B **87**, 235125 (2013).

# Efimov correlations in strongly interacting Bose gases

Marcus Barth[1, *] and Johannes Hofmann[2, †]

[1] *Technische Universität München, Physik Department, James-Franck-Strasse, 85748 Garching, Germany*
[2] *Condensed Matter Theory Center and Joint Quantum Institute, Department of Physics,*
*University of Maryland, College Park, Maryland 20742-4111 USA*
(Dated: June 24, 2015)

We compute the virial coefficients, the contact parameters, and the momentum distribution of a strongly interacting three-dimensional Bose gas by means of a virial expansion up to third order in the fugacity, which takes into account three-body correlations exactly. Our results characterize the non-degenerate regime of the interacting Bose gas, where the thermal wavelength is smaller than the interparticle spacing but the scattering length may be arbitrarily large. We observe a rapid variation of the third virial coefficient as the scattering length is tuned across the three-atom and the atom-dimer thresholds. The momentum distribution at unitarity displays a universal high-momentum tail with a log-periodic momentum dependence, which is a direct signature of Efimov physics. We provide a quantitative description of the momentum distribution at high momentum as measured by [P. Makotyn et al., Nat. Phys. **10**, 116 (2014)].

The classical problem in Newtonian mechanics of finding analytical stable orbits of three planets has only few known solutions which, moreover, exist only for certain special conditions [1]. Curiously, a generic analog of this problem in quantum mechanics – three neutral bosons of mass $m$ with a universal short-range interaction – was solved analytically by Efimov four decades ago [2–4]. If the effective range of the interparticle interaction (set by the van der Waals length $\ell_{vdW}$) is small compared to other length scales, the two-body interaction is solely characterized by the scattering length $a$. In the unitary limit of infinite scattering length, Efimov found an infinite number of three-particle bound states with energy $E_T^{(n)} = \frac{\kappa_*^2}{m}(e^{\pi/s_0})^{-2n}$, manifesting a discrete scale invariance. Here, $\kappa_*$ is a universal three-body parameter, $n$ is an integer, and $e^{\pi/s_0} \approx 22.7$. While originally predicted in nuclear physics, Efimov states were observed in atom-loss experiments and radiofrequency spectroscopy measurements in Bose gases [5–9], three-component Fermi gases [10–14] as well as mass-imbalanced mixtures [15–17]. Recently, also the Efimov trimer of $^4$He has been observed experimentally [18]. Efimov physics is thus a very general phenomenon, and beside these many experimental realizations Efimov states are also predicted to exist, for example, in universal $p$-wave interacting quantum gases [19], in condensed matter quantum magnets [20], or in mass-imbalanced two-component Fermi gases [21]. Most theoretical work focusses on few-body aspects of Efimov physics and experiments are commonly explained using universal few-body theory [4]. In this Letter, by contrast, we study the interacting Bose gas at finite density and temperature and establish signatures of three-body correlations in this system.

Most experiments on Bose gases in equilibrium are restricted to the weak-interaction regime with few exceptions [22]. This is due to enhanced three-body losses at finite interaction strength which deplete the gas with a rate $\dot{N} = L_3 n^2 N$, where $L_3$ can be determined from the solution of the three-body problem [4]. At zero temperature, the loss coefficient scales as $L_3(T = 0) \sim a^4$ [23–25] and saturates to $L_3(T) \sim \lambda_T^4 \sim 1/T^2$ [26] in the unitary limit at high temperature ($\lambda_T = \sqrt{2\pi/mT}$ denotes the thermal wavelength, and we set $\hbar = k_B = 1$). In a series of recent hallmark experiments, the loss rate of a strongly interacting Bose gas at finite temperature was measured [27–29]. It turns out that in the non-degenerate limit $n\lambda_T^3 \ll 1$, the two-body scattering rate $\gamma_2 = n\sigma v \sim n\lambda_T$ is much larger compared to the three-body loss rate $\gamma_3 = L_3 n^2 \sim n^2\lambda_T^4$, so that the gas can reach an equilibrium state before a significant fraction of particles is lost. Indeed, this is corroborated by a recent experiment that quenches a weakly interacting BEC to the unitary limit and measures the momentum distribution, which approaches a stationary equilibrium distribution shortly after the quench [29]. In the non-degenerate regime, we furthermore expect that the thermal pressure counteracts the attractive force and the system is thermodynamically stable [30–33] with possible phase transitions at lower temperature [34, 35]. Hence, the experiments [27–29] demonstrate that strongly interacting Bose gases can be experimentally prepared and studied. Strongly interacting Bose gases are of fundamental interest as they are the first interacting quantum many-body system where three-body correlations turn out to be essential.

In this Letter, we characterize the strongly interacting Bose gas in the normal phase by performing a virial expansion, allowing us to link few-body physics to the properties of an interacting many-body system in the grand-canonical ensemble in a systematic way. The virial expansion is valid if the thermal wavelength of the gas is much smaller compared to the interparticle spacing (cor-
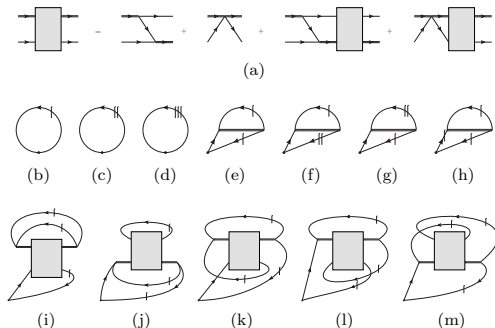
FIG. 1. (a) Integral equation for the three-body scattering matrix, denoted by a gray box. Simple lines denote atom propagators and double lines dimer propagators. (b)-(m): Diagrams that contribute to the density and the momentum distribution up to third order in the fugacity.
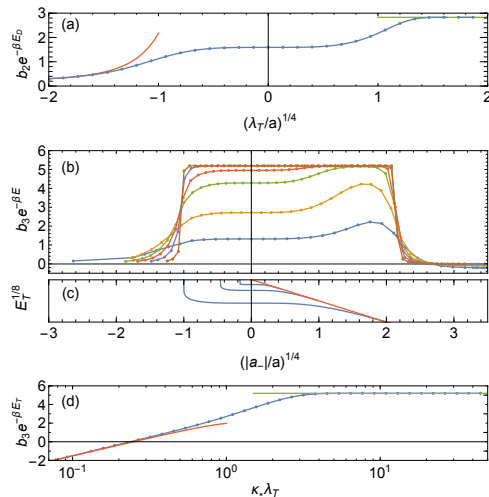


FIG. 2. (a) Second virial coefficient as a function of scattering length. The red and green lines denote the asymptotic results in the BEC and BCS limits. (b) Third virial coefficient as a function of scattering length for fixed three-body parameter (bottom to top) $\kappa_* \lambda_T = 0.5, 1, 2, 3, 5$, and 10. (c) Bound state spectrum of a Bose gas. Blue lines denote trimer branches and the red line is the dimer bound state energy. (d) Third virial coefficient of a unitary Bose gas as a function of the three-body parameter. The green and red lines correspond to the analytical asymptotic expressions [39]. The points are numerical results and the connecting lines are a guide to the eye.

responding to a small degeneracy parameter $n\lambda_T^3 \ll 1$) and is therefore ideally suited to describe current experimental work [27–29]. The virial expansion expresses the grand-canonical partition function as a sum of separate traces over the $N$-particle sectors:

$$\mathcal{Z} = \mathrm{Tr}\, e^{-\beta(H-\mu N)} = \sum_{N=0}^{\infty} z^N \mathrm{tr}_N e^{-\beta H}. \qquad (1)$$

In the non-degenerate regime $n\lambda_T^3 \ll 1$, the fugacity $z = e^{\beta\mu}$ is a small parameter and the expansion in Eq. (1) can be truncated after the first few terms. By performing the expansion up to third order in $z$, we fully include three-body correlations. Previous early work on the virial expansion of Bose gases dates back to the late 1950s [36, 37], and more recent applications are [38–40]. A previous numerical study of the virial coefficients was carried out by Bedaque and Rupak [38], but they have not included all the relevant diagrams, see Fig. 1. Note that the virial coefficients of the unitary Bose gas can even be determined analytically [39]. The virial expansion has also been successfully applied to Fermi gases, see Ref. [41] for a review. In the following, we provide numerical results for the first three virial coefficients (both at unitarity and at finite scattering length) as well as the two-body and the three-body contact coefficients which characterize the short-distance and short-time structure of the system. An essential new point of our analysis is that we develop the virial expansion for the full Green's function, which allows us to compute the momentum distribution. The momentum distribution exhibits a universal high-momentum tail that shows direct three-body Efimov correlations. We compare our calculations with a recent experiment by Makotyn et al. [29].

The Lagrangian density of an interacting Bose gas with large scattering length takes the form [4]

$$\mathcal{L} = \phi^\dagger \left( i\partial_t + \frac{\nabla^2}{2m} \right)\phi + \frac{g_2}{4} d^\dagger d - \frac{g_2}{4}\left( d^\dagger \phi\phi + \phi^\dagger \phi^\dagger d \right)$$
$$- \frac{g_3}{36} \phi^\dagger d^\dagger d\phi, \qquad (2)$$

where $\phi^\dagger$ creates a boson and $d$ is an auxiliary dimer field. The bare coupling constants $g_2$ and $g_3$ depend on the cutoff-regulator $\Lambda$ in such a way that they match low-energy observables in the two- and three-particle sector. We choose $\frac{1}{g_2} = \frac{m}{8\pi a} - \frac{m\Lambda}{4\pi^2}$ and $g_3 = -9mg_2^2 \frac{H(\Lambda)}{\Lambda^2}$ with $H(\Lambda) \sim \frac{\cos(s_0 \ln \Lambda/\Lambda_* + \arctan s_0)}{\cos(s_0 \ln \Lambda/\Lambda_* - \arctan s_0)}$, where $\Lambda_*$ is a renormalized three-body parameter, manifesting a renormalization group limit cycle [4, 42, 43]. For positive scattering length, the two-particle scattering amplitude has a dimer bound state pole with energy $E_D = \frac{1}{ma^2}$. The parameter $\Lambda_*$ is related to the Efimov binding energy at unitarity via $\kappa_* = 0.38\Lambda_*$ [44]. Each trimer branch hits the continuum of scattering states at the three-body threshold scattering length $a_-$ and terminates at positive scattering length at the atom-dimer threshold $a_*$. The theory (2)

has an infinite number of arbitrarily deep Efimov bound states. We avoid the Thomas collapse [45] in our calculations by specifying a lowest Efimov trimer state, the energy of which we denote by $E_T$. Here, we extend a diagrammatic representation of the virial expansion introduced in Ref. [46] for Fermi gases to the Bose case. The diagrammatic virial expansion is based on an expansion in imaginary time, where it turns out that the full dependence on the fugacity $z$ is encoded in the free propagator, which can be expanded in powers of $z$. In Fig. 1, we denote the $n$th-order contribution to the propagator by a line that is slashed $n$ times. The key insight underlying the expansion is that the zeroth order contribution has only a retarded component, i.e., it can only propagate forward in imaginary time. Backward propagating lines contribute higher powers of $z$. This provides a diagrammatic representation for the virial expansion of any correlation function. The Feynman diagrams constructed in this way contain subdiagrams that involve repeated scattering of either two or three forward-running particles. These are the scattering matrices of the few-body problem, and we denote them by a double line and a box, respectively.

We begin by computing the virial expansion of the density. The density is related to the virial coefficients via [36]

$$\lambda_T^3 n = b_1 z + 2b_2 z^2 + 3b_3 z^2 + O(z^4). \qquad (3)$$

The diagrams contributing to the density up to $O(z^3)$ are shown in Fig. 1, with Fig. 1(b) contributing to $b_1$, Figs. 1(c) and 1(e) to $b_2$, and all other diagrams contributing to the third virial coefficient $b_3$. Diagrams 1(b)-1(d) give the standard result $b_n^{(0)} = n^{-5/2}$ for the virial coefficients of a non-interacting three-dimensional Bose gas, while Fig. 1(e) yields the Beth-Uhlenbeck interaction correction to the density [38]. The diagrams can be evaluated analytically to some degree: we decompose the three-body scattering matrix into Legendre polynomials, allowing us to perform the angle integration directly. In our calculation, we retain the first ten angular components, finding no change in the result when including higher harmonics within our numerical accuracy. The remaining momentum integrals are performed numerically. The three-body amplitude in the integrand is obtained from a solution of the Skorniakov–Ter-Martirosian integral equation [47] shown in Fig. 1(a). Figure 2 shows the second and the third virial coefficient. The second virial coefficient [Fig. 2(a)] agrees with the analytical result [38], providing an independent check of our calculations. Figure 2(b) shows the third virial coefficient as a function of scattering length for various $\kappa_*$. We rescale the scattering length by $a_-$ for each $\kappa_*$ and plot the reduced virial coefficient $e^{-\beta E} b_3$, where $E$ is the lowest bound state energy ($E = E_T$ for $a < a_*$ and $E = E_D$ for $a > a_*$). In the scattering-dominated limit $\kappa_* \lambda_T \ll 1$,
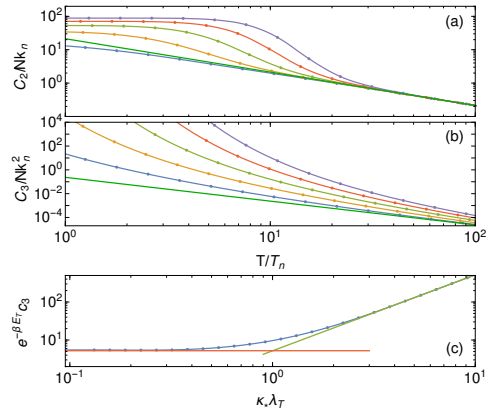


FIG. 3. (a) Two-body contact as a function of temperature. (b,c) Three-body contact at unitarity as a function of (b) temperature and (c) three-body parameter. The lines in Figs. (a) and (b) correspond to (bottom to top) $\kappa_*/k_n = 1, 2, 3, 4$, and 5. The green lines in (a) and (b) denote the asymptotic high-temperature results. The red and green lines in (c) denote the asymptotic results as stated in the main text.

the virial coefficient increases smoothly as the scattering length is tuned across the unitary limit and then decreases for $a > a_*$, assuming negative values. In the trimer limit $\kappa_* \lambda_T \gg 1$, the reduced virial coefficient is very small if no Efimov bound state is contained in the spectrum, and rapidly jumps to the trimer-dominated result $e^{-\beta E_T} b_3 = 3\sqrt{3}$ [39] otherwise, displaying only a very weak dependence on the scattering length. Figure 2(d) shows the third virial coefficient at unitarity as a function of the three-body parameter, which is in excellent agreement with the analytical results [39], providing yet another test for our numerics. The virial coefficients presented here completely characterize thermodynamic quantities such as density, compressibility, and pressure of the non-degenerate Bose gas. Note that the universal zero-range description (2) holds if the scattering length and the thermal wavelength are large compared to the effective range, which is set by the van der Waals length: $a, \lambda_T > \ell_{vdW}$ (however, $a$ and $\lambda_T$ can have arbitrary ratios). Since the three-body parameter is found to be universal with $\kappa_* \approx 0.2/\ell_{vdW}$ [48, 49], we expect that for $\kappa_* \lambda_T \ll 1$, there are effective range corrections to the results of this paper.

There exists a large set of universal relations that describe thermodynamic quantities and the short-time and short-distance structure of a quantum gas. All of these relations involve a universal quantity called the contact, which is a measure of correlations at short distances. We distinguish the two-body contact $C_2$ and the three-body

contact $C_3$. These extensive quantities are related to the energy of the system by the adiabatic theorems [50–52]:

$$C_2 = -8\pi m \frac{\partial E}{\partial a^{-1}}\bigg|_{\kappa_*} = \frac{V}{\lambda_T^4}\sum_{n\geq2} c_{2,n} z^n \qquad (4)$$

$$C_3 = -\frac{m\kappa_*}{2}\frac{\partial E}{\partial \kappa_*}\bigg|_{a^{-1}} = \frac{V}{\lambda_T^5}\sum_{n\geq3} c_{3,n} z^n, \qquad (5)$$

where $c_{2,n} = 16\pi^2 \partial b_n/\partial(\lambda_T/a)$ and $c_{3,n} = \pi\kappa_* \partial b_n/\partial\kappa_*$, and we abbreviate $c_{3,3} = c_3$. The three-body contact manifests direct Efimov correlations. In Fig. 3, we plot the intensive contact parameters $C_2/Nk_n$ [Fig. 3(a)] and $C_3/Nk_n^2$ [Fig. 3(b)] as a function of rescaled temperature $T/T_n$, where $k_n = (6\pi^2 n)^{1/3}$ and $T_n = k_n^2/2m$. For $T \gg T_n$, the contacts approach the asymptotic results $C_2/Nk_n = 64T_n/3T$ and $C_3/Nk_n^2 = 4s_0 T_n^2/\sqrt{3}\pi^2 T^2$ [green lines in Fig. 3]. As the temperature is lowered, both $C_2$ and $C_3$ increase very strongly, with $C_2$ saturating at low temperature. In addition, we show the three-body contact as a function of $\kappa_*\lambda_T$ in Fig. 3(c). The numerical results agree with the analytical limits $c_3 = 3\sqrt{3}(\kappa_*\lambda_T)^2 e^{\beta E_T}$ for large $\kappa_*\lambda_T$ and $c_3 = 3\sqrt{3}s_0$ for small $\kappa_*\lambda_T$.

A particular universal relation connects the two- and three-body contacts to the high momentum tail of the momentum distribution, which behaves as [51, 53, 54]

$$n(q) = \frac{\mathcal{C}_2}{q^4} + \frac{\mathcal{C}_3}{q^5}F(q) + O(1/q^6), \qquad (6)$$

where $\mathcal{C}_{2/3} = C_{2/3}/V$ is the intensive contact density and $F(q)$ is a log-periodic function of the momentum given by $F(q) = A\sin(2s_0 \ln q/\kappa_* + 2\phi)$, where $A = 89.26260$ and $\phi = -0.669064$. A recent experiment by Makotyn et al. [29] measures the momentum distribution of a Bose gas quenched to unitarity in a time-of-flight measurement, and a comparison with the asymptotic result (6) indicates that the observed momentum distribution is consistent with the universal three-body tail [55]. Here, we provide a full calculation of the momentum distribution to third order in the fugacity.

The momentum distribution is defined as the zero-time limit $G(0^-, q)$ of the imaginary time propagator, and we parametrize:

$$n(q) = e^{\beta E_T}\left[n_1(q)z + n_2(q)z^2 + n_3(q)z^3 + O(z^4)\right]. \quad (7)$$

Formally, the diagrams that contribute to the momentum distribution up to third order in $z$ can be represented in the same way as for the density in Fig. 1, although the black dot now denotes the number operator which inserts a momentum $q$ into the diagram, changing the structure of the calculation fundamentally. Note that the momentum distribution can be computed for a single trimer [54, 56]. Figure 4 shows our result for the $O(z^3)$ part $n_3$ of the momentum distribution at unitarity with
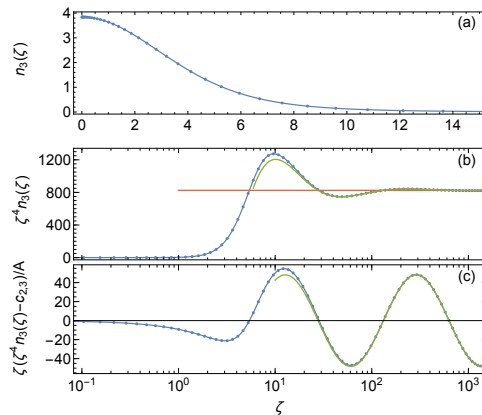


FIG. 4. Third order contribution $n_3(\zeta)$ to the momentum distribution of a homogeneous unitary Bose gas with $\kappa_*\lambda_T = 3$ as a function of dimensionless momentum $\zeta = q\lambda_T$. Points denote numerical results, the continuous blue line is a guide to the eye. The orange and green lines denote the asymptotic Tan relations (6) obtained with $e^{-\beta E_T}c_{2,3} = 825.2$ and $e^{-\beta E_T}c_3 = 48.1$.

three-body parameter $\kappa_*\lambda_T = 3$. Figure 4(a) shows the full momentum distribution as a function of rescaled dimensionless momentum $\zeta = q\lambda_T$. Figure 4(b) amplifies the high-momentum tail. This is further illustrated in Fig. 4(c) which shows the momentum distribution with subtracted leading-order two-body tail. The continuous red and green lines denote the asymptotic two- and three-body form of the Tan relation (6), respectively, where the $O(z^3)$ contact parameters are extracted from the virial coefficients in an independent calculation, providing a strong check of our results. It is important to note that there are two momentum scales at unitarity: $k_n$ (set by the density) and $k_\kappa = \sqrt{2mE_T}$ (set by the trimer energy). The onset of the asymptotic tail is set by $k_\kappa$ rather than $k_n$, which marks the asymptotic regime in Fermi gases [57].

We can compare our results with the experiment by Makotyn et al. [29], which measures the momentum distribution following a quench to the unitary limit for two different initial densities $\langle n_1\rangle = 5.5 \cdot 10^{12}\,\mathrm{cm}^{-3}$ and $\langle n_2\rangle = 1.6 \cdot 10^{12}\,\mathrm{cm}^{-3}$. Following Ref. [40], we assume a constant phase space density $n\lambda_T^3$ and average our results over a Thomas-Fermi density profile. Since our calculations are performed at fixed $\kappa_*\lambda_T$, we keep $\kappa_*/k_n$ fixed at its value at the trap center. This neglects logarithmic corrections to the fugacity, which in our fit is constant throughout the trap [40]. The experiment was performed using $^{85}$Rb, which has a three-body parameter $\kappa_* = 38(1)\,\mu m^{-1}$ [58]. Remarkably, our results are in
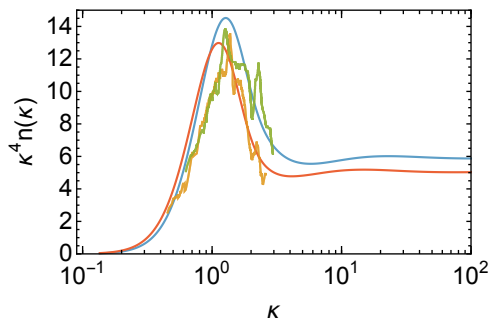
FIG. 5. Momentum distribution of a unitary Bose gas. Orange and green line: experimental measurement by Makotyn et al. [29] at two densities $\langle n_1 \rangle = 5.5 \cdot 10^{12} \, \text{cm}^{-3}$ (orange line) and $\langle n_2 \rangle = 1.6 \cdot 10^{12} \, \text{cm}^{-3}$ (green line). $\kappa = q/k_n$ denotes the dimensionless momentum. The continuous red and blue lines are the result of the trap-averaged virial expansion with fugacities $z_1 = 0.5$ and $z_2 = 0.4$, respectively. The momentum distribution is normalized to unity $\int d^3\kappa \, n(\kappa)/(2\pi)^3 = 1$.

very good agreement with the experiment provided that we exclude the lowest trimer branch from our calculation and set $\kappa'_* = \kappa_*/22.7$. In this case, the virial expansion agrees well with the experimental data with $z_1 = 0.5$ and $z_2 = 0.4$. The small values of the fugacity justify the use of the virial expansion. The results are shown in Fig. 5.

In summary, we have characterized the strongly interacting Bose gas in the normal phase by computing the first three virial coefficients, the two-body and the three-body contact, as well as the momentum distribution. Our results provide a systematic framework to compute three-body correlation effects in an interacting many-body system and are of direct relevance to ongoing and future experiments on Bose quantum gases.

---

* marcus.barth@ph.tum.de

† hofmann@umd.edu

[1] M. Šuvakov and V. Dmitrašinović, Phys. Rev. Lett. **110**, 114301 (2013).

[2] V. Efimov, Physics Letters B **33**, 563 (1970).

[3] V. Efimov, Sov. J. Nucl. Phys. **12**, 589 (1971).

[4] E. Braaten and H.-W. Hammer, Physics Reports **428**, 259 (2006).

[5] T. Kraemer, M. Mark, P. Waldburger, J. G. Danzl, C. Chin, B. Engeser, A. D. Lange, K. Pilch, A. Jaakkola, H. C. Nägerl, and R. Grimm, Nature **440**, 315 (2006).

[6] S. Knoop, F. Ferlaino, M. Mark, M. Berninger, H. Schobel, H. C. Nagerl, and R. Grimm, Nat. Phys. **5**, 227 (2009).

[7] M. Zaccanti, B. Deissler, C. D'Errico, M. Fattori, M. Jona-Lasinio, S. Muller, G. Roati, M. Inguscio, and G. Modugno, Nat. Phys. **5**, 586 (2009).

[8] N. Gross, Z. Shotan, S. Kokkelmans, and L. Khaykovich, Phys. Rev. Lett. **103**, 163202 (2009).

[9] S. E. Pollack, D. Dries, and R. G. Hulet, Science **326**, 1683 (2009).

[10] T. B. Ottenstein, T. Lompe, M. Kohnen, A. N. Wenz, and S. Jochim, Phys. Rev. Lett. **101**, 203202 (2008).

[11] J. H. Huckans, J. R. Williams, E. L. Hazlett, R. W. Stites, and K. M. O'Hara, Phys. Rev. Lett. **102**, 165302 (2009).

[12] J. R. Williams, E. L. Hazlett, J. H. Huckans, R. W. Stites, Y. Zhang, and K. M. O'Hara, Phys. Rev. Lett. **103**, 130404 (2009).

[13] T. Lompe, T. B. Ottenstein, F. Serwane, A. N. Wenz, G. Zürn, and S. Jochim, Science **330**, 940 (2010).

[14] S. Nakajima, M. Horikoshi, T. Mukaiyama, P. Naidon, and M. Ueda, Phys. Rev. Lett. **106**, 143201 (2011).

[15] G. Barontini, C. Weber, F. Rabatti, J. Catani, G. Thalhammer, M. Inguscio, and F. Minardi, Phys. Rev. Lett. **103**, 043201 (2009).

[16] S.-K. Tung, K. Jiménez-García, J. Johansen, C. V. Parker, and C. Chin, Phys. Rev. Lett. **113**, 240402 (2014).

[17] R. Pires, J. Ulmanis, S. Häfner, M. Repp, A. Arias, E. D. Kuhnle, and M. Weidemüller, Phys. Rev. Lett. **112**, 250404 (2014).

[18] M. Kunitski, S. Zeller, J. Voigtsberger, A. Kalinin, L. P. H. Schmidt, M. Schöffler, A. Czasch, W. Schöllkopf, R. E. Grisenti, T. Jahnke, D. Blume, and R. Dörner, Science **348**, 551 (2015).

[19] Y. Nishida, S. Moroz, and D. T. Son, Phys. Rev. Lett. **110**, 235301 (2013).

[20] Y. Nishida, Y. Kato, and C. D. Batista, Nat. Phys. **9**, 93 (2013).

[21] D. S. Petrov, Phys. Rev. A **67**, 010703 (2003).

[22] N. Navon, S. Piatecki, K. Günter, B. Rem, T. C. Nguyen, F. Chevy, W. Krauth, and C. Salomon, Phys. Rev. Lett. **107**, 135301 (2011).

[23] P. O. Fedichev, M. W. Reynolds, and G. V. Shlyapnikov, Phys. Rev. Lett. **77**, 2921 (1996).

[24] E. Nielsen and J. H. Macek, Phys. Rev. Lett. **83**, 1566 (1999).

[25] B. D. Esry, C. H. Greene, and J. P. Burke, Phys. Rev. Lett. **83**, 1751 (1999).

[26] J. P. D'Incao, H. Suno, and B. D. Esry, Phys. Rev. Lett. **93**, 123201 (2004).

[27] R. J. Fletcher, A. L. Gaunt, N. Navon, R. P. Smith, and Z. Hadzibabic, Phys. Rev. Lett. **111**, 125303 (2013).

[28] B. S. Rem, A. T. Grier, I. Ferrier-Barbut, U. Eismann, T. Langen, N. Navon, L. Khaykovich, F. Werner, D. S. Petrov, F. Chevy, and C. Salomon, Phys. Rev. Lett. **110**, 163202 (2013).

[29] P. Makotyn, C. E. Klauss, D. L. Goldberger, E. A. Cornell, and D. S. Jin, Nat. Phys. **10**, 116 (2014).

[30] H. T. C. Stoof, Phys. Rev. A **49**, 3824 (1994).

6

[31] E. J. Mueller and G. Baym, Phys. Rev. A **62**, 053605 (2000).

[32] G. S. Jeon, L. Yin, S. W. Rhee, and D. J. Thouless, Phys. Rev. A **66**, 011603 (2002).

[33] W. Li and T.-L. Ho, Phys. Rev. Lett. **108**, 195301 (2012).

[34] S. Piatecki and W. Krauth, Nat. Commun. **5**, 3503 (2014).

[35] W. van Dijk, C. Lobo, A. MacDonald, and R. K. Bhaduri, arXiv:1412:5112 (2014).

[36] A. Pais and G. E. Uhlenbeck, Phys. Rev. **116**, 250 (1959).

[37] R. Dashen, S.-K. Ma, and H. J. Bernstein, Phys. Rev. **187**, 345 (1969).

[38] P. F. Bedaque and G. Rupak, Phys. Rev. B **67**, 174513 (2003).

[39] Y. Castin and F. Werner, Canadian Journal of Physics **91**, 382 (2013).

[40] S. Laurent, X. Leyronas, and F. Chevy, Phys. Rev. Lett. **113**, 220601 (2014).

[41] X.-J. Liu, Physics Reports **524**, 37 (2013).

[42] P. F. Bedaque, H.-W. Hammer, and U. van Kolck, Phys. Rev. Lett. **82**, 463 (1999).

[43] P. Bedaque, H.-W. Hammer, and U. van Kolck, Nuclear Physics A **646**, 444 (1999).

[44] This holds for our choice of the deepest trimer.

[45] L. H. Thomas, Phys. Rev. **47**, 903 (1935).

[46] X. Leyronas, Phys. Rev. A **84**, 053633 (2011).

[47] G. Skorniakov and K. Ter-Martirosian, Sov. Phys. JETP **4** (1957).

[48] R. Schmidt, S. P. Rath, and W. Zwerger, EPJ B **85**, 1 (2012).

[49] J. Wang, J. P. D'Incao, B. D. Esry, and C. H. Greene, Phys. Rev. Lett. **108**, 263001 (2012).

[50] S. Tan, Annals of Physics **323**, 2952 (2008).

[51] E. Braaten, D. Kang, and L. Platter, Phys. Rev. Lett. **106**, 153005 (2011).

[52] F. Werner and Y. Castin, Phys. Rev. A **86**, 053633 (2012).

[53] S. Tan, Annals of Physics **323**, 2971 (2008).

[54] Y. Castin and F. Werner, Phys. Rev. A **83**, 063614 (2011).

[55] D. H. Smith, E. Braaten, D. Kang, and L. Platter, Phys. Rev. Lett. **112**, 110402 (2014).

[56] F. F. Bellotti, T. Frederico, M. T. Yamashita, D. V. Fedorov, A. S. Jensen, and N. T. Zinner, Phys. Rev. A **87**, 013610 (2013).

[57] J. T. Stewart, J. P. Gaebler, T. E. Drake, and D. S. Jin, Phys. Rev. Lett. **104**, 235301 (2010).

[58] R. J. Wild, P. Makotyn, J. M. Pino, E. A. Cornell, and D. S. Jin, Phys. Rev. Lett. **108**, 145305 (2012).

[59] http://www.it.umd.edu/hpcc.

# Bibliography

[1] Kenneth G. Wilson. Non-lagrangian models of current algebra. *Phys. Rev.*, 179(5):1499–1512, Mar 1969.

[2] Leo P. Kadanoff. Operator algebra and the determination of critical indices. *Phys. Rev. Lett.*, 23(25):1430–1433, Dec 1969.

[3] Gerhard Mack. Convergence of operator product expansions on the vacuum in conformal invariant quantum field theory. *Communications in Mathematical Physics*, 53(2):155–184, 1977.

[4] Duccio Pappadopulo, Slava Rychkov, Johnny Espin, and Riccardo Rattazzi. Operator product expansion convergence in conformal field theory. *Physical Review D*, 86(10):105043, 2012.

[5] Walter D Goldberger, Zuhair U Khandker, and Siddharth Prabhu. Ope convergence in non-relativistic conformal field theories. *arXiv preprint arXiv:1412.8507*, 2014.

[6] Kenneth G. Wilson and Wolfhart Zimmermann. Operator product expansions and composite field operators in the general framework of quantum field theory. *Communications in Mathematical Physics*, 24:87–106, 1972. 10.1007/BF01878448.

[7] Wilhelm Zwerger. *The BCS-BEC crossover and the unitary Fermi gas*, volume 836. Springer Science & Business Media, 2011.

[8] Kerson Huang. *Statistical Mechanics, 2nd Edition*. Wiley, 1987.

[9] Xavier Leyronas. Virial expansion with feynman diagrams. *Physical Review A*, 84(5):053633, 2011.

[10] V. Efimov. Energy levels arising from resonant two-body forces in a three-body system. *Physics Letters B*, 33(8):563, 1970.

*Bibliography*

[11] V. Efimov. Weakly bound states of three resonantly-interacting particles. *Sov. J. Nucl. Phys.*, 12:589, 1971.

[12] Predrag Nikolić and Subir Sachdev. Renormalization-group fixed points, universal phase diagram, and 1/n expansion for quantum liquids with interactions near the unitarity limit. *Physical Review A*, 75(3):033608, 2007.

[13] W. Zwerger. Strongly interacting fermi gases. *Varenna Lecture Notes*, 2014.

[14] PC Hohenberg. Existence of long-range order in one and two dimensions. *Physical Review*, 158(2):383, 1967.

[15] N David Mermin and Ho Wagner. Absence of ferromagnetism or antiferromagnetism in one-or two-dimensional isotropic heisenberg models. *Physical Review Letters*, 17(22):1133, 1966.

[16] VL Berezinskii. Destruction of long-range order in one-dimensional and two-dimensional systems possessing a continuous symmetry group. ii. quantum systems. *Soviet Journal of Experimental and Theoretical Physics*, 34:610, 1972.

[17] John Michael Kosterlitz and David James Thouless. Ordering, metastability and phase transitions in two-dimensional systems. *Journal of Physics C: Solid State Physics*, 6(7):1181, 1973.

[18] DS Petrov, MA Baranov, and GV Shlyapnikov. Superfluid transition in quasi-two-dimensional fermi gases. *Physical Review A*, 67(3):031601, 2003.

[19] Marianne Bauer, Meera M Parish, and Tilman Enss. Universal equation of state and pseudogap in the two-dimensional fermi gas. *Physical review letters*, 112(13):135302, 2014.

[20] PA Murthy, I Boettcher, L Bayha, M Holzmann, D Kedar, M Neidig, MG Ries, AN Wenz, G Zürn, and S Jochim. Observation of the berezinskii-kosterlitz-thouless phase transition in an ultracold fermi gas. *arXiv preprint arXiv:1505.02123*, 2015.

[21] Sadhan K Adhikari. Quantum scattering in two dimensions. *American Journal of Physics*, 54(4):362–367, 1986.

[22] Immanuel Bloch, Jean Dalibard, and Wilhelm Zwerger. Many-body physics with ultracold gases. *Rev. Mod. Phys.*, 80(3):885–964, Jul 2008.

[23] Paulo F Bedaque, H-W Hammer, and Ubirajara Van Kolck. The three-boson system with short-range interactions. *Nuclear Physics A*, 646(4):444–466, 1999.

[24] Paulo F Bedaque, H-W Hammer, and Ubirajara Van Kolck. Renormalization of the three-body system with short-range interactions. *Physical Review Letters*, 82(3):463, 1999.

[25] Eric Braaten and H-W Hammer. Universality in few-body systems with large scattering length. *Physics Reports*, 428(5):259–390, 2006.

[26] Aleksei Alekseevich Abrikosov, Lev Petrovich Gorkov, and Igor Ekhielevich Dzyaloshinski. *Methods of quantum field theory in statistical physics*. Courier Corporation, 1975.

[27] Marcus Barth. Tan relations in one dimension, diploma thesis. *Technische Universität München*, 2011.

[28] Michael E Peskin and Daniel V Schroeder. *An introduction to quantum field theory*. Westview, 1995.

[29] Anthony Zee. *Quantum field theory in a nutshell*. Princeton university press, 2010.

[30] Barry R Holstein. Anomalies for pedestrians. *American journal of physics*, 61(2):142–147, 1993.

[31] Johannes Hofmann. Quantum anomaly, universal relations, and breathing mode of a two-dimensional fermi gas. *Physical review letters*, 108(18):185303, 2012.

[32] Eric Braaten and Lucas Platter. Exact relations for a strongly interacting fermi gas from the operator product expansion. *Phys. Rev. Lett.*, 100(20):205301, May 2008.

[33] Eric Braaten, Daekyoung Kang, and Lucas Platter. Universal relations for a strongly interacting fermi gas near a feshbach resonance. *Phys. Rev. A*, 78(5):053606, Nov 2008.

[34] Marcus Barth and Wilhelm Zwerger. Tan relations in one dimension. *Annals of Physics*, 326(10):2544–2565, 2011.

*Bibliography*

[35] John C Collins. *Renormalization: an introduction to renormalization, the renormalization group and the operator-product expansion.* Cambridge university press, 1984.

[36] Manuel Valiente, Nikolaj T. Zinner, and Klaus Mølmer. Universal relations for the two-dimensional spin-1/2 fermi gas with contact interactions. *Phys. Rev. A*, 84:063626, Dec 2011.

[37] Shina Tan. Large momentum part of a strongly correlated fermi gas. *Annals of Physics*, 323(12):2971 – 2986, 2008.

[38] Félix Werner and Yvan Castin. General relations for quantum gases in two and three dimensions: Two-component fermions. *Physical Review A*, 86(1):013626, 2012.

[39] Shina Tan. Energetics of a strongly correlated fermi gas. *Annals of Physics*, 323(12):2952 – 2970, 2008.

[40] Shina Tan. Generalized virial theorem and pressure relation for a strongly correlated fermi gas. *Annals of Physics*, 323(12):2987 – 2990, 2008.

[41] Cheng Chin and Paul S Julienne. Radio-frequency transitions on weakly bound ultracold molecules. *Physical Review A*, 71(1):012713, 2005.

[42] C Chin, M Bartenstein, A Altmeyer, S Riedl, S Jochim, J Hecker Denschlag, and R Grimm. Observation of the pairing gap in a strongly interacting fermi gas. *Science*, 305(5687):1128–1130, 2004.

[43] M W Zwierlein, Claudiu A Stan, Christian H Schunck, Sebastian MF Raupach, Subhadeep Gupta, Zoran Hadzibabic, and Wolfgang Ketterle. Observation of bose-einstein condensation of molecules. *Physical Review Letters*, 91(25):250401, 2003.

[44] Bernd Fröhlich, Michael Feld, Enrico Vogt, Marco Koschorreck, Wilhelm Zwerger, and Michael Köhl. Radio-frequency spectroscopy of a strongly interacting two-dimensional fermi gas. *Physical review letters*, 106(10):105301, 2011.

[45] Ariel T Sommer, Lawrence W Cheuk, Mark JH Ku, Waseem S Bakr, and Martin W Zwierlein. Evolution of fermion pairing from three to two dimensions. *Physical review letters*, 108(4):045302, 2012.

[46] Christian Langmack, Marcus Barth, Wilhelm Zwerger, and Eric Braaten. Clock shift in a strongly interacting two-dimensional fermi gas. *Physical review letters*, 108(6):060402, 2012.

[47] Gabriele Giuliani and Giovanni Vignale. *Quantum theory of the electron liquid.* Cambridge university press, 2005.

[48] Matthias Punk. *Many-particle physics with ultracold gases.* PhD thesis, Technische Universität München, 2010.

[49] Alexander Altland and Ben D Simons. *Condensed matter field theory.* Cambridge University Press, 2010.

[50] M Punk and W Zwerger. Theory of rf-spectroscopy of strongly interacting fermions. *Physical review letters*, 99(17):170404, 2007.

[51] Rudolf Haussmann, Matthias Punk, and Wilhelm Zwerger. Spectral functions and rf response of ultracold fermionic atoms. *Physical Review A*, 80(6):063612, 2009.

[52] Eric Braaten, Daekyoung Kang, and Lucas Platter. Short-time operator product expansion for rf spectroscopy of a strongly interacting fermi gas. *Physical review letters*, 104(22):223004, 2010.

[53] Eric Braaten, Daekyoung Kang, and Lucas Platter. Universal relations for identical bosons from three-body physics. *Physical review letters*, 106(15):153005, 2011.

[54] Ariel T Sommer, Lawrence W Cheuk, Mark JH Ku, Waseem S Bakr, and Martin W Zwierlein. Evolution of fermion pairing from three to two dimensions. *Physical review letters*, 108(4):045302, 2012.

[55] William Schneider, Vijay B Shenoy, and Mohit Randeria. Theory of radio frequency spectroscopy of polarized fermi gases. *arXiv preprint arXiv:0903.3006*, 2009.

[56] Israel M Gel'fand and GE Shilov. *Generalized functions. Vol. I: Properties and operations, Translated by Eugene Saletan.* Academic Press, New York, 1964.

[57] Gordon Baym, CJ Pethick, Zhenhua Yu, and Martin W Zwierlein. Coherence and clock shifts in ultracold fermi gases with resonant interactions. *Physical review letters*, 99(19):190407, 2007.

[58] Bernd Fröhlich. *A Strongly Interacting Two-Dimensional Fermi Gas.* PhD thesis, St Catharine's College, University of Cambridge, 2011.

[59] G Bertaina and S Giorgini. Bcs-bec crossover in a two-dimensional fermi gas. *Physical review letters*, 106(11):110403, 2011.

[60] Eric Braaten and HW Hammer. Universal relation for the inelastic two-body loss rate. *Journal of Physics B: Atomic, Molecular and Optical Physics*, 46(21):215203, 2013.

[61] Ariel T Sommer and Martin W Zwierlein. private communication.

[62] M Bartenstein, A Altmeyer, S Riedl, R Geursen, S Jochim, C Chin, J Hecker Denschlag, R Grimm, A Simoni, E Tiesinga, et al. Precise determination of li 6 cold collision parameters by radio-frequency spectroscopy on weakly bound molecules. *Physical review letters*, 94(10):103201, 2005.

[63] Michael Köhl. private communication.

[64] William Schneider and Mohit Randeria. Universal short-distance structure of the single-particle spectral function of dilute fermi gases. *Physical Review A*, 81(2):021601, 2010.

[65] JT Stewart, JP Gaebler, and DS Jin. Using photoemission spectroscopy to probe a strongly interacting fermi gas. *Nature*, 454(7205):744–747, 2008.

[66] JP Gaebler, JT Stewart, TE Drake, DS Jin, A Perali, P Pieri, and GC Strinati. Observation of pseudogap behaviour in a strongly interacting fermi gas. *Nature Physics*, 6(8):569–573, 2010.

[67] Piotr Magierski, Gabriel Wlazłowski, Aurel Bulgac, and Joaquín E Drut. Finite-temperature pairing gap of a unitary fermi gas by quantum monte carlo calculations. *Physical review letters*, 103(21):210403, 2009.

[68] Qijin Chen and K Levin. Momentum resolved radio frequency spectroscopy in trapped fermi gases. *Physical review letters*, 102(19):190402, 2009.

[69] Michael Feld, Bernd Fröhlich, Enrico Vogt, Marco Koschorreck, and Michael Köhl. Observation of a pairing pseudogap in a two-dimensional fermi gas. *Nature*, 480(7375):75–78, 2011.

[70] Lev Davidovich Landau and EM Lifshitz. *Statistical Physics. Part 1: Course of Theoretical Physics*. Pergamon, 1980.

[71] Marcus Barth and Johannes Hofmann. Pairing effects in the nondegenerate limit of the two-dimensional fermi gas. *Physical Review A*, 89(1):013614, 2014.

[72] Vudtiwat Ngampruetikorn, Jesper Levinsen, and Meera M Parish. Pair correlations in the two-dimensional fermi gas. *Physical review letters*, 111(26):265301, 2013.

[73] Erich Beth and George E Uhlenbeck. The quantum theory of the non-ideal gas. ii. behaviour at low temperatures. *Physica*, 4(10):915–924, 1937.

[74] Xia-Ji Liu, Hui Hu, and Peter D Drummond. Exact few-body results for strongly correlated quantum gases in two dimensions. *Physical Review B*, 82(5):054524, 2010.

[75] Hui Hu, Xia-Ji Liu, Peter D Drummond, and Hui Dong. Pseudogap pairing in ultracold fermi atoms. *Physical review letters*, 104(24):240407, 2010.

[76] Xia-Ji Liu, Hui Hu, and Peter D Drummond. Virial expansion for a strongly correlated fermi gas. *Physical review letters*, 102(16):160401, 2009.

[77] Ben D Simons and Alexander Altland. *Condensed Matter Field Theory*. Cambridge University Press, 2010.

[78] Alexander L Fetter and John Dirk Walecka. *Quantum theory of many-particle systems*. Courier Corporation, 2003.

[79] Mohit Randeria, Ji-Min Duan, and Lih-Yir Shieh. Bound states, cooper pairing, and bose condensation in two dimensions. *Physical review letters*, 62(9):981, 1989.

[80] Tilman Enss, Rudolf Haussmann, and Wilhelm Zwerger. Viscosity and scale invariance in the unitary fermi gas. *Annals of Physics*, 326(3):770–796, 2011.

[81] EM Lifshitz and LP Pitaevskii. *Statistical Physics Part 2, Landau and Lifshitz Course of Theoretical Physics Vol. 9*. Pergamon Press, Oxford, 1980.

[82] R Combescot, A Recati, C Lobo, and Fv Chevy. Normal state of highly polarized fermi gases: simple many-body approaches. *Physical review letters*, 98(18):180402, 2007.

[83] Richard Schmidt, Tilman Enss, Ville Pietilä, and Eugene Demler. Fermi polarons in two dimensions. *Physical Review A*, 85(2):021602, 2012.

[84] Yusuke Nishida. Probing strongly interacting atomic gases with energetic atoms. *Physical Review A*, 85(5):053643, 2012.

[85] VV Flambaum, GF Gribakin, and C Harabati. Analytical calculation of cold-atom scattering. *Physical Review A*, 59(3):1998, 1999.

[86] L. H. Thomas. The interaction between a neutron and a proton and the structure of h$^3$. *Phys. Rev.*, 47:903, 1935.

[87] Richard Schmidt, Steffen Patrick Rath, and Wilhelm Zwerger. Efimov physics beyond universality. *EPJ B*, 85(11):386, 2012.

[88] Richard Schmidt. *From few-to many-body physics with ultracold atoms*. PhD thesis, Technische Universität München, 2013.

[89] Jia Wang, J. P. D'Incao, B. D. Esry, and Chris H. Greene. Origin of the three-body parameter universality in efimov physics. *Phys. Rev. Lett.*, 108:263001, 2012.

[90] R. J. Wild, P. Makotyn, J. M. Pino, E. A. Cornell, and D. S. Jin. Measurements of tan's contact in an atomic bose-einstein condensate. *Phys. Rev. Lett.*, 108:145305, 2012.

[91] M Berninger, A Zenesini, B Huang, W Harm, H-C Nägerl, F Ferlaino, R Grimm, PS Julienne, and JM Hutson. Universality of the three-body parameter for efimov states in ultracold cesium. *Physical review letters*, 107(12):120401, 2011.

[92] Matteo Zaccanti, Benjamin Deissler, Chiara D'Errico, Marco Fattori, Mattia Jona-Lasinio, Stefan Müller, Giacomo Roati, Massimo Inguscio, and Giovanni Modugno. Observation of an efimov spectrum in an atomic system. *Nature Physics*, 5(8):586–591, 2009.

262

[93] T Kraemer, M Mark, P Waldburger, JG Danzl, C Chin, B Engeser, AD Lange, K Pilch, A Jaakkola, H-C Nägerl, et al. Evidence for efimov quantum states in an ultracold gas of caesium atoms. *Nature*, 440(7082):315–318, 2006.

[94] P. Makotyn, C. E. Klauss, D. L. Goldberger, E. A. Cornell, and D. S. Jin. Universal dynamics of a degenerate unitary bose gas. *Nat. Phys.*, 10:1745, 2014.

[95] Richard J. Fletcher, Alexander L. Gaunt, Nir Navon, Robert P. Smith, and Zoran Hadzibabic. Stability of a unitary bose gas. *Phys. Rev. Lett.*, 111:125303, Sep 2013.

[96] B. S. Rem, A. T. Grier, I. Ferrier-Barbut, U. Eismann, T. Langen, N. Navon, L. Khaykovich, F. Werner, D. S. Petrov, F. Chevy, and C. Salomon. Lifetime of the bose gas with resonant interactions. *Phys. Rev. Lett.*, 110:163202, Apr 2013.

[97] Ulrich Eismann, Lev Khaykovich, Sébastien Laurent, Igor Ferrier-Barbut, Benno S. Rem, Andrew T. Grier, Marion Delehaye, Frédéric Chevy, Christophe Salomon, Li-Chung Ha, and Cheng Chin. Universal loss dynamics in a unitary bose gas. *arXiv:1505.04523*, 2015.

[98] B. D. Esry, Chris H. Greene, and James P. Burke. Recombination of three atoms in the ultracold limit. *Phys. Rev. Lett.*, 83:1751, 1999.

[99] Esben Nielsen and J. H. Macek. Low-energy recombination of identical bosons by three-body collisions. *Phys. Rev. Lett.*, 83:1566, 1999.

[100] José P D'Incao, Hiroya Suno, and Brett D Esry. Limits on universality in ultracold three-boson recombination. *Physical review letters*, 93(12):123201, 2004.

[101] Weiran Li and Tin-Lun Ho. Bose gases near unitarity. *Physical Review Letters*, 108(19):195301, 2012.

[102] Sébastien Laurent, Xavier Leyronas, and Frédéric Chevy. Momentum distribution of a dilute unitary bose gas with three-body losses. *Phys. Rev. Lett.*, 113:220601, 2014.

[103] Félix Werner and Yvan Castin. General relations for quantum gases in two and three dimensions. ii. bosons and mixtures. *Phys. Rev. A*, 86:053633, 2012.

[104] W. Zwerger. Strongly interacting fermi gases. *Lecture Notes*, 2014.

[105] D Hudson Smith, Eric Braaten, Daekyoung Kang, and Lucas Platter. Two-body and three-body contacts for identical bosons near unitarity. *Physical review letters*, 112(11):110402, 2014.

[106] Yvan Castin and Félix Werner. Single-particle momentum distribution of an efimov trimer. *Phys. Rev. A*, 83:063614, 2011.

[107] D. S. Petrov. Three-body problem in fermi gases with short-range interparticle interaction. *Phys. Rev. A*, 67:010703, 2003.

[108] Mingyuan Sun and Xavier Leyronas. High-temperature expansion for interacting fermions. *arXiv preprint arXiv:1506.07334*, 2015.

[109] Marcus Barth and Johannes Hofmann. Efimov correlations in strongly interacting bose gases. *arXiv preprint arXiv:1506.06751*, 2015.

[110] Chen Ji, Eric Braaten, Daniel R Phillips, and Lucas Platter. Universal relations for range corrections to efimov features. *arXiv preprint arXiv:1506.02334*, 2015.

[111] Gustav Doetsch. *Introduction to the Theory and Application of the Laplace Transformation.* Springer Science & Business Media, 2012.

[112] GV Skorniakov and KA Ter-Martirosian. Three body problem for short range forces. i. scattering of low energy neutrons by deuterons. *Sov. Phys. JETP*, 4, 1957.

[113] Wilhelm Magnus, Raj Pal Soni, and Fritz Oberhettinger. *Formulas and theorems for the special functions of mathematical physics.* Springer, 1966.

[114] Milton Abramowitz and Irene A Stegun. *Handbook of mathematical functions: with formulas, graphs, and mathematical tables.* Number 55. Courier Corporation, 1964.

[115] John R Taylor. *Scattering theory.* Wiley, 1972.

[116] DS Petrov, Christophe Salomon, and Gora V Shlyapnikov. Weakly bound dimers of fermionic atoms. *Physical Review Letters*, 93(9):090404, 2004.

[117] A. Pais and G. E. Uhlenbeck. On the quantum theory of the third virial coefficient. *Phys. Rev.*, 116:250, 1959.

[118] William H Press. *Numerical recipes 3rd edition: The art of scientific computing.* Cambridge university press, 2007.

[119] Tin-Lun Ho and Erich J Mueller. High temperature expansion applied to fermions near feshbach resonance. *Physical review letters*, 92(16):160404, 2004.

[120] Paulo F. Bedaque and Gautam Rupak. Dilute resonating gases and the third virial coefficient. *Phys. Rev. B*, 67:174513, May 2003.

[121] David B Kaplan and Sichun Sun. New field-theoretic method for the virial expansion. *Physical review letters*, 107(3):030601, 2011.

[122] Xia-Ji Liu, Hui Hu, and Peter D Drummond. Three attractively interacting fermions in a harmonic trap: Exact solution, ferromagnetism, and high-temperature thermodynamics. *Physical Review A*, 82(2):023619, 2010.

[123] Yvan Castin and Félix Werner. Le troisième coefficient du viriel du gaz de bose unitaire. *Canadian Journal of Physics*, 91:382, 2013.

[124] Chen Ji, Daniel R Phillips, and Lucas Platter. The three-boson system at next-to-leading order in an effective field theory for systems with a large scattering length. *Annals of Physics*, 327(7):1803–1824, 2012.

[125] Elliott H Lieb and Robert Seiringer. *The stability of matter in quantum mechanics.* Cambridge University Press, 2010.

[126] Philippe Nozières and David Pines. *The theory of quantum liquids.* Perseus, 1999.

[127] W Kohn and JM Luttinger. New mechanism for superconductivity. *Physical Review Letters*, 15(12):524, 1965.

[128] Reza Jamei, Steven Kivelson, and Boris Spivak. Universal aspects of coulomb-frustrated phase separation. *Physical review letters*, 94(5):056805, 2005.

[129] Tsuneya Ando, Alan B Fowler, and Frank Stern. Electronic properties of two-dimensional systems. *Reviews of Modern Physics*, 54(2):437, 1982.

*Bibliography*

[130] JC Kimball. Short-range correlations and electron-gas response functions. *Physical Review A*, 7(5):1648, 1973.

[131] JC Kimball. Short-range correlations and the structure factor and momentum distribution of electrons. *Journal of Physics A: Mathematical and General*, 8(9):1513, 1975.

[132] AK Rajagopal and John C Kimball. Correlations in a two-dimensional electron system. *Physical Review B*, 15(5):2819, 1977.

[133] Tosio Kato. On the eigenfunctions of many-particle systems in quantum mechanics. *Communications on Pure and Applied Mathematics*, 10(2):151–177, 1957.

[134] Maria Hoffmann-Ostenhof and Rudi Seiler. Cusp conditions for eigenfunctions of n-electron systems. *Physical Review A*, 23(1):21, 1981.

[135] M Hoffmann-Ostenhof, T Hoffmann-Ostenof, and Hanns Stremnitzer. Electronic wave functions near coalescence points. *Physical review letters*, 68(26):3857, 1992.

[136] Kurt Gottfried and Tung-Mow Yan. *Quantum mechanics: fundamentals.* Springer Science & Business Media, 2003.

[137] Boris Podolsky and Linus Pauling. The momentum distribution in hydrogen-like atoms. *Physical Review*, 34(1):109, 1929.

[138] Michael J Lighthill. *An introduction to Fourier analysis and generalised functions.* Cambridge University Press, 1964.

[139] Barry R Holstein. Quantum mechanics in momentum space: The coulomb system. *American Journal of Physics*, 63(8):710–716, 1995.

[140] Julian Schwinger. Coulomb green's function. *Journal of Mathematical Physics*, 5(11):1606–1608, 1964.

[141] GS Adkins. Derivation of the schrödinger-coulomb green's function from the scattering expansion. *Il Nuovo Cimento B*, 97(1):99–107, 1987.

[142] Walter Dittrich. The coulomb green's function in two dimensions. *American Journal of Physics*, 67(9):768–775, 1999.

[143] G Barton. Rutherford scattering in two dimensions. *American Journal of Physics*, 51(5):420–422, 1983.

[144] Qiong-gui Lin. Scattering by a coulomb field in two dimensions. *American Journal of Physics*, 65(10):1007–1009, 1997.

[145] AK Rajagopal, JC Kimball, and Mahadev Banerjee. Short-ranged correlations and the ferromagnetic electron gas. *Physical Review B*, 18(5):2339, 1978.

[146] Göran Niklasson. Dielectric function of the uniform electron gas for large frequencies or wave vectors. *Physical Review B*, 10(8):3052, 1974.

[147] KS Singwi, MP Tosi, RH Land, and A Sjölander. Electron correlations at metallic densities. *Physical Review*, 176(2):589, 1968.

[148] KS Singwi and MP Tosi. Correlations in electron liquids. *Solid State Physics*, 36:177–266, 1982.

[149] Harry Bateman. *Tables of Integral Transforms [Volume II]*. McGraw-Hill Book Company, 1954.

[150] Peter Lepage. How to renormalize the schrodinger equation. *arXiv preprint nucl-th/9706029*, 1997.

[151] S. K. Bogner and D. Roscher. High-momentum tails from low-momentum effective theories. *Phys. Rev. C*, 86:064304, Dec 2012.

[152] Shizhong Zhang and Anthony J Leggett. Universal properties of the ultracold fermi gas. *Physical Review A*, 79(2):023601, 2009.

[153] Paola Gori-Giorgi and Paul Ziesche. Momentum distribution of the uniform electron gas: Improved parametrization and exact limits of the cumulant expansion. *Physical Review B*, 66(23):235116, 2002.

[154] JC Kimball. High-density expansion of the electron-gas correlation function. *Physical Review B*, 14(6):2371, 1976.

[155] ND Drummond and RJ Needs. Quantum monte carlo study of the ground state of the two-dimensional fermi fluid. *Physical Review B*, 79(8):085414, 2009.

[156] Markus Holzmann, Bernard Bernu, Carlo Pierleoni, Jeremy McMinis, David M Ceperley, Valerio Olevano, and Luigi Delle Site. Momentum distribution of the homogeneous electron gas. *Physical review letters*, 107(11):110402, 2011.

[157] Johannes Hofmann, Marcus Barth, and Wilhelm Zwerger. Short-distance properties of coulomb systems. *Physical Review B*, 87(23):235125, 2013.

[158] Alexei Ivlev, Hartmut Löwen, Gregor Morfill, and C Patrick Royall. *Complex plasmas and colloidal dispersions*. World Scientific, 2012.

[159] K-F Berggren. Particle correlations in a classical one-component plasma. *Physical Review A*, 1(6):1783, 1970.

# Acknowledgements

> "Image ist das, was man
> braucht, damit die anderen
> denken, dass man so ist, wie
> man gerne wär'."
>
> *(Frank Markus Barwasser als
> Erwin Pelzig)*

First and foremost, I want to thank my advisor, Wilhelm Zwerger, for his continuous support and the opportunity to do research in this great group. Thank you also for helping me come into contact with other researchers, as well as the possibility to go to many conferences, and even to work abroad for a short while. I hope you found our discussions as fruitful as me, and I am very grateful for your helpfulness and patience whenever I had a question. Last but not least I want to express my gratitude for the huge freedom I was provided with, both when choosing and doing the research.

I also want to thank Hans-Werner Hammer for co-examining this thesis. I hope it wasn't a relentless grind for you, which might be the first impression one gets when scrolling through this thesis.

Furthermore, my thanks go to Eric Braaten and Christian Langmack for their big hospitality during my stay in the United States. Our collaboration was great, and I learned a lot in Ohio. Additionally, I want to thank Christian for the marathon of discussions we had during our overlapping time in Munich.

Special thanks also goes to Johannes Hofmann, with whom (as you might have noticed) three of the four articles that where published in the context of this thesis were written. For me, our collaboration was as fun as it was fruitful. I wish you the very best for your future in physics.

I want to also thank Marianne Bauer and Richard Schmidt, as well as all other